Additively manufactured function-tailored bone implants made of graphene-containing biodegradable metal matrix composites

Chen, Keyu; Dong, Jiahui; Putra, Niko Eka; Fratila-Apachitei, Lidy Elena; Zhou, Jie; Zadpoor, Amir A.

DOI
10.1016/j.pmatsci.2025.101517

Publication date
2026

Document Version
Final published version

Published in
Progress in Materials Science

Progress in Materials Science 155 (2026) 101517

Contents lists available at ScienceDirect

Progress in Materials Science

journal homepage: www.elsevier.com/locate/pmatsci

Additively manufactured function-tailored bone implants made of graphene-containing biodegradable metal matrix composites

Keyu Chen *, Jiahui Dong *, Niko Eka Putra, Lidy Elena Fratila-Apachitei, Jie Zhou, Amir A. Zadpoor

Department of Biomechanical Engineering, Faculty of Mechanical Engineering, Delft University of Technology, Mekelweg 2, 2628 CD Delft, the Netherlands

ARTICLE INFO

Keywords:
Bone implants
Graphene and its derivatives
Biodegradable metal
Metal matrix composite
Additive manufacturing

ABSTRACT

While conventionally manufactured metallic biomaterials can hardly meet all the requirements for bone implants including complex geometry, exact dimensions, adequate biodegradability, bone-matching mechanical properties, and biological function, two additional tools have recently appeared in the arsenal of biomaterials scientists which promise to deliver the desired combination of properties. First, the unique mechanical, electrical, and biological properties of graphene (Gr) and its derivatives (GDs), *e.g.*, a Young's modulus up to 1 TPa, can be utilized to create metal matrix composites in which GDs of varied contents (typically not more than 2 wt%), sizes (lateral sizes from a few nanometers to several micrometers), surface areas (up to the theoretical value of 2630 m^2/g), and layer numbers (typically up to 10) are embedded in the biodegradable metal matrix, thereby endowing the composite implants with extraordinary properties. Second, the distinct advantages of additive manufacturing (AM) make it possible for GD-containing composite materials to precisely mimic the complex shapes and structures of bones at multiple length scales. Here, a comprehensive review of the recent advances in the development of GD-containing biodegradable metal matrix composites (GBMMCs), ranging from composite fabrication, including composite powder preparation, and AM processes, to the evaluation of AM composites in terms of their mechanical and biological properties, is presented. Furthermore, the constraints in processing composite powders, the advantages and disadvantages of applicable AM techniques, and the mechanisms of mechanical reinforcement, biodegradation modulation, osteogenesis improvement, and cytotoxicity/antibacterial balance are critically analyzed. Thereafter, the foreseeable challenges faced in the development of the next-generation of bone implants based on GBMMCs are presented and some future directions of research are identified.

1. Introduction

The deciding factor in the clinical adoption of the next-generation of orthopedic implants [1] made from metallic biomaterials is safety, which means that biodegradable metals need to demonstrate safety once implanted in the human body. The clinical use of biodegradable metals in the treatment of bony defects has a set of requirements regarding their biocompatibility including optimum mechanical properties and biodegradation rate, osteogenic and antibacterial properties, and non-toxic degradation products [2,3].

* Corresponding authors.
E-mail addresses: K.Chen-6@tudelft.nl (K. Chen), Jiahui.dong@philips.com (J. Dong).

https://doi.org/10.1016/j.pmatsci.2025.101517
Received 11 December 2024; Received in revised form 25 March 2025; Accepted 20 May 2025
Available online 24 May 2025

Inert metals and alloys, both in the bulk form and in the porous form, such as titanium, stainless steel, and cobalt-chromium alloys, have been extensively studied as orthopedic biomaterials over the last few decades [4]. The inert nature of these biomaterials does not allow for complete bone regeneration and their residence permanently at the implantation site often causes stress shielding, chronic inflammation, or secondary removal surgeries. Biodegradable metals (BMs) are defined as a class of metallic biomaterials that become gradually corroded *in vivo* and dissolve completely with no implant residue, when they have completed their task [5]. The corrosion products released from such biomaterials should ideally elicit an appropriate host response and assist in tissue healing. Hailed as a revolutionary class of metallic biomaterials for bone repair and temporary bone substitution, BMs have, in recent years, emerged as a popular research topic in the field of biomaterials due to their biodegradability, good biomechanical properties, and low costs [6]. Representative BMs that have been developed include magnesium-based materials (*e.g.*, Mg, Mg-Ca, and Mg-Zn) [7–9], iron-based materials (*e.g.*, Fe, and Fe-Mn) [10,11], and zinc-based materials (*e.g.*, Zn, and Zn-Li) [12,13]. However, their clinical translation faces critical challenges, mainly due to the high and unpredictable degradation rates of Mg-based alloys leading to premature mechanical failure and hydrogen gas accumulation, the excessively slow degradation of Fe-based alloys hindering complete bone remodeling, and the insufficient mechanical strength and cytocompatibility of Zn-based alloys. To enhance the properties or to overcome the inherent drawbacks of these BMs, another component, mostly a ceramic biomaterial (*e.g.*, hydroxyapatite (HAP/HA) or β-tricalcium phosphate (TCP)) or a polymeric biomaterial (*e.g.*, polylactic acid (PLA) or polycaprolactone (PCL)), has been added to BMs to form metal matrix composites (MMCs) [14]. Due to the vast ranges of physical, biochemical, and mechanical properties of metal matrices and ceramic/polymer reinforcements, MMCs can offer a unique balance in physical, biochemical, and mechanical properties. By appropriate choice of composition, morphology, and distribution of ceramic/polymer reinforcements, biodegradable MMCs (BMMCs) can be equipped with customizable functionality to meet the increasing demands for adjustability and adaptation in terms of mechanical properties and degradation rate [15–18]. BMMCs require all the components to be non-toxic to humans [19] and biodegradable, with the main component being a biodegradable metal.

Graphene (Gr) is an allotrope of carbon. Intrinsically, it is a single layer of carbon atoms that are held together by a backbone of overlapping sp2 hybrid bonds [20,21]. In addition to Gr itself, several important graphene derivatives, including graphene oxide (GO), reduced graphene oxide (RGO), and carboxyl graphene oxide (CGO), have emerged due to the ease with which Gr can be modified, although other derivatives with different property profiles are also of importance for particular applications, including biomedical applications, for example, graphyne and graphdiyne for nanoelectronics, desalinator, inorganic and organic sensors and other bio-related processes [22]. These four forms of Gr-based materials exhibit distinct properties due to their different molecular structural arrangements [23–25]. In addition to their renowned mechanical properties (*e.g.*, a Young's modulus value of ~1 TPa) and large surface area, graphene and its derivatives (GDs) possess many unique properties such as high electrical conductivity, tunable surface chemistry, and bioactivity that are of direct relevance to BMMCs. Among these compounds, Gr, GO, and RGO have been widely used for enhancing the physical and chemical properties of metals due to their superior thermal and chemical stability [26–28] and other physical properties such as high thermal conductivity and optical transparency [29]. Since the invention of Gr in 2004, there have been

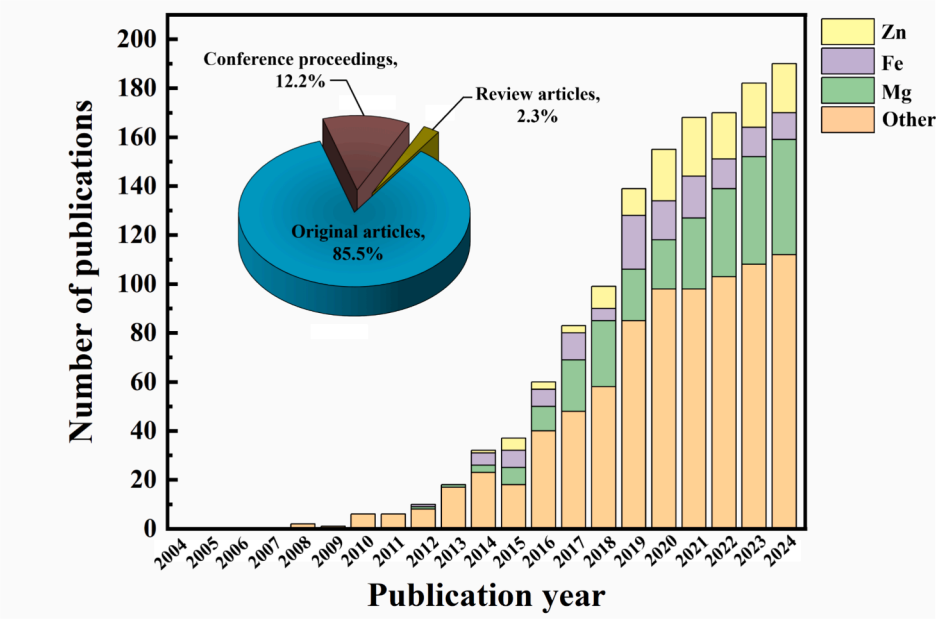

Fig. 1. Research articles on GBMMCs and other GD-containing MMCs for bone implants: the number of publications *versus* the publication year (Note: the reference database is based on bone implants or bone scaffold applications selected from online databases of the 'PubMed', 'Scopus', and 'Web of Science', and contains 'GDs' acting as the second reinforcement phase instead of coatings, *etc.*, since 2004, and 'BMs and other biometals including Ti, Co-Cr, *etc.*' acting as the metal matrix instead of functional doping phase, *etc.*, since 2012).

a plethora of studies on GD-containing metal matrix composites (GMMCs). It has been widely acknowledged that adopting GDs as a reinforcing phase for the development of orthopedic implants is, indeed, a promising way to augment the loading-bearing capacity of metallic implants [30–34]. The evidence of increasing attention to GDs as a reinforcing component added to BM bone implant biomaterials is presented in Fig. 1, showing the number of publications on bone implant biomaterials reinforced by GDs, categorized, based on the type of the metallic biomaterial (*i.e.*, BMs including Mg, Fe, and Zn, together with other metals and their alloys, such as Ti, Co-Cr, *etc.*) for bone implants over a period of 2008 to 2024. The inset of Fig. 1 indicates that 85.5 % of published articles out of the total were original research articles. As is clear from this figure, the attempts to introduce GDs into bone implant biomaterials began around 2008. However, the number of publications did not sharply rise until 2012 when the concept of BMs was introduced. The research on GD-containing BMMC (GBMMC) bone implant biomaterials has, since then, been intensified and its pace has steadily increased.

Apart from the load-bearing capability, four fundamental aspects of GDs for their use as a reinforcement phase in BMMC bone implant biomaterials need to be considered, including toxicity (both cytotoxicity and systemic toxicity), biodegradability, antibacterial properties and osteogenesis [35–39]. Yang *et al.* [40] reviewed the toxicity of GDs by describing the behaviors of GDs in microorganisms, cells, and animals. The vast existing literature on this topic indicates that the physicochemical properties of GDs, such as surface functional groups, charges, coatings on Gr, sizes, and structural defects, may all affect its *in vitro* and *in vivo* behavior as well as its toxicity in biological systems [41,42]. Biodegradability of Gr is one of the fundamental parameters determining the fate of this

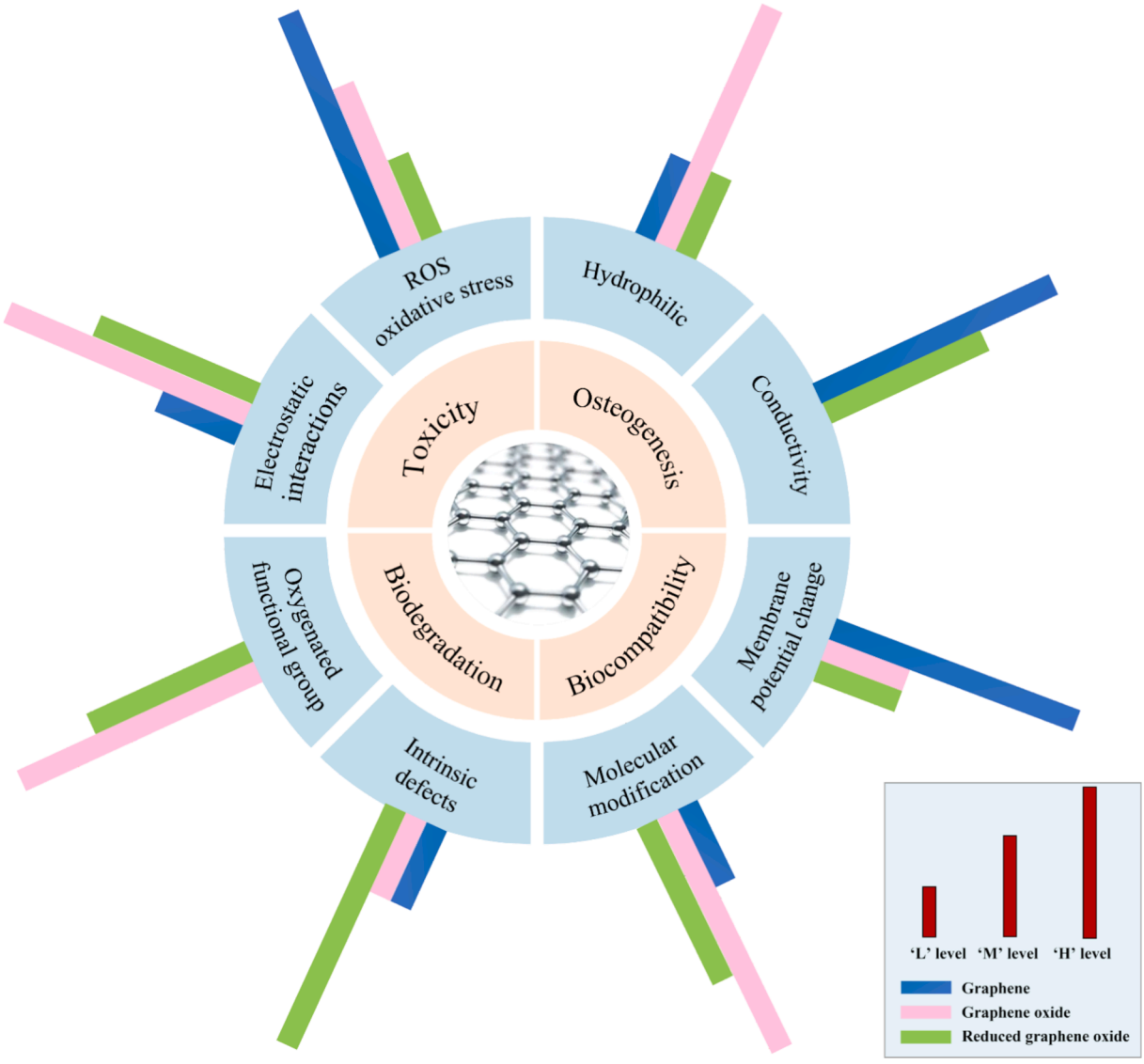

Fig. 2. A schematic diagram illustrating the intrinsic physicochemical characteristics of GDs in terms of toxicity, biodegradability, antibacterial properties and osteogenic properties.

material for application in biodegradable implants *in vivo*. For the first time, by means of confocal Raman imaging, Girish *et al.* [43] provided clear evidence of *in vivo* biodegradation of Gr and confirmed the macrophage-mediated degradation of Gr through changes in the D and G bands. Later on, it became clear that the biodegradation of GDs is strongly dependent on the oxygen content, type of functional groups, defects, lateral size, and the number of layers [44]. In addition, GDs were found to be capable of supporting cell attachment, cell growth and proliferation, cytoskeleton development, and the activation of osteogenesis and bone development pathways, thereby inducing and supporting bone tissue formation [45]. Fig. 2 illustrates the eight pathways through which Gr, GO, and RGO influence biodegradation, toxicity, antibacterial properties, and osteogenesis. These include electrostatic interactions, oxidative stress induced by oxygen reactive species (ROS), oxygenated functional group, intrinsic defects, electrical conductivity, hydrophilicity, molecular modification, and membrane potential change. The histograms quantify the degree of the influences of these three Gr types in the eight pathways by low ('L'), medium ('M'), and high ('H').

Additive manufacturing (AM), commonly referred to as 3D printing, is a disruptive technology revolutionizing the way that products are made. It offers great flexibility for the design and fabrication of complex and/or customized parts through a layer-by-layer manufacturing strategy. Over the last several years, AM has rapidly advanced in terms of material diversity, printing strategy, accuracy, and resolution, thereby expanding its application areas in optoelectronics, sensors, bioengineering, and soft robotics [46–49]. Recently, AM has been demonstrated to be capable of precisely controlling the microarchitecture of bone implant biomaterials, thereby presenting an unparalleled opportunity to tailor the mechanical properties of porous structures mimicking those of the human bone [50–52] while also adjusting the biodegradation profile of biodegradable metals [53]. There are numerous reviews on the holistic material-structure–function integrated (MSFI) analysis of GMMCs [26,28,54]. The reviews on GDs to reinforce bone implant biomaterials have also appeared in the last decade, mainly focusing on non-biodegradable inert metallic biomaterials, such as titanium alloys [55] and stainless steel alloys [56], and on non-metallic biomaterials, such as ceramics [54,57] and hydrogels [58]. To the best of the authors' knowledge, no reviews have ever been published on AM GBMMC bone implant biomaterials composed of BMs as the most promising biomaterials for bone implants, and GDs as ideal exotic reinforcement materials, enabled by AM. A state-of-the-art review on this topic is essential to foster the developments of next-generation load-bearing and function-tailored novel bone implant biomaterials.

This review article is focused on AM GBMMC bone implant biomaterials and covers composite powder preparation, AM processes, mechanical properties, biodegradation behavior, cytotoxicity, osteogenic, and antibacterial properties. Fig. 3 illustrates the fundamental framework underlying the development of AM GBMMCs for next-generation bone implants. After a brief introduction, Section 2 summarizes the limitations of traditional powder fabrication methods for GBMMCs and the recent advances in developing novel composite powder feedstock materials for preparing GBMMCs. Section 3 describes the AM technologies that can be used to fabricate porous bone implants and analyzes their advantages and disadvantages. Section 4 details the strengthening mechanisms of GBMMCs and achievable mechanical properties as well as the effects of GDs on biodegradable and biological performances of BMMCs. Section 5 lists the limitations of the current GBMMCs and the remaining practical challenges faced when developing GBMMC bone implant biomaterials. Finally, Section 6 discusses the future prospects concerning the development of the next generation of bone implants through the MSFI approach in combination with AM. All abbreviations, and their corresponding meanings that appear in this review are summarized in Table 1.

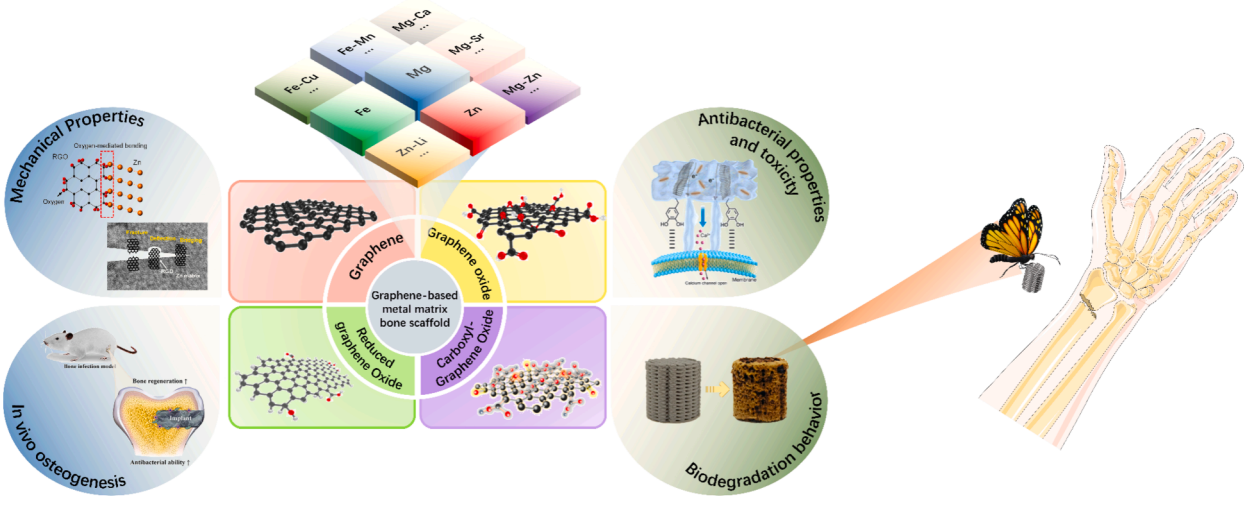

Fig. 3. An illustration of the basic framework for developing AM GD-reinforced biodegradable metals for the next generation of bone implants [59–63].

Table 1
Abbreviations used in the articles presented in the alphabetical order.

Abbreviations	Meaning
AM	Additive manufacturing
ALD	Average lateral dimension
ALP	Alkaline phosphatase
AG	Alginate/gelatin
BMs	Biodegradable metals
BMMCs	Biodegradable metal matrix composites
BJ	Binder jetting
BMP-2	Bone morphogenetic protein-2
CGO	Carboxyl graphene oxide
CMCs	Ceramic matrix composites
Cu	Copper
CTE	Coefficient of thermal expansion
CPA	Corrosion-promotion activity
CVD	Chemical vapor deposition
CMCNF	Carboxymethyl chitosan
CS	Cellular structure
DED	Directed energy deposition
DMLS	Direct metal laser sintering
DMD	Disintegrated melt deposition
DIC	Digital image correlation
EI	Elongation
EBM	Electron beam melting
EBSD	Electron Backscattered Diffraction
EIS	Electrochemical impedance spectroscopy
ECM	Extracellular matrix
E. coli	Escherichia coli
FFT	Fast Fourier Transform
FAK	Focal adhesion kinase
FACS	Fluorescence-Activated Cell Sorting
Gr	Graphene
GDs	Graphene and its derivatives
GBMMCs	GD-containing biodegradable metal matrix composites
GO	Graphene oxide
GMMCs	GD-containing metal matrix composites
GNPs	Graphene nanoplatelets
GNS	Graphene nanosheet
HSBM	High-speed ball milling
HAP/HA	Hydroxyapatite
HIP	Hot isostatic pressing
HRTEM	High resolution transmission electron microscope
HBSS	Hank's Balanced Salt Solution
hMSCs	Human mesenchymal stem cells
HUVECs	Human umbilical vein endothelial cells
HADMSCs	Human adipose-derived mesenchymal stem cells
ITOP	Integrated tissue-organ printer
ICP	Inductively coupled plasma
LSBM	Low-speed ball milling
LENS	Laser engineered net shaping
MMCs	Metal matrix composites
MSFI	Material-structure–function integrated
ME	Material extrusion
MD	Molecular dynamics
NCTE	Negative coefficient of thermal expansion
N-Gr	Nitrogen-doped graphene
NF-κB	Nuclear factor kappa-B
PCL	Polycaprolactone
PLA	Polylactic acid
P/M	Powder metallurgy
PMMA	Polymethyl methacrylate
PBF	Powder bed fusion
PMs	Pentamode metamaterial
PLLA	Poly-l-lactic acid
PDP	Potentiodynamic polarization
PDMS	Polydimethylsiloxane
PGO-AG	Polydopamine-mediated graphene oxide
PHA	polydopamine-hydroxyapatite
RGO	Reduced graphene oxide
RBCs	Red blood cells

(*continued on next page*)

Table 1 (*continued*)

Abbreviations	Meaning
ROS	Reactive oxygen species
ROCK1	Rho-kinase 1
SSA	Specific surface area
SDBS	Sodium dodecyl benzene sulfonate
SPS	Spark plasma sintering
SLM	Selective laser melting
SLS	Selective laser sintering
SBF	Simulated body fluid
S. aureus	Staphylococcus aureus
SMAs	Shape memory alloys
SME	Shape memory effect
TiC	Titanium carbide
TPMS	Triply periodic minimal surface
TLR	Toll-like receptor
TCP	Tricalcium phosphate
TO	Topology optimization
UTS	Ultimate tensile strength
UCMSCs	umbilical cord mesenchymal stem cells
VP	Vat polymerization
VEGF	Vascular endothelial growth factor
WCA	Water contact angle
YS	Yield strength
ZMCs	Zinc matrix composites
ZOI	Zones of Inhibition

2. Composite powder preparation for GBMMC development

Composite powder characteristics largely determine the quality of 3D printed GBMMCs. The main aim in the preparation of high-performance GBMMC feedstock is to achieve homogeneous dispersion of GDs in the BM matrix and to minimize agglomeration. Mechanical milling or solution-assisted mixing, typically used in conventional powder metallurgy (P/M), is performed at the macroscopic scale and is prone to Gr agglomeration and structural damage. New methods based on molecular level mixing have recently been developed, including *in-situ* coating, *in-situ* synthesis, vacuum filtration, and matrix alloying. In this section, the characteristics of various powder mixing processes, their limitations, and their effects on composite powders are presented.

2.1. Conventional methods

To date, the conventional P/M processes have played an important role in the fabrication of GMMCs. In various P/M processes, a critical step to create uniformly dispersed GDs in the metal matrix is the initial powder mixing step, while the subsequent steps of compaction, sintering, and other processes can only influence the dispersion of GDs to a limited extent [64,65]. In other words, the initial powder mixing step has a great impact on the final performance of GMMCs. Many methods have been employed to achieve homogeneous dispersion (*e.g.*, mechanical milling and solution-assisted mixing) [66,67].

2.1.1. Mechanical milling

Mechanical milling, also called ball milling, typically used for mechanical alloying in P/M, is a top-down synthesis technique that can produce materials with nanostructures. In mechanical milling, as illustrated in Fig. 4a, selected powders are sealed in a steel vial together with a number of steel balls of certain sizes under an inert atmosphere, typically argon. The high-energy rotation of the balls inside the vial causes constant collisions of the balls, leading to the crushing of powder particles entrapped between balls under a high impact force. Mechanical milling is the most widely used technique in the synthesis of GMMCs due to its simplicity, low cost, and effectiveness in dispersing GDs into metal matrices [68]. It has become a preferred technique for the fabrication of GD-reinforced bone scaffold materials due to its simplicity and scalability in preparing GD-containing Mg- [69,70], Zn- [71], and Ti [72]-matrix composites. The duration and speed of ball milling are the two most important process parameters. As the milling time increases, the metal powder particle sizes of the matrix increase due to cold welding, while Gr sizes decrease as a result of repeated collision and shearing [73]. The amount of disorder and the number of defects in Gr are increased after ball milling [74]. On the other hand, a longer ball milling time results in more uniform dispersion of Gr in the matrix, which will provide the corresponding composite with better mechanical performance [75]. Some studies have shown that Gr is not damaged by short-time high-speed ball milling (HSBM) at 360 RPM for 1.5 h [76] or by long-time low-speed ball milling (LSBM) at 75 RPM for 12 h [77]. The lateral size and specific surface area (SSA) of GDs critically determine the processability of GBMMC powders for AM. Smaller flakes with higher SSA improve dispersion homogeneity in metal matrices *via* enhanced van der Waals interactions, but may compromise powder flowability due to agglomeration. Conversely, larger flakes with lower SSA facilitate uniform laser energy absorption during powder bed fusion (PBF) processes, but bring the risk of interfacial void formation from incomplete wrapping [78–80]. Current research on GBMMCs predominantly focuses on multilayer Gr (3–10 layers) due to superior practicality compared to its single-layer counterpart. While single-layer Gr possesses ideal characteristics (*e.g.*, ultrahigh specific surface area of 2630 m^2/g and intrinsic strength of 130 GPa [81]), its scalable

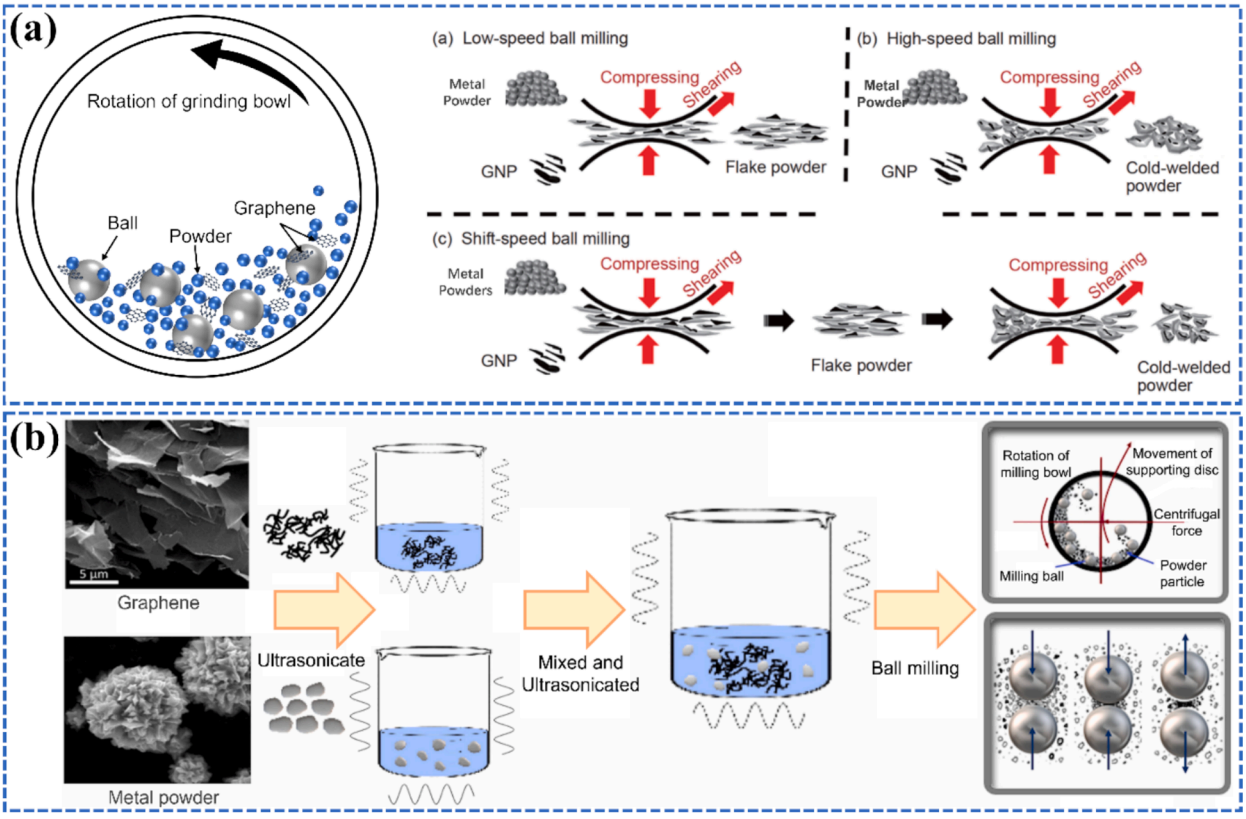

Fig. 4. (a) A schematic drawing of mechanical ball milling and the process of dispersing Gr into BM powder particles through low-speed, high-speed and shift-speed (*i.e.*, high-speed and low-speed combined) ball milling, respectively [83]. (b) A schematic drawing of the solution-assisted milling process for fabricating GBMMCs [84].

fabrication faces critical challenges including prohibitive costs, unstable wrinkled morphology in metal matrices, and limited production yields. In contrast, multilayer Gr demonstrates enhanced process compatibility and cost effectiveness, with its wavy structure adapting to metal melt flow and reducing interfacial porosity. Mechanistically, multilayer Gr leverages interlayer slipping and edge defects to strengthen interfaces. Zhao *et al.* [82] demonstrated that the presence of wrinkles and chemical modification of Gr using functional groups could significantly increase its surface roughness, enhance the van der Waals interaction and consequently lead to higher interfacial shear strength between Gr and the Cu matrix. Edge defects (dangling bonds and oxygen groups) serve as reactive sites for chemical bonding, effectively suppressing delamination. Nevertheless, the non-ideal structure of multilayer Gr fundamentally limits interfacial performance compared to theoretical single-layer models.

2.1.2. Solution-assisted mixing

Solution-assisted mixing involves mixing GDs and metal matrix in an appropriate solvent, followed by stirring and ultrasonication [85]. Once uniform dispersion of GDs in the solution is attained, the matrix material in the form of powder is added to obtain the desired composite composition. The composite mixture solution is then ultrasonicated/stirred for a short period to achieve uniformity of the components in the solution. Fig. 4b illustrates the whole process of solution-assisted milling that ends with ball milling and solvent evaporation [84]. The solvent is selected, based on certain criteria, such as non-reactivity with GDs or the metal, volatility, and ease of evaporation. The solution-assisted method is not suitable for large-scale composite fabrication, because it requires a large amount of liquid medium to ensure adequate mixing of a few grams of composite powders. More importantly, it is difficult to find an organic reagent or a salt solution that does not react with Mg or Zn because of the high chemical activity of these metals. There has, therefore, been little research on the fabrication of GD-containing Mg- or Zn-based composites using solution-assisted milling.

2.2. Novel methods

Conventional P/M methods have been found to be unable to effectively incorporate GDs into the metal matrix due to the large specific surface area of GDs and the van der Waals interactions between GDs nanosheets that promote agglomeration [86]. In addition, the relatively high temperatures involved in P/M processing is not desirable because GDs tend to decompose or become damaged, or because unintended interfacial reaction products may form during subsequent sintering [87]. Various other techniques, based on the molecular-level mixing [88,89], have been explored to address the GD agglomeration problem and achieve exceptional properties.

2.2.1. *In situ* coating of graphene

In situ coating of GDs, *via* direct electrostatic adsorption or electrostatic self-assembly, is a bottom-up way to realize uniform dispersion of GDs in metal matrices [90]. *In situ* coating of GDs can achieve uniform distribution of GDs in various metal powders through a slurry-based method that relies on electrostatic interactions between the negatively charged GDs and positively charged metal powder (*e.g.*, Zn, Ti and Fe) in aqueous suspension when mixed in the slurry. Li *et al.* [91] *in situ* coated RGO onto the surface of TiAl (Ti-43.5Al-6.5Nb-2Cr-0.5B) powder particles (a schematic diagram is presented in Fig. 5a). After being homogeneously dispersed in deionized water through ultrasonic stirring, surfactant sodium dodecyl benzene sulfonate (SDBS) with the SO^{4-} functional group firmly attaches to the surfaces of RGO. Chemical bonds then form between the SO^{4-} functional group and RGO. Under such conditions, the polar end of SDBS (θ) *in situ* reacts with the Ti alloy matrix that is absorbed on the surface of RGO, leading to the formation of a RGO coating on the surface of Ti alloy matrix powder particles. Once RGO is attached, no further agglomeration of individual RGO would be possible. Wen *et al.* [92] also reported the electrostatic assembly method to allow for the absorption of anionic surfactant SDBS-modified RGO with negative charge onto the surface of stainless steel powder particles. This process is very effective and environmentally friendly and has the ability to fabricate bulk samples with large-scale production potential. Nevertheless, the method is usually limited to certain BMMCs (*e.g.*, pure Mg and its alloys that easily react with aqueous solutions), is time-consuming, and can be only applied to small-sized samples [93].

2.2.2. *In situ synthesis*

The *in situ* synthesis method to manufacture GBMMCs is based on controlled "*in situ*" chemical reactions, involving the direct formation of reinforcing GD fillers during the process of chemical interactions between the matrix components and reactive additives [97]. Li *et al.* [94] proposed an *in-situ* vapor–liquid reaction method (Fig. 5b) to fabricate Gr-containing Mg-matrix composites through chemical reactions between CO_2 and Mg melt. This process directly realizes the *in situ* growth and surface modification of Gr. The resulting Gr was found to be homogeneously dispersed and exhibited strong interfacial bonding with the Mg matrix. Zhang *et al.* [98] fabricated few-layer Gr-containing Ni-matrix composites by implementing a facile *in situ* processing strategy involving the transformation from solid carbon precursors of polymethyl methacrylate (PMMA) molecules to Gr reinforcement during vacuum hot-press sintering. It enabled the homogeneous distribution of reinforcing Gr, effective interfacial bonding between Gr nanosheets and the Ni matrix, and resisted grain growth during the high-temperature consolidation process. The Gr/Ni composites resulting from this process had exceptionally high strength and ductility at the same time. The *in situ* synthesis of Gr reinforcement directly on metal powder particles is a subtle and successful strategy that takes advantage of the catalytic property of metal powder particles and solves the problem of structural damage to Gr that typically occurs with conventional mechanical or chemical dispersion methods [99]. A shortcoming of this method is the relatively low production efficiency, which would limit its application, where mass production is required [100].

2.2.3. *Vacuum filtration*

Vacuum filtration is also suitable for the fabrication of GBMMCs with the alignment of Gr being its most notable characteristic [101]. Chu *et al.* [95] developed an efficient and straightforward route for the fabrication of Gr/Cu composites with highly aligned Gr nanoplatelets (GNPs) by employing a vacuum filtration approach, followed by spark plasma sintering (SPS), as illustrated in Fig. 5c. It was demonstrated that a long range and highly aligned GNP network was constructed in the obtained composites, resulting in a record-high in-plane thermal conductivity of 458 W/mK, which was 35 % higher than that of the Cu matrix. Furthermore, they demonstrated that the fairly good GNP alignment achieved in the Gr/Cu composites led to remarkable anisotropic mechanical properties with an in-plane tensile strength and elongation (EI) significantly outperforming the through-the-plane ones [102]. Vacuum filtration is also a cost-effective and eco-friendly method that does involve high-temperature treatments and harmful solvents or additives. The advantage of this method lies in highly aligned GNPs that are dispersed in the composite regardless of the Gr content. Therefore, vacuum filtration paves the way for the fabrication of Gr-containing MMCs with higher Gr contents and with a low risk of agglomeration [103].

2.2.4. *Matrix alloying*

Matrix alloying introduces strong carbide-forming elements, such as Ti, Cr, B, and Zr that can favorably react with GDs to form an interfacial carbide layer [104,105]. The introduction of carbide nanostructure as an interface bridge is a practical strategy to obtain strong interface bonding in Gr/metal systems. Yang *et al.* [96] used titanium carbide (TiC) as interface bridging between the zinc matrix and RGO to improve the interface adhesion and dispersion uniformity of RGO. TiC was *in situ* generated on the RGO plane through chemical vapor deposition and was tightly bound by chemical bonds (Fig. 5d). The TiC nanoparticles grown *in situ* on RGO formed a semi-coherent interface with Zn, which led to strong semi-coherent interfacial bonding between the Zn matrix and the TiC grown on RGO. Ti carbide (Ti_8C_5) [106] and Cr carbide (Cr_7C_3) [107] were also reported to be introduced *in situ* into the transition layer between RGO and pure copper, which resulted in a strong metallurgical bonding interface and decreased the agglomeration of RGO. The matrix alloying method for *in situ* carbide formation is considered superior to the *in situ* carbide coating method, because the former is a simple and cost-effective approach that can be readily scaled up for mass production. Although matrix alloying is less complex and does not require harmful additives or solvents, the formation of undesirable hard and brittle phases at the interface is expected to affect the susceptibility of the composite to crack initiation at the interface, thereby reducing its toughness.

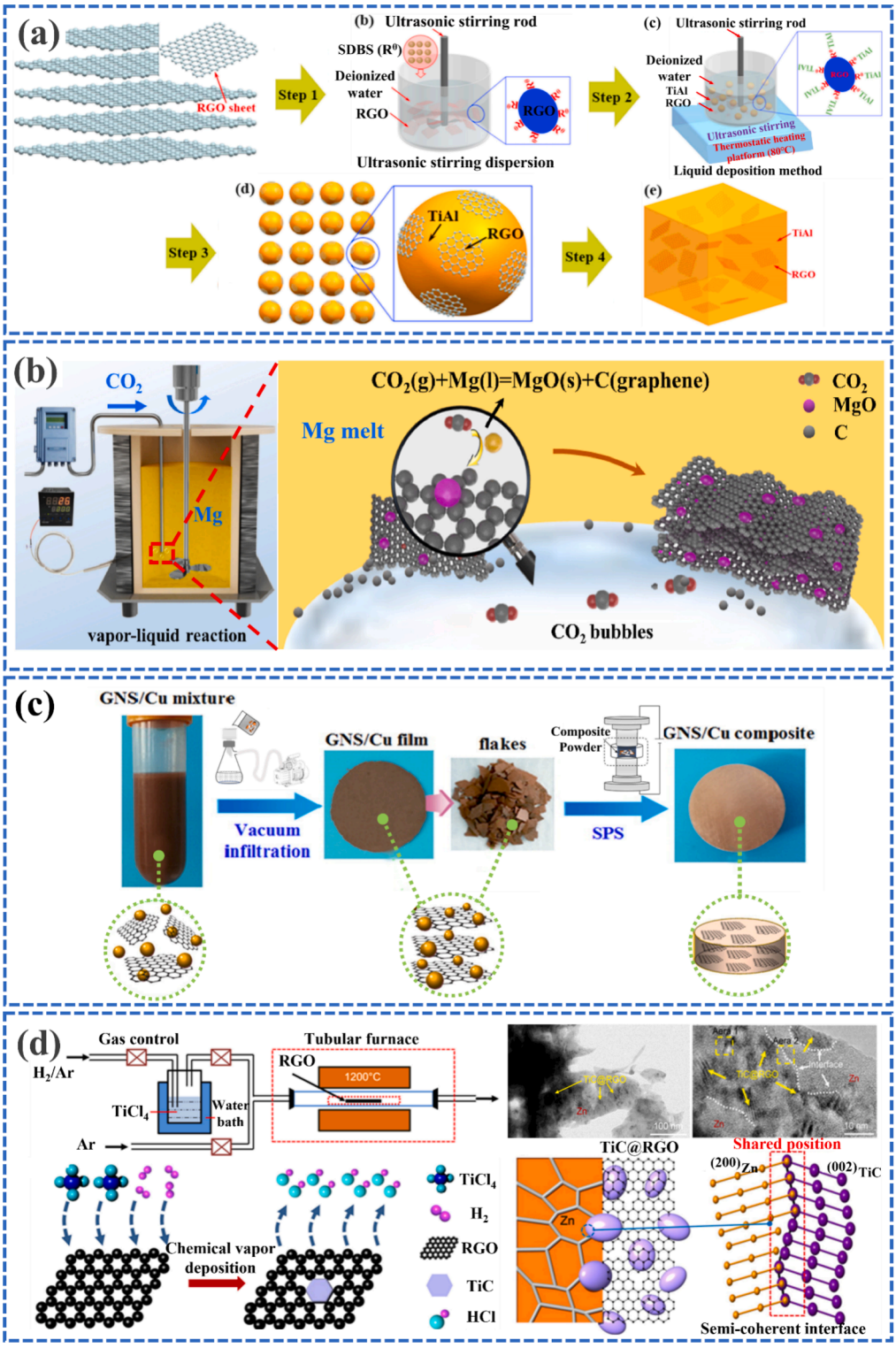

Fig. 5. (a) A schematic drawing of the fabrication process used for *in situ* coating of RGO on TiAl powder particles to fabricate RGO/TiAl composites based on the principle of electrostatic self-assembly [91]. (b) A schematic drawing illustrating the *in situ* synthesis of Gr on Mg melt surface to fabricate Gr/Mg composites [94]. (c) A schematic drawing of vacuum filtration for preparing Gr/Cu composites with good alignment of Gr [95]. (d) Schematic diagrams illustrating the in-situ growth of TiC on the RGO plane and preparation of TiC@RGO/Zn composites using the matrix-alloying method [96].

3. Additive manufacturing technologies

According to the ISO/ASTM standard 52900:2022, the current AM methods are classified into seven categories, including directed energy deposition, powder bed fusion, vat polymerization, material jetting, material extrusion, sheet lamination, and binder jetting. Powder bed fusion, vat polymerization (VP), material extrusion (ME), binder jetting (BJ), and directed energy deposition (DED) are the five categories of AM methods that are typically used for Gr-containing composites, with PBF, ME, BJ and DED being currently the most commonly used metal AM techniques. Printing speed, printing resolution, build sizes, shape complexity, printing quality, system simplicity, powder compatibility, and cost efficiency of four representative techniques, namely, selective laser melting (SLM), ME, BJ, and DED, are compared in Fig. 6. In comparison, SLM achieves superior printing resolution, shape complexity, and high print quality, though its cost efficiency and system simplicity require improvements. ME offers commendable powder compatibility, system simplicity, and moderate shape complexity, but suffers from lower printing speed, printing resolution, and printable sizes. BJ demonstrates exceptional performance in printing speed, printable sizes, shape complexity, and cost efficiency, but is comparatively limited in printing resolution and print quality. DED excels in printing speed, printable sizes, and powder compatibility, but requires enhancements in printing resolution, shape complexity, and overall print quality. The technological aspects of each of the techniques are briefly introduced and discussed in the following subsections of this section.

3.1. Powder bed fusion

Powder bed fusion, including direct metal laser sintering (DMLS), electron beam melting (EBM), selective laser sintering (SLS), and SLM, is a category of AM techniques that utilizes thermal energy to selectively melt or sinter certain pool or area of a powder bed [108]. Among the above-mentioned techniques, SLM makes use of laser that selectively scans over a powder bed, forming 2D patterns of fused material with the help of the heat generated by the laser [109]. Objects are built layer-by-layer by repeatedly laying down a new layer of powder upon a solidified layer. SLM is particularly suited for the fabrication of complex and/or precise three-dimensional (3D) metal objects with great advantages, including design complexity, production efficiency, and the flexibility to perform *in situ* alloying [110]. To date, numerous research efforts have been made to fabricate porous structures of Ti alloys [111], stainless steels [112], Ni-Ti alloys [113], Mg alloys [114], and Zn alloys [115] for bone implants. Due to the ultra-high energy input of laser, the instantaneous temperature of the melt pool during SLM can reach thousands of degrees and can melt most of metals and their alloys without losing the structural and functional integrity of Gr with a theoretical melting point between 3652—3697 °C. Theoretically, SLM allows for the fabrication of GBMMCs with a high degree of freedom in material processing. Fig. 7 illustrates the full SLM process to fabricate GMMCs, including composite powder spreading on the build plate as well as composite scaffold printing with a magnified illustration

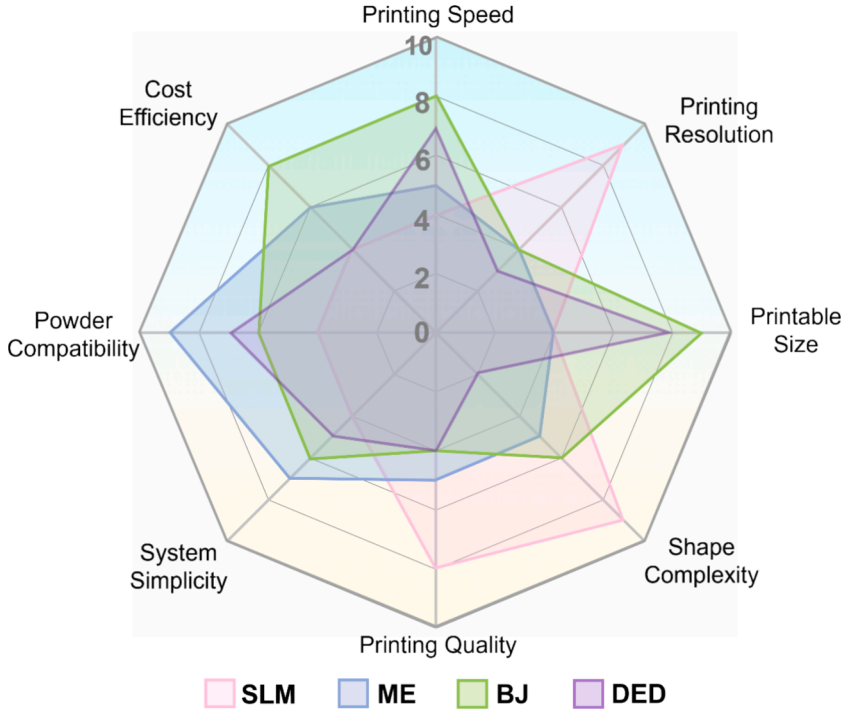

Fig. 6. A radar chart comparing the selected representative AM techniques (*i.e.*, SLM, ME, BJ and DED) in terms of printing speed, printing resolution, printable size, shape complexity, powder compatibility, system simplicity and cost efficiency. Note that a higher score suggests a more favorable condition in the corresponding technological aspect.

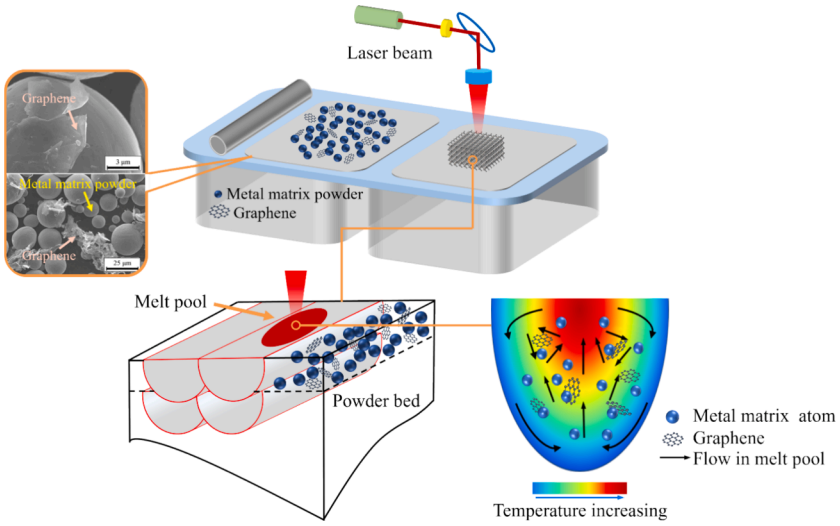

Fig. 7. A schematic illustration of the fabrication process of GBMMCs via SLM [116,117].

of the melt pool.

Bone tissue engineering [118,119] places high demands on the multi-physical properties of bone scaffolds, requiring variable porosity, bone-mimicking mechanical properties, and the ability to moderate mass-transport properties to feed metabolic pathways [120]. Micro-architected bone scaffolds reported in the literature include the structures based on (slender) struts [121], triply periodic minimal surfaces (TPMS) [122], Voronoi tessellations [123], and pentamode metamaterials (PMs) [124] with decoupled mechanical and mass-transport properties and multi-physical performance. Indeed, SLM can be used to fabricate porous metallic components and multifunctional metamaterials for novel implants [125]. As shown in Fig. 8a, Zhang *et al.* [126], inspired by the architectures of sea urchin spines in natural organisms, designed graded pentamode metamaterials (Fig. 8b). For example, sea urchin spine-like biomimetic scaffolds have been successfully fabricated using SLM (Fig. 8c) with high accuracy and sustainable control of topological features, resulting in bone-mimicking architectures, excellent mechanical properties, favorable mass-transport performance, and markedly improved osteogenic behavior. Inspired by the Hall–Petch relationship (Fig. 8d) that describes the relationship between the grain size and the yield strength of the bulk material and by modifying the unit cell length to adjust the mass, Zhang *et al.* leveraged diamond micro-lattice (Fig. 8e) metamaterials to construct bone scaffolds (Fig. 8f) with decoupled mechanical and mass-transport properties [127]. The results obtained from compression tests and transportation calculations demonstrated that the parametric design approach based on the Hall–Petch relation and collaborative optimization of the mechanical and mass-transport properties enables the realization of multi-physical properties. Such approaches for tailoring multiple physical properties of architected SLM materials (*e.g.*, pentamode metamaterials) provide a structural template for the design of bone scaffolds. To address key challenges in SLM, including residual stresses, distortion, limited material systems, low build rates, and scalability issues, researchers should implement hybrid manufacturing techniques, develop advanced post-processing methods, and incorporate *in-situ* stress relief strategies. Additionally, one can expand the material options by designing multi-material SLM processes for functionally graded structures and explore multi-laser systems to enhance build speed and efficiency [128,129]. Future research efforts should prioritize intelligent process control and monitoring systems, multi-scale modeling for microstructure prediction, energy-efficient processes, and novel applications in biomedical implants [130,131].

3.2. *Material extrusion*

The ME AM techniques work by continuously pushing metal, polymer, or ceramic powder-based feedstock through a nozzle or nozzles to build a 3D structure layer by layer [132]. ME has been considered a promising technique to fabricate (multi-material) scaffolds for tissue engineering, due to its affordability, versatility, and ability to print porous structures [133]. The general route for the design and printing route of ME AM GBMMCs (Fig. 9) includes: (i) preparation and evaluation of the rheological behavior of the prepared ink; (ii) optimization of the printing process window for inks with different percentages of metal matrix powder loading, binder content, and doping phases (including Gr), defined by various combinations of printing speeds and pressures; and (iii) investigation of the effects of sintering temperature and holding time on the density of struts, while maintaining the shape fidelity of the scaffolds.

The advent of the ME AM technique has greatly expanded the possibilities for printing not only alloyed metals but also metal/polymer or metal/ceramic composite scaffolds, also paving the way for introducing Gr into biodegradable metal scaffolds. Dong *et al.* [134] successfully fabricated biodegradable porous Mg scaffolds with an interconnected pore structure using the ME AM approach. Their results showed that all the prepared inks with 54, 58, and 62 vol% Mg powder exhibited viscoelastic behavior with adequate elastic moduli for the fabrication of self-supporting structures. Moreover, the ink loaded with 58 vol% Mg powder possessed a wide

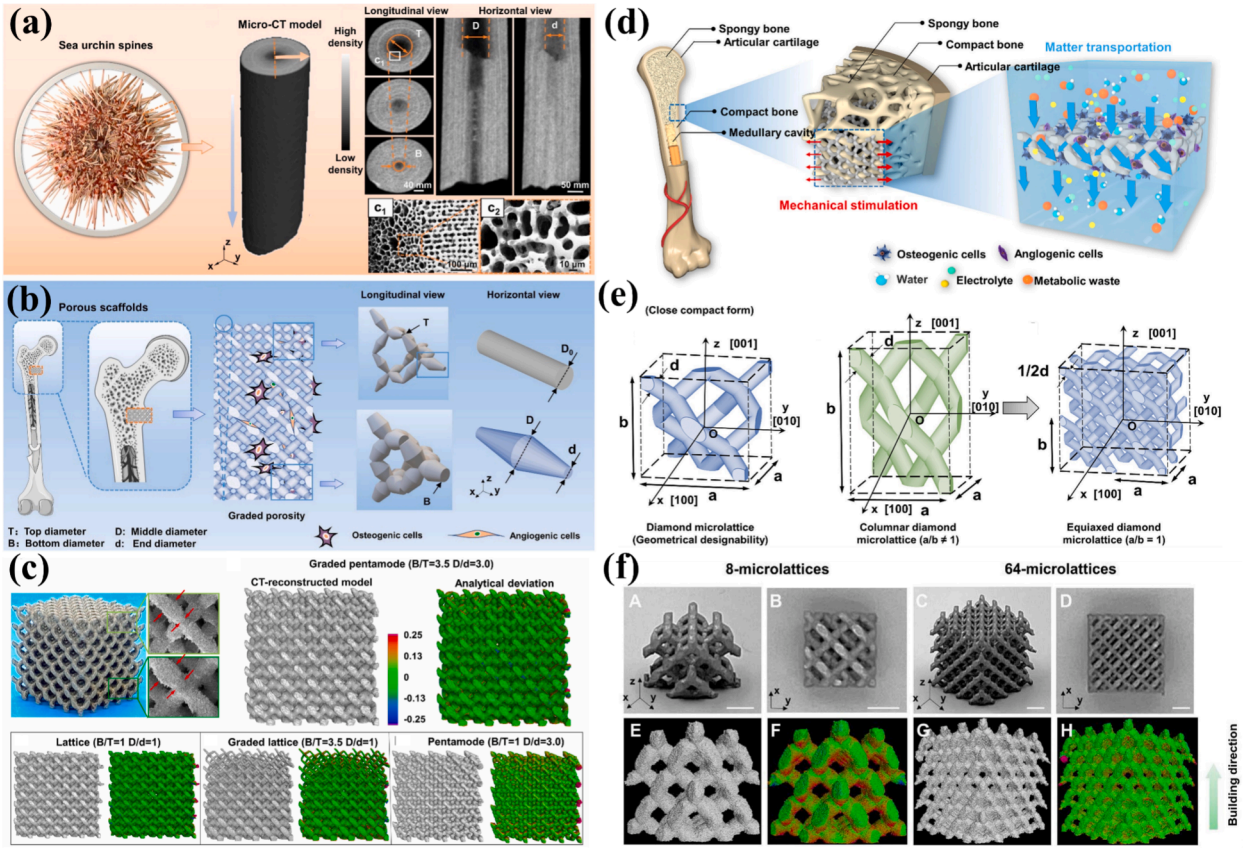

Fig. 8. (a) The microarchitecture of sea urchin spine and biomimetic scaffolds: sea urchin spines' needle-like appearance and an internal architecture with graded porosity. (b) A schematic drawing of biomimetic graded pentamode-based scaffolds, implant location, and geometrical features of the graded density. (c) Ti–6Al–4 V specimen's morphological characteristics for different topological structures fabricated by SLM: optical photographs, SEM images, and CT-reconstructed model [126]. (d) A schematic drawing of artificial biomedical scaffolds designed for repairing bone defects in which mechanical and transport properties need to be simultaneously optimized. (e) Diamond micro-lattices with geometrical designability inspired by diamond atoms. (f) The printing outcome and an analysis of the manufacturing fidelity of SLM for micro-lattices [127].

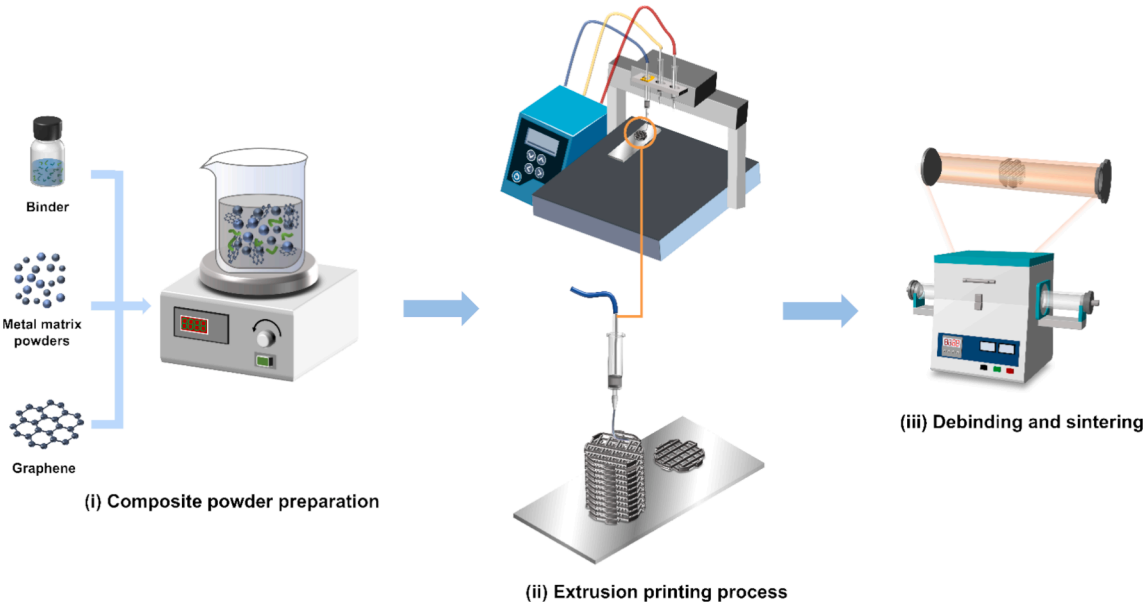

Fig. 9. A schematic drawing of GBMMC fabrication *via* material extrusion.

printability window for the fabrication of a 3D periodic lattice structure (Fig. 10a-c). Near-net struts were created with necks formed between Mg powder particles. The relative density of the struts increased with the holding time and sintering temperature (Fig. 10d). Sintering at the melting point of pure Mg within a short time was found to be suitable for neck formation and for the final Mg scaffolds with good fidelity and considerable densification (Fig. 10e). Dong *et al.* and Putra *et al.* have developed a series of alloys and composite materials (including Mg-Zn [135], Fe-Mn [136] and Mg-Zn/bioceramic [137]) based on biodegradable metals, including Fe and Mg, and have obtained composite scaffolds with adjustable rates of biodegradation (Fig. 10f).

The reason that ME with multi-material powder-based feedstock has been pursued is that this technique does not have the drawbacks that are inherent to the laser-based AM technologies, such as residual stresses, cracks, distortions, and even metallurgical defects. For multi-material AM purposes, more than one nozzle can be integrated into the printer to deliver different feedstock materials and achieve complex multi-material interfaces within the structure. Kang *et al.* [139] developed an integrated tissue–organ printer (ITOP) that could be used to fabricate stable, human-scale multi-material tissue scaffolds of any shape (Fig. 10g). Liu *et al.* [140] manufactured functionally graded multi-material osteochondral scaffolds using GelMA/nHA hydrogels through extrusion-based 3D printing (Fig. 10*h*). In the subcategory of metal-based ME AM, Fe-based composite materials (*e.g.*, Fe-$CaSiO_3$) have been realized for bone cancer treatments as well as for regenerating cortical bone defects [142]. The extruded and then dried Fe-$CaSiO_3$ composite was composed of an adhesive-bound multi-material powder mixture, which required post-AM debinding and sintering. While low speeds, resolution constraints, anisotropic properties, and material restrictions remain to be the common limitations in advancing the ME technology, metal ME faces additional challenges, including low as-printed density (50–60 % theoretical density), significant sintering shrinkage (≤20 %), and binder compatibility issues [143]. To address these challenges, researchers should focus on feedstock optimization, hybrid pressure-assisted microwave sintering, and process innovations such as catalytic *in-situ* debinding and distortion compensation [144]. Future research directions include expanding printable alloys through thermally stable binder systems, developing intelligent shrinkage prediction algorithms for dimensional accuracy control, and enabling multi-metal co-extrusion for functionally graded components [145]. Scalable ME systems with integrated real-time monitoring could revolutionize near-net-shape

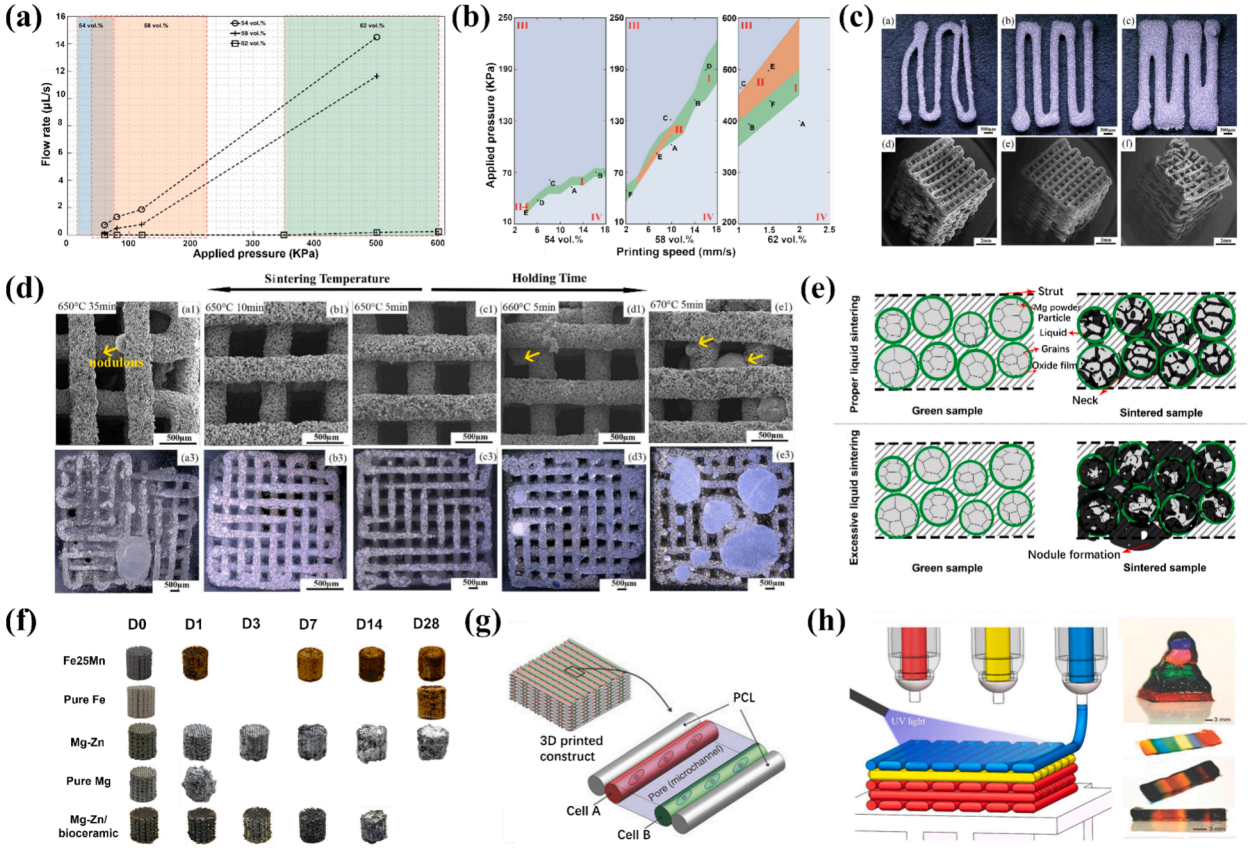

Fig. 10. The characteristic printing behavior of Mg powder-loaded inks: (a) the flow rate as a function of the applied pressure, (b) the printability windows (II: 3D printable zone; I: 2D printable zone; III and IV: unprintable zones), and (c) the results obtained from the printing trials of Mg scaffolds. (d) The sintering behavior and fidelity of scaffolds initially with 58 vol% Mg powder loading as a function of sintering temperature and holding time. (e) Schematic of liquid-phase sintering of the Mg 3D scaffolds [134]. (f) Optical images of the biodegradation behaviors of pure iron, pure magnesium, their alloys or composite scaffolds [62,135–138]. (g) An illustration of the basic patterning of 3D architecture including multiple cell-laden hydrogels and supporting PCL polymers realized by the integrated tissue-organ printer (ITOP) [139]. (h) Multi-material bioprinting of 3D GelMA/nHA hydrogel constructs containing 7 layers of different bioinks [140,141].

manufacturing of complex parts, reducing material waste [146].

3.3. Binder jetting

BJ is a powder bed-based 3D AM technique that uses an adhesive (binder), generally in the liquid form, that is ejected onto a powder bed, thereby fabricating a part layer by layer (Fig. 11a). BJ is somewhat similar to PBF, but instead of applying thermal energy to fuse metal powder feedstock, an adhesive liquid is dispensed on the surface of the powder bed, bonding powder particles to form a desired structure. This method allows for binding dissimilar powders and achieving multi-material and functionally graded parts by alleviating interfacial instability and stress concentrations. However, the resolution of the structures fabricated using this technique is relatively low (*i.e.*, a minimum feature size of several hundreds of micrometers) due to the spreading of the liquid binder within the powder bed. As reported by Farahani *et al.* [147], powder bed-based BJ is a technique suitable for manufacturing 3D parts of nanocomposites containing Gr. For example, Azhari *et al.* [148] used a blend of HAP and GO at loadings of 0.2 wt% and 0.4 wt% to develop porous structures using the BJ method. The hydrophilicity of both HAP and GO enabled the fabrication of the composites, which started from the preparation of highly dispersed solutions in a water medium to prevent agglomeration. This mixture solution was allowed to dry on a hotplate and was then placed on the feed bed on which an aqueous binder was injected to print 3D cylindrical structures.

Post-treatment, such as pre-sintering for debinding or impregnation with a high-strength substance (*e.g.*, epoxy) is typically necessary to produce the part (Fig. 11b). For instance, elemental powders are used to produce porous BJ Fe-Mn [154] and Fe-Mn-Ca biomaterials [155]. To remove the binder and then fuse multi-material powder particles together, post-AM debinding and sintering were performed. Since the adhesive-bound porous structure was created within a powder bed using the BJ process, it was necessary to clean the pores with loose powder particles entrapped before applying post-AM heat treatment without compromising the biomaterial's structural integrity. Although there are no residual stresses created during the BJ process due to the absence of direct laser heating and rapid cooling during fabrication, structural shrinkage occurs during post-AM sintering due to binder removal and powder particle rearrangement and integration. For example, Fe-Mn-Ca biomaterials [154] shrank by around 11.7 % in all directions. The application of BJ for the fabrication of multi-functional porous AM metals or GBMMCs not only requires intricate multi-material powder handling systems before and after AM, but also necessitates post-AM steps to remove loose powder particles from the adhesive-bound porous structure and to sinter the particles in the printed structure through heat treatment [156]. The critical limitations of the BJ technology include low green part strength, material constraints (primarily metals and ceramics), surface roughness, and post-processing challenges such as sintering-induced deformation [157]. To enhance mechanical performance, material innovations such as nanocomposite binders and hybrid metal-ceramic powders, coupled with process optimization such as precise binder droplet size control and multi-stage curing to minimize porosity should be conducted. Post-processing improvements involve *in-situ* polymer/metal infiltration and microwave-assisted sintering to mitigate dimensional instability. Future research priorities include multi-material BJ for functionally graded structures, machine learning-driven algorithms for shrinkage prediction and compensation, and sustainable bio-based binders to reduce environmental impact [158].

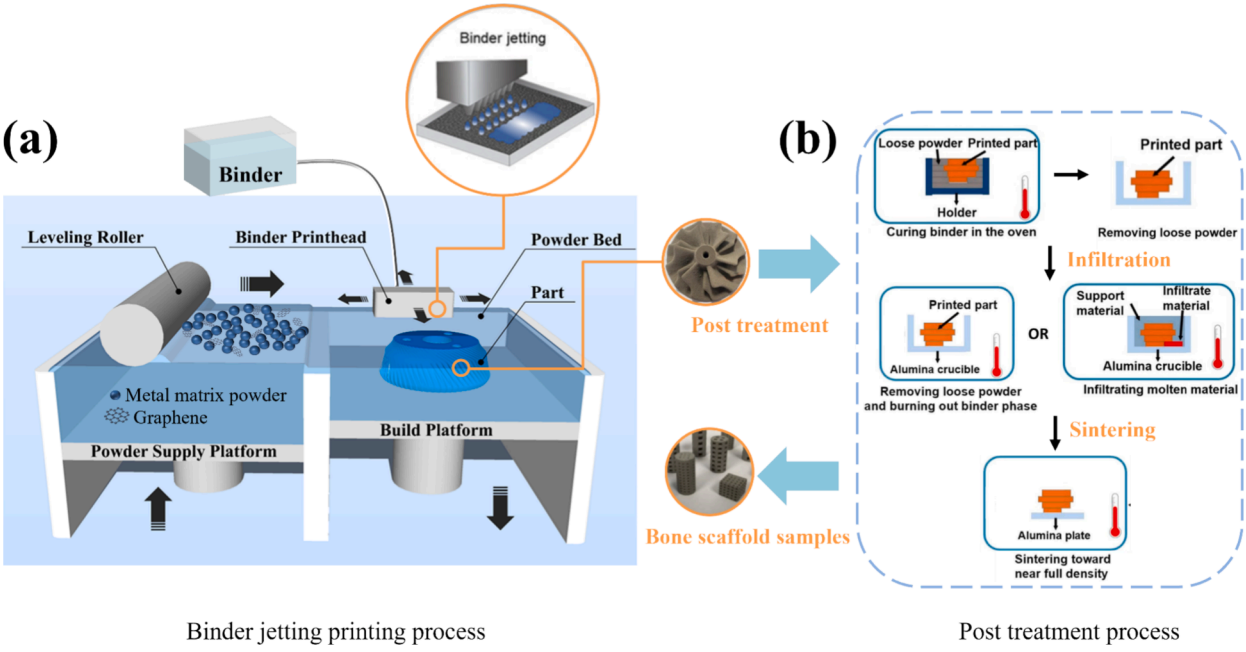

Fig. 11. A schematic drawing illustrating the fabrication of GBMMCs via binder jetting [149–153].

3.4. Directed energy deposition

In DED, a metallic material is delivered in the form of powder or wire through a nozzle, which is then melted through locally applied thermal energy. Laser engineered net shaping (LENS) is the most common commercial process in the category of DED [159]. A schematic of the DED process is presented in Fig. 12a [160]. Fig. 12b illustrates two often used traditional and continuous DED methods to fabricate products with the scan direction vertical and coaxial to the direction of the nozzle axis, respectively [161]. This technology offers a straightforward multi-material delivery system through multiple nozzles and the capability of *in situ* deposition and synthesis of different materials to obtain compositionally graded multi-material structures, such as Ti6Al4V/SS304L [162], Ti6Al4V/SS316 [163] and Ti6Al4V/Inconel625 [164] multi-materials.

As an AM process involving fusion, DED can fully melt the feedstock powder, which is then followed by fast solidification. This can refine the microstructure and increase the density and mechanical properties of the resulting parts. DED has been successfully used to fabricate structures made of biocompatible metallic materials, such as Ti-based alloys [166], CoCr alloys [167], Nitinol [168], and 316L stainless steel [169]. DED has also been used to fabricate GO-MMCs and GO-CMCs (ceramic matrix composites) due to the unique capabilities of DED, such as coating, remanufacturing, and producing functionally graded materials. However, the survival, degradation, and reactions of GO in DED-fabricated GO-MMCs are still unknown [170]. Similar to SLM, DED, as a single-step process, has important advantages over other 3D printing processes, such as ME, as it does not involve post-AM thermal treatment, such as debinding and sintering. Poor resolution, low power efficiency, and inferior surface quality are the main disadvantages of this process [171]. Although DED can deposit multiple materials *in situ*, this AM technique is less suitable for fabricating structures with fine geometries or those containing hollow passages, which are often required for complex porous biomaterial designs [172]. In addressing the key challenges of DED, three critical areas, *i.e.*, printing resolution, energy efficiency, and surface quality, need particular attention. For resolution enhancement, factors such as laser/electron beam focusing and powder delivery accuracy should be considered, with proposed solutions including adaptive optical systems and intelligent path planning. Energy efficiency optimization focuses on reducing energy consumption through innovations such as pulsed lasers, optimized scanning strategies, and real-time thermal field monitoring [131,173]. Surface quality improvement involves hybrid manufacturing (*e.g.*, *in-situ* milling) and adaptive surface treatment techniques. Future research directions emphasize the development of intelligent closed-loop control systems, exploration of novel materials, multi-scale modeling for process prediction, and quality monitoring systems, collectively advancing the precision, efficiency, and applicability of the DED technology [174].

4. Recent advances in loading-bearing and functionalities of GBMMCs

This section reviews the progress recently made in developing GBMMCs with a focus on the mechanical properties of load-bearing implants and implant-relevant properties, including biodegradability, cytotoxicity, antimicrobial properties, and osteogenesis ability. It should be noted that, given the limited number of studies on AM GBMMCs and the commonalities with and implications for other fabrication processes, the evaluation of mechanical properties as well as biological properties is not limited to those of AM GBMMCs.

4.1. Mechanical properties

It is important to first understand the strengthening mechanisms of GMMCs. Subsection 4.1.1 summarizes the four commonly recognized Gr-strengthening mechanisms applicable to BMMCs, including load transfer, Orowan looping, Coefficient of thermal expansion (CTE)-mismatch, and the Hall-Petch effect. Sections 4.1.2 and 4.1.3 summarize the current research on Gr strengthening of

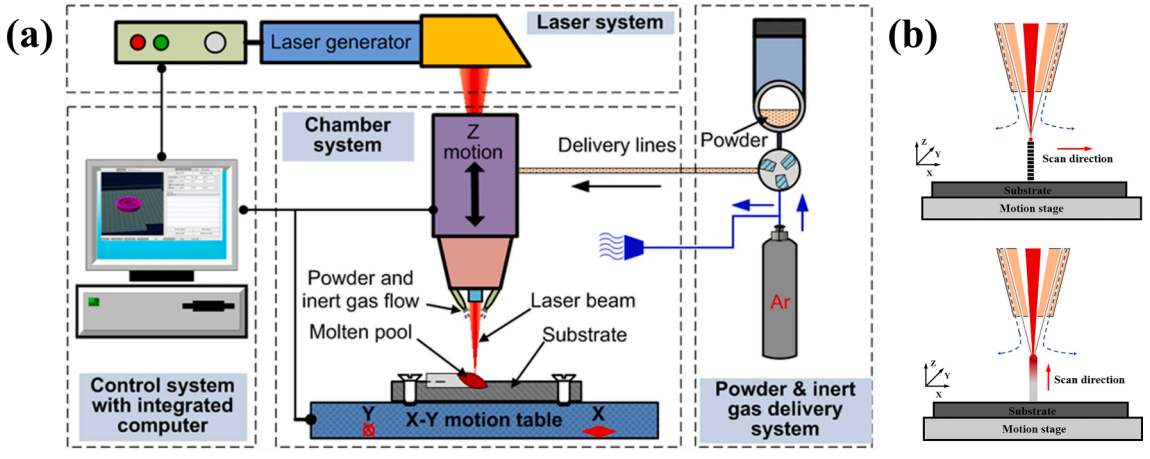

Fig. 12. (a) A schematic drawing of directed energy deposition's experimental setup [160]. (b) Traditional and continuous DED scanning methods [161,165].

Mg/Zn- and Fe-based BMMCs, respectively, primarily focusing on static and dynamic mechanical properties, such as stress–strain relationships in tension and compression, and fatigue performance, as well as the causes of failure. Subsection 4.1.4 concludes the main influences on the mechanical properties of GBMMCs, and emphasizes the role of GDs in enhancing BMMCs compared to ceramics and polymers. Finally, subsection 4.1.5 links the strengthening mechanism of GDs to clinical implant requirements.

4.1.1. Strengthening mechanisms

Load transfer is the dominant strengthening mechanism of GBMMCs [175,176]. The outstanding mechanical properties of GDs, as shown in Table 2, allow for the strengthening of metal matrices, thus improving their load-carrying capacity.

A shear-lag model [182,183] has been developed and modified to estimate the load-transfer strengthening effect. In this model, it is assumed that the applied load is transferred from the matrix to Gr through the interface shear stress developed along the Gr surface, and the actual yield strength (σ_c) specified by the shear-lag model is expressed by the following two equations:

$$\sigma_c = \sigma_r V_r \left(1 - \frac{l_c}{2l}\right) + \sigma_m (1 - V_r)(l \geq l_c) \tag{1}$$

$$\sigma_c = \sigma_r V_r \left(\frac{l}{2l_c}\right) + \sigma_m (1 - V_r)(l < l_c) \tag{2}$$

where σ_m is the yield strength of the composite matrix, V_r is the volume fraction of Gr, σ_r is the fracture strength of Gr, and l and l_c are the actual length and critical length of Gr, respectively. l_c can be expressed as:

$$l_c = \frac{\sigma_f d_f}{2\tau_m} \tag{3}$$

where σ_f is the strength of Gr, d_f is the average particle size of Gr, and τ_m is the ultimate shear strength of the metal matrix. When $l < l_c$, Gr plays a major role in load transfer until Gr is entirely pulled out from the matrix (Fig. 13a). When $l > l_c$, on the other hand, Gr bridges the cracks and also plays a role in load transfer until the final fracture [184]. Guan *et al.* [185] reported the simultaneous 'pull-out' and 'bridging cracks' roles of Cu-coated GNPs at the fracture interface of tensile specimens of GNP-containing AA6111 aluminum alloy matrix composites generated by doping large-scale GNPs (*i.e.*, $l > l_c$) (Fig. 13b and c). Due to the stir-casting process employed and the complex microscopic interactions between GNPs and the aluminum alloy matrix, parts of GNPs lost their original sizes. As a result, more than one load transfer mechanisms could operate in the MMCs. While the shear-lag model provides a theoretical framework for load-transfer strengthening, its applicability is contingent on strong interfacial bonding. Poor interfacial adhesion (*e.g.*, in the Mg-Gr and Zn-Gr systems) due to poor interface wettability, limited interface reaction, and large CTE difference can lead to premature debonding, reducing the effective load-carrying capacity of Gr. For instance, molecular dynamics (MD) simulation studies showed that weakly bonded interfaces in the Fe-GNS (graphene nanosheet) system decreased σ_c by approximately 20 %, compared to strong-bonded interfaces [186]. Strategies such as surface functionalization (*e.g.*, Cu-coated Gr [187]), interface reaction layer design (TiC [96]) and processing technology optimization [188] are critical to optimize τ_m and mitigate this limitation. Moreover, the sizes of GDs should be appropriately matched to the specific matrix material system. In GMMCs with strong interfacial bonding, larger Gr sheets can facilitate more effective load transfer due to their high stiffness, leading to increased strengthening without the risk of debonding or crack propagation. For instance, Yang *et al.* [189] found that the Cu-coated Gr/6061Al composites containing Gr sheets of a larger diameter (25.85 μm) exhibited a good balance of high tensile strength (218 MPa) and fracture strain (17.2 %), suggesting that larger Gr could significantly enhance the overall performance of 6061Al. However, larger Gr sheets also raise concerns about agglomeration and local stress concentration, which necessitates advanced dispersion and processing techniques to ensure uniform distribution and minimize these issues.

Doping Gr derivatives (*e.g.*, nitrogen doping) can further enhance their interactions with metal matrices in BMMCs. For instance, nitrogen-doped Gr (N-Gr) introduces pyrrolic/pyridinic-N sites that act as electron donors, strengthening covalent bonding with metal atoms (*e.g.*, Cu–N coordination in Cu/N-Gr composites [193]). This covalent interaction reduces interfacial slippage, thereby improving load transfer efficiency (Eqs. (1) and (2). Additionally, N-Gr's increased electrical conductivity (*versus* pristine Gr) may alter galvanic corrosion behavior, thus requiring careful re-evaluation of biodegradable composites (see Subsection 4.2.1).

High density of dislocations generated by the blocking effect of Gr at the interface is proven to be a dislocation-strengthening mechanism of GMMCs [194]. Dispersed Gr inhibits the propagation of dislocations, which can be explained using the Orowan looping system. Strength improvement from the Orowan looping system can be calculated using the Orowan-Ashby equation [195]:

Table 2
A summary of the specific surface area and mechanical properties of GDs, including fracture (tensile) strengths and Young's moduli.

Graphene types	Fracture (Tensile) strength (GPa)	Young's modulus (GPa)	Specific surface area (m^2g^{-1})	Ref.
Gr	125	1100	2630	[177]
GO	24.7	207.6 ± 23.4	368 ~ 925	[178,179,180]
RGO	30	250 ± 150	320 ~ 705	[178,179,181]

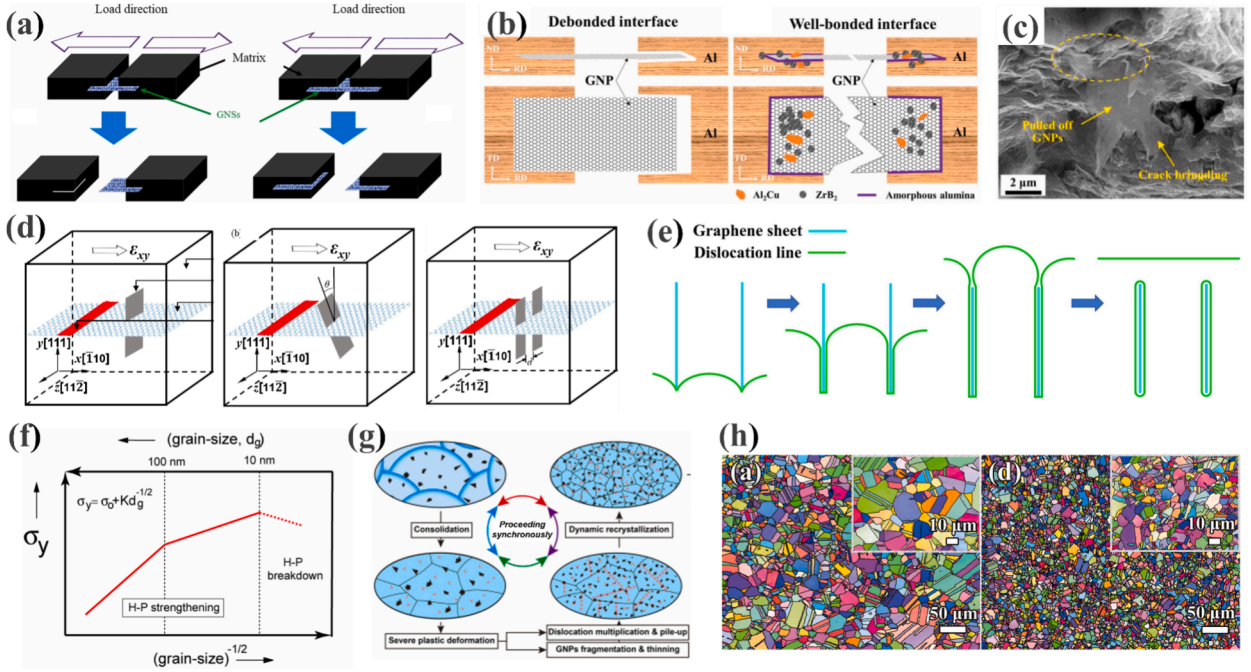

Fig. 13. (a) A schematic drawing of the fracture model corresponding to the relationship between actual and critical Gr length [184]. (b) and (c) Schematic diagrams of a debonded interface and a well-bonded interface and SEM tensile fractography of a GNP/AA6111 aluminum alloy matrix composite [185]. (d) Schematic diagrams of a Gr sheet parallel to the plane ($\bar{1}$ 10), rotated by an angle θ around its symmetry axis, and two Gr sheets separated by a distance d [190]. (e) A schematic diagram of the formation of Orowan loop when dislocations pass graphene sheets [186]. (f) A schematic drawing illustrating the Hall-Petch (H-P) relation between strength and grain size [191]. (g) Grain refinement mechanism in GNP/pure Al-matrix composites through severe plastic deformation [192]. (h) EBSD mapping of pure Ni bulk and GNP/Ni composite with 0.6 wt% Gr [98].

$$\Delta\sigma_{\text{Orowan}} = \frac{0.13Gb}{\lambda}\ln\left(\frac{d_p}{2b}\right) \tag{4}$$

where G is the shear modulus of the matrix, b is the Burgers vector of the matrix, λ is the effective planar inter-particle spacing, and d_p is the effective reinforcement particle diameter.

With Gr as the reinforced phase, the interaction between Gr and dislocations and the effect of Gr on the dislocations movement are of uttermost importance for understanding the strength enhancement mechanism of Gr. Zhu *et al.* [190] used MD simulations to investigate the strengthening effect of Gr caused by blocking dislocation propagation in Gr-containing copper matrix composites. The effects of the rotation angle of Gr, the arrangement of Gr, and the influence of the distance between two abreast Gr nanosheets on dislocation motion were considered (Fig. 13d). They found that the strengthening effect could be improved by adjusting the angle and arrangement of Gr to decrease the dislocation velocity and increase the dislocation density. Fig. 13e illustrates the formation of Orowan loop and indicates that dislocations prefer escaping rather than being pinned there when they encounter Gr nanosheets [186]. The Orowan mechanism is greatly influenced by the sizes and dispersion of GDs. A uniformly dispersed Gr system significantly enhances the Orowan strengthening effect by reducing the interparticle spacing (λ), improving the efficiency of dislocation loop formation, and ensuring uniform stress distribution. In contrast, Gr agglomeration increases λ, reducing dislocation pinning efficiency and weakening the overall strengthening effect [196]. As mentioned earlier, Zhu *et al.* [190] also emphasized the importance of reduced interparticle distance of Gr because dislocations encountered greater resistance when passing through the narrow space between two closely spaced Gr plates. Furthermore, Cao *et al.* [197] demonstrated *via* MD simulations that, for the same Gr content, the well-dispersed model required additional 1658 kcal/mol of energy for Gr separation compared to the poorly dispersed model, further underscoring the critical role of uniform dispersion. Strategies such as surface functionalization, processing technology optimization (*e.g.*, ball milling, ultrasonic dispersion, *etc.*), and interface modification are essential to achieve optimal dispersion and maximize the Orowan strengthening effect [198]. On the other hand, the sizes of GDs also play a crucial role in determining their reinforcing effect *via* the Orowan mechanism in GMMCs. Zhao *et al.* [199] found that the strength of RGO/Al composite pillars increased as the RGO size decreased (from 603 nm to 186 nm), highlighting the superior ability of smaller RGO nanosheets to constrain dislocation transmission and crack propagation within the material. Dutkiewicz *et al.* [200] observed that in Cu/GNPs composites, fine Gr (2–4 nm) resulted in a 50 % increase in hardness compared to the composites with coarse Gr platelets (14 μm), further emphasizing the beneficial effect of smaller Gr on mechanical properties. Additionally, the sizes of GDs significantly impact their dispersion in GMMCs. Yang *et al.* [201] found that in Cu/RGO composites, smaller RGO sheets (~0.92 μm) tended to distribute randomly, while middle-sized (~5.49 μm) and larger RGO sheets (~13.73 μm) formed carbon-rich aggregates with micro-layered structures. Therefore, smaller Gr sizes (or even

nanometer sizes) appear to be more conducive to the Orowan strengthening mechanism.

The difference in CTE between the metal matrix and Gr is usually large and the mismatch rate is high [31,202]. If the yield stress of the matrix is less than the stress caused by thermal mismatch, the composite material will form many dislocations at the matrix/reinforcement interface during cooling, enhancing the strengthening effect. The following equation may be used to calculate the change in the yield strength caused by the CTE mismatch [203]:

$$\Delta\sigma_{CTE} = 4.33G_{\mathrm{m}} \bullet b\sqrt{\frac{\Delta T \bullet \Delta CTE \bullet V_G}{b \bullet d_G}} \tag{5}$$

where G_m is the shear modulus of the matrix metal or alloy, b is the Bernoulli vector of the matrix, ΔT is the difference between the actual processing temperature and testing temperature, ΔCTE is the CTE difference between the matrix metal and Gr, V_G is the volume fraction of Gr, and d_G is the average particle size of Gr.

In specific temperature regimes, Gr exhibits a negative coefficient of thermal expansion (NCTE), which means that it contracts as temperature rises or expands when temperature falls [204]. The thermal expansion of Gr is theoretically expected to be -3.6×10^{-6} K^{-1} or -6×10^{-6} K^{-1} and is experimentally measured to be -7×10^{-6} K^{-1} or -8×10^{-6} K^{-1} in the armchair and zigzag directions [205,206]. The CTE of Gr is dependent on the temperature but remains negative in a specific temperature range of 200 ~ 400 K [207]. In particular, the NCTE of Gr makes it easier to create composite materials that have a smaller CTE value than their pristine equivalents. AbuShanab *et al.* [208] have found that the content of doping Gr negatively affects the thermal expansion coefficient of the Al2024 aluminum alloy with the CTE being lower for higher weight percentages of Gr but increasing with the sintering temperature due to better densification and increased relative density.

Grain refinement is an effective way to improve the strength of MMCs. Refined grains generate more grain boundaries, and if the grain boundary structure does not change, more external force is required to break the dislocation stacked at grain boundaries, thereby strengthening the material. The Hall-Petch relationship describes the dependency of the yield strength of a metal or an alloy on its microstructure [191] (Fig. 13f) as [209]:

$$\sigma_y = \sigma_o + Kd_g^{-1/2} \tag{6}$$

where σ_0 is the friction stress, K and d_g are the Hall-Petch coefficient and the average grain size of the matrix, respectively. The Hall-Petch effect is contingent on uniform grain refinement. While GDs typically act as grain refiners, excessive GDs' content can induce clustering, which destabilizes recrystallization and promotes coarse grains [210]. For instance, Li *et al.* [211] reported that increasing Gr content in Inconel 625 composites from 0.4 vol% to 1.0 vol% resulted in reduced strength and ductility. Optimal Gr content and dispersion are therefore critical to sustain Hall-Petch strengthening. The Hall-Petch relationship is also highly sensitive to Gr size. Submicrometer Gr fragments promote grain refinement [212,213], through Zener pinning effects, increasing the yield strength more, when compared to the composites reinforced with coarse-grained Gr. However, nanoscale Gr with elevated SSA accelerates galvanic corrosion, necessitating size-property optimization.

GDs have been widely utilized for grain refinement because their presence can act as nucleation sites during liquid-state processing or Zener pinning positions during solid-state processing [214]. Inducing ultra-refined grains allowed Xie *et al.* [192] to achieve remarkable strengthening-toughening efficiency by adding 1.5 wt% few-layer GNPs to pure aluminum. A schematic diagram of Fig. 13g illustrates that GNPs are consistently dispersed inter-granularly and intra-granularly due to fragmentation, thinning, and re-dispersion during severe plastic deformation. These GNPs promote localized dislocation aggregation, inhibit dislocation movement, and stimulate dynamic recrystallization during the nucleation stage. By *in situ* growing Gr from solid carbon precursors, Zhang *et al.* [98] generated a new Ni-based composite with noticeably increased strength and ductility. When Gr content was increased to 0.6 wt%, the average grain size decreased to 5.66 μm, according to the results of Electron Backscattered Diffraction (EBSD) analysis, while the pure Ni bulk exhibited a uniform coarse-grained structure with an average grain size of 8.78 μm (Fig. 13h). In comparison to the pure Ni bulk, the yield strength, tensile strength, and fracture elongation of the composite all increased by 1.16, 1.34, and 1.37 times, respectively.

The relative contributions of these mechanisms vary with processing routes and material systems. For example, in powder metallurgy-processed Mg-GNP composites [33], the significant CTE mismatch generated high dislocation densities, making $\Delta\sigma_{CTE}$ the dominant strengthening contributor. In contrast, in Fe-GO composites fabricated by solution-assisted milling and SLM [215], the homogeneous dispersion of GO enhanced load transfer and Orowan strengthening effects. Therefore, the prioritization of strengthening mechanisms must align with processing capabilities and matrix-reinforcement compatibility to optimize material performance.

4.1.2. GD-reinforced Mg- and Zn-based BMMCs

GD-reinforced pure Mg, Mg-Zn alloys, and Mg-Zr alloys have been extensively studied, whereas only a few studies have been conducted to date on GD-containing Zn-based BMMCs, mostly concerning pure Zn-matrix BMMCs and their mechanical properties. Here, we discuss the previous research on GD-containing Mg- and Zn-based BMMCs. The processing methods adopted in the current research for preparing GBMMCs can be divided into two categories: (i) conventional processing methods, including casting [216], cold/hot pressing [217], hot extrusion [218], SPS [72], and hot isostatic pressing (HIP) [219], and (ii) AM (such as SLM [220] and DED [160]).

Table 3 lists the GDs type, content, dispersion methods, processing method and parameters hardness, tensile properties, and primary and secondary phases present in GD-containing Mg- and Zn-based BMMCs. GD-reinforced pure Mg, pure Zn, and their alloys

Table 3
Summary of GDs type, content, dispersion methods, processing method and parameters, hardness and tensile properties, and primary and secondary phases in GD-containing Mg- and Zn-based BMMCs.

Matrices metal	GD type	GD content	GD dispersion method	Processing method	Processing parameters	Hardness [HV]	Tensile properties YS [MPa]	UTS [MPa]	EI [%]	Primary and second phases	Ref.
Pure Mg	Gr	0.25 and 0.75 vol%	Solution-assisted dispersion	Sintering and hot rolling	Stacking Mg/Gr layer by layer, sintering at 620 ℃ for 6 h with the pressure of 50 MPa, followed by hot rolling	—	153	179	5.5	MgO phase	[222]
		0.10 and 0.25 wt%	*In situ* coating	Disintegrated melt deposition(DMD) and hot extrusion	Heating to 750 ℃ to fabricate the composites through the DMD, and homogenized at 400 ℃ for 4 h and hot extruded at 350 °C using an extrusion ratio of 20.25:1	—	122	202	14.5	—	[175]
		0.09, 0.18 and 0.30 wt%	Solution-assisted mixing	P/M and hot extrusion	Sintering for 2 h at 630 °C under highly purified argon followed by hot extruded using an extrusion ratio of 5:1	55	178	246	16.9	—	[223]
		0.5, 1.0, 1.5, and 2.0 wt%	*In situ* synthesis	Cold-press and hot extruded	Compacting under a pressure of 500 MPa at 298 K, and the sintering at 773 K for 1 h in a hydrogen atmosphere, followed by hot-extruded at 653 K under a pressure of 700 MPa at an extrusion ratio of 16:1	72.8	173	256	7.1	—	[224]
		0.5 wt%	Solution-assisted mixing	P/M and hot extrusion	Compacting under 600 MPa pressure using hydraulic press, and sintering at 630 °C for 2 h in argon atmosphere, followed by extruded at 1 m/min extrusion speed	63	204	265	4	—	[225]
	GO	0.1, 0.3 v, 0.5 and 1.0 vol%	*In situ* coating	SPS	Consolidating at 803 K for 10 min under 30 MPa pressure	57.3	—	—	—	α-Mg phasepolycrystalline MgO and amorphous MgO	[226]
Pure Zn	Gr	0.3 and 0.7 wt%	*In situ* coating	SPS	Sintering temperature of 340 °C, heating rate of 100 °C/min, sintering pressure of 45 MPa, holding time of 10 min	65	227	254	13.8	—	[31]
		—	Electro-co-deposition	Sintering	Sintering at 330 °C for 1 h with a temperature ramping rate of 10 °C/ min	62	74	81	6	—	[227]
	RGO	0.2 wt%	Matrix alloying and ball milling	SLM	A laser power of 80 W, scanning rate of 550 mm/s, hatch spacing of 40 mm, and layer thickness of 50 mm	—	42	46	10.7	—	[96]
		0.1, 0.2, and 0.3 wt %	Ball milling	SLM	Laser power 80 W, scanning speed 550 mm/s, scanning distance 40 μm	—	143	182	14.1	—	[59]
Mg-0.5Zr	Gr	0.1 wt%	Ball milling	Cold pressing and sintering	Cold-pressing at 760 MPa for 30 min, sintering at 400 °C for 1 h to and then at 610 °C for 2 h	58	—	—	—	—	[228]
Mg-0.5Zr-1Zn	Gr	0.2, 0.3, 0.4, and 0.5 wt%	Ball milling	Cold pressing and sintering	Cold-pressing at 760 MPa maintained for 30 min, sintering at a temperatures of 400 °C for 1 h and then 610 °C for 2 h	66	—	—	—	α-Mg and γ-MgZn phases	[32]
Mg–3Al	Gr	0.1, 0.3 and 0.5 wt %	Mechanical alloying	Cold pressing and sintering	Cold compacting at a pressure of 510 MPa, sintering at a temperature of ~640 °C for 13 min	60.4	140	345	21.6	α-Mg and β-$Mg_{17}Al_{12}$ phases	[229]
Mg-0.3Sr-0.3Ca	Gr	0.1, 0.2, and 0.4 wt %	—	Stir casting	Pure Mg was melted, and GNPs were incorporated into the molten Mg, followed by mechanical stirring at 450 rpm for 15 min. The molten slurry was then cast into a preheated steel mold at 400 °C	—	223	245	8.8	α-Mg, $Mg_{17}Sr_2$ and Mg_2Ca phases	[230]

(*continued on next page*)

Table 3 (*continued*)

Matrices metal	GD type	GD content	GD dispersion method	Processing method	Processing parameters	Hardness [HV]	Tensile properties YS [MPa]	UTS [MPa]	EI [%]	Primary and second phases	Ref.
					and subsequently hot-extruded at 370 °C with an extrusion ratio of 12:1.						
Mg6Zn	GO	0.1 and 0.3 vol%	Matrix alloying	Ultrasonic assisted stir casting	The Mg ingot was melted at 720 °C under CO2 + SF6 gas protection, and Zn ingot was added to the molten Mg. After cooling to 600 °C, GO@ZnO was added under mechanical stirring (800–1200 rpm), followed by sonication at 690 °C for 20 min, and then solidified.	86	221	316	14.8	MgO phases	[99]
	Gr	0.7 and 1.0 vol%	Bubbles assisted assembly method	Liquid metallurgy method and hot extrusion	—	—	220	330	8.3	—	[231]
		0.32 and 0.61 vol%	*In situ* synthesis	Pressure casting and hot extrusion	Solidified under 100 MPa, homogenized at 340 °C for 24 h and quenched in cold water, and then extruded at 300 °C with an extrusion ratio of 20:1 and extrusion speed of 0.1 mm/s	—	292	341	8.0	Primary α-Mg and the eutectic β-Mg_4Zn_7 phasesMgO phase	[94]
		0.7, 1.0, and 1.6 vol %	*In situ* coating	Semi-solid stirring and hot extrusion	—	—	271	352	6.3	Polycrystalline Mg phases	[232]
		0.7 vol%	*In situ* coating	Semi-solid stirring and hot extrusion	—	—	161	276	11	$[0001]_{Mg}$ rod precipitates	[233]
		0.5 and 1.5 wt%	*In situ* coating	Disintegrated melt deposition and hot extrusion	Mg ingot was melted at 720 °C to fabricate the composites through the DMD, homogenized at 350 °C for 12 h, and hot extruded at 300 °C with a 5.2:1 extrusion ratio.	75.8	214	313	21	—	[234]
		—	*In situ* synthesis	Stirring and casting	Mg ingot was melted at 720 °C, and 6 wt% Zn ingot was then added and cooled at 680 °C. CO_2 flow at 0.5 L/min was introduced into the molten Mg and magnesiothermic reactions was carried out for 30 min.	59	—	—	—	MgO phase	[235]
Mg9Al1Zn	Gr	0.25 and 0.5 wt%	—	Liquid-state ultrasonic dispersion and stir casting	The AZ91 alloy was melted and stirred at 675 °C and 1000 rpm. The pellets containing the GNPs were introduced into the melt and mechanical stirring for 15 min. The melt was reheated to 700 °C and was ultrasonically processed for 15 min at 675 °C.	69	128	190	2.8	Primary α-Mg and secondary β phases	[236]
		0.5, 1.0 and 1.5 wt %	—	Stirring casting	—	282	86	114	2.8	—	[237]
		0.1, 0.3, 0.5, 0.8 and 1.2 wt %	Solution-assisted mixing	Sintering and hot extrusion	Compacted under a hydraulic pressure of 120 MPa, and then sintered at 873 K for 2 h under Ar atmosphere, and hot extruded at 673 K with an extrusion ratio of 11:1.	88.5	296	335	8.7	—	[238]
		0.6 wt%	—	Thixomolding	—	87.6	—	247	4.3	MgO and Mg17Al12 phases	[239]
	RGO	0.1, 0.3, 0.5, 0.8	*In situ* coating	Hot extrusion	Compacting under 120 MPa, sintering at 873 K for 2 h in an Ar atmosphere, and then hot extruded at 673 K with a ram speed of 0.3 mm/min to obtain	96.1	312	355	11.3	α-Mg phaseMgO phase	[240]

(*continued on next page*)

Table 3 (*continued*)

Matrices metal	GD type	GD content	GD dispersion method	Processing method	Processing parameters	Hardness [HV]	Tensile properties YS [MPa]	UTS [MPa]	EI [%]	Primary and second phases	Ref.
		and 1.2 wt %			12 mm diameter rods, followed by T4 treatment at 686 K for 18 h and air quenching.						
Mg6Zn0.5Zr	Gr	—	Solution-assisted mixing	Stir casting and hot-extruded	The GNP/Mg powder was hot-extruded at 493 K with a ratio of 12 to form precursor rods, which were then added to the molten matrix alloy (~993 K), stirred for homogeneity, and cast. The cast ingot was subsequently hot-extruded at 523 K with an extrusion ratio of 12.	75	283	343	17	Primary α-Mg and $MgZn_2$ phases	[217]
		0.05 wt%	Solution-assisted mixing	Stirring casting and hot extrusion	The mixed powder was hot extruded (493 K, ratio of 12) to GNP/Mg precursor for adding into the Mg melt (~993 K), and then stirring casted under the protection of N2-SF6 atmosphere. At last, the cast ingot was hot extruded (523 K, ratio of 12).	—	265	336	22.5	α-Mg and $MgZn_2$ phases	[241]
		0.04 and 0.08 wt%	Solution-assisted mixing	Stirring casting and hot extrusion	The mixed powder was hot extruded (493 K, ratio of 12) to GNP/Mg precursor for adding into the Mg melt (~993 K), and then stirring casted. At last, the cast ingot was hot extruded (523 K, ratio of 12).	79.8	256	326	14	ZnZr, Zn_2Zr and Zn_2Zr_3 phases	[218]
		0.05 wt%	Solution-assisted mixing	Hot compaction and extrusion	The composite powder underwent compression following a preheating step at 553 K for 30 min. Then, the obtained compact was preheated at 598 K for 20 min and then hot extruded.	76.2	257	342	24.7	—	[242]
	GO	0.05, 0.1, 0.2, and 0.3 wt%	Ball milling	Hot pressing and thixomolding	The powder mixture was compacted under 270 MPa at 573 K for 35 min, heated to 863 K for 60 min to form a semisolid ingot, and then thixoformed at 190 MPa for 20 s.	75.9	160	288	19.5	α-Mg and $MgZn_2$ phases	[243]
			In situ coating +ball milling	Hot pressing and thixomolding	The composite powder was compacted into billets at 270 MPa and 573 K for 35 min. The billets were then partially remelted at 863 K for 60 min to achieve semisolid ingots, which were thixoforged at 190 MPa for 20 s.	—	146	273	23.2	Near-spheroidal primary α-Mg phasesMgO phase	[244]
		0.05, 0.1, 0.2, and 0.3 wt%	Ball milling	Hot pressing and thixomolding	K and 270 MPa for 35 min, then heated to 863 K for 60 min to achieve semisolid ingots, which were subsequently thixoforged at 190 MPa.	73	177	303	23.1	MgO phase	[245]
	Gr	—	Solution-assisted mixing	Hot extrusion and Stir casting	The composite powder was compacted and hot-extruded with a 10:1 extrusion ratio to form precursor rods. A pure Mg ingot was heated to ~ 993 K, followed by the sequential addition of the Mg–30Zr master alloy, pure Zn plate, and GNPs/Mg precursor into the melt, stirred for 3 min, held for 10 min, and then cooled.	80	146	261	12.1	α-Mg andMgO phase	[246]
Mg6Zn1Zr	RGO	0.5 and 1.0 wt%	Solution-assisted mixing	SPS	Sintering at 793 K with a 6-min holding time under an axial pressure of 60 MPa	70.2	—	—	—	—	[247]
		0.1, 0.25, 0.4 and 0.6 wt%	Solution-assisted mixing	Hot-press sintering and hot extruded	The mixed powders were sintered at 473 K under 200 MPa to form green billets, which were then hot-extruded at 623 K with an extrusion speed of 1 mm/s and an extrusion ratio of 25:1.	79.9	203	—	17.5	Nano-MgO phase	[248]

(*continued on next page*)

Table 3 (*continued*)

Matrices metal	GD type	GD content	GD dispersion method	Processing method	Processing parameters	Hardness [HV]	Tensile properties YS [MPa]	UTS [MPa]	EI [%]	Primary and second phases	Ref.
Mg3Al1Zn	Gr	—	—	Disintegrated melt deposition and hot extrusion	The Mg ingot was melted at 740 °C to fabricate the composites through the DMD, homogenized at 430 °C for 24 h and hot-extruded at 350 °C.	102	136	230	10.3	Primary α-Mg and β-$Mg_{17}Al_{12}$ phases	[249]
		0.18 wt%	Solution-assisted mixing	Sintering and extrusion	Sintered at 630 °C for 2 h under a high-purity argon atmosphere, then extruded at 400 °C using a 500 T hydraulic press with a 9:1 extrusion ratio to produce 9 mm diameter bars	71	173	275	21.7	β-$Mg_{17}Al_{12}$ phase	[250]
		0.5, 1.0, 2.0 wt%	Ball milling	Sintering and hot-pressing	Sintered at 500 °C for 3 h under an Ar gas atmosphere without demolding, followed by hot pressing at 400 °C under 300 MPa.	87.5	215	278	8.9	α-Mg phase	[251]
		1.5 and 3.0 wt%	—	Stirring casting andhot extruded	The Mg ingot was melted at 740 °C. Gr powder was introduced into the AZ31 molten slurry, stirred for 1.0 min, reheated to 740 °C, and held for 10 min before solidification. The billets were then hot-extruded at 350 °C with a 5.2:1 extrusion ratio.	68.9	199	295	12.5	α-Mg and β-$Mg_{17}Al_{12}$ phases	[252]
	RGO	0.2, 0.3, 0.4, and 0.5 wt%	Solution-assisted mixing	Cold pressing and sintering	The composite powder was compacted at 580 MPa at room temperature, then sintered at 560 °C in an argon environment.	62	—	—	—	—	[253]
Mg6Al1Zn	RGO	1.0, 2.0, 3.0, and 4.0 wt%	*In situ* coating	SLM	Laser power 80 W, scanning speed 15 mm/s and laser spot size 50 μm	108	—	—	—	α-Mg phaseMgO nanoparticles	[254]

Table 4
The standard electrode potential values of the elements relevant to metallic biomaterials (298 K)[255,256,257,258].

Electrode reaction	Standard electrode potential, E^0 (V)
$Mg \leftrightarrow Mg^{2+} + 2e^-$	−2.36
$Al \leftrightarrow Al^{3+} + 3e^-$	−1.66
$Ti \leftrightarrow Ti^{2+} + 2e^-$	−1.63
$H_2 + 2OH^- \leftrightarrow 2H_2O + 2e^-$	−0.8281
$Zn \leftrightarrow Zn^{2+} + 2e^-$	−0.763
$Cr \leftrightarrow Cr^{3+} + 3e^-$	−0.744
$Fe \leftrightarrow Fe^{2+} + 2e^-$	−0.440
GO	−0.400
$Co \leftrightarrow Co^{2+} + 2e^-$	−0.277
$Ni \leftrightarrow Ni^{2+} + 2e^-$	−0.250
$H2 \leftrightarrow 2H^+ + 2e^-$	±0.000
RGO	0.160
Gr	0.200
$Ag \leftrightarrow Ag^+ + e^-$	0.799
$Pd \leftrightarrow Pd^{2+} + 2e^-$	0.987
$Pt \leftrightarrow Pt^{2+} + 2e^-$	1.188
$2H2O \leftrightarrow O_2 + 4H^+ + 4e^-$	1.229
$Au \leftrightarrow Au^{3+} + 3e^-$	1.498

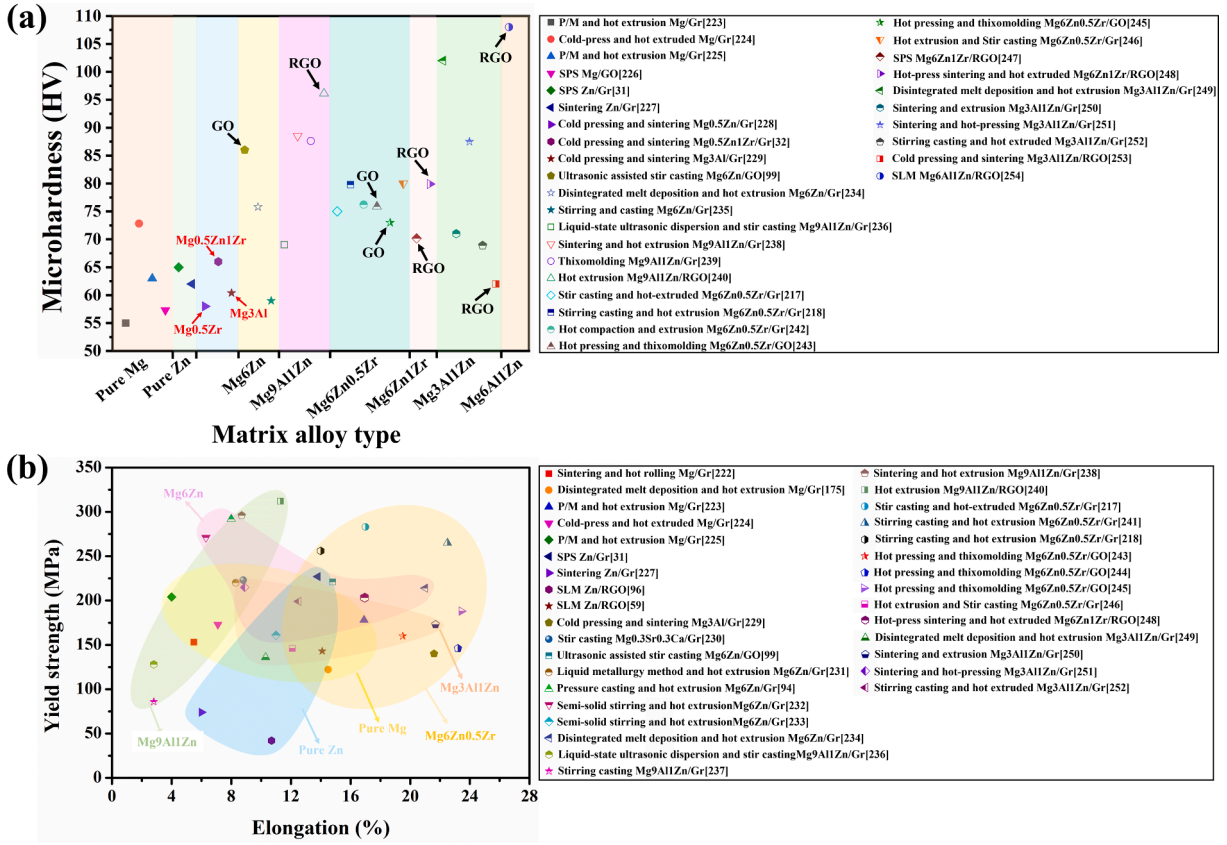

Fig. 14. The mechanical properties of GD-containing Mg- and Zn-based BMMCs: (a) A summary of microhardness and (b) yield strength of various materials *versus* elongation.

exhibit microhardness values ranging between 55 and 108 HV (Fig. 14a). As compared with the microhardness values of GD-containing pure Mg- and pure Zn-based BMMCs, the hardness values of GD-containing Mg-Zn alloy matrix BMMCs, such as those based on Mg6Zn, Mg9Al1Zn, Mg6Zn0.5Zr and Mg3Al1Zn, are much higher. This is attributed to the introduction of heteroatoms into the α-Mg lattice caused by alloying elements, which results in local solute lattice distortions and lattice dislocation accumulation

[221]. In addition, for various Mg-Zn alloys, higher hardness values have been achieved with GO or RGO additions, regardless of alloy composition and content, indicating that the Gr derivatives significantly influence the hardness of these materials in which an independent hardening mechanism operates [79]. From Table 2 and Table 9, it is evident that GO and RGO have a larger strengthening effect than pure Gr due to their adsorption of oxygen-containing functional groups on the surface and, thus, their good hydrophilicity and flexibility, resulting in better dispersion in the initial powder mixtures and in the metal matrices [88].

The strength-ductility relationships of GD-containing Mg- and Zn-based BMMCs are illustrated in Fig. 14b. The wide ranges of strength and elongation values are more dependent on the compositions of the matrix alloys and processing methods together with their processing parameters than on the types of Gr. Biodegradable magnesium alloy matrix composites exhibit a wide range of ductility values from 2.8 % to 24.7 % and the yield strengths are all lower than 350 MPa. The hot-extruded RGO-reinforced Mg9Al1Zn1 (AZ91) composite exhibits the highest ultimate tensile strength of 355 MPa, which can be attributed to the synergistic effects of optimized RGO content, enhanced dispersion, and refined processing techniques that maximize the strengthening efficiency of RGO. Currently, the data of newly developed GD-containing Mg- and Zn-based BMMCs fabricated by SPS and SLM are rather limited. Although SPS leads to higher tensile strength and comparable ductility, as compared with SLMed counterparts, the ultimate tensile

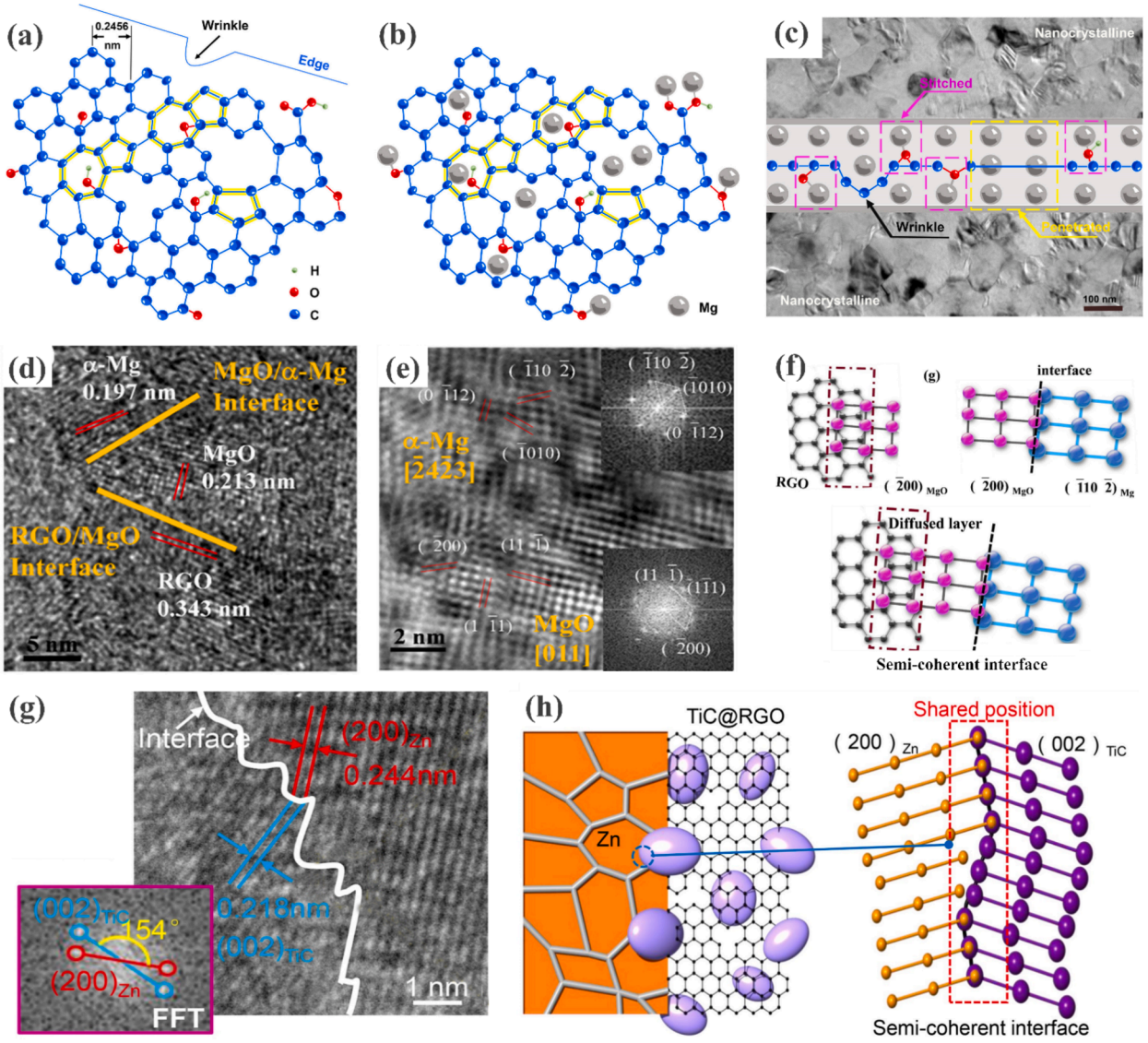

Fig. 15. (a) The in-plane atomic structure of GNPs with defects (The defects include non-hexagonal rings, pores of carbon vacancies, dangling carbon bonds at edges, and wrinkles. The symbols 'H', 'O', and 'C' represent hydrogen, oxygen, and carbon atoms, respectively.) (b) GNPs combined with Mg atoms. (c) The interaction between defective GNPs and the Mg matrix on the cross-section [241]. (d) HRTEM images of an AZ61-RGO/MgO composite. (e) Fast Fourier transform (FFT) patterns of the specified areas in the AZ61-RGO/MgO composite. (f) A schematic drawing of the interfacial characteristics of the AZ61-RGO/MgO composite [254]. (g) HRTEM, FFT, and inverse FFT images of the Zn-TiC interface. (h) A sketch map showing the interface structure of Zn-TiC [96].

strength and elongation obtained are below 250 MPa and 15 %, respectively. For load-bearing bone implant applications, the mechanical properties of BMs should at least be comparable with pure Ti (Grade 4A) whose ultimate tensile strength should be higher than 550 MPa and elongation higher than 15 %, according to ISO 5832–2 [259,260]. High strength Zn alloys, such as micro-alloyed Zn-Mg [261] and Zn-Li [262], may be considered good substitutes of pure Zn to achieve more adjustable mechanical properties.

From a microstructure perspective, the presence of Gr itself and its inherent defects can profoundly influence the strengthening effect through: (i) the interfacial bonding behavior with the magnesium alloy matrix and precipitated nanoscale phases and (ii) lattice orientation relationships [263]. Du *et al.* [241] introduced multilayer Gr with a large number of in-plane defects into the ZK60 magnesium alloy (Fig. 15a). After being dispersed in the Mg matrix, the defective Gr closely combined with Mg atoms (Fig. 15b). On the one hand, Mg atoms filled the pores in Gr and donated electrons for restoring the sp2 hybridized structure of Gr. On the other hand, Mg reacted with oxygen in chemical groups, resulting in the formation of MgO nanoparticles at the interface between Gr and Mg [233]. Fig. 15c shows that the restoring effect of Mg leads to "penetration" into Gr and MgO nanoparticles perform the function as "stitches", leading to strong interfacial bonding in the composite. Meanwhile, Gr defects scattering at the nanoscale trigger the nucleation of Mg nano-grains, which connect the "hard" Gr and "soft" Mg matrix for the effective transfer of stress and strain [238]. Shuai *et al.* [254] further characterized the lattice orientation relationship and interfacial bonding type between the nano-sized MgO/Mg matrix and RGO dispersed in the ZK61 alloy matrix. High resolution transmission electron microscope (HRTEM) and Fourier-filtered images of MgO/α-Mg interface revealed that MgO and α-Mg formed a semi-coherent interfacial structure in which an orientation relationship of MgO (—200)//α-Mg (—110–2) and a small planar disregistry of 7.5 % were detected (Fig. 15d and 15e). MgO was found to act as an interfacial bridge between the Mg matrix and RGO and construct nanoscale-contact and distortion areas with RGO (Fig. 15f). These interfacial characteristics indicate strong bonding at both the RGO/MgO and MgO/α-Mg interfaces, thereby ensuring the strengthening effect of RGO.

It is, however, difficult to achieve strong interfacial bonding between Gr and the Zn matrix, because there is a large mismatch in surface tension between Zn (815 mN/m) and Gr (46.7 mN/m) [264,265]. As a result, Gr is non-wetting with Zn, and rather poor contacting interfaces within Zn/Gr MMCs tend to form, which is insufficient for the efficient load transfer and strength enhancement. Yang *et al.* [96] introduced a carbide nanostructure as an interface bridge to obtain strong interface bonding in the Gr/Zn composites by *in situ* growing TiC on RGO to prepare TiC@RGO nanohybrids and then incorporated them into Zn scaffolds as reinforcement. Fig. 15g illustrates a twin-like relationship between the (200) Zn plane and (002) TiC plane, accompanied by an intersection angle of 154° between their lattice fringes. According to the Bramfitt lattice matching theory [266], a lattice misfit less than 15 % will contribute to strong interface bonding by means of semi-coherent or coherent patterns [267]. The lattice misfit between (200) Zn plane and (002) TiC plane was only 10.6 %. Therefore, semi-coherent bonding was formed (Fig. 15h) between TiC and the Zn matrix because of the small lattice misfit and similar atomic arrangement between the (200) Zn plane and (002) TiC plane. The formed semi-coherent Zn/TiC interface with reduced interface energy was, thus, expected to generate more powerful interfacial bonding.

4.1.3. GD-reinforced Fe-based BMMCs

Fe-based BMMCs have higher mechanical strengths than Mg-, Zn-, polymer-, and ceramic-based biodegradable materials [268]. In addition to sufficient strength, bone-substituting biomaterials are expected to undergo millions of cycles of mechanical loading *in vivo* [269], and in the case of BMs, fatigue failure is more likely to occur due to biodegradation and fatigue interactions [270]. Geometrically ordered porous Fe scaffolds have been reported to retain quasi-static mechanical properties within the range of the trabecular bone even after 4 weeks of *in vitro* biodegradation [53]. However, the current quasi-static mechanical properties of Fe and Fe-alloy scaffolds remain insufficient for biomaterial applications under physiological loading, particularly for load-bearing bones subjected to complex fatigue stresses. The development of Gr-containing Fe-based BMMCs with higher strength and fatigue resistance remains important for the widespread clinical use of iron-based scaffolds.

For the first time, Lin *et al.* [271] integrated single-layer GO powder into a pure Fe matrix and investigated its effect on mechanical strength and fatigue life. As shown in Fig. 16a, a laser-based AM process was used to sinter GO and iron powder and form GO/Fe nanocomposites with GO aligned vertically on the cross section. The Young's moduli of the GO/Fe nanocomposites exhibited a linear relationship with the volume fraction of GO (Fig. 16b). Surface microhardness increased by 93.5 % after laser sintering due to the presence of 2 wt% GO (the inset in Fig. 16b), which was attributed to dislocation piling up against GO, thereby forming dislocation forests during laser sintering and plastic deformation of the Fe/GO nanocomposites. Recently, improvements in microhardness (16.8 %) and yield strength (48.7 %) have been reported in pure Fe/GO composites [215] and biodegradable high entropy alloy-based composites (Fe50Mn30Co10Cr10/Gr) [272], respectively. The authors of another study reported more significant improvements in the mechanical properties of Fe-Mn-Co/Gr composites [273]. In terms of both fatigue strength and fatigue limit, the fatigue performances of laser-sintered iron and laser-sintered Fe-GO (2 wt%) were evaluated. From Fig. 16c, it is quite clear that laser sintering of the composite with 2 wt% GO led to better fatigue performance. The fatigue strengths of the laser-sintered iron and laser-sintered Fe-GO (2 wt%) composite were roughly $>$ 500 and 600 MPa, respectively, for a fatigue life of 300,000 cycles. When compared to laser-sintered iron, the fatigue life of the 2 wt% GO-containing composite enhanced by 167 %. Embedded GO provided a greater hardness enhancement, higher dislocation density, and better dislocation pinning, all of which increased the resistance to crack initiation. GO reinforcement was proven to be an effective way to improve the fatigue life of Fe.

In recent years, MD simulation has emerged as a uniquely powerful approach to studying the deformation, failure, and strengthening mechanisms of Gr-containing Fe-based BMMCs at the atomic level. For example, Ishraaq *et al.* [275] predicted the mechanical properties of Gr-containing Fe-matrix composites by applying the MD method under various temperature conditions for application in the automotive and aerospace industries. Shuang *et al.* [274] investigated dislocation-Gr interaction mechanisms and possible influencing factors, including the number of GNS layers through MD simulations and concluded that the shear strength of the

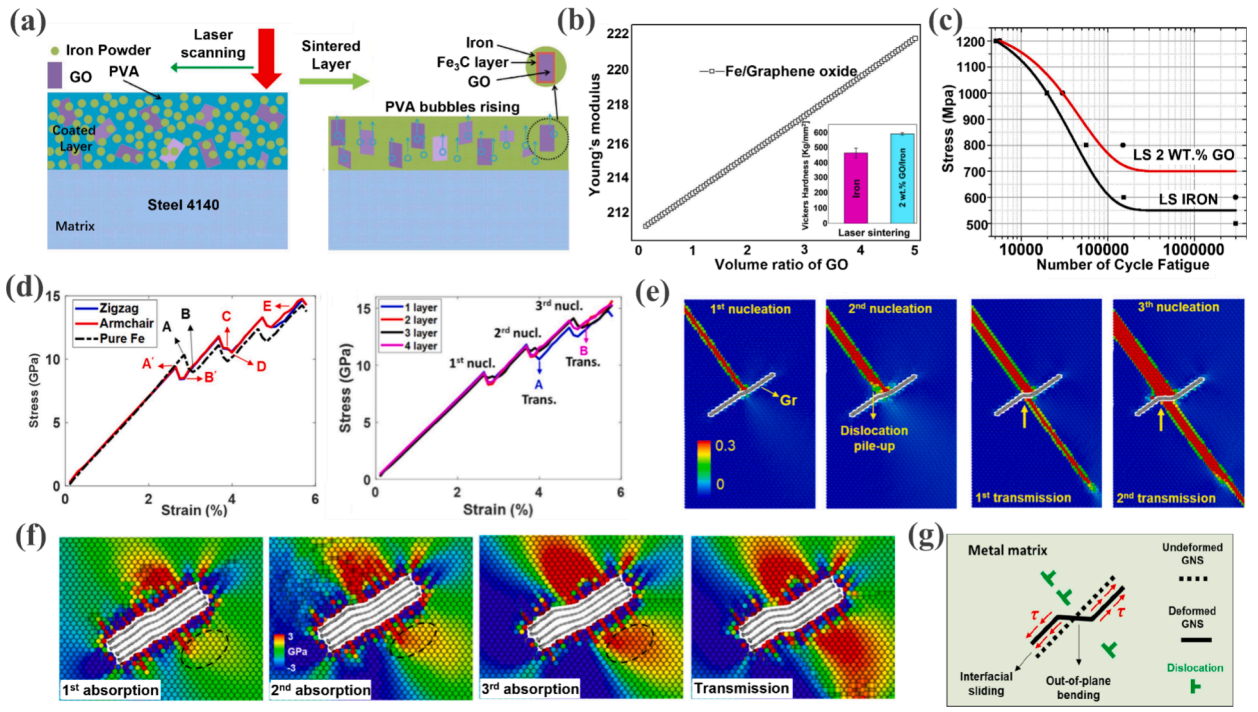

Fig. 16. (a) A schematic cross-sectional view illustrating the laser sintering of a GO/Fe nanocomposite layer on a steel 4140 build plate. (b) Young's moduli of GO/Fe nanocomposites with different volume ratios. The inset image presents the surface microhardness values of the laser-sintered iron and laser-sintered iron reinforced by 2 wt% GO. (c) Three-point bending fatigue lives of laser-sintered iron and laser-sintered iron reinforced by 2 wt % GO [271]. (d) Compressive stress–strain curves of pure Fe specimens and Fe-GNS composite specimens with armchair, zigzag GNS, and different GNS layers. (e) Atomic von Mises strains at different stages in Fe/single layer GNS composites. (f) Atomic shear stresses of neighboring Fe atoms around multiple layer GNS at different stages. (g) A mechanistic model of dislocation-GNS interaction [274].

metal/GNS interface and the bending stiffness of GNS, instead of the C–C bond strength, determined the slip resistance and strengthening effects. Fig. 16d depicts the compressive stress–strain behaviors of pure Fe and an Fe-GNS composite with single or multiple GNS layers. Typically, dislocation nucleation begins at the top corners and each dislocation results in a stress drop. Dislocation pileups formed at the rigid bottom lead to a hardening effect. Atomic von Mises strains around a monolayer Gr sheet at different stages reflect the complete evolution of dislocation nucleation, pile-up, and transmission (Fig. 16e). It can be seen in Fig. 16f that the atomic stresses of Fe near multilayer GNS interface are clearly lower than those of the monolayer GNS even after the third absorption of dislocation, indicating that multilayer GNS can effectively blunt the stress concentration caused by dislocation pileups, which means that dislocation transmission will become harder. The mechanistic model shown in Fig. 16g explains two necessary physical processes existing prior to the occurrence of dislocation transmission: (i) relative sliding of the metal/GNS interface, and (ii) out-of-plane bending of the GNS. Some strategies have been proposed to further improve the strength by blunting the accumulated stress, such as (i) increasing the number of GNS layers and introducing an amorphous layer, and (ii) increasing the shear strength of the metal/GNS interface by adding functional groups, and introducing interfacial chemical reactions and defective Gr [276].

4.1.4. Factors affecting the mechanical properties of GBMMCs

The content of GDs plays a dual role in determining the mechanical properties of BMMCs. Overcoming agglomeration of GDs is a major challenge in developing GBMMCs, particularly in the alloy systems with limited interfacial reactivity. For Mg-based BMMCs, moderate Gr additions (0.5–1.5 wt%) [224,251] significantly enhance hardness and tensile strength by promoting dislocation pinning and grain refinement *via* the Hall-Petch effect. However, excessive Gr content (≥2 wt%) leads to agglomeration, which weakens interfacial bonding, promotes crack propagation, and reduces relative density (from 98.5 % to 96.4 %). These effects create stress concentration sites that significantly decrease ductility, causing elongation to drop from 13.2 % to 8.9 % [251]. Conversely, insufficient Gr content (<0.5 wt%) may fail to provide effective reinforcement, resulting in minimal strengthening and suboptimal mechanical properties. For instance, in Mg9Al1Zn-based composites, RGO content below 0.5 wt% yielded a hardness range of 82–89 HV, being significantly lower than the 108 HV hardness achieved with 1.2 wt% RGO [240]. Similarly, in Zn-based BMMCs, the inherent poor wettability between Zn and Gr limits load transfer efficiency. An excessive RGO content (*e.g.*, 0.3 wt% [59]) further exacerbated agglomeration and interfacial mismatch, resulting in non-wetting interfaces and premature fracture during tensile loading. Compared to 0.2 wt% RGO/Zn composites, the yield strength and elongation decreased from 142.9 MPa to 115.7 MPa and from 14.1 % to 12.9 %, respectively. On the other hand, when the RGO content was only 0.1 wt%, it failed to effectively bridge the interfacial mismatch between Zn and RGO, resulting in poor load transfer and a low tensile strength of 111.3 MPa. For Fe-based BMMCs, the optimal GD

content appears to be broader, as some studies have reported prolonged fatigue life through dislocation pinning at 2 wt% GO [271], while 0.8 wt% GO [215] contributed to a more refined grain structure. While these studies suggest suitable GD content ranges for different BMMCs, it is important to note that the optimal content is not a fixed parameter. Instead, it must be determined comprehensively by considering additional factors such as GD dispersion methods, processing techniques, and the specific matrix-reinforcement interactions. For GBMMCs, advanced processing techniques, such as those employing hybrid dispersion methods (*e.g.*, ball milling combined with ultrasonic treatment) and *in-situ* reactions (*e.g.*, MgO nanoparticle formation at Gr/Mg interfaces [238]) to improve GDs' dispersion and interfacial bonding, introducing interfacial "bridges" (*e.g.*, TiC@RGO [96]) to reduce lattice mismatch, enabling semi-coherent interfaces and enhanced load transfer, and aligning GD sheets in a specific direction (SLM combined with solution dispersion [271]) to minimizing agglomeration and maximizing dislocation interaction, are the possible ways to effectively solve the problems related to excessive GD addition.

To highlight the distinct advantages of GBMMCs, it is essential to compare their key properties with those of BMMCs containing ceramic- and polymer-based biodegradable materials. GDs form an interconnected network that enhances stress redistribution and efficient load transfer across the interface, while, unlike HA or β-TCP reinforcements in ceramic-based BMMCs, which act as rigid stress concentration sites, it also bridges microcracks to prevent early fracture. For example, HA [277] and β-TCP [278] have been incorporated into Mg-based BMMCs to improve bioactivity, but they often lead to brittle behavior due to the weak Mg/ceramic interface. Mg-2Zn-0.5Sr/HA composites exhibited declines in UTS and elongation as HA content increased from 0 to 0.3 wt% [279]. When HA reached 0.3 wt%, elongation dropped to ~ 4.3 % due to stress concentration induced by ceramic particles, which hindered plastic deformation and promoted early fracture. In contrast, Mg-based GMMCs (*e.g.*, Mg6Zn/GO [99]) exhibited a higher UTS value of 316 MPa and improved ductility (~14.8 %), which was attributed to Gr's effective load transfer and crack bridging mechanisms, enhancing both strength and toughness. Polymer-reinforced Mg-matrix composites improve flexibility and corrosion resistance, but their low mechanical strength (<200 MPa) and thermal instability limit their structural applications [280]. Mg-PLA composites, for example, showed good elongation but low tensile strength (<170 MPa) and poor creep resistance [281]. Mg/Poly-l-lactic acid (Mg/PLLA) composites maintained higher ductility (~53.2 %) but with a drop in tensile strength (~104 MPa), making them unsuitable for load-bearing implants [282]. In contrast, Gr-reinforced Mg composites offer a better strength-ductility balance, making them more suitable for orthopedic applications. For Zn-based MMCs, GDs' interfaces facilitate dislocation pile-up, forming tangles that enhance matrix strength, whereas ceramics phase interacts with dislocations *via* Orowan looping but induces brittle fracture under excessive stress. Zn-HA composites exhibited high hardness (~46 HV) but experienced declines in compressive strength and elongation when HA content exceeded 5 wt% [283]. Similarly, Zn-Al-Cu/SiC/TiB_2 [284] composites improved tensile strength (UTS ~ 260 MPa) at the expense of ductility, with elongation dropping to ~ 1 %, highlighting the trade-off between strength and toughness in ceramic-reinforced Zn-based composites. In contrast, Zn-based GMMCs achieve superior tensile strength (~250–300 MPa) and ductility (~10–15 %) due to effective dislocation strengthening and load transfer [31]. Polymer-reinforced Zn-based composites (Zn-Montmorillonite/PCL [285]) lacked Gr's stiffness, leading to limited load transfer and poor fatigue resistance due to polymer creep, whereas Zn-Gr composites [286] maintained stable strength and structural robustness over time. For Fe-based MMCs, GD sheets dissipate energy along crack paths, reducing crack growth rates under cyclic loading, whereas ceramic reinforcements in ceramic-reinforced BMMCs create stress concentrations, leading to early microcracks and brittle fracture. For instance, Fe-HA composites [287] exhibited both reduced tensile strength and elongation with increasing HA content due to ceramic-induced brittleness. Similarly, Fe35Mn/Akermanite composites [288] showed lower mechanical properties than the Fe35Mn alloy and experienced accelerated biodegradation over time, further compromising fatigue resistance. In contrast, Fe-GO composites exceeded 600 MPa in fatigue strength and enhanced fatigue resistance by > 167 % [271]. In summary, ceramic-containing BMMCs and polymer-containing BMMCs face challenges with ceramic phase agglomeration and polymer phase separation, respectively, limiting their reinforcement efficiency. GBMMCs leverage Gr-induced dislocation pinning and crack bridging to enhance fatigue life, outperforming both ceramic- and polymer-based BMMCs by providing superior load transfer, stress redistribution, and long-term structural stability for load-bearing applications.

4.1.5. Linking strengthening mechanisms to clinical implant requirements

For GBMMC implants, achieving sufficient compressive and tensile strengths along with an appropriate elastic modulus is crucial to prevent premature failure and ensure that the implants can withstand dynamic loading conditions [289]. The ideal mechanical properties for orthopedic and vascular implants should meet specific requirements; the yield strength should be at least 230 MPa for orthopedic implants and 200 MPa for vascular implants [290]. Additionally, the tensile strength for both types of implants should exceed 300 MPa to ensure adequate mechanical performance. Notably, natural bone itself exhibits compressive yield strengths ranging from 130 to 180 MPa [8], providing reference values for designing implants to adequately carry physiological loads. For orthopedic implants specifically, the elastic modulus should closely match that of the cortical bone, typically ranging between 10 and 20 GPa, to promote optimal load transfer and reduce stress shielding effects. In orthopedic implant applications, if load transfer is compromised by poor interfacial bonding between Gr and the metal matrix, the reinforcement may debond prematurely, thereby reducing the overall mechanical integrity of the implant. Therefore, strong interfacial adhesion, for example, achieved through surface functionalization of GDs, is critical to ensuring that the load-transfer mechanism provides sufficient strength for orthopedic applications. Weak interfacial bonding, combined with corrosion in physiological fluids, can accelerate interfacial debonding and lead to load-transfer failure *in vivo*. For Mg-based BMMCs, the weak van der Waals forces [291] at the Mg/Gr interface result in low interfacial shear strength, making the interface prone to debonding under mechanical loads. Effective load transfer from the matrix to Gr can be achieved when strong interfacial bonding is present, particularly through the formation of an *in-situ* reaction layer, such as MgO formation [292], which enhances adhesion and load-bearing capability. In Zn-based MMCs, the significant surface tension mismatch between Zn (815 mN/m [265]) and Gr (46.7 mN/m [264]) leads to poor wettability and weak interfacial bonding, severely limiting

load transfer efficiency. As a result, unmodified Zn-Gr composites exhibit minimal reinforcement from the load transfer mechanism, with the contribution of RGO added to pure Zn to improving the yield strength by only ~ 20 MPa. However, surface functionalization, such as the *in-situ* growth of a TiC layer on RGO, has been shown to substantially enhance load transfer, increasing the yield strength from ~ 90 MPa to 165 MPa while simultaneously improving elongation from ~ 10 % to 15 % [96]. This outcome highlights the importance of synergizing load-transfer strengthening with appropriate GD surface modifications to meet the mechanical requirements of orthopedic implants. For Fe-based MMCs, strong covalent bonding [293] between Fe and GDs enables efficient load transfer, significantly enhancing mechanical performance. Additionally, Fe's high surface energy (~2.5 J/m2) compared to Zn (~1.0 J/m2) promotes better wettability with Gr, further facilitating effective load transfer and reinforcing the interface [294].

Implants often experience cyclic loading *in vivo*, which can lead to fatigue-induced failure. If certain strengthening mechanisms, such as Orowan strengthening, rely heavily on dispersed Gr, any agglomeration or degradation of Gr over time could lead to a loss of strengthening benefits [295]. Hwang *et al.* [296] utilized chemical vapor deposition (CVD) to fabricate multilayered Cu-Gr composites with *in-situ* grown Gr, maintaining an interparticle spacing (λ) of ~ 100 nm along the growth direction. They observed a 5- to 6-fold improvement in fatigue strength compared to monolithic Cu. Similarly, Lin *et al.* [271] reported a ~ 167 % increase in fatigue life for GO-reinforced Fe composites and attributed it to enhanced dislocation density and crack pinning, which resisted crack initiation. Conversely, Kumar *et al.* [297] observed a decline in fatigue life in Al6061-Gr composites with increasing Gr content, likely due to aggregation-induced crack nucleation. Investigating long-term fatigue resistance of GMMC implants is essential to ensuring their suitability for orthopedic applications. The cyclic loading in physiological fluids may exacerbate Gr agglomeration (increasing λ), weakening the Orowan effect. Thus, long-term dispersion stability must be ensured through techniques like ultrasonic dispersion combined with *in-situ* synthesis.

Ideally, implants *in vivo* should retain performance at body temperature (~37 ℃) and during transient temperature spikes (≤45 ℃) caused by postoperative inflammation [298,299]. Prolonged thermal fluctuations may accumulate residual stresses, inducing microcracks. For example, the large CTE difference between Gr and Mg (−6 to − 8 × 10^{-6} K^{-1} [300] and ~ 28.9 × 10^{-6} K^{-1} [301] at near physiological temperature, respectively) may induce stress concentration and even interfacial delamination under repeated thermal cycling. This thermal mismatch plays a more significant role in Mg-based BMMCs, as it generates high dislocation densities at the Gr/Mg interface, promoting dislocation accumulation and strengthening. In contrast, Zn has a lower CTE (~19 × 10^{-6} K^{-1}) [96] compared to Mg, resulting in a smaller thermal mismatch with Gr, thereby limiting dislocation generation and reducing the contribution of CTE mismatch strengthening. Fe, with an even lower CTE (~11.8 × 10^{-6} K^{-1}) [302], experiences minimal thermal mismatch with Gr, making the contribution of CTE mismatch strengthening negligible, as the induced mismatch stress is insufficient to generate significant dislocation accumulation. Additionally, physiological fluids (pH ~ 7.4, containing Cl^- and PO_4^{3-} ions) [303] may corrode the metal matrix or Gr interface, compromising load-transfer mechanisms. Corrosion-induced Cl^- penetration could also enlarge intergraphene spacing (λ), reducing Orowan strengthening effects.

Orthopedic implants also need to maintain moderate plasticity (elongation at break > 15 %) [304] to avoid brittle fracture and adapt to micro-deformation after implantation. Grain refinement tailored for orthopedic implants must balance strength and ductility. Excessive strengthening at the expense of ductility can lead to brittle fracture, which is undesirable for implants subjected to cyclic physiological loads. Wang *et al.* [243] reported that adding 0.2 wt% GO to the ZK60 magnesium alloy refined grain size from ~ 7.5 μm to ~ 2 μm while maintaining fracture elongation at 19.5 % (*versus* 22.6 % for ZK60), demonstrating that moderate refinement achieves strength-toughness synergy, and reducing the risk of catastrophic failure *in vivo*. However, Hall-Petch strengthening *via* grain refinement may accelerate degradation rates. For instance, in Zn-RGO composites, refining grain size from 6.9 μm to 3.1 μm increased tensile yield strength by 56 %, but raised *in vitro* degradation rates by 145 % [59], potentially altering the strength-degradation relationship during bone remodeling.

In summary, optimizing strengthening mechanisms (load transfer, dislocation strengthening, thermal mismatch, and/or grain refinement) for clinical implants involves a comprehensive strategy that integrates interface engineering, multiscale structural regulation, and environment-adaptive design. Ensuring interfacial stability within physiological fluids can be achieved through techniques such as surface functionalization and gradient interface design, while the synergy of nanoscale dispersion, microscale grain refinement, and macroscopic 3D architectures helps balance strength, ductility, and degradation rates. Additionally, employing temperature- and pH-responsive composites enables dynamic adaptation to *in vivo* environmental changes.

4.2. Biodegradable behavior

The corrosion processes of biodegradable metals, accompanied by Gibbs free energy changes, form the basic framework for their biodegradation processes. However, the uncontrollable corrosion rates of BMs, the difficulties associated with preparing some biodegradable alloys, the lack of uniform standards for alloy composition design [305], and the ambiguity to effectively achieve controllability and predictability of biodegradation rates are some of the unresolved issues in the current research and development of BM bone implant materials [306–309]. GDs have been considered of great potential either to speed up biodegradation or to improve the corrosion resistance, both of which can lead to customized degradation rates of different BMs to meet different application requirements [310]. This subsection will provide a comprehensive discussion of the intrinsic mechanisms of biodegradation and the recent achievements of GDs in regulating the biodegradation rates of Mg-, Fe-, and Zn-based BMMCs.

4.2.1. Corrosion promotion and protection mechanisms

In recent years, the high electric conductivity and positive potential of Gr have made GMMC scaffolds exhibit a high corrosion-promotion activity (CPA), which is reported to accelerate the corrosion of the metal matrix by inducing (micro-)galvanic corrosion

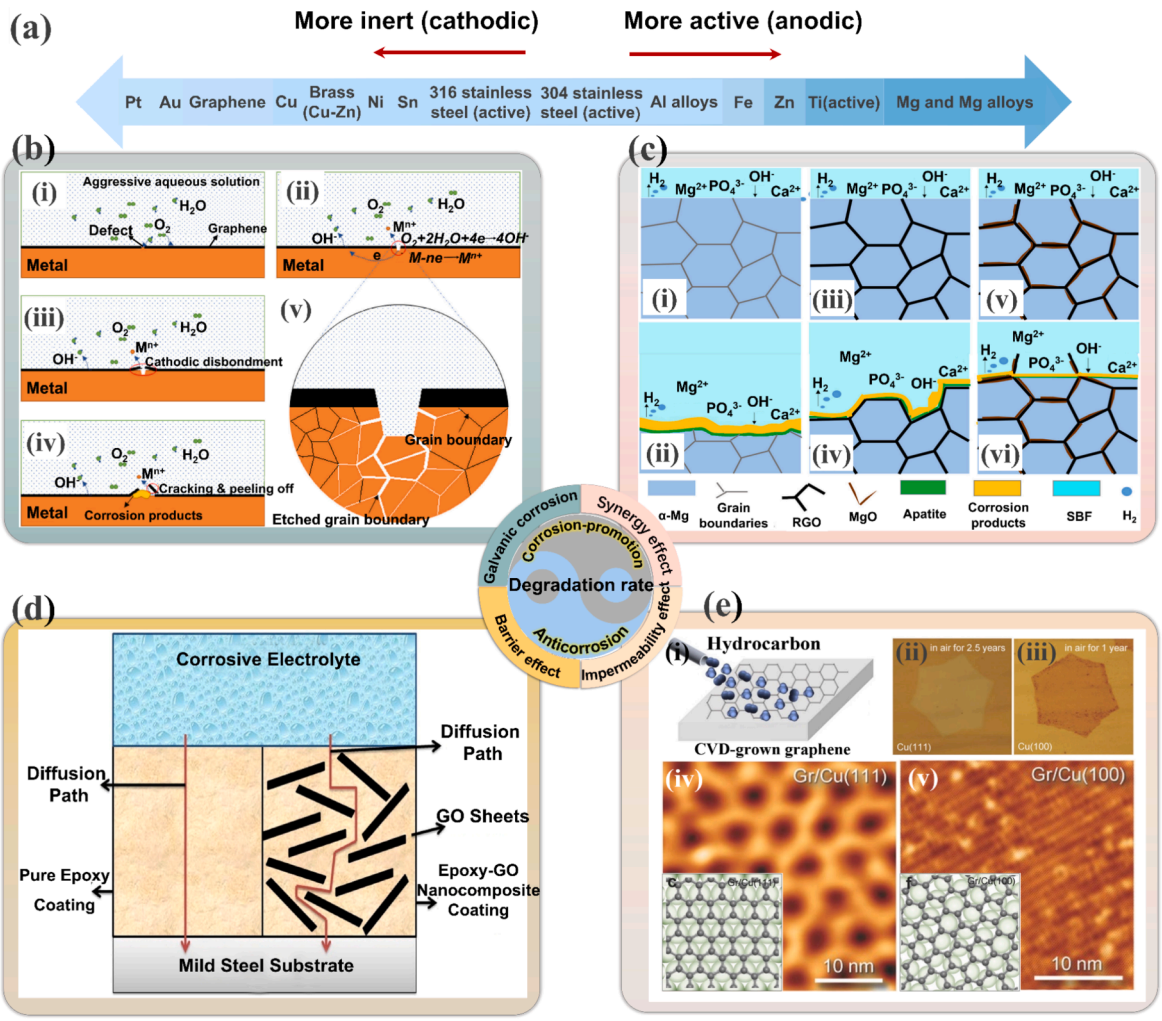

Fig. 17. (a) The galvanic sequence, listing various metals and Gr in the order of their tendency to corrode [319]. Gr's position between Cu and brass highlights its role as a cathode in Mg-based and Zn-based MMCs, driving micro-galvanic corrosion. Mg alloys, as the most anodic materials, exhibit accelerated degradation when coupled with Gr ($\Delta E > 1.5$ V), while Fe-based MMCs show reduced corrosion risks due to smaller potential gaps ($\Delta E < 0.3$ V). This sequence directly correlates with practical corrosion behavior, guiding material design to balance degradation kinetics and structural integrity. (b) A schematic diagram of CPA mechanism of Gr in an aqueous environment when coated/incorporated into BMMCs: (i) H_2O and O_2 diffusion, (ii) galvanic corrosion, (iii) cathodic disbondment, (iv) formation of corrosion products, Gr cracking and peeling off at defect sites, and (v) localized corrosion [255]. (c) A schematic diagram showing the corrosion processes of AZ61, AZ61-RGO, and AZ61-RGO/MgO MMCs [254]. (d) A schematic representation of the microscale corrosion protection mechanism of 'barrier effect' by GO nanocomposite coatings [320]. (e) A schematic drawing of the nanoscale corrosion protection mechanism of 'impermeability effect' by Gr: (i) CVD-grown graphene film [321]. (ii) and (iii) optical images of Gr/Cu (111) and Gr/Cu (100) system at ≈22 °C in air for 2.5 years and 1 year, respectively. (iv) and (v) scanning tunnelling microscopy (STM) topographies of Gr on Cu (111) and Cu (100), showing two distinct surface configurations. The inset images are the corresponding schematic diagrams of graphene lattice on Cu (1 1 1) and Cu (1 0 0) [322].

[311] at the defect sites of GDs in aggressive environments (Fig. 17b) [255]. The anodic dissolution of the metal in the surrounding of Gr and the reduction reaction (*i.e.*, cathodic reaction) in the nearly neutral or acid physiological environment are engaged in biodegradation [256,312]. Fig. 17a illustrates the whole progress of galvanic corrosion between the metal and Gr in an aqueous environment. When coupled with a relatively active metal (*e.g.*, Mg, Fe, Cu, and Zn), the high electrically conductive and electrochemical stable Gr will behave like a noble metal, acting as a cathode in the Gr-metal galvanic cell [313–316]. The cathodically polarized Gr leads to the formation of micro-galvanic Gr-metal corrosion that initiates the anodic dissolution and boosts the localized corrosion of the metal [255,317]. The galvanic sequence, which sorts common metals by their tendency to corrode, is listed in Fig. 17a. The standard electrode potential values of the elements relevant to metallic biomaterials at 298 K are listed in Table 4. The standard electrode potential is equivalent to the electromotive force of an element or, in other words, the tendency of its dissolution reaction to proceed [256,318]. When BMMCs doped or coated with GDs are immersed in aggressive aqueous solutions at near room temperature, water molecules preferentially accumulate at GD defect sites, forming interconnected percolation channels. Simultaneously, oxygen

molecules diffuse through intrinsic or processing-induced defects in the GD structure, ultimately reaching the GD/metal interface (Fig. 17b(i)). The exposed metallic regions at these defects, exhibiting lower electrochemical inertness compared to GDs, function as localized anodes that undergo oxidative dissolution ($M \rightarrow Mn^{+} + ne^{-}$). In contrast, the extensive GD surface serves as a collective cathode, facilitating oxygen reduction reactions ($O_2 + 2H_2O + 4e^{-} \rightarrow 4OH^{-}$), as depicted in Fig. 17b(ii). This micro-galvanic coupling creates substantial potential gradients, significantly accelerating corrosion kinetics through enhanced anodic current densities. As corrosion progresses (Fig. 17b(iii)), water infiltration at the GD/metal interface synergizes with cathodic delamination effects to progressively degrade coating adhesion strength. Concurrently, metallic corrosion products (*e.g.*, $Mg(OH)_2$ or Fe_3O_4) accumulate beneath the GD layer, generating compressive stresses that induce coating cracking and spallation (Fig. 17b(iv)). These mechanical failures expose fresh metal surfaces, creating autocatalytic corrosion hotspots (Fig. 17b(v)). The cyclic nature of this degradation mechanism ultimately leads to complete GDs' detachment. The actual role of Gr in influencing the biodegradation rates of BMMCs is, however, more complex and is not limited to simply enhancing the corrosion rates. Indeed, the role of Gr must be regarded as a synergistic effect coupling the CPA of galvanic corrosion and the protecting and supporting function of Gr. As shown in Fig. 17c, Shuai *et al.* [254] found an enhanced corrosion resistance effect in biodegradable AZ61-RGO/MgO MMCs when an optimized content of 3 wt % MgO modified RGO was added. For AZ61-RGO and AZ61-RGO/MgO MMCs, the corrosion mechanism was mainly galvanic corrosion between the intermetallic phase ($Mg_{17}Al_{12}$) and α-Mg matrix at the initial stage of *in vitro* immersion in the simulated body fluid (SBF). Then, the α-Mg grains were corroded quickly by the corrosive medium and the matrix was penetrated into (Fig. 17c (iii) and (v)), which led to the exposure of continuous RGO to the SBF solution. Subsequently, RGO encapsulated Mg grains to form a dense and stable honeycomb structure that acted as a protective shield, relying on the excellent anti-permeability of RGO. Additionally, the presence of MgO as an interfacial bridge helped prevent the detachment of RGO. This effectively slowed down the process of corrosion, thereby making the composites more corrosion resistant as compared to the AZ61 alloy (Fig. 17c(iv) and (vi)). Therefore, the effect of GDs doping on the degradation rate of BM materials is not merely based on the effect of accelerated galvanic corrosion, but may manifest as a synergistic effect interacting with some other relevant processes.

GDs, on the one hand, can play a microscale 'barrier effect' on the MMC matrix to improve the corrosion resistance by increasing the path of corroding agents to the metal interface and enhancing the barrier effect on the matrix to improve corrosion resistance [323,324]. Pourhashem *et al.* [320] have demonstrated that dispersed GO could reduce the penetration and access of H_2O and O_2 necessary for the corrosion of mild steel substrates and successfully alleviate the corrosion phenomena. Owing to their sheet-like shape, GO nanosheets have a considerable impact on the barrier characteristics of the matrix in this respect and make the diffusion pathway of corrosive species more difficult, as schematically illustrated in Fig. 17d. On the other hand, although GDs can be independently or concertedly applied as barriers against metal corrosion in the form of layered structures or composites at microscales, numerous attempts have been made to determine the corrosion protection mechanism of GDs between metals and corrosive environment at the nanoscale [325]. GDs, in principle, can be revolutionary anticorrosion materials due to their dense delocalized 2D electronic states and excellent 'impermeability effect' to atom or molecule under ambient conditions [326]. As shown in Fig. 17e (i), the CVD method is commonly used to produce nanoscale and graphene films. Such films can be directly used for the corrosion protection of metals [321]. Xu *et al.* [322] grew individual single-crystal Gr domains on Cu (111) (Fig. 17e (ii)) and Cu (100) (Fig. 17e (iii)), faceted Cu foils using the CVD method, and demonstrated that H_2O would not diffuse into the interface in commensurate Gr/Cu (111). Therefore, Gr clearly satisfied the anticorrosion requirement. In incommensurate Gr/Cu (100), however, H_2O could easily diffuse into the interface and accelerate corrosion. The as-grown graphene can protect Cu (111) surface from oxidation in humid air for a period of more than 2.5 years, which is in sharp contrast with the accelerated oxidation of graphene-coated Cu (100) surface. The atomically resolved structural characteristics, as shown in Fig. 17e (iv) and (v), together with first-principles calculations (the inset of Fig. 17e (iv) and (v)), further reveal that the facet-dependent anticorrosion behavior can be attributed to the difference of interfacial coupling between the commensurate and incommensurate Gr/Cu systems [327,328]. Gr films prepared by the CVD method have excellent corrosion protection for metals due to the 'impermeability effect' of Gr to reduce the transmission rate of moisture for corrosion to proceed [329].

4.2.2. The influence of GDs on the biodegradation of Mg-based BMMCs

To investigate the role of GDs in changing the corrosion behaviors of Mg-based BMMCs, Turan *et al.* [313] fabricated pure Mg composites with different Gr contents (0.1, 0.25 and 0.5 wt%) *via* a P/M method, and the curves obtained from electrochemical tests are illustrated in Fig. 18a. The fitted electrochemical results indicated that even a low concentration of Gr (0.1 wt%) increased the annual corrosion rate from 249.9 mm/y for pure Mg to 1048 mm/y, demonstrating that Gr acted as an effective cathode, accelerating corrosion through micro-galvanic reactions.

However, the *in vitro* degradation behavior of Mg-based GMMCs is often complex, as the introduction of GDs into Mg-based MMCs can sometimes improve corrosion resistance [254,228,230,253,333,334]. Therefore, beyond the micro-galvanic effect induced by GDs, which accelerates corrosion, other factors must be considered when evaluating the role of GDs in modulating the degradation behavior of Mg-based MMCs. Among these, grain refinement is often the primary factor to be assessed. GDs usually serve the function of grain refinement for Mg-based MMCs, as described in subsection 4.1.2, significantly decreasing the grain size and narrowing the grain size distribution to some extent. The literature consistently suggests that as grain size decreases, the corrosion resistance of Mg is improved in neutral and alkaline sodium chloride (NaCl) electrolytes with little dissent [335,336]. Aung *et al.* [330] evaluated the effect of grain size on the corrosion behavior of the AZ31B Mg alloy with different grain sizes by applying heat treatments that enabled grain growth (Fig. 18b). Potentiodynamic polarization tests (Fig. 18c) showed that E_{corr} shifted from − 1.48 V *vs.* Ag/AgCl to − 1.38 V *versus* Ag/AgCl when the average grain size decreased from 250 to 65 μm. Moreover, the hydrogen evolution volume (Fig. 18d) of the sample with an average grain size of 65 μm was the lowest (36.5 ml cm^{-2}) throughout the immersion tests of 10 h, suggesting that the corrosion rate significantly increased as the average grain size increased from 65 to 250 μm. For Mg-based GMMCs, finer grains result

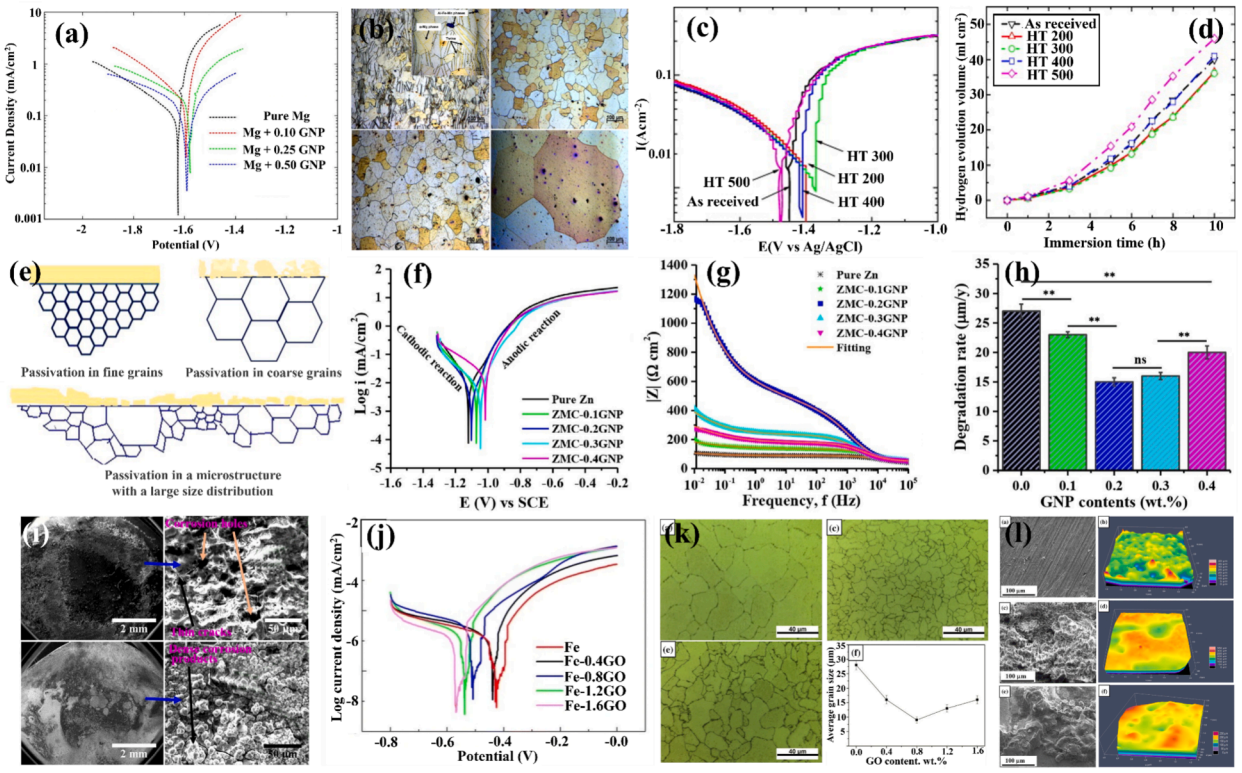

Fig. 18. (a) Current density *versus* polarization potential curves of pure Mg and Mg/GNP composites [313]. (b) Optical micrographs showing the microstructures of the AZ31B-H24 alloy at different heat-treated conditions of HT 200, HT 300, HT 400, and HT 500. (c) Potentiodynamic polarization curves of differently heat-treated samples in the 3.5 % NaCl solution. (d) Volume of hydrogen evolved from differently heat-treated samples during 10 h immersion in a 3.5 % NaCl solution [330]. (e) A schematic drawing of passive layer formation in fine- and coarse-grained microstructures [331]. The electrochemical corrosion properties of pure Zn, ZMC-0.1GNP, ZMC-0.2GNP, ZMC-0.3GNP, and ZMC-0.4GNP composites: (f) PDP curves; (g) Bode plots of impedance module |Z| *versus* frequency. (h) Degradation rates of pure Zn and GNP-reinforced ZMCs calculated by using the weight loss method after 30 d of immersion. (i) Surface morphologies of sintered pure Zn and ZMC-0.2GNP composites immersed in HBSS for 30 d [71]. (j) Polarization curves of SLMed pure-iron and SLMed Fe/GO composites. (k) Microstructures of the SLMed Fe-xGO composites: x = 0, 0.8, and 1.6 wt%, and average grain sizes. (l) Surface morphologies and corresponding topographic maps of the SLMed Fe, SLMed Fe-0.8 GO, and SLMed Fe-1.6 GO [332].

in more grain boundaries, which facilitate the accumulation of graphene at the interfaces. This increased graphene distribution forms more effective physical corrosion barriers, enhancing the material's resistance to corrosion compared to coarse-grained microstructures. Superior corrosion resistance of fine-grained Mg observed has been also attributed to an improved passive film. The notion of a more protective passive film is supported by the observation of reduced cathodic kinetics on grain-refined Mg in 0.1 M NaCl [337]. Gollapudi [331] provided a schematic illustration of passivation in nanocrystalline and coarse-grained materials (Fig. 18e). The nanocrystalline microstructure has a more uniform and compact passive layer, whereas the coarse-grained microstructure is shown to have a more open passive layer in a passivating environment [338]. A reduced grain size may contribute to an increase in the activity of electrons near grain boundaries, making the surface more reactive and prone to the formation of a stable passive film [336]. Furthermore, a high density of grain boundaries may also contribute to increased adherence of the passive film to the base metal possibly through the oxide pegging mechanism [339]. Based on the above discussion, the effect of GDs on the corrosion resistance of Mg-based MMCs is not solely accelerating or inhibiting corrosion. In practical applications, a comprehensive assessment of the influencing factors of GDs is necessary to achieve an optimal strategy for slowing down the degradation rate of Mg-based GBMMC bone implant materials [340].

4.2.3. The influence of GDs on the biodegradation of Zn-based BMMCs

The biodegradation rates of Zn-based BMMCs are moderate, being lower than those of Mg-based BMMCs, which implies a prolonged strength retention period *in vivo*. Kabir *et al.* [71] evaluated the biodegradable corrosion behavior of GNP/Zn matrix composites (ZMCs) by performing electrochemical tests, electrochemical impedance spectroscopy (EIS), and immersion tests in Hank's Balanced Salt Solution (HBSS). According to potentiodynamic polarization (PDP) curves shown in Fig. 18f, the i_{corr} values of all the ZMC-GNP composites were measured to be lower than that of pure Zn, indicating an enhanced corrosion resistance of the GNP-reinforced ZMCs. It was reported that GDs acted as an impermeable barrier that prevented the penetration of corrosive agents, leading to improved corrosion resistance in a corrosive environment as schematically illustrated in Fig. 17d. The Bode plot (Fig. 18g) also demonstrated

that the maximum impedance modulus |Z| of the composite with the optimum GNP content (0.2 wt%) at the low and intermediate frequency regions (0.1∼100 Hz) in the electrolyte (*i.e.*, Hanks' balanced salt solution) was about 4 to 6 times higher than that of the pure Zn specimens. Additionally, the surface film resistance (R_{sf}) values of all the ZMCs were measured to be higher than those of pure Zn, revealing that the surface film played an enhanced role in inhibiting corrosion due to the GNP addition. The intact corrosion surface morphology of the 0.2 wt% GNP-enhanced ZMCs further indicated the formation of dense corrosion product films with high corrosion resistance in HBSS, while pure zinc showed the most corroded surface, displaying the large pits formed (Fig. 18i). Due to the grain refinement and dense microstructure, the GNP-reinforcing phases imparted more nucleation sites and hindered grain growth, contributing to a more stable and uniform passivation layer on the sample surface. At the same time, the GNP-reinforcing phases filled up with defects such as cracks, gaps, crevices, and microscale pores, thereby alleviating stress concentration phenomena as well as preferential corrosion. Among all the specimens, the ZMC-0.2GNP composite exhibited the lowest degradation rate of 15 ± 0.7 μm/y calculated by using the weight loss method after 30 d of immersion (Fig. 18h). This might be attributed to the optimum content and homogenous dispersion of GNP in the ZMC-0.2GNP composite to maximize the 'barrier effect'. However, Yang *et al.* [59] reported a contrasting result: compared to pure Zn, the addition of 0.2 wt% RGO led to an increase in i_{corr} and a decrease in E_{corr}, indicating that RGO accelerated the electrochemical corrosion of the Zn matrix. This corrosion acceleration was attributed to two key factors: (i) the grain refinement induced by RGO, which increases the overall grain boundary area and enhances the corrosion tendency of Zn; and (ii) the formation of numerous micro-galvanic cells between RGO and the Zn matrix, which intensifies localized corrosion. Although the relationship between the grain size introduced by GDs doping and the degradation rate of Zn has not been confirmed, it is an indisputable fact that controlling the addition of GDs can effectively change the corrosion rate of Zn-based MMCs.

In addition, second-phase particles in Zn-based alloys often act as the initiation sites for localized micro-galvanic corrosion in Zn alloy-based BMMCs, causing pitting corrosion and promoting susceptibility to stress corrosion cracking [341]. Yang *et al.* [342] determined the biodegradation properties of Zn-Cu binary and Zn–Ca–Cu ternary alloys. The degradation behaviors of the Zn–Ca–Cu alloys were primarily influenced by micro-galvanic corrosion between the Zn–Cu matrix and $CaZn_{13}$ phase in these alloys, where 0.5 % and 1.0 % Ca were added to Zn, leading to increases in corrosion rate from 11.5 μm/y to19.8 μm/y and 29.6 μm/y during 4 weeks of immersion tests, respectively. Furthermore, the area fraction of $CaZn_{13}$ dendrites increased with Ca content, corresponding to an increased corrosion rate. Shi *et al.* [343] analyzed the features of 23 non-toxic alloying elements that form second phases in Zn-based alloys. An alloying element with standard electrode potential (E°) lower than that of Zn ($E^{\circ} = -0.76$ V) is likely to be preferentially corroded, which could lead to the formation of a protective passive film on the alloy's surface, resulting in an enhanced corrosion resistance. Li ($E^{\circ} = -3.04$ V), Mg ($E^{\circ} = -2.37$ V) and Mn ($E^{\circ} = -1.19$ V) have such an effect. Analogously, as the Ca ($E^{\circ} = -2.87$ V) content increases, Zn-(0.5–2 wt%) Ca alloys corrode more quickly due to increased volume fractions of coarse $CaZn_{13}$ dendrites. Overall, any second phase has a significant impact on enhancing the degradation rate of biodegradable zinc-based alloys and their composites. Zinc alloy-based BMMCs modified by GDs are expected to contain various carbides as second phases, and their quantity, distribution, and morphology will all affect the progress of galvanic corrosion, pitting corrosion, and subsequent destruction of passivation films.

4.2.4. The influence of GDs on the biodegradation of Fe-based BMMCs

In vivo experiments have shown that the degradation rates of Fe-based BMMC implants are extremely low [344], which will not only hinder the formation of new tissue but can also cause side effects similar to those of permanent implants [345]. Although biodegradable Fe stents demonstrated short-term (28-day) safety and efficacy in porcine coronary arteries [346], the studies on Fe stents implanted in the descending aorta of New Zealand white rabbits reported insufficient *in vivo* degradation rates, raising concerns about the feasibility of iron as a biodegradable implant material [347]. The Fe-Mn-5Si alloy implant tested in the mouse model exhibited a slow corrosion rate of 0.013–0.024 mm/year [348], which delayed bone remodeling and triggered mild inflammation due to prolonged iron ion release. Similarly, Kraus *et al.* investigated the *in vivo* degradation performance of three Fe-based alloy implants (*i.e.*, pure Fe, Fe–10Mn–1Pd, and Fe–21Mn–0.7C–1Pd) in a rat femur model over a 52-week period [349]. Their findings indicated that degradation occurred at slow rates, with no significant differences observed among the tested materials. Due to the relatively sluggish degradation of pure Fe and Fe-based alloys, their feasibility for bulk temporary implants, such as those used in osteosynthesis applications, remains questionable. Zhao *et al.* [215] incorporated GO into pure iron to increase its biodegradation rate. Fig. 18j presents the potentiodynamic polarization curves of the as-SLMed pure iron and Fe/GO composites, showing that the corrosion potential decreased while the corrosion current density increased after incorporating GO into pure iron. Fig. 18k shows the microstructures of the SLMed pure-iron and Fe/GO composites, consisting of irregular polygonal grains. The average grain sizes of the SLMed pure-iron and Fe/GO composites were in the range of 28 to 8 μm. Fig. 18l shows the surface morphologies and topographic maps of the SLMed pure-iron and Fe/GO composites after immersing in the SBF solution for 30 days. As compared to the SLMed pure-iron, the SLMed Fe/GO composites had much more corrosion attack with numerous tiny corrosion pits lying evenly on the surface [332]. Likewise, the corrosion depth of pits within the SLMed pure iron was shallow with the deepest corrosion pit measuring 20 μm. In contrast, the corrosion depths of the SLMed Fe/GO composites were much greater. Most of the surface area was corroded with pits whose depths reached 50 μm or more, and the deepest corrosion pits were 150 μm. The Fe/GO composites had higher biodegradation rates than pure iron, since the corrosion rates from the mass loss measurements were measured to be 0.41 mm/y for the SLMed Fe-0.8GO composite, 0.09 mm/year for the SLMed pure iron, and 0.008 mm/y for the as-cast pure iron [215].

In addition to the galvanic corrosion and grain-refining effect induced by GDs, a change in crystallographic texture can have implications for corrosion resistance. Factors such as crystallographic orientation and packing density have direct effects on the reactivity and passive film formation. It is widely accepted that if grains are oriented in the closely packed direction (*e.g.* {111} for BCC Fe), corrosion resistance would increase because the removal of surface atoms would be more difficult, relative to the grains oriented in

a more loosely packed direction [350]. Dong *et al.* [351] examined the corrosion rates of 316L stainless steel by examining hundreds of grains that featured diverse crystallographic orientations. Their results showed that the grain-specific corrosion rates decreased as the surface plane progressively deviated from the {111} direction. Particularly, the corrosion rates followed the order of {001} < {101} < {111}. Embedding GDs into an Fe-based alloy refines the grain structure, imparts stresses and strains, and modifies dislocation density, which will have varied impacts on corrosion. Wang *et al.* [352] found that the passive current density rose when the residual tensile stress was raised in Fe-based amorphous metallic coatings and its susceptibility to corrosion was enhanced by a higher tensile residual stress. The residual stress, initiated by GDs inducing grain refinement, accelerated the anodic dissolution by creating more initiation sites coupled with increased surface activity. GDs could effectively increase the biodegradation rate of pure iron and its alloys through the micro-galvanic corrosion effect and residual stress.

4.2.5. Critical analysis of GD-mediated degradation mechanisms in GBMMCs

Through systematic compilation of reported studies (summarized in Table 5), we demonstrate that GDs exert material-specific modulation on the degradation rates of Mg-, Zn-, and Fe-based BMMCs. Firstly, grain refinement induced by GDs has dual influences on the degradation behavior of BMMCs, as it can both accelerate and inhibit corrosion *via* two competing mechanisms. On the one hand, grain boundaries generally serve as high-energy regions that act as preferential initiation sites for corrosion, while elemental segregation at grain boundaries may induce local electrochemical potential differences, thereby promoting localized corrosion [353]. On the other hand, refined grains facilitate the formation of a more uniform passivation film, while also reducing dislocation accumulation and mitigating localized stress corrosion susceptibility, ultimately enhancing corrosion resistance [354]. The impact of grain refinement on degradation behavior varies significantly across different matrix materials. In Mg-based GMMCs, the effect of Gr on corrosion is not unidirectional but depends critically on its dispersion state, content, and interfacial chemistry. At low Gr content with uniform dispersion, corrosion resistance is enhanced through three possible mechanisms: (i) Gr accumulation at grain boundaries physically blocks Cl^- and H_2O penetration, reducing cathodic reaction kinetics (O_2 reduction rate decreases by ~ 60 % [113]); (ii) the formation of semi-coherent MgO nanoparticles (semi-coherent interfaces) at the Gr/Mg interface further mitigates micro-galvanic corrosion [254]; (iii) grain refinement promotes a dense Mg(OH) $_2$/MgO bilayer film, lowering passive current density by an order of magnitude [331,355]. However, when Gr content exceeds a threshold or dispersion quality deteriorates, corrosion acceleration dominates due to agglomeration-induced micro-galvanic cells, defective amorphous MgO interfaces prone to microcracking, and Gr-mediated precipitation of cathodic secondary phases like β-$Mg_{17}Al_{12}$ in Mg-Al alloys [249]. As revealed in Table 5, these competing effects lead to divergent outcomes even within the Mg alloy system, governed by alloy composition and GD's content and functionalization. For Zn-based GMMCs, the effect of grain refinement remains complex, exhibiting bidirectional regulation. On the one hand, grain refinement increases the grain boundary area, enhancing Zn's corrosion tendency and providing more sites for micro-galvanic corrosion reactions [59]. Additionally, surface defects (*e.g.*, edge sites and broken C–C bonds) and uneven distribution of GDs may accelerate local corrosion, promote ZnO dissolution, and reduce the effect of the ZnO protective layer [356]. On the other hand, high-quality Gr layers can form dense barriers that reduce the infiltration of corrosive agents (*e.g.*, Cl^- and H_2O), thereby preventing localized corrosion propagation. Furthermore, the introduction of an optimal weight or volume fraction of GDs and grain refinement can induce a dense microstructure, which enhances the ZnO protective layer's densification, improving corrosion resistance and extending the stability of the ZnO film [286]. This divergence highlights the delicate balance between Gr's barrier effects and its role in modifying Zn alloy microstructures. In contrast, Fe-based GMMCs generally experience accelerated degradation due to grain refinement. Finer grains in Fe-based MMCs introduce residual tensile stress, which promotes crack initiation and deteriorates the corrosion resistance [357]. Additionally, nano-grained Fe has a higher density of active sites, leading to a situation, where the passivation film's formation/repair rate is lower than its dissolution rate, thereby accelerating the corrosion process [353].

For GBMMCs, GDs' high conductivity and noble potential make them effective cathodes, promoting oxygen reduction ($O_2 + 2H_2O + 4e^- \rightarrow 4OH^-$) and accelerating metal dissolution. The severity of micro-galvanic corrosion depends on the potential difference between GDs and the BMs. Mg (−2.36 V) has the largest potential difference with Gr (~0.2 V), leading to severe micro-galvanic corrosion. Zn (−0.76 V) has a smaller difference than Mg, but Gr still induces micro-galvanic corrosion, especially if ZnO film stability is compromised. Fe (−0.44 V) has the smallest difference with Gr, resulting in weaker micro-galvanic effects compared to Mg and Zn, though localized corrosion can occur in Cl^- environments. The dispersion state of GDs significantly influences the extent of micro-galvanic corrosion. Uniformly dispersed Gr can form a protective layer over the metal matrix, acting as a corrosion barrier that mitigates micro-galvanic effects and reduces corrosion rates. In contrast, agglomerated Gr can create localized corrosion sites, leading to intensified localized dissolution or pitting corrosion [359]. Additionally, Gr can suppress micro-galvanic effects by isolating cathodic active sites and homogenizing electrochemical potential distribution. For example, the Gr coating layer reduces the exposure of impurities such as Cu to the corrosive medium, thereby lowering their cathodic activity and minimizing localized micro-galvanic cells [255]. Beyond its direct electrochemical influence, Gr can also affect micro-galvanic corrosion indirectly by altering the precipitation behavior of alloy phases. In Mg-based GMMCs, Gr may change the formation of secondary phases such as $MgZn_2$ [243] or β-$Mg_{17}Al_{12}$ [94], modifying corrosion behavior. Similarly, in Zn-based composites, secondary phases like $CuZn_5$ in 3 vol% CuO/Zn composites achieved by GO-assisted hetero-aggregation and SPS process [360] can serve as preferential corrosion sites. The presence of Gr may alter the precipitation dynamics of alloying elements, potentially influencing the corrosion rate and stability of the material.

Thus, the impact of GDs on micro-galvanic corrosion in different metal matrix composites varies, depending on potential difference, dispersion state, and interfacial bonding. By optimizing GDs' dispersion and implementing functionalization strategies, their effects on corrosion behavior can be fine-tuned, enabling precise control over the degradation rates of GBMMCs. Fig. 19 illustrates the comprehensive network of factors influencing Gr-mediated biodegradation in Mg-, Zn-, and Fe-based BMMCs. The diagram categorizes key factors into three levels: (i) material-intrinsic factors (*e.g.*, alloy composition and secondary phases), (ii) processing-dependent

Table 5
Summary of the *in vitro* corrosion rate of GD-Containing Mg-, Zn- and Fe- Based BMMCs.

Matrices metal	GD type	GD content	Static immersion test		Potentio dynamic test			Promotion (+)/Prohibition (−) ratio		Ref.
			Corrosion rate (mm/year)	Testing medium and immersion time	Corrosion rate (mm/year)	E_{corr}	I_{corr}	Static immersion	Potentio dynamic	
Pure Mg	Gr	0 wt%	—	—	249.9	–1.63 V	0.12 mA/cm^2	—	—	[313]
		0.1 wt%			1048	–1.59 V	0.51 mA/cm^2		+ 319 %	
		0.25 wt%			1813	–1.58 V	0.89 mA/cm^2		+ 625 %	
		0.5 wt%			2090	–1.59 V	1.02 mA/cm^2		+ 763 %	
Mg-0.5Zr	Gr	0 wt%	4.5	HBSS	19	–1602.4 mV	683.1 μA/cm^2	—	—	[228]
		0.5 wt%	3.0	24 h	11	–1595.9 mV	μA/cm^2	− 33 %	− 42 %	
Mg-0.5Zr	Gr	0.2 wt%	3.60	HBSS—	9.7	−1521.27 mV	0.43 mA/cm^2	—	—	[32]
		0.3 wt%	4.73		11.6	−1556.96 mV	0.51 mA/cm^2	+ 31 %	+ 20 %	
		0.4 wt%	6.78		13.0	−1562.44 mV	0.57 mA/cm^2	+ 88 %	+ 34 %	
		0.5 wt%	7.62		18.0	−1581.52 mV	0.79 mA/cm^2	+ 112 %	+ 86 %	
Mg-0.3Sr-0.3Ca	Gr	0 wt%	—	—	0.171	–1.878 mV	7.486 μA/cm^2	—	—	[230]
		0.2 wt%			0.153	–1.823 mV	6.730 μA/cm^2	—	− 11 %	
Mg3Al1Zn		0 wt%	—	—	—	−1.416 V	371.54 μA/cm^2	—	—	
		0.2 wt%				−1.456 V	992.08 μA/cm^2		~ +167 %	
	RGO	0.3 wt%				−1.464 V	207.25 μA/cm^2		~ − 44 %	[253]
		0.4 wt%				−1.328 V	61.21 μA/cm^2		~ − 84 %	
		0.5 wt%				−1.464 V	207.41 μA/cm^2		~ − 44 %	
Mg6Al1Zn	MgO modified	0 wt%	1.5	SBF	—	−1.50 ± 0.02 V	59 ± 3 μA/cm^2	—	—	
	RGO	1.0 wt%	~ 2.3	360 h		−1.47 ± 0.02 V	199 ± 12 μA/cm^2	+ 53 %		
		2.0 wt%	~ 2.0			−1.48 ± 0.03 V	132 ± 8 μA/cm^2	+ 33 %		[254]
		3.0 wt%	1.1			−1.48 ± 0.05 V	42 ± 2 μA/cm^2	− 27 %		
		4.0 wt%	~ 1.7			−1.48 ± 0.02 V	105 ± 4 μA/cm^2	+ 13 %		
Mg-8Li	Gr	0 wt%	—	—	2.741	−1630.2 mV	84.45 μA/cm^2	—	—	[333]
		0.2 wt%			1.605	−1636.02 mV	50.05 μA/cm^2		− 41 %	
		0.4 wt%			1.065	−1624.28 mV	32.95 μA/cm^2		− 61 %	
		0.6 wt%			1.588	−1641.21 mV	49.17 μA/cm^2		− 42 %	
Mg-3Zn		0 wt%	—	SBF—	2.92 ± 0.32	−1.41 ± 0.014 V	127.7 ± 11 μA/cm^2	—	—	[334]
	Gr	—			2.26 ± 0.26	−1.31 ± 0.021 V	99.1 ± 8 μA/cm^2		− 23 %	
	MgO modifiedGr	—			1.84 ± 0.29	−1.19 ± 0.018 V	80.4 ± 10 μA/cm^2		− 37 %	
Mg-1Ca	Gr		—	Hank's—	2.065	−1.427 V	90.4 μA/cm^2	—	—	[358]
					2.335	−1.414 V	102.2 μA/cm^2		+ 13 %	
					4.919	−1.446 V	215.3 μA/cm^2		+ 138 %	
Pure Zn	Gr	0 wt%	~ 7.5	SBF36 d	0.069	–1.097 V	277.6 μA/cm^2	—	—	[31]
		0.3 wt%	~ 14.4		0.213	–1.159 V	223.1 μA/cm^2	+ 92 %	+ 209 %	
		0.7 wt%	~ 26.5		0.301	–1.237 V	195.8 μA/cm^2	+ 253 %	+ 336 %	
Pure Zn	RGO	0 wt%	—	—	0.11 ± 0.02	–0.96 ± 0.06 V	7.48 ± 1.37 μA/cm^2	—	—	[59]
		0.2 wt%			0.27 ± 0.03	–1.03 ± 0.08 V	18.6 ± 2.32 μA/cm^2	—	+ 145 %	
Pure Zn	Gr	0 wt%	27 ± 1.2 μm/y	HBSS30 d	0.264 ± 0.033	−1.031 ± 0.008 V	± 3.257 μA/cm^2	—	—	[286]

(*continued on next page*)

Table 5 (*continued*)

Matrices metal	GD type	GD content	Static immersion test		Potentio dynamic test			Promotion (+)/Prohibition (−) ratio		Ref.
			Corrosion rate (mm/year)	Testing medium and immersion time	Corrosion rate (mm/year)	E_{corr}	I_{corr}	Static immersion	Potentio dynamic	
		0.1 wt%	23 ± 0.5 μm/y		0.224 ± 0.076	−1.084 ± 0.066 V	4.720 μA/cm^2	− 15 %	− 15 %	
		0.2 wt%	15 ± 0.7 μm/y		0.090 ± 0.006	−1.113 ± 0.011 V	5.456 ± 0.298 μA/cm^2	− 44 %	− 66 %	
		0.3 wt%	16 ± 0.6 μm/y		0.143 ± 0.031	−1.061 ± 0.019 V	8.286 ± 1.775 μA/cm^2	− 41 %	− 45 %	
		0.4 wt%	20 ± 1.1 μm/y		0.187 ± 0.043	−1.110 ± 0.020 V	10.555 ± 2.411 μA/cm^2	− 26 %	− 29 %	
Pure Fe	GO	0 wt%	—	—	0.09 ± 0.01	–0.43 V	14.5 μA/cm^2	—	—	[215]
		0.8 wt%			0.41 ± 0.01	–0.51 V	32.7 μA/cm^2		+ 356 %	

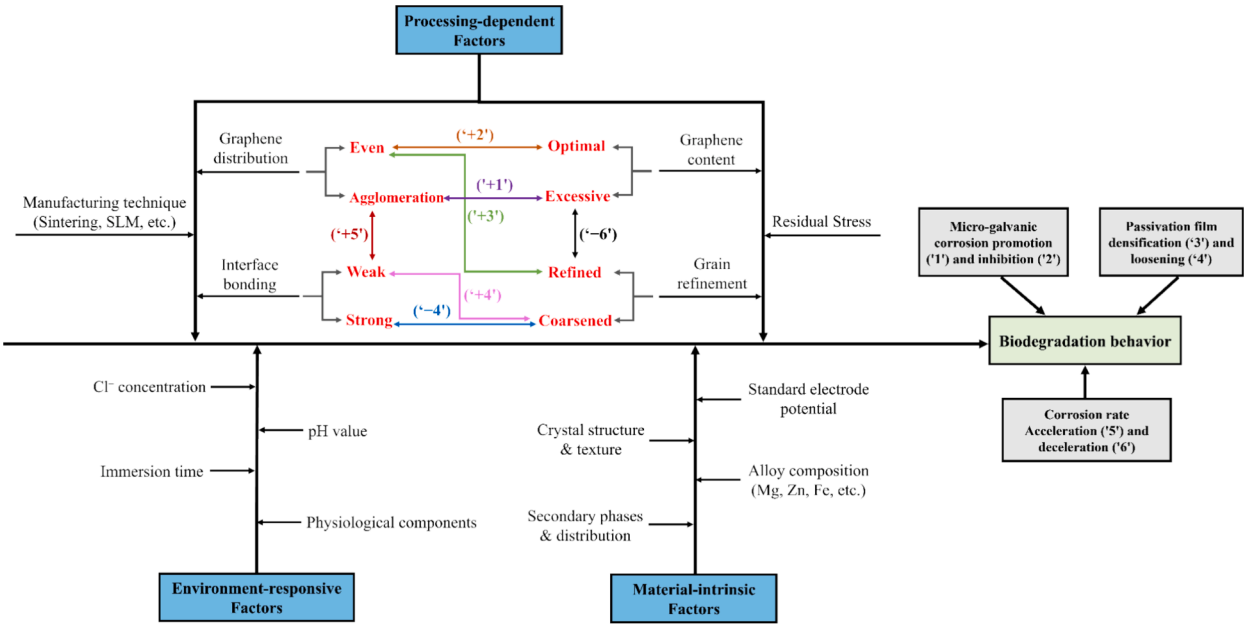

Fig. 19. Schematic overview of the hierarchical factors governing GD-mediated biodegradation in Mg-, Zn-, and Fe-based BMMCs.

factors (*e.g.*, Gr dispersion and grain refinement), and (iii) environment-responsive factors (*e.g.*, pH and Cl^- concentration). The bidirectional arrows depict interactions between these factors, highlighting their synergistic ('+') or antagonistic ('-') effects on biodegradation. The bidirectional arrows depict the interactions between these factors, highlighting their synergistic or antagonistic effects on biodegradation. This framework provides a roadmap for optimizing degradation profiles through material design and processing strategies.

In summary, the influence of GDs on the degradation behavior of Mg-, Zn-, and Fe-based BMMCs is highly complex, encompassing their effects on the microstructural characteristics of the metal matrix (grain size and second-phase distribution), micro-galvanic corrosion, and the regulation of corrosion products and protective films. Therefore, in practical applications, optimizing the addition of Gr and its interfacial bonding with the matrix requires careful consideration of the specific material system, Gr properties (type, dispersion, and functionalization), corrosion environment, and even processing conditions. By fine-tuning these parameters, the corrosion behavior of GBMMCs can be precisely controlled to achieve desired durability and performance.

4.2.6. Linking GD-mediated degradation mechanisms to implant applications

The corrosion-modulating effects of GDs in BMMCs offer significant potential for clinical applications. For instance, incorporating only 0.18 wt% Gr into an Mg–1Al–Cu matrix reduces the degradation rate of the Mg alloy by approximately fourfold [361]. Moreover, Mg-based nanocomposites containing 0.18 wt% Gr exhibit compressive properties comparable to native cancellous bone (with an elastic modulus value of about 6 GPa) and demonstrate excellent cytocompatibility and enhanced osteogenic capacity in human mesenchymal stromal cell (hMSCs) cultures, compared to non-Gr-modified Mg–1Al–Cu. These findings lay a solid foundation for developing mechanically compatible, fully resorbable Mg-based bone implants, and underscore GDs' future role in synchronizing implant degradation with tissue healing *in vivo*. In another study, Xia *et al.* [362] employed SLM to fabricate pure Zn porous scaffolds, which were implanted into a rabbit femoral critical-size defect model for 24 weeks. Their results revealed that these scaffolds possessed compressive strength and stiffness similar to cancellous bone and exhibited a suitable degradation rate to support bone regeneration; by week 24, newly formed bone was well-integrated with the Zn scaffolds. However, at week 4, a layer of fibrous tissue was observed between the scaffold and the host bone. This phenomenon was attributed to relatively high levels of Zn degradation products during the early post-implantation stage, exceeding the local tissue tolerance threshold. Incorporating functionalized Gr into future material designs could further enhance mechanical strength, aligning it with that of the cortical bone, while simultaneously slowing early-stage *in vivo* degradation to maintain a safer concentration of by-products and shorten the new bone growth cycle. Fe-based MMCs implants have also been widely investigated in animal models [346]. While the results from biocompatibility studies in rabbits appear promising, *in vivo* degradation rates of Fe implants have generally proven insufficient for the use of iron as a biodegradable material [347]. Nevertheless, Fe scaffolds modified with GO have exhibited accelerated degradation *in vitro* [215] and improved fatigue life in air [271]. Future endeavors should thus focus on optimizing the *in vivo* corrosion rate and fatigue strength of GD-enhanced Fe-based MMCs in physiological environments, potentially expanding their use as reliable bone implant materials. Persistent challenges include the need for long-term (over two years) degradation data in large animal models, as well as the development of standardized testing protocols that correlate *in vitro* corrosion with (pre-)clinical outcomes. By establishing robust methods for assessment and ensuring interdisciplinary collaboration, GBMMCs hold considerable promise for advancing the field of bone tissue engineering and beyond.

4.3. Biological performance of GBMMCs

4.3.1. Cytotoxicity

The host response triggered by GDs is an important aspect that must be considered for the biocompatibility of GBMMCs. The cytotoxicity of GBMMCs is a complex issue that may be affected by both the GDs themselves and the interaction between GDs and BMMCs [363]. At present, the understanding of the physicochemical properties of GBMMC scaffolds is still a subject of research and therefore, the information on both *in vitro* and *in vivo* toxicity is scarce. Hence, there is an immediate need to explore and establish the cytotoxicity of GBMMCs for optimized bone-specific applications. In this section, the overall cytotoxicity performance of GD-containing Mg-, Fe-, and Zn-based BMMCs and the effects of three independent characteristics of GDs, namely the GDs' type, their lateral size (*i.e.*, the size of the graphene sheets/particles typically measured along their largest dimension (length or width)) and their concentration, on cytotoxicity for relevant bone and progenitor cells will be discussed in detail.

4.3.1.1. The effect of GDs on GBMMCs' cytotoxicity. The current research on the biocompatibility of Gr-containing Mg-, Zn-, and Fe-based BMMCs is mainly focused on cytotoxicity (Table 6). Most of the studies were performed on Mg-based BMMCs [33,254,364–368] followed by Zn-based BMMCs [96,59,286,369]. Only one study reporting the cytotoxicity of Fe-based BMMCs [332] was found.

In terms of cell viability in contact with Mg-*x*GNP composites ($x = 0$, 0.5, 1.0 and 2.0 wt%), MG-63 cells cultured on the Mg-Zn-Ca alloy showed a lower viability than those cultured on Mg-Zn-Ca/GNP composites with lower GNP concentrations [364]. Cell viability and proliferation were observed to enhance in the presence of the Mg-GNP composites at the lower GNP concentrations (0.5–1.0 wt%), whereas the reverse effect was noted for the composite with the highest GNP concentration (2.0 wt%) owing to the excessive release of GNPs. Another study on Mg-Zn and Mg-Zn-GO composite scaffolds investigated the cytotoxicity after 1 and 3 days of culture of L-929 cells with the extracts of 10, 50, and 100 % concentrations [367]. Based on the results, the viability of the L-929 cells after 24 and 72 h of culture in the 10 % extracts was higher than in the extract concentrations of 50 % and 100 % in the Mg-6Zn, Mg-6Zn-1GO and Mg-6Zn-2GO groups. Interestingly, after 72 h, the cell viability in the Mg-6Zn extracts at concentrations of 10 % and 50 % was higher than that of the samples containing GO. According to the Inductively Coupled Plasma (ICP) results, the extracts from the samples with GO released higher amounts of magnesium and zinc ions compared to the Mg-6Zn samples, leading to increased cytotoxicity.

Yang *et al.* [96] *in situ* introduced RGO into laser AM Zn-based scaffolds and studied the viability and attachment of human umbilical cord stem cell cultured on Zn and Zn-RGO scaffolds. When compared to the Zn scaffolds, the cells on the Zn-RGO scaffolds displayed comparatively enhanced proliferation, according to the CCK-8 proliferation assay. At day 7, the cells in contact with the Zn-RGO group were clearly spread, and formed a large number of filopodia. According to earlier research, the biocompatibility of Zn scaffolds was closely related to their degradation rate [59]. In general, the addition of RGO is expected to slightly accelerate the degradation of Zn scaffolds, leading to the release of excessive Zn ions [370], that may have a negative impact on cell growth. Nevertheless, the incorporated RGO with high bioactivity may positively affect the cell behavior and overshadow the negative influence exerted by the slightly accelerated degradation of Zn scaffolds, as shown by Yang *et al.* [96]. In short, the RGO-Zn scaffolds could offer a favorable microenvironment for bone cell growth.

Cell viability of SaOS2 cells cultured for 3 days with sintered pure Zn and GNP (0.1–0.4 wt%)-reinforced Zn matrix composite extracts [286] increased as extract concentrations decreased. At a 75 % extract concentration, cell viability was below 40 %, indicating moderate to severe cytotoxicity (grade '3') [371]. When diluted to 12.5 %, cell viability significantly increased, exceeding 75 % of the control (grade '1'). Further dilution to 6.25 % resulted in cell viability over 90 %, indicating no cytotoxicity (grade '0'). Notably, the ZMC-0.4GNP extract at 6.25 % concentration achieved the highest cell viability, demonstrating excellent cytocompatibility. The lower cell viability at 75 % extract concentration was likely due to higher metal ion concentrations inhibiting cell growth, whereas the 6.25 % extract concentration promoted cell proliferation.

Reports regarding the cytotoxicity of GD-containing Fe-based BMMCs are scarce. Zhao *et al.* [332] attempted to prepare Fe-*x*GO composites ($x = 0.4$, 0.8, 1.2, and 1.6 wt%) from pure Fe and GO powders *via* SLM and explored the associated viability of MG63 cells. For the Fe-*x*GO composites in that work, the Fe^{2+}, Fe^{3+}, and $Fe(OH)_3$ ions were collected during degradation in the SBF. The mean concentration of Fe^{3+} released daily from the Fe-0.8GO composites in the SBF reached a maximum (*i.e.*, 6.33 μg/(ml day)), which is much lower than the half-maximal inhibitory concentration (IC_{50}) of Fe (30–70 μM) [372]. CCK-8 assay was used to examine the proliferation of MG63 cells cultured on the Fe-*x*GO composites. The CCK-8 assay results of MG63 cells cultured on the specimens for 1, 4, and 7 days showed that the number of cells present on the Fe and Fe-*x*GO specimens gradually increased with culture time, and there were no significant differences between the cell proliferation rates on the Fe-*x*GO composites at different time points. In addition, the cells cultured on Fe, Fe-0.8GO, and Fe-1.6GO samples for 1 and 3 days exhibited well-spread morphologies with no notable differences between the groups of the Fe and Fe-*x*GO composites, while the MG63 cells cultured with the Fe-*x*GO extracts exhibited a morphology with spindle shapes, which is the normal morphology of these cells. Therefore, the findings suggest that the studied Fe-*x*GO composites are not cytotoxic for the MG63 cells.

AM techniques, particularly laser-based methods like SLM, fundamentally alter the microstructural characteristics of GBMMCs through rapid melting/solidification cycles, which profoundly influence Gr distribution, interfacial bonding, and degradation behavior, and even affect cytotoxicity. Compared to conventional manufacturing methods, AM possesses unique advantages such as tailored porous architectures (enhancing nutrient transport for bone regeneration), graded Gr dispersion (mitigating agglomeration-related toxicity), and refined grain structures (improving mechanical stability during biodegradation). However, the extreme thermal gradients in laser-based AM may induce Gr structural defects (*e.g.*, edge oxidation and sheet fragmentation) that enhance ROS generation. Mandal *et al.* [373] illustrated this effect in their study on SLM-processed Gr/SS 316L composites, where laser melting led to an

Table 6
The cytotoxicity of GBMMCs in relation to the GD type, concentration, composite powder preparation process, and MMC fabrication process.

Metallic matrix	GD type and concentration	Powder preparation	Sample fabrication	Cytotoxicity performance	Ref.
Pure Mg	GNP, 0, 0.1, 0.2, 0.3 wt%, 15 μm and 5 μm	High energy ball milling	Compacting and sintering	An increase of 12 % in Saos-2 cell viability by an addition of 0.1 wt% GNPs to the Mg matrix. The Mg–0.1 wt% GNP composite exhibited higher cell viability than the Mg–GNP composites containing higher GNP contents (0.2–0.3 wt%)	[33]
Mg-3Zn-1Ca	GNP, 0, 0.5, 1, 2 wt%	Ball milling	P/M	MG-63 cell viability and proliferation were enhanced for the composites at the lowest GNP concentration (0.5–1 wt%), whereas the reverse effect was noted for the composite with the highest GNP concentration of 2 wt%.	[364]
Mg-3Zn-1Mn (MZM)	GO, 0, 0.5, 1, 1.5 wt%	Wetting ball milling	P/M	The increase in culture time slowly increased the numbers of MG63 live cells on the MZM/GO nanocomposites containing 0.5 wt% and 1 wt% GO after 3 and 7 d of culture.	[365]
Mg-6Zn	GO, 0, 0.2, 0.4 wt%	Wet ball milling	P/M	According to the MTT assay and ALP expression, GO nanosheets in the Mg-GO composite promoted cell viability and osteoblastic cell differentiation. Incorporating GO nanosheets could effectively improve the biocompatibility of Mg-6Zn-based composites.	[366]
Mg-6Zn	GO 0, 0.1, 0.2 wt%	Milling	Pressing and sintering	The MTT assay proved that the extract of Mg-6Zn-2GO scaffolds was not cytotoxic in contact with L-929 cells which validated the studied scaffolds for bone tissue applications.	[367]
Mg-6Al-1ZnAZ61	RGO, 0, 1, 2, 3, 4 wt%	Wet stirring	SLM	More MG-63 cells were observed in the extracts of AZ61-3.0RGO/MgO composites than in AZ61 extracts. Cells cultured on AZ61-3.0RGO/MgO composites showed highly dense ALP staining compared to AZ61 alloy, but AZ61-1.0RGO/MgO, AZ61-2.0RGO/MgO and AZ61-4.0RGO/MgO composites showed lower densities than AZ61 alloy.	[254]
Mg-3Zn-0.5Zr, ZK30	GO, 0, 0.3, 0.6, 0.9 wt%	Wet stirring	SLM	MG-63 cells on all the samples exhibited a well-spread morphology and an increased number after being cultured for 3 days, indicating a good cytocompatibility of SLMed ZK30-*x*GO.	[368]
Pure Zn	GNS, 0, 0.3, 0.7 wt%	Wet ball milling	SPS	Relative activity of cells in 5 % and 10 % concentration of Zn-GNS composites extract was greater than 90 %. MG-63 cells could grow on the surface of Zn-GNS composites. Zn-GNS composites had excellent cytocompatibility.	[369]
Pure Zn	RGO, 0, 0.1, 0.2, 0.3 wt%, 0.3 to 2 μm	——	SLM	Optical density of cells on the Zn-0.2RGO scaffold group was considerably higher than that on the Zn scaffold group at day 7 ($^{*}p < 0.05$) by CCK-8 assay. The cells cultured on the Zn-RGO scaffold exhibited a significantly improved ALP activity than those on the Zn scaffold at day 7 and day 14, which revealed that the Zn-RGO scaffold promoted cell growth and differentiation.	[59]
Pure Zn	RGO, 1–3 μm	CVD	SLM	The CCK-8 assay, fluorescence staining together with ALP analysis revealed that Zn/RGO scaffolds promoted cell proliferation, adhesion, and differentiation. Zn/RGO scaffolds showed relatively high cell viability and favorable cell adhesion behavior compared with Zn scaffolds.	[96]
Pure Zn	GNP, 0, 0.1, 0.2, 0.3, 0.4 wt%, 15 μm	Ball milling	Hydraulic pressing	Among all the GNP-reinforced Zn matrix composites, the cell viability of the ZMC-0.4GNP reached 124.3 ± 3.7 %, displaying the best cytocompatibility with superior cell proliferation function.	[71]
Pure Fe	GO, 0, 0.4, 0.8, 1.6 wt%	Ball milling	SLM	The CCK-8 assay results of MG63 cells and fluorescence staining of the MG63 cells results suggested that the Fe-*x*GO composites had good cytocompatibility.	[332]

increased I_D/I_G ratio, indicative of elevated defect density within the Gr structure. Conversely, conventional powder metallurgy typically preserves Gr's structural integrity but struggles with inhomogeneous dispersion, leading to localized cytotoxicity hotspots at agglomerated regions. On the other hand, AM-processed Fe/GO composites exhibited about 5 × higher degradation rates than cast pure iron due to GO-induced micro-galvanic corrosion intensified by AM's refined microstructure [332], while their cytotoxicity remained comparable to conventional counterparts owing to controlled ion release kinetics. AM introduces both opportunities and challenges that require process-specific cytotoxicity evaluation frameworks, particularly critical for bone implants, where a balance between porous architecture, degradation and cell viability must be synergistically optimized.

4.3.1.2. The effect of lateral size of GDs. Numerous studies have confirmed that the possible cytotoxic and inflammatory effects of all types of GDs depend strongly on their lateral sizes when released from GBMMCs. Graphene sheets can vary significantly in lateral size, from a few nanometers (nm) to several centimeters (cm) or more, depending on the production method and intended application. Table 7 lists the typical morphologies of GDs, their corresponding morphological features, size ranges and preparation methods. When producing GBMMC samples, powder mixing processes (such as P/M) and scaffold preparation processes (such as SLM) can also drastically change the initial morphological features and lateral sizes of GDs [374]. Hence, the independent effect of actual lateral size of GDs on cells should be taken into consideration in evaluating the impact of GDs on GBMMC biocompatibility. It has been reported that RGO nanoparticles with a diameter of 11 ± 4 nm could enter the nucleus of hMSCs and cause chromosomal aberrations and DNA fragmentation after 1 h, even at very low concentrations of 0.1 and 1.0 mg/mL. However, RGO with an average lateral dimension (ALD) of 3.8 ± 0.4 μm exhibited no notable genotoxicity in hMSCs until a high dose of 100 mg/mL after 24 h [375]. Mendes *et al.* [376] investigated the effect of the lateral size of GOs (*i.e.,* 89 and 277 nm) on the viability of macrophage (J7742) and HeLa (Kyoto) cells. Their results showed that large GO flakes induced higher levels of toxicity than small flakes, especially at a longer incubation time of 48 h. Similarly, Ma *et al.* [377] demonstrated that small GOs with lateral sizes of 50 ~ 350 nm were easily internalized by murine J774A.1 macrophages, while large GOs (750 ~ 1300 nm) were preferentially adsorbed on their plasma membranes, thereby activating toll-like receptors (TLR) and nuclear factor kappa-B (NF-κB) pathways to promote pro-inflammatory response. In general, nanoparticles (*i.e.*, sizes < 100 nm) can enter the cell, those smaller than 40 nm can enter nucleus, and those smaller than 35 nm can cross the blood brain barrier [378].

4.3.1.3. The concentration of GDs. GDs were first demonstrated to have size- and concentration-dependent cytotoxic and genotoxic effects on hMSCs about a decade ago. Akhavan *et al.* [375] found that 1.0 g/mL RGO with an average lateral size of 11 ± 4 nm significantly damaged cells, whereas RGO with an ALD of 3.8 ± 0.4 μm significantly harmed cells only at a high dose of 100 g/mL with a one-hour exposure time. Besides hMSCs, the concentration-dependent nanotoxicity of Gr, RGO, and GO was also evident in their interactions with numerous other cells, such as human erythrocytes, U87, U118 glioblastoma cells and human umbilical vein endothelial cells (HUVECs) [380]. For instance, Liao *et al.* [381] proved that both GO and RGO exhibited toxicity on red blood cells (RBCs) in a dose-dependent manner (dose > 60 μg/mL), thus decreasing the cell viability, increasing the generation of ROS, and releasing lactate dehydrogenase. In another study, Ruiz et al [382] observed that GO films at a concentration of 20 μg/mL in the culture media decreased cell viability of mammalian colorectal adenocarcinoma cells (HT-29 cells) by 20 %, while at a concentration of 50 μg/mL, cell viability decreased to 50 %.

Considering the observation that GDs essentially does not decompose or biodegrade in the body fluid environment but enters the body with the degradation of the metallic matrix of BMMCs and participates in various metabolisms, the concentration of GDs, in other words, the amount of GDs added to BMMCs, has a critical impact on the *in vivo* cellular biocompatibility, *e.g.*, with osteocytes and osteoblasts. In addition, the subsequent metabolic processes, such as internalization and excretion of excess GDs from the human body, need to be considered.

4.3.1.4. The effect of the type of GDs. In addition to the lateral size and concentration, the intrinsic properties of GDs, such as the oxidation state and reactive functional groups, play a significant role in determining their cytotoxicity, because cell viability is affected by physical damages and/or chemical effects [383]. Many researchers have proposed that oxidative stress is one of the mechanisms involved in the toxic effects of GDs [384]. The oxidative stress in target cells is caused by the generation of ROS that can damage the cellular membrane, DNA, and proteins [385]. Furthermore, the surface oxidation state and carbon radical content play major roles in the induction of toxicity to cells [386]. Liao *et al.* [381] found that the disruption of the RBC membrane was likely attributed to the

Table 7
The different GD's morphologies and their corresponding morphological features, dimension ranges, and preparation methods[379].

Type	Morphology feature	Dimension range	Preparation method
Two-dimensional flake/sheet graphene	Folds, in-plane overlap	More than 1000 nm, even to the centimeter scale in both directions	Mechanical stripping, epitaxial growth, redox method and chemical vapor deposition
Graphene nanoribbon	Strips with a certain width, with the edge carbon atoms showing both 'Zigzag' (ZGNRs) and 'Armchair' types (AGNRs).	100 nm to several hundred nanometers	Plasma etching, oxidation cutting carbon nanotube and plasma etching carbon nanotube method
Graphene quantum dot	Zero-dimensional carbon-based nanomaterials	Less than 100 nm in both directions	Solvent heat, chemical stripping, electrochemicaland electron beam etching method

Table 8
In vitro and *in vivo* osteogenic performances and corresponding osteogenic mechanisms of GBMMCs.

Metallic matrix	GD type	*In vitro* and *in vivo* osteogenic properties	Osteogenic mechanism	Ref
Mg	GO	Improved expressions of ALP in MC3T3-E1 cells. Promoted expression of (p)Smad 2/3 and Runx2, OCN and vascularized bone regeneration.	Activated the TGF-β and BMP signaling pathways. Conditioned macrophage culture medium treated with GO and Mg^{2+} promoted the osteogenic differentiation.	[403]
Mg-Zn-Mn	GO	Mg-Zn-Mn/1 wt% GO nanocomposite increased the MG63 cell viability and ALP activity, indicating the increasing level of osteogenesis.	——	[365]
Mg-3Zn-1Ca	GNP	The expression of ALP indicated that the Mg-GNP composites containing lower concentrations of GNPs favored the attachment, proliferation and differentiation of osteoblasts.	——	[364]
Mg-6Zn	GO	The ALP expression of Mg-6Zn extract and especially Mg-6Zn/ GO extract was strongly enhanced, compared to that of pure Mg extract. The Mg-GO composite comprising GO nano-sheets profited osteogenic cell differentiation.	——	[366]
Mg-6Al-1ZnAZ61	RGO	The cells cultured on the AZ61–3.0RGO/MgO composite presented highly intensive ALP staining, as compared with the AZ61 alloy. The cells cultured on the AZ61–3.0RGO/MgO composite showed numerous and well-developed pseudopods that extended to the neighboring cells.	——	[254]
Mg–1Al–Cu	Gr	The ALP activity of cells on Mg–1Al–Cu/0.18Gr implants was enhanced by approximately 3.4-fold in the basal medium and 1.8-fold in the osteogenic medium, when compared to the cells on on-Gr-modified Mg–1Al–Cu samples.	Contact of metallic ions and Gr nanoparticles with hMSCs could support osteogenic differentiation of hMSCs, which promoted the expression of *RUNX2*, *COL1A1*, and *SPP1*.	[361]
Zn	GO-COOH	ALP expression, OCN and Runx2 production were enhanced in the Zn/GO-COOH nanocomposites group.	This effect was related to the mitogen-activated protein kinase (MAPK) pathway. Zinc ions and GO-COOH increased osteoblastic collagen matrix production and thus increased the binding of osteoblasts to the matrix activating the MAPK pathway.	[404]
Zn	β-TCP/ GO	Improved expressions of ALP in MC3T3-E1 cells.	——	[405]
Zn	RGO	Promoted expression of ALP.	——	[59]

strong electrostatic interactions between negatively charged oxygen groups on the GO surface and positively charged phosphatidylcholine lipids that were present on the RBC outer membrane.

In summary, the toxicity mechanism of GBMMC scaffolds on cells is strongly dependent on the surface of GDs. Cytotoxicity depends on the physicochemical properties of Gr-based materials, such as the density of the functional groups, size, conductivity, and chemical nature of the reducing agent used for the deoxygenation of GO, as well as on the cell types exposed to these materials.

4.3.2. Osteogenic properties

Since the advent of Gr [387], researchers have been trying to introduce GDs to improve the osteogenic properties of bone implants [388–390]. Numerous studies have indeed shown that GDs can independently and significantly enhance the osteogenic differentiation of hMSCs [388,391–394]. However, there has not been a systematic and comprehensive understanding of the underlying mechanisms, and the observations of the osteogenic properties improved by GDs are sometimes inconsistent and fragmented [395–398]. Herein, we attempt to systematically summarize the osteogenic properties of GBMMCs and elucidate the role of GDs in inducing osteogenic differentiation and new bone growth from three aspects: GDs' physical cues, GDs' structure and chemistry, and GDs' exogenous conduction channels/signaling pathways.

4.3.2.1. The effect of GDs on GBMMCs' osteogenic properties. The *in vitro* and *in vivo* osteogenic properties and the corresponding mechanisms of GBMMCs, including Mg- and Zn-based BMMCs have been extensively studied (Table 8). For Mg-based MMCs, the role of GDs in promoting osteogenesis is diverse. Firstly, GDs can be used as a bioactive component to improve the osteogenic properties of bone substitutes [399]. Safari *et al.* [361] found that the addition of Gr to Mg-1Al-Cu samples could improve their osteogenic potential. After 7 and 14 days of *in vitro* culture of hMSCs, the alkaline phosphatase (ALP) activity for the Mg-1Al-Cu/0.18Gr composite enhanced approximately 3.4-fold in the basal medium and 1.8-fold in the osteogenic medium when compared to the non-Gr-modified Mg-1Al-Cu samples, which was attributed to the noncovalent binding of proteins and osteogenic inducers by the Gr nanoparticles [400]. Secondly, GDs with open structures at both ends could have a space-confining effect [401] to ensure sustained release of Mg^{2+} ions in the long term and could be utilized as an attractive drug delivery platform for vascularized bone regeneration. Thirdly, GDs have been reported to have immunomodulatory effects to drive the tissue regeneration and related osteogenic gene expression, which has emerged as a potential solution to repairing bone defects [402]. To figure out the capability of Mg/GDs composite materials in repairing bone defects as immunomodulatory agents, Zheng *et al.* [403] integrated Mg nanoparticles into GO *via* an electrostatic interaction method to form a self-assembled Mg/GO composite, thereby forming a delivery platform capable of sustained release of Mg^{2+}. Immunomodulatory behavior tests revealed that: the Raw 264.7 macrophages incubated with GO (20 μg mL^{-1}) demonstrated a significant change in morphology (Fig. 20a); the M1/M2 polarization of macrophages monitored by the qRT-PCR (real-time, reverse transcription polymerase chain reaction) test demonstrated that M1-relevant *IL1B* expression levels were increased by GO and decreased in the magnesium-enriched microenvironment, whereas M2-relevant *RETNLA* gene expression levels were increased in cells treated with Mg^{2+} (Fig. 20b). The results of Fluorescence-Activated Cell Sorting (FACS) analysis revealed an increase in the density of iNOS cells (representative of M1 macrophages) in the GO-treated group, and acceleration in the induction of CD206 cells (representative of M2 macrophages). Therefore, GO has been proven to activate inflammatory M1 macrophages and Mg^{2+} facilitated polarization of M1 macrophages to the pro-healing M2 phenotype. The inflammatory response induced by Mg/GO has been proven to successfully stimulate *in vitro* osteogenic differentiation and *in vivo* osteogenesis (Fig. 20c). The ALP, von Kossa, and Alizarin Red staining results demonstrated that the induced osteogenic differentiation of bone marrow-derived mesenchymal stem cells (BMSCs) was promoted by conditioned macrophage culture medium (CM) treated with GO and Mg^{2+} (Fig. 20d). Obvious vascularized bone regeneration was also achieved in a rat cranial bone defect model (Fig. 20e).

As for zinc-based MMCs, the osteogenic effect of GDs is mainly reflected in enhancing the osteogenic differentiation of stem cells. Yang *et al.* [59] fabricated the RGO-reinforced pure zinc scaffolds by LPBF, and achieved a coherent interface between RGO and the zinc matrix by oxygen-mediated bonding. *In vitro* ALP activity assay of umbilical cord mesenchymal stem cells (UCMSCs) demonstrated an osteogenic differentiation behavior engaged by RGO. The UCMSCs cultured on the Zn-RGO scaffold exhibited a more significantly improved ALP activity than that on the Zn scaffolds at day 7 and day 14. Similarly, it has been proven that the addition of GO to the Zn matrix could also promote the ALP activity and facilitate the osteogenic differentiation [405]. In general, the findings suggest that the combined effects of active ions, such as Mg and Zn ions, and GDs upregulate the expression of osteogenic markers *in vitro* and enhance the ability to repair bone damage *in vivo*. No studies focusing on the osteogenesis-promoting effects of GDs in Fe-based BMMCs are yet available in the literature. The increased potential for osteogenic differentiation is closely related to the various osteogenic differentiation-promoting factors of GDs.

Table 9
Reactive functional groups and oxidation state of GDs, '—' stands for none, '*' stands for a low level, and '**' stands for a high level[406].

Reactive functional group	Gr	GO	RGO
Epoxy (C-O-C)	—	**	*
Carboxylic acid (C-O)	—	**	*
Hydroxyl (C-OH)	—	**	*
π–π stacking	**	**	**
Oxidation state	—	**	*

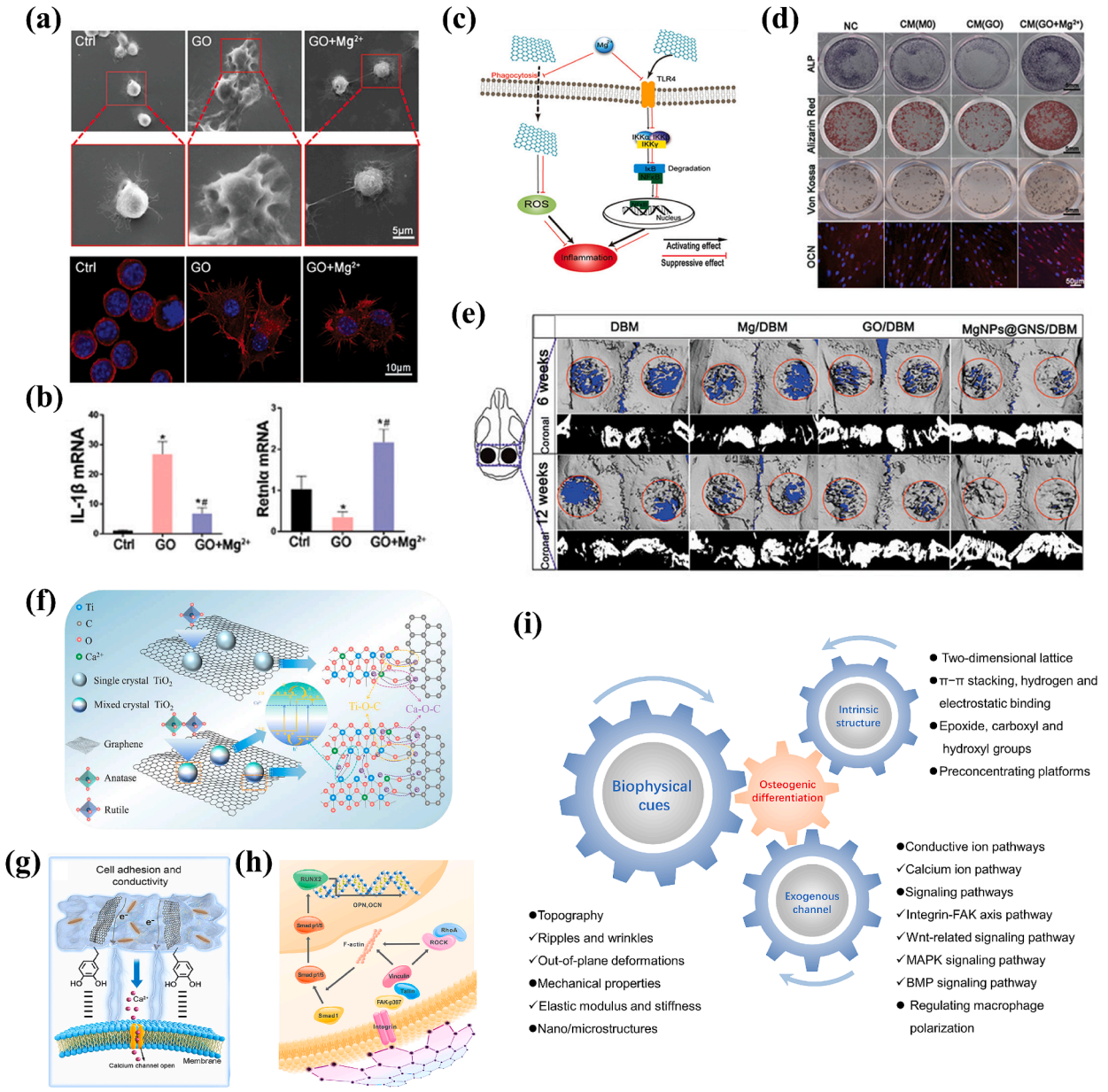

Fig. 20. (a-g) The immunomodulatory and osteogenic performance of Mg-based MMCs. (a) SEM images and confocal images showing the cellular and membrane morphological alterations of RAW264.7 macrophages after 24 h of treatment with GO and GO + Mg^{2+}; (b) real-time quantitative PCR for the M1 (IL1b) and M2 (Retnla) genes after 24 h of treatment; (c) schematics elucidating the mechanisms responsible for magnesium-induced anti-inflammatory properties; (d) images of ALP staining for 7 days, and Alizarin Red and von Kossa staining for 14 days of BMSCs after cultured in various macrophage CMs supplemented with osteogenic supplements; (e) Radiological analysis of the calvarial bone defects (red circles) repaired by DBM, Mg/DBM, GO/DBM and MgNPs@GNS-coated DBM scaffolds for 6 and 12 weeks post-implantation [403] (DBM = Decellularized bone matrix; GNS = Graphene oxide nanoscrolls). (f-h)The functions of GDs in serving as exogenous conduction channels: (f) a schematic drawing illustrating the mechanism of enhanced conductivity of Ca^{2+}-doped mixed-phase TiO_2/GO composites [407]; (g) the scaffold promoted cell adhesion and transferred the endogenous electrical signals to cells, activating Ca^{2+} channels [60]. (h) Mono-atomic graphene film promoted osteogenic differentiation of hMSCs via the activation of the integrin-FAK axis [408]. (i) An overview of the cues involved in the osteogenic differentiation of stem cells induced by GDs. (For interpretation of the references to colour in this figure legend, the reader is referred to the web version of this article.)

It is well established that vascularized bone regeneration is critical for implant integration, as nascent blood vessels not only supply oxygen and nutrients but also secrete paracrine factors (*e.g.*, vascular endothelial growth factor (VEGF) and bone morphogenetic protein (BMP)-2)) to orchestrate osteogenesis [409]. GDs, particularly GO and RGO, enhance angiogenesis through multiple mechanisms. Their high surface area and functional groups enable adsorption and sustained release of pro-angiogenic growth factors (*e.g.*,

VEGF, *etc.*) *via* π-π stacking and electrostatic interactions, as demonstrated by Pan *et al.* [330], where chitosan functionalized GO up-regulated the expression of VEGF and promoted the endothelial cell adhesion and proliferation [410]. Furthermore, GDs' conductive properties facilitate endogenous electrical signal transduction, activating $Ca2^{+}$ channels and endothelial nitric oxide (NO) synthase to promote vascular network formation, as observed in polydopamine-mediated GO scaffolds that simultaneously induce the osteogenic differentiation of BMSCs and upregulated ALP activity [60]. Surface topography (*e.g.*, nanoripples and wrinkles) mimics extracellular matrix cues, promoting endothelial cell adhesion and lumen formation while synergistically enhancing osteoblast differentiation. GDs' immunomodulatory effects, such as polarizing macrophages toward the pro-healing M2 phenotype, further enhance angiogenesis-osteogenesis coupling by secreting TGF-β and VEGF, as shown in Mg-GO composites [403]. Supporting this synergy, Xue *et al.* [411] demonstrated that GO not only enhanced the osteogenic differentiation of BMSCs, evidenced by an approximately 3-fold increase in ALP expression, but also upregulated vascular-related receptor expression in HUVECs, leading to over a 6-fold increase in VEGF secretion compared to controls, highlighting GDs' multifunctional role in vascularized bone regeneration. In summary, GD concurrently promotes osteogenesis and angiogenesis – the two interdependent processes critical for successful bone repair, thereby bridging a key gap in implant design for complex defects.

4.3.2.2. The influence of GDs' physical cues. Biomaterials physical cues, which encompass morphological and mechanical properties, act through cell-substrate interactions to alter cytoskeletal dynamics and gene expression, which can ultimately modulate cellular functions, such as differentiation [412–414]. The ultimate morphology of GDs in the composites and the remarkable stiffness of GDs are their most important features that may function as physical cues. Nayak *et al.* [388] demonstrated the controllable increase in the osteogenic differentiation of hMSCs by Gr. The Si/SiO_2 substrates exhibited significant osteogenesis-induced calcium deposition only under the action of the Gr with nanoripples, and the differentiation rate promoted by Gr was comparable to that in the presence of the typical growth factor BMP-2 alone. The ability of Gr to independently regulate the osteogenic differentiation of hMSCs was found to stem from the fact that the ripples and wrinkles of Gr sheet, mimicking the disordered nano-pit array, could effectively adsorb proteins, facilitate cell adhesion, and promote cell proliferation and differentiation [415]. Akhavan *et al.* [391] achieved rapid osteogenic differentiation of hMSCs, stimulated by Gr nano-grids, which was attributed to the presence of edge defects of Gr nano-ribbons, providing suitable out-of-plane deformations (irregular protrusions, on a 100 nm scale) for the topographical induction of osteogenic differentiation. Gr's extremely high Young's modulus can withstand lateral strain and provide moderate local cytoskeletal tension, allowing mechanosensitive proteins of interest to unfold and change conformation [416]. Material stiffness is known for altering the adhesion state of stem cells and other cell types [417–419]. Gr itself induces changes in the morphology of cell during adhesion, leading to changes in cytoskeletal tension [420]. This effect can cause the activation of mechanotransduction pathways, thereby directly influencing the cellular gene expression profile [421].

4.3.2.3. The influences of GDs' structure and chemistry. The two-dimensional honeycomb lattice structure and the functional groups present in the GDs (Table 7 and Table 9) have the potential to mediate stem cell lineage specific differentiation for tissue regeneration [422,423]. Lee *et al.* [393] explored the extent of mineralization by hMSCs after osteogenic induction and the drug loading capacities of Gr, GO, and polydimethylsiloxane (PDMS) surfaces. As confirmed by spectrophotometric quantification, under identical culture conditions, the mineralization associated with the hMSCs cultured on Gr was 7 times higher than that of the cells cultured on the PDMS specimens. Ultraviolet spectrophotometry revealed that Gr adsorbed the largest amounts of dexamethasone (400 mg) and β-glycerophosphate (8 g) per gram of Gr after 1 day of incubation. The large amount of $\pi - \pi$ stacking, hydrogen bonding, and electrostatic binding of Gr and GO not only promoted the adsorption of fibronectin to directly mediate cell adhesion [424] but also enriched growth factors and hormones, thereby improving a series of biological events including the initial attachment of stem cells, their proliferation and differentiation [425,426]. Based on the above, Gr and GO could favor the enrichment of soluble factors required for stem cell growth and differentiation through molecular interactions.

La *et al.* [427] reported that the GO coating on a Ti substrate enabled the loading of large doses and sustained the release of BMP-2 with the preservation of the structure and bioactivity of the protein. Li *et al.* [423] also proposed a similar "nano-reservoir" mechanism, by using GO nanosheets to adsorb and release endogenous BMPs produced by cells, thereby establishing a dynamic deposition-release process and reducing the loss of BMPs to the cell culture medium [428,429].

4.3.2.4. The influences of GDs' exogenous conduction channels and signaling pathways. GDs play the role of exogenous conduction channels by forming a conductive pathway that may activate specific ion pathways and possibly mediate the expression of specific osteogenic genes [430,431]. Cai *et al.* [407] explored the effects of adding Ca^{2+} and Gr on the electrical conductivity of a Ca^{2+}-doped mixed-phase TiO_2/Gr composite (Fig. 20f). Their results showed that the composite had the lowest resistivity of 0.082 Ω cm and 7 times higher electrical conductivity than the Ca, TiO_2, Gr single-crystals. A new 3D conductive path of Ca-O-C was formed and effectively increased the interfacial charge transfer rate. Gr-containing scaffolds can, therefore, better transfer endogenous electrical signals to cells and activate specific ion channels participating in osteogenesis. Li *et al.* [60] developed alginate/gelatin (AG) composites with polydopamine-graphene oxide (PGO-AG), polydopamine-hydroxyapatite (PHA-AG), and combination thereof (PGO-PHA-AG) to accelerate periodontal bone regeneration by modulating the diabetic inflammatory microenvironment. Micro-CT analysis showed that the bone mineral density of the PGO-PHA-AG group was higher than the values of the AG and PHA-AG groups at 28 days post-surgery. The conductive scaffold promoted bone regeneration by transferring endogenous electrical signals to cells and activating Ca^{2+} channels (Fig. 20g) under the synergistic effects of PHA.

Since Gr has a very high elastic modulus, high in-plane stiffness, and remarkable out-of-plane deformation flexibility, it triggers and

mediates osteogenic differentiation through the activation of the mechanotransductory pathways involving the integrin-FAK (focal adhesion kinase) axis [432–434]. Xie *et al.* [408] found that the chemistry and mechanical properties of Gr were capable of activating the integrin-FAK transmembrane complex that recruited both ROCK1 (rho-kinase 1) and F-actin (filamentous actin) that, in turn, stimulated the phosphorylation of Smad p1/5 proteins, upstream of the gene expression of osteogenic specific markers, *RUNX2*, *OPN*, and *OCN* (Fig. 20h). This then brought osteogenesis closer to completion and ultimately ascertained the participation of the integrin/FAK mechanotransduction pathway during the osteogenic differentiation induced by Gr.

The Wnt canonical signaling pathway is also known for playing an important role in regulating cellular events in a bone microenvironment [435]. Wu *et al.* [436] produced GO-modified β-TCP bioceramics and found that the GO-modified β-TCP scaffolds had greater *de novo* bone formation in the calvarial defects 8 weeks post-implantation compared to the β-TCP groups. GO modification could enhance the binding of the ligand Wnt3a with the receptor LRP5 and further increase intracellular *AXIN2* and *CTNNB* gene expression, which led to enhanced *in vitro* osteogenesis. Mirza *et al.* [437] identified the effectiveness of GO on the expression of BMP-2 by evaluating bone cement composites of GO and poly(methyl methacrylate)(GO-PMMA). The expression of ALP was significantly higher for the GO-PMMA in comparison to the control group of PMMA specimens, and the gene *BMP2* was expressed in specimens containing 0.05 wt% GO only.

The M2-type macrophages favors osteoblast differentiation [438], as their presence can promote the secretion of potential osteogenic factors, such as VEGF, BMP-2, and TGF-β [439] and lead to calcium deposition and increase in bone mineralization. GDs have been shown to have the ability to induce macrophages polarization towards the M2 type. For example, Zou *et al.* [440] demonstrated that GO-carboxymethyl chitosan (CMC) hydrogel loaded with IL-4 and BMP-2 could induce macrophage polarization into the M2 type and enhance the osteogenic differentiation capacity of BMSCs *in vitro* when compared to the control groups without GO and BMP-2. In addition, GO could regulate macrophage polarization through TLRs [441]. In the study conducted by Su *et al.* [442], GO coating was found to increase the gene expression of Myd88 and Ticam2 in RAW 264.7 cells. On the other hand, M2 cytokines could inhibit osteoclast differentiation by downregulating the NF-κB pathway [443]. Inferred from the mechanisms of osteogenesis enhanced by Gr and GDs, as described above, Fig. 20i hypothesizes the factors by which Gr and GDs induce osteogenic differentiation of stem cells and depicts their involvement in cell differentiation and new bone formation in the case of GBMMCs.

4.3.3. Antibacterial properties

GBMMCs have attracted the attention of researchers also for their potential to provide antibacterial biofunctionality [444]. Recent studies have demonstrated that GBMMCs exhibit superior antimicrobial properties compared to their non-modified counterparts and show effective activity against a wide range of pathogens [445]. This broad-spectrum antimicrobial activity, combined with controlled degradation, positions GBMMCs as a valuable solution in the fight against implant-associated infections and the growing threat of antibiotic resistance. In this section, the overall antibacterial performance of graphene-containing Mg-, Fe-, and Zn-based BMMCs as well as the antibacterial effects caused by either GDs themselves or through their effects on the composites biodegradation rate will be reviewed and discussed in detail.

4.3.3.1. The effect of GDs on GBMMCs' antibacterial properties. The literature on the antibacterial properties of GD-containing Mg-, Zn-, and Fe-based BMMCs, and the analysis of the antibacterial mechanism of GDs is scarce (Table 10).

Saberi *et al.* [364] fabricated GNP-incorporated Mg-based MMCs *via* P/M techniques. Their study delved into the antibacterial efficacy of these samples against both Gram-positive (*Staphylococcus aureus, S. aureus*) and Gram-negative (*Escherichia coli, E. coli*) bacteria, demonstrating pronounced growth inhibition of both of the bacterial strains. The Mg-GNP nanocomposites exhibited dose-dependent antibacterial properties, with Mg-2 wt% GNP displaying significantly greater effectiveness in inhibiting bacterial growth compared to Mg-0.5 wt% GNP (Fig. 21a). Exposure of bacterial cells to GNP ultimately resulted in their destruction through various mechanisms, including cell wall damage, oxidative stress, and/or encapsulation [452]. These mechanisms could operate individually or concurrently, collectively inhibiting bacterial growth. Fig. 21b illustrates the proposed antibacterial mechanism of the Mg-GNP composites above, wherein oxidative stress plays a pivotal role in antibacterial activity [364]. Oxidative stress induced by ROS can lead to the oxidation of bacterial lipids, nucleic acids, and proteins, ultimately causing degradation of cell walls and reduction in cell growth [453]. ROS, comprising hydroxyl radicals, superoxide radicals, and hydrogen peroxide can dismantle cellular components, particularly proteins and DNA [454].

Additionally, GO has been reported to exhibit superior antibacterial efficacy compared to Gr and RGO at equivalent concentrations [455]. Saberi *et al.* further investigated the antibacterial properties of the Mg-Zn composites reinforced with GO and Cu nanofillers [446]. Incorporation of GO and Cu substantially enhanced the antibacterial performance of the composites, as evidenced by larger inhibition zone diameters, indicative of stronger antibacterial activity. This enhancement in antibacterial effect was attributed to the combined action of GO and Cu. GO nanosheets, characterized by a large specific surface area and numerous oxygen-containing functional groups, facilitated the interaction with bacterial cell wall, causing physical disruption. Cu nanoparticles, on the other hand, released Cu ions and generated ROS, further damaging bacterial cell structures and inhibiting their functions. This dual mechanism, involving physical disruption by GO and chemical damage by Cu, underscores the observed superior antibacterial properties of the composites. Additionally, Safari *et al.* [361] observed that the addition of Gr significantly augmented the antibacterial properties of Mg-1Al-Cu implants, particularly in the case of 0.18 wt% Gr samples, which exhibited approximately 5- and 3-fold increases in inhibition zone diameter against *S. aureus* and *E. coli*, respectively. Importantly, the addition of Gr did not appreciably alter the release of Cu ions, suggesting that Cu ion release alone could not account for the observed enhancement in antibacterial effect in the 0.18 wt% Gr implants.

Table 10
The antibacterial properties of GBMMCs in relation to the GD type, concentration, composite powder preparation process, and MMC fabrication process.

Metallic matrix	GD type	GD concentration	GD dispersion method	Processing method	Antibacterial properties							Remarks	Ref.
					Diameter of inhibition zone (mm)				ROS generation		Antibacterial rate		Metal ion release concentration (mg/L)		
					S. aureus		*E. coli*		*S. aureus*	*E. coli*	*S. aureus*	*E. coli*			
Mg-3Zn-1Ca	Gr	0 wt% 0.5 wt% 1 wt% 2 wt%	Solution-assisted dispersion	Sintering	0.1 1.9 2.7 3.1		0.1 1.8 2.4 2.8		—		—		—	All the Mg-GNP composites exhibited antibacterial properties against S. aureus and E. coli bacteria and increasing GNP concentration enhanced antibacterial activity.	[364]
Mg-3Zn-1Mn	GO	0.5 wt% 1 wt% 1.5 wt%	Ball milling	Sintering	Salmonella–Shigella	1.91 3.32 3.61	Klebsiella pneumoniae	~ 1.84 ~ 2.33 ~ 2.86	—		—		—	Mg–Zn–Mn (MZM)/1.5GO nanocomposite exhibited higher antibacterial activity than the MZM/0.5GO and MZM/1GO nanocomposites against *Salmonella–Shigella* bacteria.	[365]
Mg-Zn	GO GO/Cu	0 wt% 0.5 wt% 0.5 wt% GO and 0.12 wt% Cu 0.5 wt% GO and 0.25 wt% Cu	Solution-assisted dispersion	SPS	0.1 2.47 3.51 4.03		0.1 2.34 ~ 3.12 3.64		—		—		—	The high Cu-GO content in the MZ/GO-Cu composites exhibited significant antibacterial activity, destroying 90–94 % of *S. aureus* bacteria.	[446]
Mg–1Al–Cu	Gr	0 wt% 0.18 wt% 0.5 wt%	Ball milling	SPS	~ 0.98 ~ 4.67 ~ 2.36		~ 1.39 ~ 3.66 ~ 1.39		~ 0.37 ~ 0.68 ~ 0.29	~ 0.17 ~ 0.41 ~ 0.18	—		Mg^{2+}: ~ 84.8 Cu^{2+}: ~ 0.32 Mg^{2+}: ~ 69.7 Cu^{2+}: ~ 0.23 Mg^{2+}: ~ 82.8 Cu^{2+}: ~ 0.16	The 0.18 wt% Gr samples increased the diameter of the inhibition zone approximately 5- and 3-fold against *S. aureus* and *E. coli*, respectively, while the 0.5 wt% Gr samples increased the diameter of the inhibition zone approximately 3- and 1.1-fold against *S. aureus* and *E. coli*, respectively, when compared to non-Gr-modified Mg–1Al–Cu samples.	[361]
Mg-3Zn-1Mn	RGO	0 wt% 0.5 wt% 1 wt% 1.5 wt%	Solution-assisted dispersion	Sintering	0.3 1.1 2.3 3.1		0.5 2.3 3 4.2		—		—		—	The reduction in the number of colonies indicated that ZM31–1.5RGO with high RGO amounts has the best preventing bacterial attachment and growth.	[447]

(*continued on next page*)

Table 10 (*continued*)

Metallic matrix	GD type	GD concentration	GD dispersion method	Processing method	Antibacterial properties						Remarks	Ref.
					Diameter of inhibition zone (mm)		ROS generation		Antibacterial rate		Metal ion release concentration (mg/L)	
					S. aureus	*E. coli*	*S. aureus*	*E. coli*	*S. aureus*	*E. coli*		
Mg-3Zn-0.5Zr	FunctionalizedGr	0 wt% 0.25 wt% 0.5 wt% 1 wt%	Ball milling	SPS	0.98 1.35 8.98 9.46	0.69 1.31 8.69 9.28	—		— 31.3 % 83.8 % 99.4 %	— 28.5 % 85.9 % 99.3 %	—	FGNPs could impressively prevent the growth and colonization of *E. coli* and Staphylococcus aureus *S. aureus*.	[448]
Zn-2Ag	Cu2O modified GO	0 wt% 1 wt%	Ball milling	SPS + hot extrusion	0 7.2 ± 0.5	0 5.7 ± 0.6	—		—		—	In the 1Cu2O-GO/Zn-2Ag group, *E. coli* showed blurred membranes, shrinkage, and signs of electrolyte leakage, while still retaining their rod shape, indicating a robust cell wall. In contrast, *S. aureus* exhibited rough, chapped surfaces with cytoplasmic leakage, demonstrating cell wall rupture and death.	[449]
Zn	Cu2O modified GO	0 wt% 0.5 wt% 1 wt% 2 wt% 4 wt%	Ball milling	SPS	—	—	—		~ 66.1 ~ 74.4 91.8 % 96.6 % 98.6 %	—	Zn^{2+}: ~ 15.4 Cu^{2+}: 0 Zn^{2+}: ~ 14.2 Cu^{2+}: ~ 0.29 Zn^{2+}: ~ 15.2 Cu^{2+}: ~ 0.36 Zn^{2+}: 19.9 Cu^{2+}: ~ 0.43 Zn^{2+}: 35.7 Cu^{2+}: ~ 0.42	The addition of Cu2O-GO contributed to the significantly reduced number of bacterial colonies, and bacterial colonies were rarely observed in the 4Cu2O-GO/Zn groups.	[450]
Zn	*f*-Gr	0 mg/L 25 mg/L 50 mg/L 100 mg/L	Electrolytic co-deposition	SPS	17 ± 1 18 ± 0.5 19 ± 0.5 23 ± 1.5	15 ± 0.5 16 ± 2 18.5 ± 1 21 ± 1	—		—		—	Zn/f-GNP (100 mg/L) nanocomposites have shown a strong inhibition against both bacteria strains with average zone of inhibition of 23 mm and 21 mm, which were 35.2 % and 40 % higher than that of 17 mm and 15 mm across pure Zn for gram-positive and gram-negative bacteria, respectively.	[451]

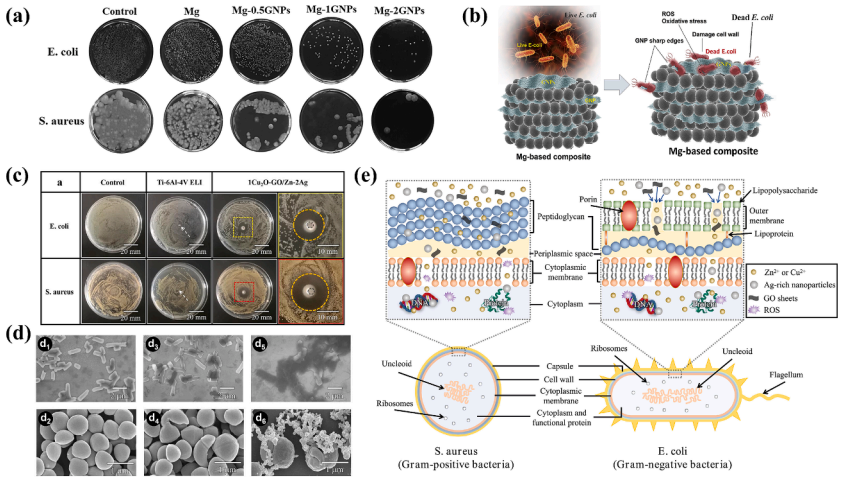

Fig. 21. (a-b) The antibacterial performance and mechanism of Mg-based MMCs: (a) antibacterial activities of the Mg-xGNPs composites against both Gram-positive (S. aureus) and Gram-negative (E. coli) tested by the plate count technique; (b) a schematic illustration of the antimicrobial mechanism of Mg-GNP composites [364]; . (c-e) The antibacterial mechanism and performance of Zn-based MMCs: (c) digital micrographs of the inhibition zone of hot extruded $1Cu_2O$-GO/Zn-2Ag composites against E. coli and S. aureus after co-culture for 1 day; (d) representative bacterial morphologies of pristine (d1) E. coli and (d2) S. aureus, model bacteria cultured with 2-fold diluted extracts derived from (d3, d4) reference material of standard Ti6Al4V and (d5, d6) $1Cu_2O$-GO/Zn-2Ag components for 1 day; (e) antibacterial mechanisms of the 1Cu2O-GO/Zn-2Ag composites against S. aureus and E. coli [449].

The antimicrobial potential of Zn-based MMCs was explored through the investigation of hot extruded $1Cu_2O$-GO/Zn-2Ag composites against *E. coli* and *S. aureus* strains [449]. The $1Cu_2O$-GO/Zn-2Ag composites demonstrated significant bacteriostatic activity, particularly pronounced against *S. aureus* (Fig. 21c). Microscopic examination revealed distinctive alterations in bacterial morphology upon the interaction with the surface of the composites. *E. coli* cells displayed membrane blurring and shrinkage, indicating intracellular leakage and cellular disintegration, whereas *S. aureus* cells exhibited roughened surfaces and cytoplasmic leakage, suggestive of cell wall rupture and death (Fig. 21d). For *S. aureus*, metallic ions could penetrate the cell wall, directly disrupt protein synthesis, and interfere with DNA transcription, contributing to their strong antibacterial properties. However, *E. coli* cells have an impenetrable outer membrane that significantly limits the entry of metallic ions [456]. The composites, which included Ag-rich nanoparticles and GO, could denature and perforate this protective membrane, facilitating the passage of Zn^{2+} and Cu^{2+}. This led to a synergistic antibacterial effect of the metallic ions, Ag-rich nanoparticles, and GO against *E. coli* (Fig. 21e).

Owhal *et al.* [451] employed the modified electro co-deposition technique to modify pristine GNPs with functional groups, thereby mitigating their toxicity, and subsequently fabricated Zn/f-GNPs (functionalized GNPs) composites *via* sintering. Their results unveiled expanded Zones of Inhibition (ZOI) against gram-positive bacteria and reduced ZOI against gram-negative bacteria, attributed to the additional outer protective membrane in the latter. Notably, the Zn/f-GNP (100 mg/L) nanocomposites exhibited robust inhibitory effects against both strains, with average ZOI of 23 mm and 21 mm, respectively, markedly surpassing pure Zn (ZOI of 17 mm and 15 mm.). Moreover, increasing the f-GNP content in the Zn matrix augmented the antibacterial efficacy of the nanocomposites, owing to the synergistic interplay between Zn and f-GNPs. This increased antibacterial activity involves direct interaction between Zn/f-GNPs and bacterial cell membranes, disrupting membrane permeability and causing bacterial demise. At the time of writing, no work on the antibacterial properties of Fe-based MMCs has been reported in conjunction with GDs. Recent studies suggest that doped Gr (*e.g.*, N-Gr and S-Gr) and GDs exhibit enhanced antibacterial activity. For example, Wang *et al.* [457] demonstrated the effective inhibitory effect of nitrogen-doped Gr on E. coli and found that the damage to E. coli was not simply caused by the physical destruction of Gr, but was related to the ability of Gr-N to serve as active sites in providing a unique oxidative stress mechanism. These findings underscore the potential of the doping strategy for infection-resistant implants.

Based on the findings reported in the literature (summarized in Table 10), GBMMCs have demonstrated antibacterial activity against a broad range of clinically relevant pathogens, with distinct efficacy profiles depending on the matrix material and Gr functionalization. Gram-positive bacteria, particularly *S. aureus*, are the most extensively studied targets, as their single-layered peptidoglycan cell wall is vulnerable to Gr-mediated physical disruption (*e.g.*, edge penetration and membrane wrapping) and oxidative stress from ROS. For instance, Mg-GNP composites achieved $>$ 80 % inhibition (Fig. 21a) against *S. aureus via* synergistic effects of Mg^{2+} release and Gr-induced lipid peroxidation. Gram-negative bacteria, such as *E. coli* [446], Salmonella–Shigella and Klebsiella pneumoniae [365], are also effectively inhibited by GBMMCs, though their outer membrane necessitates higher ion concentrations or combinatorial mechanisms (*e.g.*, GO-mediated outer membrane perforation, followed by Zn^{2+}/Cu^{2+} influx). In addition, Zn-based GMMCs incorporating Cu_2O-GO showed about 3.5 $\times$ and 3 $\times$ greater inhibition zones against *E. coli* and *S. aureus* compared to pure Zn, respectively, attributed to Gr-enhanced $Zn2^{+}$ release and GO's membrane-disrupting action. However, systematic evaluation of anaerobic bacteria (*e.g.*, Bacteroides fragilis) and fungal pathogens (*e.g.*, Candida albicans) is highly limited. Future work should prioritize the expansion of the pathogen spectrum to include multidrug-resistant and biofilm-forming strains critical in implant-

associated infections.

The safety of GBMMCs is a critical consideration in their design and application. While GBMMCs exhibit antibacterial activity by physically or chemically disrupting bacterial cell structures, their potential impact on normal human cells should be carefully managed through selective toxicity mechanisms, material design optimization, and biological compatibility validation. Antibacterial metal ions (*e.g.*, Zn^{2+}, Mg^{2+}, and Cu^{2+}) exhibit concentration-dependent toxicity. Their release rates in GBMMCs need to be tuned to remain below their cytotoxic thresholds for human cells while exceeding bactericidal levels. For example, a Zn^{2+} concentration of about 0.8 μg/mL exhibits antibacterial properties against *S. aureus* and *E. coli* and is tolerated by MC3T3-E1 osteoblasts, because it is below 13 μg/mL [458]. ROS generated by GBMMCs primarily act at the material-bacteria interface, while mammalian cells counteract ROS through robust antioxidant systems [459]. Safety is engineered into GBMMCs through surface functionalization, coating with controlled ion release, and bioactive additives. Gr incorporated with anti-inflammatory agents (*e.g.*, strontium) or osteogenic factors (*e.g.*, BMP-2) counteracts residual oxidative stress and promotes tissue repair [460]. In addition, GBMMCs need to undergo rigorous biological compatibility testing to ensure safety. For example, direct/indirect contact tests with human osteoblasts, fibroblasts, and immune cells confirm viability $>$ 70–80 % at therapeutic doses. Animal models demonstrate minimal inflammatory response, controlled fibrosis, and no systemic toxicity. In summary, the design of GBMMCs needs to effectively exploit the structural and metabolic differences between bacterial and human cells, ensuring selective antibacterial action while safeguarding normal tissue.

4.3.3.2. GDs-mediated antibacterial mechanism. In 2010, Hu *et al.* [461] first reported the antibacterial activity of GO and RGO nanosheets. In the presence of 85 g/mL GO/RGO for 2 h, the growth of (*E. coli*) bacteria was highly suppressed with a viability loss of up to $>$ 90 %. GO nanosheets exhibited excellent antibacterial activity and minimal cytotoxicity, while RGO nanosheets possessed antibacterial properties that were only slightly lower than those of GO nanosheets. In a follow-up study, Gurunathan *et al.* [462] demonstrated that the effectiveness of GO at inactivating bacteria was related to its sharp edges and the generation of ROS. With the continuous deepening of relevant research, physical damage and oxidative stress are widely considered to be the two main mechanisms of GDs-mediated antibacterial effects. The sharp edges of GDs are considered to directly pierce or cut the cell wall of bacteria, causing the cell contents to leak and ultimately causing the death of the bacteria. Under certain conditions, GDs can generate ROS, such as hydrogen peroxide (H_2O_2), superoxide (O_2^-) and hydroxyl radicals (OH^-). These ROS attack bacterial cell wall, proteins, and DNA, causing oxidative stress and cell damage, ultimately causing bacterial death. In addition, electron transfer, molecular capture and chemical interference [39,463] are also generally considered effective mechanisms by which GDs participate in antibacterial activity. The synergistic effect of these antibacterial mechanisms enables Gr-containing materials to exhibit significant antibacterial activity against a variety of pathogenic bacteria, including drug-resistant strains.

The wetting behavior of GBMMCs is a crucial property for promoting new tissue development by providing active surface sites that facilitate cellular attachment, migration, and proliferation, while also inhibiting bacterial adhesion to improve antibacterial properties [464]. It has been reported that the hydrophilicity positively affects protein adsorption and osteoblast attachment [465]. GO, being rich in hydrophilic functional groups (*e.g.*, hydroxyl and carboxyl groups), contrasts with RGO or Gr that exhibits hydrophobicity due to the partial or complete removal of oxygen-containing groups. It is however important to note that the wettability and biological performance of GBMMCs are not solely governed by the properties of the GDs themselves. The content, dispersion extent of GDs, and the microstructure and roughness changes within the metallic matrix all significantly impact the final biological performance. For Mg-based GMMCs, the content of GDs plays a major role in determining their wettability. Saberi *et al.* [364] reported that the wettability of pure Mg increased with the addition of Gr; with an addition of 2 wt% Gr, the surface changed from hydrophobic (contact angle 102°) to hydrophilic (contact angle 78°). The type of metallic matrix also influences wettability, as the Mg-3Zn-0.5Zr alloy without any addition of Gr exhibited a higher contact angle (115°), which decreased to 59° with an addition of 1 wt% Gr [448]. Shahin *et al.* [32] also observed a similar decrease in water contact angle (WCA) in the Mg-0.5Zr alloy, with the WCA decreasing from 81° for Mg-0.5Zr to 60° for Mg-0.5Zr-0.4 wt% Gr. Although pure Gr is theoretically hydrophobic due to its perfect sp^2 carbon structure, in practice, Gr added to Mg alloys is often imperfect. Processing defects, edge effects, and partial oxidation can introduce oxygen functional groups (*e.g.*, carboxyl and hydroxyl) onto the Gr surfaces, enhancing its hydrophilicity. Additionally, the dispersion of Gr (and potential agglomeration due to excessive addition) in BMMCs can alter the microstructure and roughness of the alloy surface, which, together, increase the overall surface hydrophilicity. While there is a significant difference in wettability between GO and RGO, studies have shown similar outcomes for both of the Gr derivatives when incorporated into BMMCs, as both increase surface hydrophilicity. For example, Jabbarzare *et al.* [365] found that the WCA in Mg-Zn-Mn alloys decreased from 62.3° to 47.1° with an addition of 1.5 wt% GO, and Abazari *et al.* [447] reported a decrease in WCA from 98 ± 3° to 87 ± 1° when 1.5 wt% RGO was added to the Mg-3Zn-1Mn alloy. Unlike the direct coating of dense GO or RGO onto BMMC surfaces, the intrinsic differences in hydrophilicity and hydrophobicity of GBMMCs have been significantly reduced due to the content, dispersion, and defects introduced during processing, as well as the microstructural and roughness changes in GBMMCs. For Zn-based GMMCs, the addition of a certain amount of Gr (*e.g.*, 0.3 wt%) also reduced the WCA from 82.8 ± 2.4° (pure Zn) to 66.4 ± 1.2° [369]. However, currently, there is no direct evidence suggesting that the change in wettability of GBMMCs due to the addition of GDs significantly impacts osteoblast attachment, migration, proliferation, or bacterial adhesion inhibition. Future research should focus on: (i) exploring the potential of RGO and Gr's hydrophobicity to create hydrophobic surfaces on GBMMCs, or to increase surface hydrophobicity to inhibit bacterial attachment; (ii) designing moderately hydrophilic surfaces to balance antibacterial and cell-adhesion requirements; and (iii) adapting the wettability of GBMMCs dynamically during *in vivo* degradation, such as inhibiting bacterial adhesion *via* the hydrophobicity of RGO-mediated surfaces during initial implantation and promoting osteoblast migration and osseointegration through the gradual exposure of GO during degradation, which enhances hydrophilicity.

4.3.3.3. Antibacterial mechanism triggered by GDs regulating GBMMCs biodegradation rate. In addition to the antibacterial effects brought by GDs themselves, GDs trigger different biodegradation rates when integrated into BMMCs as a doping phase (as discussed in Section 4.2), resulting in different concentrations of antibacterial active metal ions. This process is accompanied by the entire bone implant biodegradation cycle, which results in long-term changes in antibacterial properties. Ag^{+}, Cu^{2+} and Zn^{2+} are the most common antibacterial metal ions and are often introduced into BMMCs [466–468]. They inhibit bacterial growth by binding to thiol groups on the bacteria cell wall, damaging it, and by inhibiting enzyme function, interfering with DNA replication, and causing oxidative stress [469–471]. Secondly, different ion concentrations will also have a significant impact on antibacterial activity. For example, the concentrations of Zn^{2+} and Cu^{2+} significantly affect their antibacterial properties. At low concentrations, they primarily serve as essential nutrients for bacteria, potentially offering mild antibacterial effects. At high concentrations, both Zn^{2+} and Cu^{2+} can substantially inhibit or kill bacteria through various mechanisms. Zn^{2+} ion typically disrupts cell wall and inhibit enzyme activity, while Cu^{2+} ion is more potent, generating ROS and causing extensive cellular damage [472,473]. It was reported that a concentration of $Zn^{2+} > 15$ mg·mL^{-1} or a concentration of $Cu^{2+} > 0.09$ mg·mL^{-1} could contribute to a strong antibacterial performance [474,475]. These differences are crucial when designing antimicrobial biomaterials to achieve optimal biofunctionalities. Sun *et al.* [450] found the addition of Cu_2O-GO endowed Cu_2O-GO/Zn composites with high antibacterial activity. As compared to the pure Zn groups, the extracts of 2Cu2O-GO/Zn and 4Cu2O-GO/Zn specimens exhibited significantly increased Zn^{2+} concentrations of 19.9 μg·mL^{-1} and 35.7 μg·mL^{-1}, respectively, which was attributed to the enhancement of biodegradation rate due to GO. Moreover, all the Cu_2O-GO/Zn specimens released low levels of Cu^{2+} (0.3–0.4 μg·mL^{-1}). The effect of released Cu^{2+} and increased Zn^{2+} were responsible for the enhanced antibacterial property of Cu_2O-GO/Zn composites when compared to the pure Zn samples. Furthermore, Fe^{2+}/Fe^{3+} can also achieve antibacterial effects by promoting free radical generation, causing oxidative stress, and interfering with cell metabolism [476]. Mg^{2+} can affect the stability and function of cell wall and inhibit the activity of certain enzymes [477]. Therefore, it is expected that regulating the biodegradation rate with GDs to achieve enhanced antibacterial effects is not limited to zinc-based BMMCs, but is applicable to other BMMCs.

4.3.4. Discussion

4.3.4.1. Cytotoxicity. While GDs intensify antibacterial activity through mechanisms such as ROS generation, ion release modulation, *etc.*, their cytotoxicity is critically influenced by their concentration, lateral size, and oxidation state. For instance, high GD concentrations (>2 wt%) [364] or sub-100 nm lateral dimensions [478] can induce oxidative stress and physical damage to mammalian cells. To mitigate risks, material design strategies, such as optimizing GD dispersion to prevent agglomeration, surface functionalization, and controlled degradation kinetics, are highlighted, ensuring that ion concentrations remain below cytotoxic thresholds. Fe-GO composites, for example, demonstrated safe Fe^{3+} release rates (6.33 μg/(mL·day)), well below the IC_{50} value for MC3T3-E1 [372]. Additionally, GD-mediated immunomodulation (*e.g.*, M2 macrophage polarization) and bioactive ion release counteract residual cytotoxicity by promoting tissue repair and antioxidant responses, as seen in Mg/GO composites, which reduces inflammatory IL1B expression while enhancing pro-healing RETNLA levels [403]. Future studies should systematically correlate GD physicochemical properties with long-term *in vivo* biocompatibility, particularly for Fe-based systems, where cytotoxicity data remain limited. This integration underscores that GD-enhanced antibacterial efficacy in GBMMCs should not compromise safety when design parameters are carefully balanced.

4.3.4.2. Osteogenic properties. The combination of GDs and BMMCs exhibits a synergistic effect on enhancing overall bone regeneration performance. Firstly, most of the degradation products of BMs are known for their good biocompatibility, which supports osteocyte activity through the release of bioactive metal ions [479]. Secondly, the incorporation of GDs can effectively regulate the corrosion rates of these metals by forming physical barriers, reducing the adverse effects of rapid degradation on the local biological environment [368]. GDs further stabilize surface corrosion products, such as magnesium hydroxide and phosphate layers, reducing local pH fluctuations and maintaining a favorable environment for bone growth. In the case of iron-based alloys, the addition of Gr can mitigate the issues related to uneven corrosion and localized degradation, optimizing the overall degradation kinetics to better align with the time frame required for bone regeneration [480]. Beyond corrosion control, GDs also actively contribute to osteogenesis through multiple mechanisms. Their high mechanical strength and specific surface topography, such as folded porous layers, can generate mechanical stimuli that promote bone formation. Additionally, GDs influence extracellular matrix (ECM) dynamics, modulate macrophage activity, and engage various signaling pathways involved in osteogenesis. Among different GD types, GO has been shown to be able to effectively enhance osteocyte adhesion and differentiation, while RGO improves the structural stability of the metallic matrix to provide osteogenic support and ensure long-term mechanical compatibility throughout the dynamic degradation process *in vivo*. The optimum concentration of GDs in BMMCs typically ranges from 0.1 to 1.0 wt%, balancing corrosion resistance and osteogenic activity without significantly altering metal degradation rates [31,33,228]. Furthermore, studies suggest that Gr with lateral dimensions smaller than 5 μm, as well as GO and RGO with sizes below 1 μm, can negatively affect osteocyte viability [481].

4.3.4.3. Antibacterial properties. In the BMMC systems, the metal matrix not only serves as the primary structural component but also plays a crucial role in regulating antibacterial performance through its degradation behavior. During degradation, metals such as Mg and Zn release metal ions that exhibit intrinsic antibacterial properties. Furthermore, metal corrosion products, such $Mg(OH)_2$, contribute to inhibiting bacterial adhesion and reducing biofilm formation [482]. For iron-based implants, the corrosion products, like iron oxide (Fe_2O_3), can create a physical barrier that impedes bacterial colonization [483]. The degradation rate of the metal is a key

factor that influences the release kinetics of antibacterial ions and the alteration of the local environment. Proper control over the degradation process is essential to striking a balance between antibacterial efficacy and tissue regeneration.

The incorporation of GDs into BMs can further enhance their antibacterial properties by moderating their corrosion rates, stabilizing corrosion products, and optimizing surface characteristics. This not only improves the antibacterial efficacy but also enhances the overall stability and functionality of the implant. GO exhibits potent antibacterial activity due to its surface carboxyl and hydroxyl functional groups, which can physically disrupt bacterial cell walls or generate ROS to kill pathogens. In contrast, RGO exhibits lower oxidative activity but contributes to the enhanced durability and antibacterial performance of metal implants due to its superior conductivity and mechanical strength [484]. At low concentrations, Gr can significantly enhance the antibacterial properties of BMMCs without substantially affecting the degradation rate of the metal matrix. However, excessive Gr content may alter surface energy, potentially affecting cellular adhesion and inhibiting osteogenesis. Additionally, smaller graphene sheets with a higher surface area may provide more effective bacterial interaction, enhancing antibacterial performance [485]. Conversely, larger graphene structures may impede the degradability of metal substrates, thereby indirectly diminishing antibacterial effects.

4.3.4.4. Integrated analysis of cytotoxicity, osteogenesis, and antibacterial properties. The biological performance of GBMMCs hinges on the delicate balance between cytotoxicity, osteogenesis, and antibacterial activity, governed by the interplay of GDs' physicochemical properties and degradation dynamics [486]. While GDs enhance antibacterial efficacy through mechanisms such as ROS generation and metal ion release, their cytotoxicity is critically influenced by concentration, lateral size, and oxidation state. GDs' osteogenic effects, such as enhanced ALP activity and stem cell differentiation, often coexist with antibacterial functionality, but these dual benefits may conflict with cytotoxicity risks. For example, GO's hydrophilicity and carboxyl groups enhance antibacterial activity but may elevate oxidative stress, potentially harming osteoblasts, while RGO's lower oxygen content reduces cytotoxicity while maintaining osteoconductivity [487]. The surface microstructure of GDs further modulates this triad; nanoscale ripples or edge defects on Gr sheets promote osteoblast adhesion *via* integrin-FAK mechanotransduction while selectively inhibiting bacterial colonization through physical disruption [488]. Additionally, GD-mediated immunomodulation, such as macrophage polarization toward the M2 phenotype, links cytotoxicity and pro-osteogenesis effects [403]. However, challenges remain in harmonizing these properties, particularly for Fe-based BMMCs, where cytotoxicity data are scarce despite their corrosion products showing antibacterial potential. Future work should systematically map GD properties (*e.g.*, C/O ratio and lateral size) to cytotoxicity thresholds and biofunctional efficacy, enabling predictive models for clinical-grade GBMMCs. By integrating cytotoxicity as a core design parameter, GD-engineered composites may achieve the elusive trifecta of safety, antibacterial potency, and osteogenic capacity.

4.3.4.5. Selection of Gr and its derivatives for biomedical applications. The distinct physicochemical properties of Gr, GO, and RGO enable their targeted use in specific biomedical applications. For example, GO's hydrophilicity suits hydrophilic polymer coatings for corrosion protection, while RGO aligns with applications demanding both electrical and mechanical performance. Standardization of reduction protocols (*e.g.*, C/O ratio control *via* XPS quantification) is essential to ensure reproducibility in biomedical outcomes [489,490]. The selection of GDs should prioritize the synergy between their intrinsic properties (*e.g.*, conductivity and functional groups) and target clinical requirements. Gr itself exhibits high electrical conductivity ($>$ 3000 S/cm), exceptional mechanical properties (*e.g.*, Young's modulus $\sim$ 1 TPa), and chemical inertness [23,178]. Its most suitable applications include electroactive implants, such as neural interfaces or cardiac patches requiring rapid electron transfer [491,492] and high-strength, load-bearing scaffolds, exemplified by Mg-based GMMCs that leverage Gr's load-transfer capability to achieve tensile strengths exceeding 350 MPa [238], making them appropriate for femoral bone repair. GO typically possesses oxygen-rich functional groups (C/O: 2–3) [493], hydrophilicity, and high drug-loading capacity *via* π-π stacking/hydrogen bonding. This makes GO ideal for drug delivery systems and immunomodulatory interfaces. For example, GO can adsorb antibiotics through its carboxyl groups, enabling sustained release to combat biofilm infections [494,495]. Moreover, GO is an excellent candidate as a controlled release carrier for IL-4 and BMP-2, promoting immune regulation and bone repair by polarizing macrophages toward the M2 phenotype [440]. RGO is characterized by a tunable reduction degree (C/O ratio of 5–15), intermediate conductivity (10–500 S/cm), and defect-mediated reactivity [496,497]. This makes it promising for balancing bioactivity; for instance, partially reduced RGO in Mg-6Al-1Zn/RGO composites enhances osteogenesis while minimizing cytotoxicity [254].

5. Current challenges and limitations

Although AM GBMMCs have the potential to enhance the mechanical and biological properties of bone scaffolds, and expand their structural design horizon to an unprecedented extent, these biomaterials have not yet made inroads into large-scale industrial manufacturing and clinical practices. The main challenges and limitations hindering their developments towards application are listed below from the perspectives of biomaterials, processing, and functionality.

5.1. Biomaterial perspective

There is a lack of accurate predictive models, built on a Gr 'genome', including its 'genetic' information, such as lateral size, thickness, morphology, type, and number of functional groups, to guide the design and fabrication of GBMMCs, based on the understanding of the possible impacts of such genetic information on improving the mechanical and biological properties of GBMMCs [498,499]. To fabricate high-performance and large-scale GBMMCs, two challenges must be overcome, namely the agglomeration of

GDs and poor interfacial bonding [500]. Surface engineering strategies can be utilized to improve the wettability between the metal matrix and GDs by coating GDs with metallic elements [79]. Some specific elements can even react with GDs to form compounds that can act as an intermediate bridge between GDs and the metal matrix so that the interfacial strength is enhanced [501]. Beyond the intrinsic properties of GDs, intentional doping (*e.g.*, N, B, and P) offers a promising route to tailor their electronic, chemical, and biological functionalities. However, doping processes must be standardized to ensure reproducibility. When implementing the described strategies above, the possible effects of the chosen elements and dopants on the biological properties of the resulting GBMMCs must be taken into consideration. Rigorous re-evaluation must be performed for long-term biosafety of surface-modified and dopped GBMMCs.

Currently, there are no commercially available BM powder materials that are certified for use in AM medical devices, according to ISO 13485:2016. The standardization and commercialization of medical-grade powder materials are one of the main barriers to the research on and application of AM BMMCs. Laser-based AM techniques, such as PBF and DED, are prone to differential evaporation rates of the alloying elements in magnesium- and zinc-based alloys [502] and, thus, to changes in chemical composition due to burn-out, resulting in large deviations of the actual composition of the printed implant from that of the pre-alloyed powder or elemental powders, which may have important implications for the properties of the as-fabricated implant [503]. The addition of GDs to metal matrix powders tends to further deteriorate laser energy absorption, powder flowability, and printability [188]. Therefore, the development of powder materials specific to AM and aimed to meet the requirements for the AM of biodegradable medical implants and for their clinical applications, is a key technical issue that needs to be addressed urgently.

For GBMMCs, new biomedical functions, such as antimicrobial property, shape memory behavior, anti-tumor activity, and drug delivery function, need to be further explored through the search for ideal biomaterial and structure designs, and processing technologies, which can lead to the development of new implant materials with new biomedical functions and even smart material responses. For antimicrobial functions, metal ions, such as Ag^{+} and Cu^{2+}, have been used in BMMCs [472,504]. Grain boundary engineering and alloying are considered to have the ability to introduce heterogeneous or homogeneous alloying elements by rational design to introduce extraordinary properties [505]. The Mg-18.3 %Sc alloy, for example, has been reported to undergo martensitic transformation starting at −90 °C and exhibit room temperature superelasticity [506]. The integration of GDs into biodegradable shape memory alloys (SMAs), such as the Mg-Sc [507] and Fe-Mn-based [508] alloy systems, offers a promising yet underexplored avenue for tailoring the shape memory effect (SME) while balancing degradation kinetics. In conventional non-degradable SMAs (*e.g.*, Ni-Ti) added with Gr, Gr has been shown to effectively dissipate the latent heat released during the solid-state phase transition [509]. This facilitates a larger volume of material transition from the austenite phase to the martensite phase, leading to an increase in the nanoindentation depth. While current research on Gr-enhanced biodegradable shape-memory MMCs is highly limited, the studies on polymer-based and metal oxide composites suggest that Gr can enhance SME by improving thermal and electrical conductivity, thereby enabling a more efficient response to stimuli [510]. Translating these principles to biodegradable SMA-based composites requires careful consideration of degradation-SME coupling. For instance, GD's impermeable structure may locally inhibit corrosion at phase boundaries, thus preserving regions crucial for the SME. However, accelerated ion release at the Gr-metal interfaces, such as $Fe3^{+}/Fe2^{+}$ in Fe-Gr composites, has the potential to destabilize the matrix, highlighting the necessity for microstructural design that spatially separates degradation zones from SME-active regions. Beyond advancing the research on Gr-reinforced degradable shape memory MMCs, future research on the impact of GD doping on SME performance should search for answers to some fundamental questions as to, for example, whether Gr can stabilize austenite/martensite phase boundaries through interfacial oxygen bonding, thus improving recoverable strain, and whether Gr can enhance phase transformation efficiency by reducing interfacial energy barriers during martensitic reorientation, contributing to the establishment of an adaptable theoretical mechanism. The answers will indicate the possibilities of designing Mg- and Fe-based biodegradable alloys with extraordinary properties at the body temperature for specific medical devices, similar to those exhibited by non-degradable metals, such as Ni-Ti alloys [511].

5.2. Processing perspective

Despite the interesting properties of GBMMCs for potential biomedical applications, most of GBMMCs are still at the exploratory stage and far from entering the commercial manufacturing stage. The research on scalable, standardized composite powder preparation and implant manufacturing techniques will be an important direction of research in the field. Composite powder preparation techniques are desired to be able to control the lateral size and thickness characteristics of GDs, while reducing its agglomeration and structural damage (*i.e.*, structure retention/control) [512]. Standardizing Gr derivative dimensions (lateral size and thickness) and SSA ranges for specific AM processes remains a critical challenge. Machine learning-assisted parameter optimization could help map Gr size-SSA-process windows to target properties (*e.g.*, strength *versus* corrosion), accelerating clinical translation of GBMMCs.

Currently, structural design, feedstock materials, AM methods, and processing conditions for the fabrication of scaffolds or implants made of BMs, such as Mg, Fe, Zn and their alloys, vary widely [502]. There is a lack of optimum AM techniques that are compatible with materials and the geometrical designs of choice. For example, while current laser-based PBF and DED processes can safely produce pure Fe and Fe alloy scaffolds with exact strut sizes and expected properties [513], they can cause spatter of powder particles, evaporation, and smoke formation, when printing pure Zn or Zn alloys due to their low melting and boiling points [503], which can affect the density of the as-printed scaffolds, and can even cause powder combustion if the laser energy is too high when printing pure Mg [514]. At the same time, the current powder mixing processes for GBMMCs, as described above, tend to deteriorate the flowability, fluidity, and printability of composite powders to a certain extent [515], which may affect the printing result or even prevent the designed scaffolds from being printed. The adhesive-assisted ME and MJ processes do not need to consider powder spreading on the build plate or the interactions of laser with the powdered material, thus giving a great deal of freedom to optimize material and

architectural design, but given their low printing accuracy, they are unable to print fine structures, which in turn greatly limits their ability to support the development of microarchitecture-driven properties. Furthermore, post-AM processes, including debinding and sintering, will inevitably affect dimensional accuracy, phase composition, and related properties. To deal with these challenges, advanced composite powder preparation and hybrid manufacturing processes need to be developed and implemented to fully exploit the benefits of Gr and the full capabilities of AM in terms of material selection and form freedom.

5.3. Function perspective

5.3.1. Mechanical properties

A match in mechanical properties between the host tissue and implant is required to ensure favorable clinical outcomes after implantation. Tailoring the mechanical properties of bone implants requires a full understanding of the strengthening mechanisms of the implant materials, which can be used to guide material selection and architectural design. Establishing the interactions of GDs with the matrices of the major BMs and their alloys and the way in which GDs affect microstructural evolution during processing will aid in improving our understanding of the interplay between the strengthening mechanisms of GDs on the one hand and their characteristics on the other hand. At present, there is a lack of quantitative methods to measure interfacial strength and to clarify what interface is most favorable for optimum combination between GDs and metal matrices [514]. Even for given combinations of GDs and BMs, the types of interfaces formed may be vastly different, which makes the prediction of their mechanical performance and biodegradation behavior difficult. A better understanding of the formation of the different types of interfaces will also enable the design, control, and optimization of processing methods for desired interfaces. To meet the specific requirements in terms of mechanical properties for GBMMC bone implants (*e.g.*, fatigue strength and *in vivo* corrosion fatigue strength), it is important to quantify the interface strength and design sound Gr/matrix bonding interfaces based on an in-depth understanding of the strengthening mechanisms and their relation with the characteristics of GDs.

5.3.2. Biodegradation

Adjusting the rate of biodegradation to match that of bone tissue regeneration is the key to the clinical adoption of personalized GBMMC implants. At present, our understanding of the impact of GDs on the biodegradation of BM implants is incomplete. GDs' content, lateral size, shape, number of functional groups, contact, and interactions with second phase(s) and with the matrix, the effects on grain size and texture orientation all have varied influences on the biodegradation rates of GBMMCs [516]. In addition to the optimization of the alloy composition and structural design, AM processes and surface treatments for bio-functionalization are the key approaches that can be used to adjust the biodegradation rate of the resulting biomaterials [59]. Therefore, the concept of "design for biodegradation" needs to be considered, based on a better understanding of micro/nano-galvanic corrosion at the interfaces between GDs and second phases and between GDs and matrices, as well as on the corrosion protection mechanism of Gr coating. This understanding can be gained by combining experimental data with numerical simulation and machine learning techniques to establish an efficient and reliable evaluation method for composition optimization and architectural design, and ultimately to achieve tailored degradation rates. Secondly, assessing the biodegradability of GDs during *in vivo* degradation of GBMMCs and tracking and monitoring the entire degradation process of GDs are required for safe translation of the developed biomaterials into clinical applications. No study has been performed to understand the biodegradation and metabolic processes of GDs during and after BM degradation independently and in the presence of cells or in humans. The consideration of the eventual internalization of GDs will guide the choices of GD sizes and composite powder mixing processes. We believe that with the introduction of the 'degradation by design' concept, the development of new surface functionalization strategies and the use of *in vitro* and *in vivo* models relevant to Gr-containing biomaterials will be the way towards understanding the possible risks of short- and long-term bio-persistence of such materials and to make them safe to use.

5.3.3. Biological properties

The research on the biological properties of GBMMCs is currently at the experimental trial-and-error stage and lacks comprehensive information on the structure and properties of AM GBMMCs. Such information is crucial for understanding the interactions between GDs and BM matrices and between GDs and second phase(s) during the whole degradation process, including synergistic or counteracting effects. This can also help in establishing a comprehensive picture of the effects of morphological characteristics, dimensional characteristics, chemical and physical properties, and interfacial properties of GDs on the biocompatibility of the resulting biomaterials for bone regeneration, which can be used to advance the research towards clinics. To date, essentially all the experiments investigating the effects of GDs on cytocompatibility have been based on pristine, defect-free GDs. However, it is generally accepted that both composite powder mixing and AM processes will have significant effects on the morphology, integrity, and functional groups of Gr, resulting in significant deviations from the morphology and chemical state of pristine Gr. This requires the investigations of the cytotoxicity of promising Gr/BM composite powder mixtures and the scaffolds produced by mainstream AM processes, and necessitates the application of a systematic scientific approach to characterizing the effects of Gr addition.

Gr has excellent electrical conductivity and can be used to conduct electrical signals and promote bone regeneration [60,517,518]. The effects of the GD content as well as the structural characteristics of GD, such as content, defect density, and modification of specific functional groups, on the electrical conductivity of composites have been investigated [519]. In the future, the effects of interfacial interactions between GDs and matrices on the electrical conductivity of the resulting MMCs should be systematically investigated. Furthermore, the influence of the electrical conductivity of GD-containing composites on osteogenic function and bone tissue regeneration behavior should be investigated *in vitro* and *in vivo*. Furthermore, it is necessary to develop more functional BMMCs

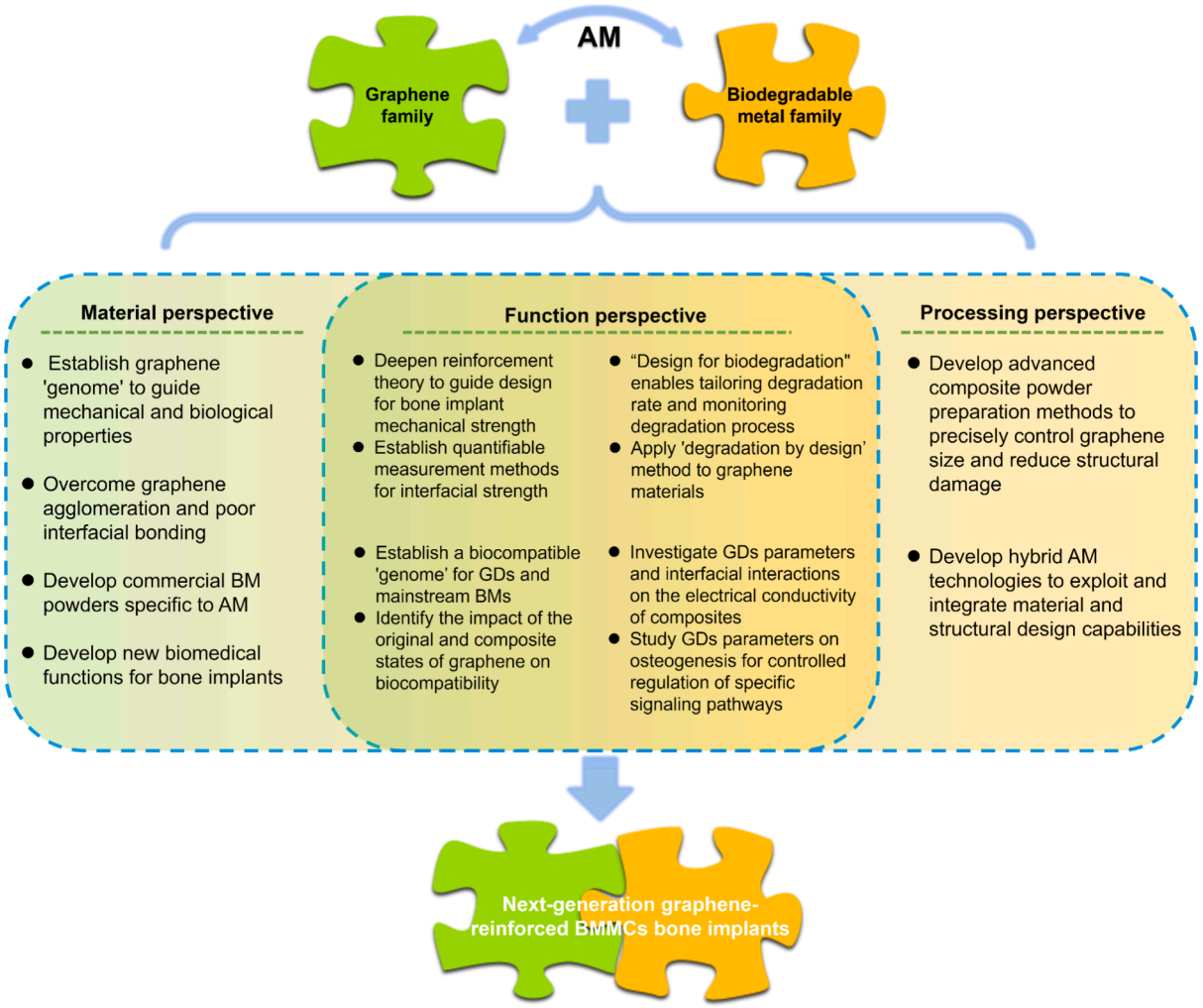

Fig. 22. A systemic illustration of limitations and challenges in the development of the next generation of bone implants based on AM GBMMCs.

containing GDs to convert various external stimuli, such as magnetic and thermal stimuli, into electrical signals, thereby further stimulating the osteogenic behavior of cells. Secondly, some progress has been made in understanding the mechanisms of osteogenesis and immunomodulation induced by GDs [398]. To achieve controlled regulation of specific signaling pathways, it is necessary to further investigate how the addition and structural characteristics of GDs, such as the amount, size, shape, and microstructure, on the one hand and the preparation techniques of BMMCs with different matrices on the other hand affect the mechanisms of biomaterial-induced osteogenesis and immunomodulation.

Overall, achieving safe and effective integration of GDs with BMs for customized bone implants through AM requires overcoming the limitations and challenges posed by the GDs, such as GD agglomeration and interfacial bonding, BM powder characteristics, requirements for new biomedical functions, advanced composite powder preparation techniques, hybrid AM process optimizations, and specific properties including mechanical properties, biodegradation, and osteogenesis (Fig. 22). Future research on AM GBMMCs will need to extend into the multifunctional, multi-scale, multi-material, multi-process, and multi-dimensional design and fabrication approaches. The development of GBMMCs and suitable AM technologies may lead to breakthroughs in functional biomaterials and structures for next-generation bone implants.

6. Conclusion and future prospects

In this review, we have provided a comprehensive assessment of GBMMCs for potential use as bone implants and the associated fabrication processes, especially those based on the newly emerging AM technologies. We have covered the relevant material properties, composite powder preparation, AM processes, and overall performance enhancements and their underlying mechanisms. We have outlined the progress made and the limitations encountered with the conventional methods in comparison with the novel processes for the preparation of GBMMC powders. We have also reviewed the AM techniques suitable for manufacturing porous bone

implants and evaluated their advantages and disadvantages in terms of BM powder processability, BM powder compatibility, printing accuracy, and forming complexity. Moreover, we have analyzed the strengthening mechanisms, compared the mechanical properties of various GBMMCs, the biodegradation promotion or retardation mechanisms of GDs, and summarized the effects of GDs on the osteogenic and antimicrobial properties of GBMMCs. In conclusion, the integration of GDs into BMMCs represents a paradigm shift in the design and fabrication of next-generation bone implants. Through the use of AM techniques, GBMMCs offer unprecedented opportunities to tailor mechanical, degradation and biological properties, addressing the limitations of conventional metallic biomaterials. The incorporation of GDs into BMMCs enhances mechanical performance through mechanisms such as load transfer, grain refinement, and dislocation strengthening. These improvements are achieved without compromising the biodegradability or biocompatibility of the implants, thus enabling a balance between structural integrity and functional performance. GDs play a dual role in modulating degradation rates. While its high electrical conductivity can accelerate micro-galvanic corrosion, its impermeability and barrier effects can stabilize degradation products, offering a pathway to tailor degradation kinetics to match bone regeneration timelines. This dual functionality underscores the potential of GDs to address the challenges of premature mechanical failure or delayed degradation in biodegradable implants. Beyond mechanical reinforcement, GDs can enhance osteogenesis and antibacterial properties. Its unique surface chemistry and electrical conductivity promote cellular adhesion, differentiation, and bone formation, while its unique morphologies and ability to generate ROS provides broad-spectrum antimicrobial activity. These properties position GBMMCs as multifunctional biomaterials capable of supporting tissue regeneration while mitigating infection risks. AM enables the fabrication of complex, patient-specific architectures with precise control over material distribution and porosity. This capability, combined with the versatility of Gr, opens new avenues for designing implants that mimic the hierarchical structure of natural bone, optimizing both mechanical and biological performance. Finally, in this section, we aim to highlight the future prospects of the "material-structure-process-function" AM approach (MSPFI-AM) [520] for the development of the next-generation of bone implants.

6.1. Cross-scale material design

Cross-scale material design for MSPFI-AM requires the controlled incorporation of reinforcing phases into different metal matrices at different locations to form composites that exhibit diverse properties across different length scales in terms of the type, content, morphology, and distribution of reinforcing phase. Nanoscale multiphase distributions with zero to two-dimensional reinforcing phases (*e.g.*, Gr) are the simplest types of multi-scale material distribution at the nanoscale. Among these, introducing zero-dimensional nanoparticles by means of alloying is the most common nanoscale material design strategy. Recent research on *in situ* alloying during AM and boundary engineering strategy (*e.g.*, grain boundary or particle boundary) (Fig. 23A [505]) has yielded remarkable mechanical properties in Zn-Mg-Cu bone implants that are made by adding Mg and Cu elemental powders to Zn powder during laser PBF. This approach results in introducing more grain boundaries and phase boundaries into the matrix because of grain refinement and nanoscale precipitation. Secondly, nanoscale gradient grain structure refers to the materials whose structural grain size varies spatially with gradients, increasing continuously from the nanoscale to microscale (Fig. 23B [521]). The introduction of gradient nanostructures can solve the current problem of incompatibility between the strength and ductility of single biodegradable metals and allows for a wide range of mechanical behaviors. In addition, the gradient nanostructure can effectively inhibit the development of fatigue cracks and improve the fatigue performance of GBMMC bone implants. GBMMCs processed under high uniaxial pressures exhibit a preferential alignment of the reinforcing phase, leading to anisotropic mechanical and functional properties. The control and design of anisotropy may enable the formation of gradient structures that show great promise in terms of improved strength and ductility [521]. Thirdly, the progress in AM has made it possible to design and manufacture porous bone implants with free-form spatial layouts and made from multiple materials (Fig. 23C [522]). For example, it is now possible to combine different types of biodegradable metals, such as pure magnesium with good biocompatibility, pure iron with superior mechanical strength, and pure zinc with a moderate biodegradation rate, or even go beyond pure metals and explore the combinatorial possibilities offered by the more varied properties of their alloys and GBMMCs.

6.2. Customized structural design for AM

The architectural features of the next generation of bone implants are the key to providing temporary structural support in clinical orthopedic treatments and regulating cell functions and tissue formation for the successful repair of bony defects. Customized structural design for AM comprises, among others, topologically optimized structures, *meta*-biomaterial structures, and biomimetic structures, all of which may integrate multiscale levels into the implant design, ranging from material-level design with microstructural complexity to component-level design with macrostructural complexity, and will enable the fabrication of custom-made implants with well-controlled and diverse multiscale architectures and with specific shapes designed to match the bone defect. Topology optimization (TO) is of particular importance for the application of AM in building bone implants. For example, satellite scaffolds were topologically optimized in internal lattice structure to reduce the weight by 17 % (Fig. 23D [533]) and achieve uniform stress distribution and prolonged fatigue life *in vivo*. When designing orthopedic implants, it is desirable to have a continuous transition from a denser microstructure in the central region to a highly porous microstructure at the bone-implant interface. This functional gradation promotes bony ingrowth at the bone-implant interface, while maintaining structural integrity and increasing the mechanical properties in the areas, where bony ingrowth is irrelevant [534]. A challenging aspect in the design of such materials is ensuring mechanical compatibility between adjacent microstructures. The works of Zadpoor et al [535] ensured geometric connectivity between adjacent microstructural unit cells by finding the optimal connectivity between topology-optimized microstructures and finally demonstrated the application in the design of functionally graded materials for implant design, and in the multiscale topology optimization of

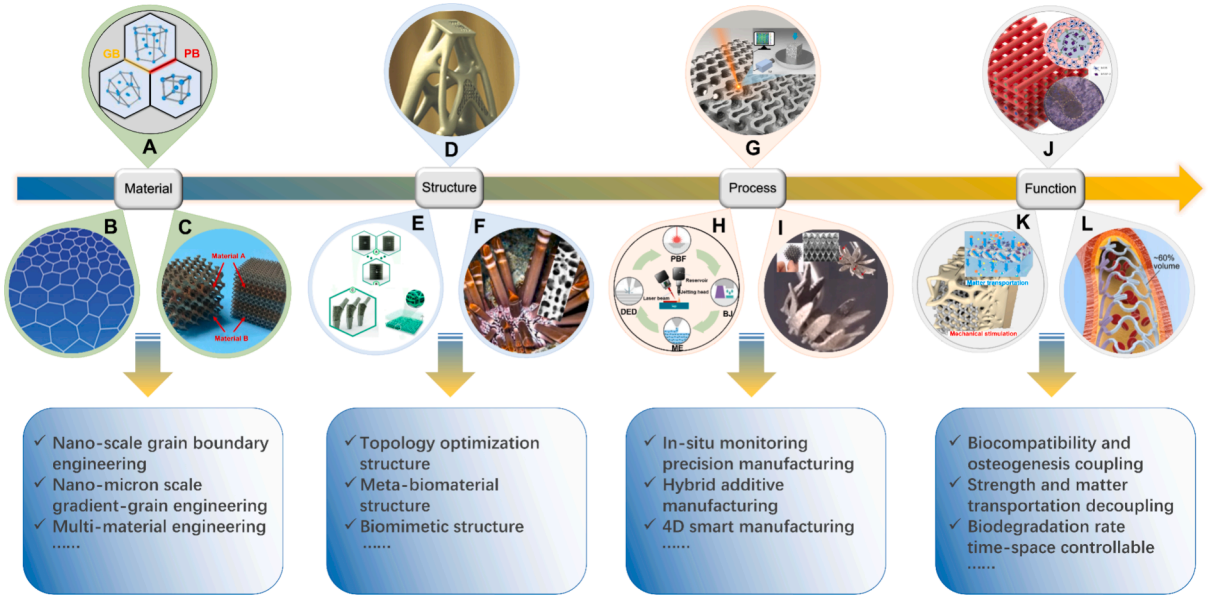

Fig. 23. A systematic illustration of the MSPFI-oriented development trend: (A) A schematic diagram of the nanoscale boundary engineering approach to construct grain boundaries and phase boundaries [505]. (B) A schematic diagram of nano/microscale gradient-grain engineering [521]. (C) A macroscopic millimeter-scale multi-material design approach integrating heterogeneous materials A and B [522]. (D) Topology optimization design of the satellite scaffold created by applying AM [520]. (E) An example diagram of the design of hybrid *meta*-biomaterials containing auxetic and conventional *meta*-biomaterials [523]. (F) A schematic diagram of a gradient porous microstructure inspired by sea urchin ridges [524]. (G) A schematic drawing of the digital image correlation method for *in situ* monitoring of precision manufacturing [525]. (H) Hybrid AM process system integrating PBF, ME, MJ, and BJ into advanced manufacturing of the next generation of bone implants [526,527]. (I) 4D smart manufacturing of biodegradable alloys demonstrating the shape memory effect or superelasticity [528,529,530]. (J) A schematic diagram of the coupled osteogenic and biocompatible properties of a multi-material core–shell structure [531]. (K) A metamaterial structural design decoupling the mechanical and mass transfer properties of bone implants [127]. (L) Surface modification and coating design for time–space controlled biodegradation behavior [532].

structures. Meta-biomaterials with rationally designed structure present unprecedented combinations of mechanical, mass transport, and biological properties favorable for tissue regeneration. Such *meta*-biomaterials are usually topologically ordered and are designed by repeating a number of regular unit cells in different directions to create a lattice structure. Establishing accurate topology-property relationships is of critical importance for these materials. For instance, unlike conventional implants, *meta*-implants designed by hybrid *meta*-biomaterials with rationally distributed values of negative (auxetic) and positive Poisson's ratios (Fig. 23E [523]) did not retract from the bone under biomechanical loading, thereby improving implant–bone contact and potentially implant longevity. To simultaneously minimize the risks of load-induced interface fracture and *peri*-prosthetic bone remodeling due to stress shielding, Garner and Zadpoor *et al.* [536] first developed a novel parametric micro-architecture *meta*-biomaterial with desirable functional attributes and a wide range of effective mechanical properties, including both positive and negative Poisson's ratios. The optimized implant resulted in a performance improvement of 64.0 % in terms of bone remodeling, and 13.2 % in terms of interface fracture risk, compared to a conventional solid implant design. For GBMMC metamaterials, as discussed in Subsection 4.1, the incorporation of Gr is intended to significantly enhance the mechanical properties, such as compressive strength, without compromising the material's mass-transport properties. Furthermore, a novel Gr-inspired metamaterial structure has been reported, demonstrating its unique ability to effectively distribute stress during dynamic loading [537]. Such a stress distribution results in substantial improvements in specific energy absorption (up to 88 % higher energy absorption) and a remarkable increase in compressive strength (an unexpected 609 % enhancement). These findings offer valuable design insights for developing GBMMC metamaterial implants that can withstand more complex stress states. In addition, Gr's 2D network not only acts as a nano-reinforcement to suppress local buckling but also adsorbs osteogenic factors (*e.g.*, BMP-2) *via* surface functional groups (*e.g.*, carboxyl and epoxy), enabling synergistic optimization of mechanical and bioactive properties. GDs are also expected to enable spatially graded designs in metamaterials. For instance, through LPBF with electric field-assisted alignment [271,538], Gr can be locally concentrated within Fe-based graded metamaterials. At the bone-implant interface, where porosity is high, Gr forms conductive networks that enhance osteogenic electrical signaling, as discussed in Subsection 4.3.2. In contrast, in the dense core region, Gr reinforces grain boundaries *via* Fe-O-C bonds, effectively inhibiting the propagation of fatigue cracks. This spatially selective distribution approach allows the metamaterials to achieve both high fatigue resistance and efficient osseointegration simultaneously. Gr's hydrophobicity and chemical inertness typically slow down biodegradation, but its edge defects can serve as catalytic sites, facilitating controlled dissolution. For instance, Zn-based metamaterials can be designed by modifying GO with carboxyl groups, which interact with the Zn matrix to form pH-responsive interfaces [539]. These interfaces accelerate degradation in inflammatory microenvironments (pH 5.5), promoting the release of antibacterial Zn^{2+}, while

maintaining stability under physiological pH (7.4). This dynamic degradation behavior, coupled with topological optimization (*e.g.*, auxetic designs), allows for the spatiotemporal decoupling of antibacterial and osteogenic functions. Biomimetic structure design for AM implies the printing of bioinspired, naturally optimized structures to yield multifunctional bone implants. Examples include the SLMed lightweight sandwich structures and functionally graded TPMS structures with superior strength-to-weight ratios, inspired by the spine of sea urchin consisting of an open-cell porous microstructure (Fig. 23F [524]), which has controlled gradients in porosity along with structural variations.

6.3. Advanced manufacturing of bone implants

With the continuing development of AM, bone implant materials, including biodegradable ones, will evolve into bio-inspired paradigms of heterogeneity and gradients in mechanical properties, functionally graded structures, and hybrid material components, which will have superior mechanical properties and functions as compared to their homogeneous counterparts. Advanced manufacturing of bone implants requires process monitoring and precision manufacturing to create implants with, for example, predetermined strain distributions across the gradient structure, particularly at the cell or sub-cell-scale. Process monitoring in combination with post-AM accurate material characterization and numerical simulation will speed up process optimization based on key features, including defects, residual stresses, geometric deformation, and strain measurements. Digital image correlation (DIC) is increasingly recognized as a powerful tool for measuring the shape, motion, and deformation of lattice structures (Fig. 23G [525]). Secondly, the fabrication of the next generation of bone implants tends to move toward more elaborate components, more complex structures, as well as cost-effective and high-volume production techniques. Current hybrid manufacturing refers to a combination of AM and conventional (*e.g.*, subtractive) manufacturing processes. Future advanced manufacturing of bone implants will consider combining two or more AM process systems (Fig. 23H [526,527]) to create a system with overall enhancements and combined advantages, thereby reducing the disadvantages and drawbacks of individual systems. For example, combining the relatively high accuracy and good surface finish of the PBF process with the rapid deposition rates of DED and the ability to produce larger parts would greatly facilitate the development of advanced bone implants. Implant design and the use of the right AM technology at the right place to achieve perfect compatibility and maximize performance will be the key challenges in hybrid AM of bone implants. Thirdly, 4D smart manufacturing processes are expected to develop into a new research avenue for the future of tissue engineering, incorporating the concept of time as a fourth dimension into 3D (bio)printing technology and promising the potential to reshape the next generation of MSPFI-oriented implant design. 4D smart manufacturing ensures that the shape and/or function of the implant changes over time once triggered through external stimulation. AM Ni-Ti- and Fe-Mn-based shape memory alloys, as typical non-degradable and biodegradable implant materials with shape memory behaviors (Fig. 23I [528,529]), respectively, have been demonstrated. Future research should address how the shape memory effect can be maximized in combination with the design of smart structures while also considering the *in vivo* degradation conditions of the implants in light of physiological and environmental conditions.

6.4. Controllable coupling and decoupling of multiple functionalities

With the unified construction of material-structure-processing maps, the development of the next generation of bone implants, including biodegradable bone implants, will inevitably tend towards multifunctionality and customization. Combining two or more functionalities, such as ultra-fatigue resistance, good *in vivo* osteogenesis, and long-period antibacterial and immunomodulatory properties, would allow designers to develop customized multifunctional bone implants. Multi-scale material design based on nanoscale grain boundary engineering and macroscopic multi-materials, advanced manufacturing concepts based on hybrid AM and 4D smart manufacturing, as well as rational cross-scale structural design and material endowment will all give this concept a strong design foundation. For example, a multi-material core–shell structure based on coaxial extrusion printing reported in the literature (Fig. 23J [531]) enables osteogenic stimulation through precise local control over the delivery of growth factors, while providing the scaffolds with osteogenic properties. Secondly, it is not necessarily straightforward to endow bone-substituting biomaterials with more biological functions so as to improve the clinical outcome associated with their use. One of the reasons for this complication is the inherent coupling between some properties. For example, simultaneously maximizing the mechanical properties and mass transport properties of porous scaffolds is inherently incompatible. Another example is the incompatibility between maximizing osteogenic and antimicrobial properties of bone-substituting biomaterials [540]. In the case of the first example, increasing the mass transport properties of porous scaffolds usually necessitates decreasing their relative density (*i.e.*, increasing their porosity). Increased porosity, in turn, leads to lower mechanical properties. Recently, researchers have proposed multi-material design approaches that could be used to decouple mechanical and mass transport properties of porous scaffolds [541]. As for the second example, most approaches used to maximize bactericidal effects adversely affect the viability of host cells too [542]. Next-generation bone tissue engineering requires bone scaffolds with suitable porosity, mechanical properties, mass transport properties, osteogenic, and antibacterial properties. Therefore, the spatial distributions of materials and the (micro)architectural design of such biomaterials need to be carefully optimized for simultaneously meeting all the abovementioned criteria. Recently, the use of metamaterial structures, such as pentamode structures and diamond configurations to construct micro-lattice metamaterials with decoupled mechanical and mass transport properties, has been reported, allowing the preparation of scaffolds with suitable strength and significant improvements in cell seeding efficiency, permeability, and impact resistance (Fig. 23K [127]). Thirdly, material composition, geometrical design, and the AM processing parameters, all influence the biodegradation rate in a complex and interrelated manner. At the same time, surface modifications and coatings (Fig. 23L [532]) can alter the surface chemistry and metallurgical microstructure of BM-based scaffolds and can be used to improve their biodegradation behavior. Advanced predictive models are, therefore, needed to quantify the complex relationships

between material composition, architectural design, processing parameters, surface coatings on the one hand, and the biodegradation profiles of BMs on the other hand to establish the biodegradation profiles of various biomaterials and to replace the trial-and-error approach currently in use with the ultimate aim of achieving real controllability of biodegradation and cellular behavior in both temporal and spatial dimensions.

In summary, achieving high performance and multifunctionality of 'MPSFI'-oriented next-generation bone implants requires cross-scale coordination of material design, architectural design, and AM process innovations from the nano/micro scale to the macroscopic scale. With GDs strategically placed inside BMs, simultaneous realization of bio-adaptive performances, elaborate structure, and multifunctionality is expected to be within reach.

CRediT authorship contribution statement

Keyu Chen: Writing – original draft, Visualization, Methodology, Investigation, Funding acquisition, Formal analysis, Data curation, Conceptualization. **Jiahui Dong:** Writing – review & editing, Validation, Methodology, Investigation, Formal analysis, Data curation, Conceptualization. **Niko Eka Putra:** Validation, Methodology, Investigation, Formal analysis, Data curation. **Lidy Elena Fratila-Apachitei:** Writing – review & editing, Validation, Methodology, Formal analysis. **Jie Zhou:** Writing – review & editing, Validation, Supervision, Project administration, Methodology, Formal analysis. **Amir A. Zadpoor:** Writing – review & editing, Validation, Supervision, Resources, Project administration, Funding acquisition.

Declaration of competing interest

The authors declare that they have no known competing financial interests or personal relationships that could have appeared to influence the work reported in this paper.

Acknowledgements

K.C. thanks the China Scholarship Council (CSC) for financial support.

Data availability

I have shared the link to my data/code at the Attach File Step

References

[1] Hench LL, Polak JM. Third-generation biomedical materials. Science 2002;295:1014–7. https://doi.org/10.1126/science.1067404.
[2] Petite H, Viateau V, Bensaïd W, Meunier A, de Pollak C, Bourguignon M, et al. Tissue-engineered bone regeneration. Nat Biotechnol 2000;18:959–63. https://doi.org/10.1038/79449.
[3] Chen Q, Thouas GA. Metallic implant biomaterials. Mater Sci Eng R Rep 2015;87:1–57. https://doi.org/10.1016/j.mser.2014.10.001.
[4] Geetha M, Singh AK, Asokamani R, Gogia AK. Ti based biomaterials, the ultimate choice for orthopaedic implants – a review. Prog Mater Sci 2009;54:397–425. https://doi.org/10.1016/j.pmatsci.2008.06.004.
[5] Zheng YF, Gu XN, Witte F. Biodegradable metals. Mater Sci Eng R Rep 2014;77:1–34. https://doi.org/10.1016/j.mser.2014.01.001.
[6] Li C, Guo C, Fitzpatrick V, Ibrahim A, Zwierstra MJ, Hanna P, et al. Design of biodegradable, implantable devices towards clinical translation. Nat Rev Mater 2020;5:61–81. https://doi.org/10.1038/s41578-019-0150-z.
[7] Zhang S, Zhang X, Zhao C, Li J, Song Y, Xie C, et al. Research on an Mg–Zn alloy as a degradable biomaterial. Acta Biomater 2010;6:626–40. https://doi.org/10.1016/j.actbio.2009.06.028.
[8] Staiger MP, Pietak AM, Huadmai J, Dias G. Magnesium and its alloys as orthopedic biomaterials: a review. Biomaterials 2006;27:1728–34. https://doi.org/10.1016/j.biomaterials.2005.10.003.
[9] Yang Y, He C, Dianyu E, Yang W, Qi F, Xie D, et al. Mg bone implant: features, developments and perspectives. Mater Des 2020;185:108259. https://doi.org/10.1016/j.matdes.2019.108259.
[10] Lin W, Qin L, Qi H, Zhang D, Zhang G, Gao R, et al. Long-term in vivo corrosion behavior, biocompatibility and bioresorption mechanism of a bioresorbable nitrided iron scaffold. Acta Biomater 2017;54:454–68. https://doi.org/10.1016/j.actbio.2017.03.020.
[11] Carluccio D, Xu C, Venezuela J, Cao Y, Kent D, Bermingham M, et al. Additively manufactured iron-manganese for biodegradable porous load-bearing bone scaffold applications. Acta Biomater 2020;103:346–60. https://doi.org/10.1016/j.actbio.2019.12.018.
[12] Guo H, Hu J, Shen Z, Du D, Zheng Y, Peng J. In vitro and in vivo studies of biodegradable Zn-Li-Mn alloy staples designed for gastrointestinal anastomosis. Acta Biomater 2021;121:713–23. https://doi.org/10.1016/j.actbio.2020.12.017.
[13] Md Yusop AH, Ulum MF, Al Sakkaf A, Nur H. Current status and outlook of porous Zn-based scaffolds for bone applications: a review. J Bionic Eng 2022;19:737–51. https://doi.org/10.1007/s42235-022-00152-w.
[14] Yang J, Guo JL, Mikos AG, He C, Cheng G. Material processing and design of biodegradable metal matrix composites for biomedical applications. Ann Biomed Eng 2018;46:1229–40. https://doi.org/10.1007/s10439-018-2058-y.
[15] Xu C, Ban M, Zhang H, Liu Q, Ren L. Direct ink writing of porous Fe-HA metal-matrix composites (MMCs) with independently adjustable porosity and degradation rate for bone implant applications. Mater Des 2022;224:111319. https://doi.org/10.1016/j.matdes.2022.111319.
[16] Huang LJ, Geng L, Peng H-X. Microstructurally inhomogeneous composites: Is a homogeneous reinforcement distribution optimal? Prog Mater Sci 2015;71:93–168. https://doi.org/10.1016/j.pmatsci.2015.01.002.
[17] Bakshi SR, Lahiri D, Agarwal A. Carbon nanotube reinforced metal matrix composites - a review. Int Mater Rev 2010;55:41–64. https://doi.org/10.1179/095066009X12572530170543.
[18] Ouyang S, Liu Y, Huang Q, Gan Z, Tang H. Effect of composition on in vitro degradability of Ti–Mg metal-metal composites. Mater Sci Eng C 2020;107:110327. https://doi.org/10.1016/j.msec.2019.110327.
[19] Wu S, Liu X, Yeung KWK, Liu C, Yang X. Biomimetic porous scaffolds for bone tissue engineering. Mater Sci Eng R Rep 2014;80:1–36. https://doi.org/10.1016/j.mser.2014.04.001.

[20] Novoselov KS, Geim AK, Morozov SV, Jiang D, Katsnelson MI, Grigorieva IV, et al. Two-dimensional gas of massless Dirac fermions in graphene. Nature 2005; 438:197–200. https://doi.org/10.1038/nature04233.
[21] Geim AK, Novoselov KS. The rise of graphene. Nat Mater 2007;6:183–91. https://doi.org/10.1038/nmat1849.
[22] Banerjee AN. Graphene and its derivatives as biomedical materials: future prospects and challenges. Interface Focus 2018;8:20170056. https://doi.org/10.1098/rsfs.2017.0056.
[23] Stankovich S, Dikin DA, Dommett GHB, Kohlhaas KM, Zimney EJ, Stach EA, et al. Graphene-based composite materials. Nature 2006;442:282–6. https://doi.org/10.1038/nature04969.
[24] Lee C, Wei X, Kysar JW, Hone J. Measurement of the elastic properties and intrinsic strength of monolayer graphene. Science 2008;321:385–8. https://doi.org/10.1126/science.1157996.
[25] Geim AK. Graphene: status and prospects. Science 2009;324:1530–4. https://doi.org/10.1126/science.1158877.
[26] Tjong SC. Recent progress in the development and properties of novel metal matrix nanocomposites reinforced with carbon nanotubes and graphene nanosheets. Mater Sci Eng R Rep 2013;74:281–350. https://doi.org/10.1016/j.mser.2013.08.001.
[27] Kulyk B, Freitas MA, Santos NF, Mohseni F, Carvalho AF, Yasakau K, et al. A critical review on the production and application of graphene and graphene-based materials in anti-corrosion coatings. Crit Rev Solid State Mater Sci 2022;47:309–55. https://doi.org/10.1080/10408436.2021.1886046.
[28] Hu Z, Tong G, Lin D, Chen C, Guo H, Xu J, et al. Graphene-reinforced metal matrix nanocomposites – a review. Mater Sci Technol 2016;32:930–53. https://doi.org/10.1080/02670836.2015.1104018.
[29] Kalpana Devi P, Singh KK. Enhancement of electronic and optical characteristics of graphene by doping with transition metals – DFT method. Phys B Condens Matter 2023;669:415309. https://doi.org/10.1016/j.physb.2023.415309.
[30] Wang L, Jin J, Cao J, Yang P, Peng Q. Interaction of edge dislocations with graphene nanosheets in graphene/Fe composites. Crystals 2018;8:160. https://doi.org/10.3390/cryst8040160.
[31] Dai Q, Peng S, Zhang Z, Liu Y, Fan M, Zhao F. Microstructure and mechanical properties of zinc matrix biodegradable composites reinforced by graphene. Front Bioeng Biotechnol 2021;9.
[32] Shahin M, Wen C, Munir K, Li Y. Mechanical and corrosion properties of graphene nanoplatelet–reinforced Mg–Zr and Mg–Zr–Zn matrix nanocomposites for biomedical applications. J Magnesium Alloys 2022;10:458–77. https://doi.org/10.1016/j.jma.2021.05.011.
[33] Munir K, Wen C, Li Y. Graphene nanoplatelets-reinforced magnesium metal matrix nanocomposites with superior mechanical and corrosion performance for biomedical applications. J Magnesium Alloys 2020;8:269–90. https://doi.org/10.1016/j.jma.2019.12.002.
[34] Zhao Y, Liu Y, Kang S, Sun D, Liu Y, Wang X, et al. Peripheral nerve injury repair by electrical stimulation combined with graphene-based scaffolds. Front Bioeng Biotechnol 2024;12. https://doi.org/10.3389/fbioe.2024.1345163.
[35] Lu J, Cheng C, He Y-S, Lyu C, Wang Y, Yu J, et al. Multilayered graphene hydrogel membranes for guided bone regeneration. Adv Mater 2016;28:4025–31. https://doi.org/10.1002/adma.201505375.
[36] Ye R, James DK, Tour JM. Laser-induced graphene: from discovery to translation. Adv Mater 2019;31:1803621. https://doi.org/10.1002/adma.201803621.
[37] Zhang X, Hu W, Li J, Tao L, Wei Y. A comparative study of cellular uptake and cytotoxicity of multi-walled carbon nanotubes, graphene oxide, and nanodiamond. Toxicol Res 2012;1:62–8. https://doi.org/10.1039/c2tx20006f.
[38] Bianco A. Graphene: safe or toxic? The two faces of the medal. Angew Chem Int Ed 2013;52:4986–97. https://doi.org/10.1002/anie.201209099.
[39] Jakus AE, Secor EB, Rutz AL, Jordan SW, Hersam MC, Shah RN. Three-dimensional printing of high-content graphene scaffolds for electronic and biomedical applications. ACS Nano 2015;9:4636–48. https://doi.org/10.1021/acsnano.5b01179.
[40] Yang K, Li Y, Tan X, Peng R, Liu Z. Behavior and Toxicity of Graphene and Its Functionalized Derivatives in Biological Systems. Small 2013;9:1492–503. https://doi.org/10.1002/smll.201201417.
[41] Liu Z, Robinson JT, Sun X, Dai H. PEGylated nanographene oxide for delivery of water-insoluble cancer drugs. J Am Chem Soc 2008;130:10876–7. https://doi.org/10.1021/ja803688x.
[42] Park S, Mohanty N, Suk JW, Nagaraja A, An J, Piner RD, et al. Biocompatible, Robust Free-Standing Paper Composed of a TWEEN/Graphene Composite. Adv Mater 2010;22:1736–40. https://doi.org/10.1002/adma.200903611.
[43] Girish CM, Sasidharan A, Gowd GS, Nair S, Koyakutty M. Confocal Raman imaging study showing macrophage mediated biodegradation of graphene in vivo. Adv Healthc Mater 2013;2:1489–500. https://doi.org/10.1002/adhm.201200489.
[44] Li Y, Feng L, Shi X, Wang X, Yang Y, Yang K, et al. Surface coating-dependent cytotoxicity and degradation of graphene derivatives: towards the design of non-toxic. Degradable Nano-Graphene Small 2014;10:1544–54. https://doi.org/10.1002/smll.201303234.
[45] Dinescu S, Ionita M, Ignat S-R, Costache M, Hermenean A. Graphene Oxide Enhances Chitosan-Based 3D Scaffold Properties for Bone Tissue Engineering. Int J Mol Sci 2019;20:5077. https://doi.org/10.3390/ijms20205077.
[46] Murphy SV, Atala A. 3D bioprinting of tissues and organs. Nat Biotechnol 2014;32:773–85. https://doi.org/10.1038/nbt.2958.
[47] Chen P, Wang H, Su J, Tian Y, Wen S, Su B, et al. Recent Advances on High-Performance Polyaryletherketone Materials for Additive Manufacturing. Advanced Materials n.d.;n/a:2200750. DOI: 10.1002/adma.202200750.
[48] Han C, Fang Q, Shi Y, Tor SB, Chua CK, Zhou K. Recent Advances on High-Entropy Alloys for 3D Printing. Adv Mater 2020;32:1903855. https://doi.org/10.1002/adma.201903855.
[49] Ngo TD, Kashani A, Imbalzano G, Nguyen KTQ, Hui D. Additive manufacturing (3D printing): A review of materials, methods, applications and challenges. Compos B Eng 2018;143:172–96. https://doi.org/10.1016/j.compositesb.2018.02.012.
[50] Kumar A, Mandal S, Barui S, Vasireddi R, Gbureck U, Gelinsky M, et al. Low temperature additive manufacturing of three dimensional scaffolds for bone-tissue engineering applications: Processing related challenges and property assessment. Mater Sci Eng R Rep 2016;103:1–39. https://doi.org/10.1016/j.mser.2016.01.001.
[51] Yuan L, Ding S, Wen C. Additive manufacturing technology for porous metal implant applications and triple minimal surface structures: A review. Bioact Mater 2019;4:56–70. https://doi.org/10.1016/j.bioactmat.2018.12.003.
[52] Wang X, Xu S, Zhou S, Xu W, Leary M, Choong P, et al. Topological design and additive manufacturing of porous metals for bone scaffolds and orthopaedic implants: A review. Biomaterials 2016;83:127–41. https://doi.org/10.1016/j.biomaterials.2016.01.012.
[53] Li Y, Jahr H, Lietaert K, Pavanram P, Yilmaz A, Fockaert LI, et al. Additively manufactured biodegradable porous iron. Acta Biomater 2018;77:380–93. https://doi.org/10.1016/j.actbio.2018.07.011.
[54] Nieto A, Bisht A, Lahiri D, Zhang C, Agarwal A. Graphene reinforced metal and ceramic matrix composites: a review. Int Mater Rev 2017;62:241–302. https://doi.org/10.1080/09506608.2016.1219481.
[55] Fattah-alhosseini A, Molaei M, Nouri M, Babaei K. Review of the role of graphene and its derivatives in enhancing the performance of plasma electrolytic oxidation coatings on titanium and its alloys. Appl Surf Sci Adv 2021;6:100140. https://doi.org/10.1016/j.apsadv.2021.100140.
[56] Radhamani AV, Lau HC, Ramakrishna S. CNT-reinforced metal and steel nanocomposites: A comprehensive assessment of progress and future directions. Compos A Appl Sci Manuf 2018;114:170–87. https://doi.org/10.1016/j.compositesa.2018.08.010.
[57] Porwal H, Grasso S, Reece MJ. Review of graphene–ceramic matrix composites. Adv Appl Ceram 2013;112:443–54. https://doi.org/10.1179/174367613X13764308970581.
[58] Nezakati T, Seifalian A, Tan A, Seifalian AM. Conductive Polymers: Opportunities and Challenges in Biomedical Applications. Chem Rev 2018;118:6766–843. https://doi.org/10.1021/acs.chemrev.6b00275.
[59] Yang Y, Cheng Y, Peng S, Xu L, He C, Qi F, et al. Microstructure evolution and texture tailoring of reduced graphene oxide reinforced Zn scaffold. Bioact Mater 2021;6:1230–41. https://doi.org/10.1016/j.bioactmat.2020.10.017.
[60] Li Y, Yang L, Hou Y, Zhang Z, Chen M, Wang M, et al. Polydopamine-mediated graphene oxide and nanohydroxyapatite-incorporated conductive scaffold with an immunomodulatory ability accelerates periodontal bone regeneration in diabetes. Bioact Mater 2022;18:213–27. https://doi.org/10.1016/j.bioactmat.2022.03.021.

[61] Nurrohman DT, Chiu N-F. A Review of Graphene-Based Surface Plasmon Resonance and Surface-Enhanced Raman Scattering Biosensors: Current Status and Future Prospects. Nanomaterials 2021;11:216. https://doi.org/10.3390/nano11010216.
[62] Putra NE, Leeflang MA, Minneboo M, Taheri P, Fratila-Apachitei LE, Mol JMC, et al. Extrusion-based 3D printed biodegradable porous iron. Acta Biomater 2021;121:741–56. https://doi.org/10.1016/j.actbio.2020.11.022.
[63] Yuan B, Chen H, Zhao R, Deng X, Chen G, Yang X, et al. Construction of a magnesium hydroxide/graphene oxide/hydroxyapatite composite coating on Mg–Ca–Zn–Ag alloy to inhibit bacterial infection and promote bone regeneration. Bioact Mater 2022;18:354–67. https://doi.org/10.1016/j.bioactmat.2022.02.030.
[64] Yu M, Cai Z, Gu Y, Ma Y, Song G, Wen C. Effect of Processing Techniques on Interface Bonding of Graphene Reinforced Metal Matrix Composites: A Review. JOM 2023;75:488–505. https://doi.org/10.1007/s11837-022-05625-1.
[65] Yoo SC, Lee D, Ryu SW, Kang B, Ryu HJ, Hong SH. Recent progress in low-dimensional nanomaterials filled multifunctional metal matrix nanocomposites. Prog Mater Sci 2023;132:101034. https://doi.org/10.1016/j.pmatsci.2022.101034.
[66] Asgharzadeh H, Sedigh M. Synthesis and mechanical properties of Al matrix composites reinforced with few-layer graphene and graphene oxide. J Alloy Compd 2017;728:47–62. https://doi.org/10.1016/j.jallcom.2017.08.268.
[67] Bastwros M, Kim G-Y, Zhu C, Zhang K, Wang S, Tang X, et al. Effect of ball milling on graphene reinforced Al6061 composite fabricated by semi-solid sintering. Compos B Eng 2014;60:111–8. https://doi.org/10.1016/j.compositesb.2013.12.043.
[68] Buzaglo M, Bar IP, Varenik M, Shunak L, Pevzner S, Regev O. Graphite-to-Graphene: Total Conversion. Adv Mater 2017;29:1603528. https://doi.org/10.1002/adma.201603528.
[69] Servant A, Leon V, Jasim D, Methven L, Limousin P, Fernandez-Pacheco EV, et al. Graphene-Based Electroresponsive Scaffolds as Polymeric Implants for On-Demand Drug Delivery. Adv Healthc Mater 2014;3:1334–43. https://doi.org/10.1002/adhm.201400016.
[70] Jing J, Chen L, Li Z, Guo Q, Feng S, Hou H, et al. Interfacial bonding mechanism of graphene nanoplatelets reinforced AZ91D magnesium alloy prepared by semi-solid injection molding. J Alloy Compd 2024;1006:176171. https://doi.org/10.1016/j.jallcom.2024.176171.
[71] Kabir H, Munir K, Wen C, Li Y. Microstructures, mechanical and corrosion properties of graphene nanoplatelet–reinforced zinc matrix composites for implant applications. Acta Biomater 2023;157:701–19. https://doi.org/10.1016/j.actbio.2022.11.060.
[72] Zhang W, Zhou S, Ren W, Yang Y, Shi L, Zhou Q, et al. Uniformly dispersing GNPs for fabricating graphene-reinforced pure Ti matrix composites with enhanced strength and ductility. J Alloy Compd 2021;888:161527. https://doi.org/10.1016/j.jallcom.2021.161527.
[73] Jiang Y, Tan Z, Xu R, Fan G, Xiong D-B, Guo Q, et al. Tailoring the structure and mechanical properties of graphene nanosheet/aluminum composites by flake powder metallurgy via shift-speed ball milling. Compos A Appl Sci Manuf 2018;111:73–82. https://doi.org/10.1016/j.compositesa.2018.05.022.
[74] Kwon H, Mondal J, AlOgab KA, Sammelselg V, Takamichi M, Kawaski A, et al. Graphene oxide-reinforced aluminum alloy matrix composite materials fabricated by powder metallurgy. J Alloy Compd 2017;698:807–13. https://doi.org/10.1016/j.jallcom.2016.12.179.
[75] Jinlong L, Wang Z, Miura H. The effects of ball milling on microstructures of graphene/Ni composites and their catalytic activity for hydrogen evolution reaction. Mater Lett 2017;206:124–7. https://doi.org/10.1016/j.matlet.2017.07.001.
[76] Liu G, Zhao N, Shi C, Liu E, He F, Ma L, et al. In-situ synthesis of graphene decorated with nickel nanoparticles for fabricating reinforced 6061Al matrix composites. Mater Sci Eng A 2017;699:185–93. https://doi.org/10.1016/j.msea.2017.05.084.
[77] Yan SJ, Dai SL, Zhang XY, Yang C, Hong QH, Chen JZ, et al. Investigating aluminum alloy reinforced by graphene nanoflakes. Mater Sci Eng A 2014;612:440–4. https://doi.org/10.1016/j.msea.2014.06.077.
[78] Ghodrati H, Ghomashchi R. Effect of graphene dispersion and interfacial bonding on the mechanical properties of metal matrix composites: An overview. FlatChem 2019;16:100113. https://doi.org/10.1016/j.flatc.2019.100113.
[79] Zhao Z, Bai P, Du W, Liu B, Pan D, Das R, et al. An overview of graphene and its derivatives reinforced metal matrix composites: Preparation, properties and applications. Carbon 2020;170:302–26. https://doi.org/10.1016/j.carbon.2020.08.040.
[80] Guo H, Lv R, Bai S. Recent advances on 3D printing graphene-based composites. Nano Mater Sci 2019;1:101–15. https://doi.org/10.1016/j.nanoms.2019.03.003.
[81] Zhang S, Wang H, Liu J, Bao C. Measuring the specific surface area of monolayer graphene oxide in water. Mater Lett 2020;261:127098. https://doi.org/10.1016/j.matlet.2019.127098.
[82] Zhao S, Zhang Y, Yang J, Kitipornchai S. Significantly improved interfacial shear strength in graphene/copper nanocomposite via wrinkles and functionalization: A molecular dynamics study. Carbon 2021;174:335–44. https://doi.org/10.1016/j.carbon.2020.12.026.
[83] Zheng Z, Zhang X, Li J, Geng L. High-content graphene nanoplatelet reinforced aluminum composites produced by ball milling and hot extrusion. Sci China Technol Sci 2020;63:1426–35. https://doi.org/10.1007/s11431-020-1670-4.
[84] Patil A, Kiran Kumar Yadav Nartu MS, Ozdemir F, Banerjee R, Gupta RK, Borkar T. Enhancement of the mechanical properties of graphene nanoplatelet (GNP) reinforced nickel matrix nanocomposites. Materials Science and Engineering: A 2021;817:141324. DOI: 10.1016/j.msea.2021.141324.
[85] Prashantha Kumar HG, Anthony XM. Encapsulation and microwave hybrid processing of Al 6061–Graphene–SiC composites. Mater Manuf Process 2018;33:19–25. https://doi.org/10.1080/10426914.2017.1279320.
[86] Varol T, Canakci A. Microstructure, electrical conductivity and hardness of multilayer graphene/Copper nanocomposites synthesized by flake powder metallurgy. Met Mater Int 2015;21:704–12. https://doi.org/10.1007/s12540-015-5058-6.
[87] Kurapova OY, Lomakin IV, Sergeev SN, Solovyeva EN, Zhilyaev AP, Archakov IY, et al. Fabrication of nickel-graphene composites with superior hardness. J Alloy Compd 2020;835:155463. https://doi.org/10.1016/j.jallcom.2020.155463.
[88] Zhang D, Zhan Z. Strengthening effect of graphene derivatives in copper matrix composites. J Alloy Compd 2016;654:226–33. https://doi.org/10.1016/j.jallcom.2015.09.013.
[89] Hwang J, Yoon T, Jin SH, Lee J, Kim T-S, Hong SH, et al. Enhanced Mechanical Properties of Graphene/Copper Nanocomposites Using a Molecular-Level Mixing Process. Adv Mater 2013;25:6724–9. https://doi.org/10.1002/adma.201302495.
[90] Carvalho AF, Kulyk B, Fernandes AJS, Fortunato E, Costa FM. A Review on the Applications of Graphene in Mechanical Transduction. Adv Mater 2022;34:2101326. https://doi.org/10.1002/adma.202101326.
[91] Li W, Li M, Liu J, Yang Y, Wen S, Wei Q, et al. Microstructure control and compressive properties of selective laser melted Ti-43.5Al-6.5Nb-2Cr-0.5B alloy: Influence of reduced graphene oxide (RGO) reinforcement. Mater Sci Eng A 2019;743:217–22. https://doi.org/10.1016/j.msea.2018.08.087.
[92] Wen S, Chen K, Li W, Zhou Y, Wei Q, Shi Y. Selective laser melting of reduced graphene oxide/S136 metal matrix composites with tailored microstructures and mechanical properties. Mater Des 2019;175:107811. https://doi.org/10.1016/j.matdes.2019.107811.
[93] Wang L, Chen T, Pu P. Mixing of graphene nanoplatelets with magnesium alloy powders by electrostatic adsorption. Mater Res Express 2020;7:036524. https://doi.org/10.1088/2053-1591/ab7e48.
[94] Li X, Shi H, Wang X, Hu X, Xu C, Shao W. Direct synthesis and modification of graphene in Mg melt by converting CO2: A novel route to achieve high strength and stiffness in graphene/Mg composites. Carbon 2022;186:632–43. https://doi.org/10.1016/j.carbon.2021.10.017.
[95] Chu K, Wang X, Li Y, Huang D, Geng Z, Zhao X, et al. Thermal properties of graphene/metal composites with aligned graphene. Mater Des 2018;140:85–94. https://doi.org/10.1016/j.matdes.2017.11.048.
[96] Yang Y, Cheng Y, Yang M, Qian G, Peng S, Qi F, et al. Semicoherent strengthens graphene/zinc scaffolds. Mater Today Nano 2022;17:100163. https://doi.org/10.1016/j.mtnano.2021.100163.
[97] Wu X, Du X, Wang Z, Li S, Liu K, Du W. Surface etched graphene nanoplatelets and their heterogeneous interface to reinforce magnesium alloys for high strength and ductility. Mater Sci Eng A 2024;913:147080. https://doi.org/10.1016/j.msea.2024.147080.
[98] Zhang X, Liu Y, Liu X, Zhang J, Chen X, Wu Y, et al. In-situ grown few-layer graphene reinforced Ni matrix composites with simultaneously enhanced strength and ductility. Mater Sci Eng A 2021;828:142118. https://doi.org/10.1016/j.msea.2021.142118.
[99] Wang M, Zhao Y, Wang L-D, Zhu Y-P, Wang X-J, Sheng J, et al. Achieving high strength and ductility in graphene/magnesium composite via an in-situ reaction wetting process. Carbon 2018;139:954–63. https://doi.org/10.1016/j.carbon.2018.08.009.

[100] Zhang X, Zhao N, He C. The superior mechanical and physical properties of nanocarbon reinforced bulk composites achieved by architecture design – A review. Prog Mater Sci 2020;113:100672. https://doi.org/10.1016/j.pmatsci.2020.100672.
[101] Zhao C, Zhang P, Zhou J, Qi S, Yamauchi Y, Shi R, et al. Layered nanocomposites by shear-flow-induced alignment of nanosheets. Nature 2020;580:210–5. https://doi.org/10.1038/s41586-020-2161-8.
[102] Chu K, Wang F, Wang X, Huang D. Anisotropic mechanical properties of graphene/copper composites with aligned graphene. Mater Sci Eng A 2018;713:269–77. https://doi.org/10.1016/j.msea.2017.12.080.
[103] Yun K, Zhou J, Zhao C, Jiang X, Qi L. Graphene reinforced magnesium metal matrix composites by infiltrating coated-graphene preform with melt. J Mater Process Technol 2024;334:118639. https://doi.org/10.1016/j.jmatprotec.2024.118639.
[104] Chu K, Jia C, Guo H, Li W. On the thermal conductivity of Cu–Zr/diamond composites. Mater Des 2013;45:36–42. https://doi.org/10.1016/j.matdes.2012.09.006.
[105] Chu K, Jia C, Li W. Thermal conductivity enhancement in carbon nanotube/Cu–Ti composites. Appl Phys A 2013;110:269–73. https://doi.org/10.1007/s00339-012-7450-0.
[106] Chu K, Wang F, Wang X, Li Y, Geng Z, Huang D, et al. Interface design of graphene/copper composites by matrix alloying with titanium. Mater Des 2018;144:290–303. https://doi.org/10.1016/j.matdes.2018.02.038.
[107] Chu K, Wang F, Li Y, Wang X, Huang D, Zhang H. Interface structure and strengthening behavior of graphene/CuCr composites. Carbon 2018;133:127–39. https://doi.org/10.1016/j.carbon.2018.03.018.
[108] Bose S, Ke D, Sahasrabudhe H, Bandyopadhyay A. Additive manufacturing of biomaterials. Prog Mater Sci 2018;93:45–111. https://doi.org/10.1016/j.pmatsci.2017.08.003.
[109] Carter LN, Essa K, Attallah MM. Optimisation of selective laser melting for a high temperature Ni-superalloy. Rapid Prototyp J 2015;21:423–32. https://doi.org/10.1108/RPJ-06-2013-0063.
[110] Read N, Wang W, Essa K, Attallah MM. Selective laser melting of AlSi10Mg alloy: Process optimisation and mechanical properties development. Materials & Design (1980-2015) 2015;65:417–24. DOI: 10.1016/j.matdes.2014.09.044.
[111] Chen C, Hao Y, Bai X, Ni J, Chung S-M, Liu F, et al. 3D printed porous Ti6Al4V cage: Effects of additive angle on surface properties and biocompatibility; bone ingrowth in Beagle tibia model. Mater Des 2019;175:107824. https://doi.org/10.1016/j.matdes.2019.107824.
[112] Stašić J, Božić D. The effect of NiB additive on surface morphology and microstructure of 316L stainless steel single tracks and layers obtained by SLM. Surf Coat Technol 2016;307:407–17. https://doi.org/10.1016/j.surfcoat.2016.09.019.
[113] Ren DC, Zhang HB, Liu YJ, Li SJ, Jin W, Yang R, et al. Microstructure and properties of equiatomic Ti–Ni alloy fabricated by selective laser melting. Mater Sci Eng A 2020;771:138586. https://doi.org/10.1016/j.msea.2019.138586.
[114] Ng CC, Savalani MM, Lau ML, Man HC. Microstructure and mechanical properties of selective laser melted magnesium. Appl Surf Sci 2011;257:7447–54. https://doi.org/10.1016/j.apsusc.2011.03.004.
[115] Montani M, Demir AG, Mostaed E, Vedani M, Previtali B. Processability of pure Zn and pure Fe by SLM for biodegradable metallic implant manufacturing. Rapid Prototyp J 2017;23:514–23. https://doi.org/10.1108/RPJ-08-2015-0100.
[116] Mu XN, Zhang HM, Cai HN, Fan QB, Zhang ZH, Wu Y, et al. Microstructure evolution and superior tensile properties of low content graphene nanoplatelets reinforced pure Ti matrix composites. Mater Sci Eng A 2017;687:164–74. https://doi.org/10.1016/j.msea.2017.01.072.
[117] Zhao D, Liang H, Han C, Li J, Liu J, Zhou K, et al. 3D printing of a titanium-tantalum Gyroid scaffold with superb elastic admissible strain, bioactivity and in-situ bone regeneration capability. Addit Manuf 2021;47:102223. https://doi.org/10.1016/j.addma.2021.102223.
[118] An J, Teoh JEM, Suntornnond R, Chua CK. Design and 3D Printing of Scaffolds and Tissues. Engineering 2015;1:261–8. https://doi.org/10.15302/J-ENG-2015061.
[119] Kim S-J, Kim M-G, Kim J, Jeon JS, Park J, Yi H-G. Bioprinting Methods for Fabricating In Vitro Tubular Blood Vessel Models. Cyborg Bionic Syst 2023;4. https://doi.org/10.34133/cbsystems.0043.
[120] Hedayati R, Leeflang AM, Zadpoor AA. Additively manufactured metallic pentamode meta-materials. Appl Phys Lett 2017;110:091905. https://doi.org/10.1063/1.4977561.
[121] Zhang L, Song B, Liu R, Zhao A, Zhang J, Zhuo L, et al. Effects of Structural Parameters on the Poisson's Ratio and Compressive Modulus of 2D Pentamode Structures Fabricated by Selective Laser Melting. Engineering 2020;6:56–67. https://doi.org/10.1016/j.eng.2019.06.009.
[122] Yang L, Yan C, Cao W, Liu Z, Song B, Wen S, et al. Compression–compression fatigue behaviour of gyroid-type triply periodic minimal surface porous structures fabricated by selective laser melting. Acta Mater 2019;181:49–66. https://doi.org/10.1016/j.actamat.2019.09.042.
[123] Gómez S, Vlad MD, López J, Fernández E. Design and properties of 3D scaffolds for bone tissue engineering. Acta Biomater 2016;42:341–50. https://doi.org/10.1016/j.actbio.2016.06.032.
[124] Yu X, Zhou J, Liang H, Jiang Z, Wu L. Mechanical metamaterials associated with stiffness, rigidity and compressibility: A brief review. Prog Mater Sci 2018;94:114–73. https://doi.org/10.1016/j.pmatsci.2017.12.003.
[125] Zhang M, Yu Q, Liu Z, Zhang J, Tan G, Jiao D, et al. 3D printed Mg-NiTi interpenetrating-phase composites with high strength, damping capacity, and energy absorption efficiency. Sci Adv 2020;6:eaba5581. https://doi.org/10.1126/sciadv.aba5581.
[126] Zhang L, Wang B, Song B, Yao Y, Choi S-K, Yang C, et al. 3D Printed Biomimetic Metamaterials with Graded Porosity and Tapering Topology for Improved Cell Seeding and Bone Regeneration. Bioact Mater 2023;25:677–88. https://doi.org/10.1016/j.bioactmat.2022.07.009.
[127] Zhang L, Song B, Zhang J, Yao Y, Lu J, Shi Y. Decoupling microlattice metamaterial properties through a structural design strategy inspired by the Hall–Petch relation. Acta Mater 2022;238:118214. https://doi.org/10.1016/j.actamat.2022.118214.
[128] Badoniya P, Srivastava M, Jain PK, Rathee S. A state-of-the-art review on metal additive manufacturing: milestones, trends, challenges and perspectives. J Braz Soc Mech Sci Eng 2024;46:339. https://doi.org/10.1007/s40430-024-04917-8.
[129] Kanishka K, Acherjee B. Revolutionizing manufacturing: A comprehensive overview of additive manufacturing processes, materials, developments, and challenges. J Manuf Process 2023;107:574–619. https://doi.org/10.1016/j.jmapro.2023.10.024.
[130] Toprak CB, Dogruer CU. A Critical Review of Machine Learning Methods Used in Metal Powder Bed Fusion Process to Predict Part Properties. Int J Precis Eng Manuf 2024;25:429–52. https://doi.org/10.1007/s12541-023-00905-5.
[131] Chen L, Bi G, Yao X, Su J, Tan C, Feng W, et al. In-situ process monitoring and adaptive quality enhancement in laser additive manufacturing: A critical review. J Manuf Syst 2024;74:527–74. https://doi.org/10.1016/j.jmsy.2024.04.013.
[132] Lewis JA. Direct Ink Writing of 3D Functional Materials. Adv Funct Mater 2006;16:2193–204. https://doi.org/10.1002/adfm.200600434.
[133] Lee H. Engineering In vitro Models: Bioprinting of Organoids with Artificial Intelligence. Cyborg Bionic Syst 2023;4:0018. https://doi.org/10.34133/cbsystems.0018.
[134] Dong J, Li Y, Lin P, Leeflang MA, van Asperen S, Yu K, et al. Solvent-cast 3D printing of magnesium scaffolds. Acta Biomater 2020;114:497–514. https://doi.org/10.1016/j.actbio.2020.08.002.
[135] Dong J, Tümer N, Leeflang MA, Taheri P, Fratila-Apachitei LE, Mol JMC, et al. Extrusion-based additive manufacturing of Mg-Zn alloy scaffolds. J Magnesium Alloys 2022;10:2491–509. https://doi.org/10.1016/j.jma.2021.11.018.
[136] Putra NE, Leeflang MA, Taheri P, Fratila-Apachitei LE, Mol JMC, Zhou J, et al. Extrusion-based 3D printing of ex situ-alloyed highly biodegradable MRI-friendly porous iron-manganese scaffolds. Acta Biomater 2021;134:774–90. https://doi.org/10.1016/j.actbio.2021.07.042.
[137] Dong J, Lin P, Putra NE, Tümer N, Leeflang MA, Huan Z, et al. Extrusion-based additive manufacturing of Mg-Zn/bioceramic composite scaffolds. Acta Biomater 2022;151:628–46. https://doi.org/10.1016/j.actbio.2022.08.002.
[138] Dong J, Tümer N, Putra NE, Zhu J, Li Y, Leeflang MA, et al. Extrusion-based 3D printed magnesium scaffolds with multifunctional MgF2 and MgF2–CaP coatings. Biomater Sci 2021;9:7159–82. https://doi.org/10.1039/D1BM01238J.
[139] Kang H-W, Lee SJ, Ko IK, Kengla C, Yoo JJ, Atala A. A 3D bioprinting system to produce human-scale tissue constructs with structural integrity. Nat Biotechnol 2016;34:312–9. https://doi.org/10.1038/nbt.3413.

[140] Liu J, Li L, Suo H, Yan M, Yin J, Fu J. 3D printing of biomimetic multi-layered GelMA/nHA scaffold for osteochondral defect repair. Mater Des 2019;171:107708. https://doi.org/10.1016/j.matdes.2019.107708.
[141] Liu W, Zhang YS, Heinrich MA, De Ferrari F, Jang HL, Bakht SM, et al. Rapid Continuous Multimaterial Extrusion Bioprinting. Adv Mater 2017;29:1604630. https://doi.org/10.1002/adma.201604630.
[142] Ma H, Li T, Huan Z, Zhang M, Yang Z, Wang J, et al. 3D printing of high-strength bioscaffolds for the synergistic treatment of bone cancer. NPG Asia Mater 2018;10:31–44. https://doi.org/10.1038/s41427-018-0015-8.
[143] Gonzalez-Gutierrez J, Cano S, Schuschnigg S, Kukla C, Sapkota J, Holzer C. Additive Manufacturing of Metallic and Ceramic Components by the Material Extrusion of Highly-Filled Polymers: A Review and Future Perspectives. Materials 2018;11:840. https://doi.org/10.3390/ma11050840.
[144] Rau DA, Williams CB, Bortner MJ. Rheology and printability: A survey of critical relationships for direct ink write materials design. Prog Mater Sci 2023;140:101188. https://doi.org/10.1016/j.pmatsci.2023.101188.
[145] Parsazadeh M, Sharma S, Dahotre N. Towards the next generation of machine learning models in additive manufacturing: A review of process dependent material evolution. Prog Mater Sci 2023;135:101102. https://doi.org/10.1016/j.pmatsci.2023.101102.
[146] Zhou L, Miller J, Vezza J, Mayster M, Raffay M, Justice Q, et al. Additive Manufacturing: A Comprehensive Review. Sensors 2024;24:2668. https://doi.org/10.3390/s24092668.
[147] Farahani RD, Dubé M, Therriault D. Three-Dimensional Printing of Multifunctional Nanocomposites: Manufacturing Techniques and Applications. Adv Mater 2016;28:5794–821. https://doi.org/10.1002/adma.201506215.
[148] Azhari A, Toyserkani E, Villain C. Additive Manufacturing of Graphene–Hydroxyapatite Nanocomposite Structures. Int J Appl Ceram Technol 2015;12:8–17. https://doi.org/10.1111/ijac.12309.
[149] Do T, Kwon P, Shin CS. Process development toward full-density stainless steel parts with binder jetting printing. Int J Mach Tool Manu 2017;121:50–60. https://doi.org/10.1016/j.ijmachtools.2017.04.006.
[150] Özcan M, Magini EB, Volpato GM, Cruz A, Volpato CAM. Additive Manufacturing Technologies for Fabrication of Biomaterials for Surgical Procedures in Dentistry: A Narrative Review. J Prosthodont 2022;31:105–35. https://doi.org/10.1111/jopr.13484.
[151] Gilmer D, Han L, Hong E, Siddel D, Kisliuk A, Cheng S, et al. An in-situ crosslinking binder for binder jet additive manufacturing. Addit Manuf 2020;35:101341. https://doi.org/10.1016/j.addma.2020.101341.
[152] Vangapally S, Agarwal K, Sheldon A, Cai S. Effect of lattice design and process parameters on dimensional and mechanical properties of binder jet additively manufactured stainless steel 316 for bone scaffolds. Procedia Manuf 2017;10:750–9. https://doi.org/10.1016/j.promfg.2017.07.069.
[153] Li M, Du W, Elwany A, Pei Z, Ma C. Metal binder jetting additive manufacturing: a literature review. J Manuf Sci Eng 2020;142. https://doi.org/10.1115/1.4047430.
[154] Chou D-T, Wells D, Hong D, Lee B, Kuhn H, Kumta PN. Novel processing of iron–manganese alloy-based biomaterials by inkjet 3-D printing. Acta Biomater 2013;9:8593–603. https://doi.org/10.1016/j.actbio.2013.04.016.
[155] Hong D, Chou D-T, Velikokhatnyi OI, Roy A, Lee B, Swink I, et al. Binder-jetting 3D printing and alloy development of new biodegradable Fe-Mn-Ca/Mg alloys. Acta Biomater 2016;45:375–86. https://doi.org/10.1016/j.actbio.2016.08.032.
[156] Putra NE, Mirzaali MJ, Apachitei I, Zhou J, Zadpoor AA. Multi-material additive manufacturing technologies for Ti-, Mg-, and Fe-based biomaterials for bone substitution. Acta Biomater 2020;109:1–20. https://doi.org/10.1016/j.actbio.2020.03.037.
[157] Armstrong M, Mehrabi H, Naveed N. An overview of modern metal additive manufacturing technology. J Manuf Process 2022;84:1001–29. https://doi.org/10.1016/j.jmapro.2022.10.060.
[158] Mostafaei A, Elliott AM, Barnes JE, Li F, Tan W, Cramer CL, et al. Binder jet 3D printing—Process parameters, materials, properties, modeling, and challenges. Prog Mater Sci 2021;119:100707. https://doi.org/10.1016/j.pmatsci.2020.100707.
[159] Balla VK, DeVasConCellos PD, Xue W, Bose S, Bandyopadhyay A. Fabrication of compositionally and structurally graded Ti–TiO2 structures using laser engineered net shaping (LENS). Acta Biomater 2009;5:1831–7. https://doi.org/10.1016/j.actbio.2009.01.011.
[160] Li Y, Zhang D, Ye Z, Ye G, He R, Wang H, et al. The reinforcement mechanisms of graphene oxide in laser-directed energy deposition fabricated metal and ceramic matrix composites: a comparison study. Int J Adv Manuf Technol 2022;119:1975–88. https://doi.org/10.1007/s00170-021-08337-z.
[161] Gao S, Bodunde P, Qin M, Liao W-H, Guo P. Slender structure of nickel-titanium shape memory alloy fabricated by continuous directed energy deposition. Active and Passive Smart Structures and Integrated Systems XV, vol. 11588, SPIE; 2021, p. 146–54. DOI: 10.1117/12.2583410.
[162] Bobbio LD, Bocklund B, Otis R, Borgonia JP, Dillon RP, Shapiro AA, et al. Characterization of a functionally graded material of Ti-6Al-4V to 304L stainless steel with an intermediate V section. J Alloy Compd 2018;742:1031–6. https://doi.org/10.1016/j.jallcom.2018.01.156.
[163] Li W, Karnati S, Kriewall C, Liou F, Newkirk J, Brown Taminger KM, et al. Fabrication and characterization of a functionally graded material from Ti-6Al-4V to SS316 by laser metal deposition. Addit Manuf 2017;14:95–104. https://doi.org/10.1016/j.addma.2016.12.006.
[164] Sun Z, Ji X, Zhang W, Chang L, Xie G, Chang H, et al. Microstructure evolution and high temperature resistance of Ti6Al4V/Inconel625 gradient coating fabricated by laser melting deposition. Mater Des 2020;191:108644. https://doi.org/10.1016/j.matdes.2020.108644.
[165] Gao S, Weng F, Bodunde O P, et al. Spatial characteristics of nickel-titanium shape memory alloy fabricated by continuous directed energy deposition[J]. Journal of Manufacturing Processes 2021;71:417–28.
[166] Bandyopadhyay A, Mitra I, Shivaram A, Dasgupta N, Bose S. Direct comparison of additively manufactured porous titanium and tantalum implants towards in vivo osseointegration. Addit Manuf 2019;28:259–66. https://doi.org/10.1016/j.addma.2019.04.025.
[167] Sommer N, Kluge P, Stredak F, Eigler S, Hill H, Niendorf T, et al. Additive Manufacturing of Compositionally-Graded AISI 316L to CoCrMo Structures by Directed Energy Deposition. Crystals 2021;11:1043. https://doi.org/10.3390/cryst11091043.
[168] Bimber BA, Hamilton RF, Keist J, Palmer TA. Anisotropic microstructure and superelasticity of additive manufactured NiTi alloy bulk builds using laser directed energy deposition. Mater Sci Eng A 2016;674:125–34. https://doi.org/10.1016/j.msea.2016.07.059.
[169] Saboori A, Aversa A, Bosio F, Bassini E, Librera E, De Chirico M, et al. An investigation on the effect of powder recycling on the microstructure and mechanical properties of AISI 316L produced by Directed Energy Deposition. Mater Sci Eng A 2019;766:138360. https://doi.org/10.1016/j.msea.2019.138360.
[170] Huang X, Yin R, Qian L, Zhao W, Liu H, Liu C, et al. Processing conditions dependent tunable negative permittivity in reduced graphene oxide-alumina nanocomposites. Ceram Int 2019;45:17784–92. https://doi.org/10.1016/j.ceramint.2019.05.349.
[171] Feenstra DR, Banerjee R, Fraser HL, Huang A, Molotnikov A, Birbilis N. Critical review of the state of the art in multi-material fabrication via directed energy deposition. Curr Opin Solid State Mater Sci 2021;25:100924. https://doi.org/10.1016/j.cossms.2021.100924.
[172] Dutta B, (Sam) Froes FH. 24 - The additive manufacturing (AM) of titanium alloys. In: Qian M, (Sam) Froes FH, editors. Titanium Powder Metallurgy, Boston: Butterworth-Heinemann; 2015, p. 447–68. DOI: 10.1016/B978-0-12-800054-0.00024-1.
[173] Liu W, Wang T, Liu B, Li W, Hu G, Lyu Z. Research of on-line monitoring technology and control strategy for laser-directed energy deposition: a review. Int J Adv Manuf Technol 2024;133:3105–32. https://doi.org/10.1007/s00170-024-13893-1.
[174] Zhao T, Yan Z, Zhang B, Zhang P, Pan R, Yuan T, et al. A comprehensive review of process planning and trajectory optimization in arc-based directed energy deposition. J Manuf Process 2024;119:235–54. https://doi.org/10.1016/j.jmapro.2024.03.093.
[175] Xiang SL, Gupta M, Wang XJ, Wang LD, Hu XS, Wu K. Enhanced overall strength and ductility of magnesium matrix composites by low content of graphene nanoplatelets. Compos A Appl Sci Manuf 2017;100:183–93. https://doi.org/10.1016/j.compositesa.2017.05.011.
[176] Tabandeh-Khorshid M, Kumar A, Omrani E, Kim C, Rohatgi P. Synthesis, characterization, and properties of graphene reinforced metal-matrix nanocomposites. Compos B Eng 2020;183:107664. https://doi.org/10.1016/j.compositesb.2019.107664.
[177] Park S, Ruoff RS. Chemical methods for the production of graphenes. Nature Nanotech 2009;4:217–24. https://doi.org/10.1038/nnano.2009.58.
[178] Zhu Y, Murali S, Cai W, Li X, Suk JW, Potts JR, et al. Graphene and Graphene Oxide: Synthesis, Properties, and Applications. Adv Mater 2010;22:3906–24. https://doi.org/10.1002/adma.201001068.
[179] Smith AT, LaChance AM, Zeng S, Liu B, Sun L. Synthesis, properties, and applications of graphene oxide/reduced graphene oxide and their nanocomposites. Nano Mater Sci 2019;1:31–47. https://doi.org/10.1016/j.nanoms.2019.02.004.

[180] Cao C, Daly M, Singh CV, Sun Y, Filleter T. High strength measurement of monolayer graphene oxide. Carbon 2015;81:497–504. https://doi.org/10.1016/j.carbon.2014.09.082.
[181] Zandiatashbar A, Lee G-H, An SJ, Lee S, Mathew N, Terrones M, et al. Effect of defects on the intrinsic strength and stiffness of graphene. Nat Commun 2014;5:3186. https://doi.org/10.1038/ncomms4186.
[182] Shin SE, Choi HJ, Shin JH, Bae DH. Strengthening behavior of few-layered graphene/aluminum composites. Carbon 2015;82:143–51. https://doi.org/10.1016/j.carbon.2014.10.044.
[183] Mu XN, Cai HN, Zhang HM, Fan QB, Zhang ZH, Wu Y, et al. Interface evolution and superior tensile properties of multi-layer graphene reinforced pure Ti matrix composite. Mater Des 2018;140:431–41. https://doi.org/10.1016/j.matdes.2017.12.016.
[184] Ma S, Zhou S, Zhang W, Wang S, Liu M. A facile synthesis of Inconel718-GNSs composites with high strength via spark plasma sintering. J Alloy Compd 2022;922:166270. https://doi.org/10.1016/j.jallcom.2022.166270.
[185] Guan C, Chen G, Kai X, Huang L, Zhao P, Chen W, et al. Strengthening-toughening of graphene nanoplates and in situ ZrB2 nanoparticles reinforced AA6111 matrix composites with discontinuous layered structures. Mater Sci Eng A 2022;853:143750. https://doi.org/10.1016/j.msea.2022.143750.
[186] Wang L, Jin J, Yang P, Li S, Tang S, Zong Y, et al. Effect of interfacial bonding on dislocation strengthening in graphene nanosheet reinforced iron composite: A molecular dynamics study. Comput Mater Sci 2021;191:110309. https://doi.org/10.1016/j.commatsci.2021.110309.
[187] Zhou H, Xie F, Liu Y, Li B. Mechanical and tribological properties of Ti6Al4V alloy reinforced with Cu-coated multilayer graphene. Mater Today Commun 2023;35:105698. https://doi.org/10.1016/j.mtcomm.2023.105698.
[188] Li Y, Feng Z, Huang L, Essa K, Bilotti E, Zhang H, et al. Additive manufacturing high performance graphene-based composites: A review. Compos A Appl Sci Manuf 2019;124:105483. https://doi.org/10.1016/j.compositesa.2019.105483.
[189] Yang X, Yang L, Zhu D, Wang H, Chen T, Chu C, et al. Effect of graphene sheet diameter on the microstructure and properties of copper-plated graphene-reinforced 6061-aluminum matrix composites. J Mater Res Technol 2024;28:3286–96. https://doi.org/10.1016/j.jmrt.2023.12.259.
[190] Zhu J, Liu X, Zhou X, Yang Q. Strengthening effect of graphene-edge dislocation interaction in graphene reinforced copper matrix composites. Comput Mater Sci 2021;188:110179. https://doi.org/10.1016/j.commatsci.2020.110179.
[191] Prasad A. Sliding contact at plastically graded surfaces and applications to surface design. Massachusetts Institute of Technology: Thesis; 2007.
[192] Xie Y, Meng X, Li Y, Mao D, Wan L, Huang Y. Insight into ultra-refined grains of aluminum matrix composites via deformation-driven metallurgy. Compos Commun 2021;26:100776. https://doi.org/10.1016/j.coco.2021.100776.
[193] Liu L, Bao R, Zhao W, Liu P, Yi J, Ge Z, et al. Vacant defect and nitrogen doping effects on the interface of graphene/Cu composites: Computational and experimental evaluation. J Alloy Compd 2022;907:164531. https://doi.org/10.1016/j.jallcom.2022.164531.
[194] Kim Y, Lee J, Yeom MS, Shin JW, Kim H, Cui Y, et al. Strengthening effect of single-atomic-layer graphene in metal–graphene nanolayered composites. Nat Commun 2013;4:2114. https://doi.org/10.1038/ncomms3114.
[195] Yang M, Weng L, Zhu H, Fan T, Zhang D. Simultaneously enhancing the strength, ductility and conductivity of copper matrix composites with graphene nanoribbons. Carbon 2017;118:250–60. https://doi.org/10.1016/j.carbon.2017.03.055.
[196] Zhang Z, Chen DL. Contribution of Orowan strengthening effect in particulate-reinforced metal matrix nanocomposites. Mater Sci Eng A 2008;483–484:148–52. https://doi.org/10.1016/j.msea.2006.10.184.
[197] Cao M, Wang S, Zang J, Liu M, Qian C, Zhang Y, et al. Experimental and simulation analysis of the effect of GNPs on the mechanical and interfacial properties of CF/PEEK-Ti fiber metal laminates. Compos Sci Technol 2024;246:110387. https://doi.org/10.1016/j.compscitech.2023.110387.
[198] Liang A, Jiang X, Hong X, Jiang Y, Shao Z, Zhu D. Recent Developments Concerning the Dispersion Methods and Mechanisms of Graphene. Coatings 2018;8:33. https://doi.org/10.3390/coatings8010033.
[199] Zhao L, Guo Q, Li Z, Xiong D-B, Osovski S, Su Y, et al. Strengthening and deformation mechanisms in nanolaminated graphene-Al composite micro-pillars affected by graphene in-plane sizes. Int J Plast 2019;116:265–79. https://doi.org/10.1016/j.ijplas.2019.01.006.
[200] Dutkiewicz J, Ozga P, Maziarz W, Pstruś J, Kania B, Bobrowski P, et al. Microstructure and properties of bulk copper matrix composites strengthened with various kinds of graphene nanoplatelets. Mater Sci Eng A 2015;628:124–34. https://doi.org/10.1016/j.msea.2015.01.018.
[201] Yang Z, Wang L, Li J, Shi Z, Wang M, Sheng J, et al. Lateral size effect of reduced graphene oxide on properties of copper matrix composites. Mater Sci Eng A 2021;820:141579. https://doi.org/10.1016/j.msea.2021.141579.
[202] Mag-isa AE, Kim S-M, Kim J-H, Oh C-S. Variation of thermal expansion coefficient of freestanding multilayer pristine graphene with temperature and number of layers. Mater Today Commun 2020;25:101387. https://doi.org/10.1016/j.mtcomm.2020.101387.
[203] Rashad M, Pan F, Tang A, Asif M, Hussain S, Gou J, et al. Improved strength and ductility of magnesium with addition of aluminum and graphene nanoplatelets (Al+GNPs) using semi powder metallurgy method. J Ind Eng Chem 2015;23:243–50. https://doi.org/10.1016/j.jiec.2014.08.024.
[204] Islam MZ, Mahboob M, Lowe LR, Bechtel ES. Characterization of the thermal expansion properties of graphene using molecular dynamics simulations. J Phys D: Appl Phys 2013;46:435302. https://doi.org/10.1088/0022-3727/46/43/435302.
[205] Mounet N, Marzari N. First-principles determination of the structural, vibrational and thermodynamic properties of diamond, graphite, and derivatives. PhysRevB 2005;71:205214. https://doi.org/10.1103/PhysRevB.71.205214.
[206] Bao W, Miao F, Chen Z, Zhang H, Jang W, Dames C, et al. Controlled ripple texturing of suspended graphene and ultrathin graphite membranes. Nature Nanotech 2009;4:562–6. https://doi.org/10.1038/nnano.2009.191.
[207] Zhao S, Zhang Y, Chen D, Yang J, Kitipornchai S. Enhanced thermal buckling resistance of folded graphene reinforced nanocomposites with negative thermal expansion: From atomistic study to continuum mechanics modelling. Compos Struct 2022;279:114872. https://doi.org/10.1016/j.compstruct.2021.114872.
[208] AbuShanab WS, Moustafa EB, Ghandourah E, Taha MA. Effect of graphene nanoparticles on the physical and mechanical properties of the Al2024-graphene nanocomposites fabricated by powder metallurgy. Results Phys 2020;19:103343. https://doi.org/10.1016/j.rinp.2020.103343.
[209] Sanaty-Zadeh A. Comparison between current models for the strength of particulate-reinforced metal matrix nanocomposites with emphasis on consideration of Hall–Petch effect. Mater Sci Eng A 2012;531:112–8. https://doi.org/10.1016/j.msea.2011.10.043.
[210] Luqman M, Ali Y, Zaghloul MMY, Sheikh FA, Chan V, Abdal-hay A. Grain refinement mechanism and its effect on mechanical properties and biodegradation behaviors of Zn alloys – A review. J Mater Res Technol 2023;24:7338–65. https://doi.org/10.1016/j.jmrt.2023.04.219.
[211] Li X, Yi D, Liu B, Zhang J, Yang X, Wang C, et al. Graphene-strengthened Inconel 625 Alloy Fabricated by Selective Laser Melting. Mater Sci Eng A 2020;798:140099. https://doi.org/10.1016/j.msea.2020.140099.
[212] Shin SE, Bae DH. Deformation behavior of aluminum alloy matrix composites reinforced with few-layer graphene. Compos A Appl Sci Manuf 2015;78:42–7. https://doi.org/10.1016/j.compositesa.2015.08.001.
[213] Zhao M, Xiong D-B, Tan Z, Fan G, Guo Q, Guo C, et al. Lateral size effect of graphene on mechanical properties of aluminum matrix nanolaminated composites. Scr Mater 2017;139:44–8. https://doi.org/10.1016/j.scriptamat.2017.06.018.
[214] Han T, Li J, Zhao N, He C. Microstructure and properties of copper coated graphene nanoplates reinforced Al matrix composites developed by low temperature ball milling. Carbon 2020;159:311–23. https://doi.org/10.1016/j.carbon.2019.12.029.
[215] Zhao Y-C, Tang Y, Zhao M-C, Liu L, Gao C, Shuai C, et al. Graphene Oxide Reinforced Iron Matrix Composite With Enhanced Biodegradation Rate Prepared by Selective Laser Melting. Adv Eng Mater 2019;21:1900314. https://doi.org/10.1002/adem.201900314.
[216] Yook S-W, Jung H-D, Park C-H, Shin K-H, Koh Y-H, Estrin Y, et al. Reverse freeze casting: A new method for fabricating highly porous titanium scaffolds with aligned large pores. Acta Biomater 2012;8:2401–10. https://doi.org/10.1016/j.actbio.2012.03.020.
[217] Du X, Du W, Wang Z, Liu K, Li S. Ultra-high strengthening efficiency of graphene nanoplatelets reinforced magnesium matrix composites. Mater Sci Eng A 2018;711:633–42. https://doi.org/10.1016/j.msea.2017.11.040.
[218] Du X, Du W, Wang Z, Liu K, Li S. Simultaneously improved mechanical and thermal properties of Mg-Zn-Zr alloy reinforced by ultra-low content of graphene nanoplatelets. Appl Surf Sci 2021;536:147791. https://doi.org/10.1016/j.apsusc.2020.147791.
[219] Shu R, Jiang X, Liu W, Shao Z, Song T, Luo Z. Synergetic effect of nano-carbon and HBN on microstructure and mechanical properties of Cu/Ti3SiC2/C nanocomposites. Mater Sci Eng A 2019;755:128–37. https://doi.org/10.1016/j.msea.2019.04.002.

[220] Huo P, Zhao Z, Du W, Zhang Z, Bai P, Tie D. Deformation strengthening mechanism of in situ TiC/TC4 alloy nanocomposites produced by selective laser melting. Compos B Eng 2021;225:109305. https://doi.org/10.1016/j.compositesb.2021.109305.
[221] Lee C, Song G, Gao MC, Feng R, Chen P, Brechtl J, et al. Lattice distortion in a strong and ductile refractory high-entropy alloy. Acta Mater 2018;160:158–72. https://doi.org/10.1016/j.actamat.2018.08.053.
[222] Meng L, Hu X, Wang X, Zhang C, Shi H, Xiang Y, et al. Graphene nanoplatelets reinforced Mg matrix composite with enhanced mechanical properties by structure construction. Mater Sci Eng A 2018;733:414–8. https://doi.org/10.1016/j.msea.2018.07.056.
[223] Rashad M, Pan F, Hu H, Asif M, Hussain S, She J. Enhanced tensile properties of magnesium composites reinforced with graphene nanoplatelets. Mater Sci Eng A 2015;630:36–44. https://doi.org/10.1016/j.msea.2015.02.002.
[224] Sun X, Li C, Dai X, Zhao L, Li B, Wang H, et al. Microstructures and properties of graphene-nanoplatelet-reinforced magnesium-matrix composites fabricated by an in situ reaction process. J Alloy Compd 2020;835:155125. https://doi.org/10.1016/j.jallcom.2020.155125.
[225] Rashad M, Pan F, Tang A, Asif M, Aamir M. Synergetic effect of graphene nanoplatelets (GNPs) and multi-walled carbon nanotube (MW-CNTs) on mechanical properties of pure magnesium. J Alloy Compd 2014;603:111–8. https://doi.org/10.1016/j.jallcom.2014.03.038.
[226] Sun X, Chen M, Liu D. Fabrication and characterization of few-layer graphene oxide reinforced magnesium matrix composites. Mater Sci Eng A 2021;803:140722. https://doi.org/10.1016/j.msea.2020.140722.
[227] Owhal A, Pingale AD, Belgamwar SU, Rathore JS. Preparation of novel Zn/Gr MMC using a modified electro-co-deposition method: Microstructural and tribo-mechanical properties. Mater Today Proc 2021;44:222–8. https://doi.org/10.1016/j.matpr.2020.09.459.
[228] Shahin M, Munir K, Wen C, Li Y. Magnesium-based composites reinforced with graphene nanoplatelets as biodegradable implant materials. J Alloy Compd 2020;828:154461. https://doi.org/10.1016/j.jallcom.2020.154461.
[229] Kumar P, Mallick A, Kujur MS, Tun KS, Shabadi R, Gupta M. Strength of Mg–3%Al alloy in presence of graphene nano-platelets as reinforcement. Mater Sci Technol 2018;34:1086–95. https://doi.org/10.1080/02670836.2018.1424380.
[230] Ramezanzade S, Ebrahimi G, Parizi MT, Ezatpour H. Microstructure and mechanical characterizations of graphene nanoplatelets-reinforced Mg–Sr–Ca alloy as a novel composite in structural and biomedical applications. J Compos Mater 2020;54:711–28. https://doi.org/10.1177/0021998319867464.
[231] Shi H, Xiang S, Hu X, Wang X, Xu C, Wu K. Fabrication and strengthening mechanisms of magnesium matrix composites with bimodal microstructure induced by graphene nanoplatelets. J Mater Res 2021;36:764–74. https://doi.org/10.1557/s43578-021-00112-w.
[232] Xiang S, Wang X, Gupta M, Wu K, Hu X, Zheng M. Graphene nanoplatelets induced heterogeneous bimodal structural magnesium matrix composites with enhanced mechanical properties. Sci Rep 2016;6:38824. https://doi.org/10.1038/srep38824.
[233] Xiang SL, Hu XS, Wang XJ, Wang LD, Wu K. Precipitate characteristics and synergistic strengthening realization of graphene nanoplatelets reinforced bimodal structural magnesium matrix composites. Mater Sci Eng A 2018;724:348–56. https://doi.org/10.1016/j.msea.2018.03.107.
[234] Rashad M, Pan F, Asif M. Exploring mechanical behavior of Mg–6Zn alloy reinforced with graphene nanoplatelets. Mater Sci Eng A 2016;649:263–9. https://doi.org/10.1016/j.msea.2015.10.009.
[235] Li X, Wang X, Hu X, Xu C, Shao W, Wu K. Direct conversion of CO2 to graphene via vapor–liquid reaction for magnesium matrix composites with structural and functional properties. J Magnesium Alloys 2023;11:1206–12. https://doi.org/10.1016/j.jma.2021.06.012.
[236] Kandemir S. Development of Graphene Nanoplatelet-Reinforced AZ91 Magnesium Alloy by Solidification Processing. J of Materi Eng and Perform 2018;27:3014–23. https://doi.org/10.1007/s11665-018-3391-x.
[237] Kumar NS, Sozhamannan GG. Investigating the effect of mechanical properties of magnesium alloy (AZ91D) reinforced with graphene metal matrix composite by stir casting method. Mater Today Proc 2022;64:95–100. https://doi.org/10.1016/j.matpr.2022.03.718.
[238] Yuan Q, Zhou G, Liao L, Liu Y, Luo L. Interfacial structure in AZ91 alloy composites reinforced by graphene nanosheets. Carbon 2018;127:177–86. https://doi.org/10.1016/j.carbon.2017.10.090.
[239] Chen L, Zhao Y, Jing J, Hou H. Microstructural evolution in graphene nanoplatelets reinforced magnesium matrix composites fabricated through thixomolding process. J Alloy Compd 2023;940:168824. https://doi.org/10.1016/j.jallcom.2023.168824.
[240] Yuan Q, Qiu Z, Zhou G, Zeng X, Luo L, Rao X-X, et al. Interfacial design and strengthening mechanisms of AZ91 alloy reinforced with in-situ reduced graphene oxide. Mater Charact 2018;138:215–28. https://doi.org/10.1016/j.matchar.2018.02.011.
[241] Du X, Du W, Wang Z, Liu K, Li S. Defects in graphene nanoplatelets and their interface behavior to reinforce magnesium alloys. Appl Surf Sci 2019;484:414–23. https://doi.org/10.1016/j.apsusc.2019.04.111.
[242] Zhu B, Du X, Meng F, Wu X, Liu K, Li S, et al. Simultaneously Enhanced Thermal and Mechanical Properties of ZK60 Alloy Reinforced by Oriented Graphene Nanoplatelets. Acta Metall Sin (Engl Lett) 2023;36:1999–2012. https://doi.org/10.1007/s40195-023-01578-9.
[243] Wang L, Chen T, Pu P. Synthesis of graphene oxide reinforced ZK60 magnesium matrix composite with high ductility via powder thixoforming. Mater Sci Eng A 2022;830:142307. https://doi.org/10.1016/j.msea.2021.142307.
[244] Wang L, Chen T. Simultaneously enhancing strength and toughness of graphene oxide reinforced ZK60 magnesium matrix composites through powder thixoforming. Compos A Appl Sci Manuf 2022;161:107097. https://doi.org/10.1016/j.compositesa.2022.107097.
[245] Wang L, Chen T. Regulation of bimodal structure and mechanical properties of powder-thixoformed GO/ZK60 magnesium matrix composite through adjusting GO content. J Mater Sci Technol 2023;162:74–89. https://doi.org/10.1016/j.jmst.2023.03.047.
[246] Wei Z, Du X, Du W, Meng F, Liu K, Li S. Influence of the residual oxygen amount in reduced graphene nanoplatelets on microstructure and mechanical properties of ZK60 matrix composites. Mater Sci Eng A 2022;842:143094. https://doi.org/10.1016/j.msea.2022.143094.
[247] Fan Y, Ye L, Tian Q, Zhuang Y, Zhang Y, Li X. Effects of aligned graphene sheets on mechanical properties of ZK61 alloy. Mater Sci Eng A 2021;801:140417. https://doi.org/10.1016/j.msea.2020.140417.
[248] Liu F, Wang Z, Du X, Li S, Du W. Microstructure and Mechanical Properties of Magnesium Matrix Composites Reinforced by In Situ Reduced Graphene Oxide. Materials 2023;16:2303. https://doi.org/10.3390/ma16062303.
[249] Rashad M, Pan F, Lin D, Asif M. High temperature mechanical behavior of AZ61 magnesium alloy reinforced with graphene nanoplatelets. Mater Des 2016;89:1242–50. https://doi.org/10.1016/j.matdes.2015.10.101.
[250] Rashad M, Pan F, Zhang J, Asif M. Use of high energy ball milling to study the role of graphene nanoplatelets and carbon nanotubes reinforced magnesium alloy. J Alloy Compd 2015;646:223–32. https://doi.org/10.1016/j.jallcom.2015.06.051.
[251] Lu T, Zhou M, Ren L, Fan L, Guo Y, Qu X, et al. Effect of Graphene Nanoplatelets Content on the Mechanical and Wear Properties of AZ31 Alloy. Metals 2020;10:1265. https://doi.org/10.3390/met10091265.
[252] Rashad M, Pan F, Liu Y, Chen X, Lin H, Pan R, et al. High temperature formability of graphene nanoplatelets-AZ31 composites fabricated by stir-casting method. J Magnesium Alloys 2016;4:270–7. https://doi.org/10.1016/j.jma.2016.11.003.
[253] Kavimani V, Soorya Prakash K, Thankachan T. Investigation of graphene-reinforced magnesium metal matrix composites processed through a solvent-based powder metallurgy route. Bull Mater Sci 2019;42:39. https://doi.org/10.1007/s12034-018-1720-1.
[254] Shuai C, Wang B, Bin S, Peng S, Gao C. Interfacial strengthening by reduced graphene oxide coated with MgO in biodegradable Mg composites. Mater Des 2020;191:108612. https://doi.org/10.1016/j.matdes.2020.108612.
[255] Sun W, Yang Y, Yang Z, Wang L, Wang J, Xu D, et al. Review on the corrosion-promotion activity of graphene and its inhibition. J Mater Sci Technol 2021;91:278–306. https://doi.org/10.1016/j.jmst.2020.12.084.
[256] Hiromoto S. 4 - Corrosion of metallic biomaterials. In: Niinomi M, editor. Metals for Biomedical Devices (Second Edition), Woodhead Publishing; 2019, p. 131–52. DOI: 10.1016/B978-0-08-102666-3.00004-3.
[257] Cui J, Lai Y, Wang W, Li H, Ma X, Zhan J. Galvanic displacement induced reduction of graphene oxide. Carbon 2014;66:738–41. https://doi.org/10.1016/j.carbon.2013.09.078.
[258] Sun W, Wang L, Wu T, Pan Y, Liu G. Synthesis of low-electrical-conductivity graphene/pernigraniline composites and their application in corrosion protection. Carbon 2014;79:605–14. https://doi.org/10.1016/j.carbon.2014.08.021.

[259] Liu Y, Zheng Y, Chen X-H, Yang J-A, Pan H, Chen D, et al. Fundamental theory of biodegradable metals—definition, criteria, and design. Adv Funct Mater 2019;29:1805402. https://doi.org/10.1002/adfm.201805402.
[260] ISO 5832-2:2018(en), Implants for surgery — Metallic materials — Part 2: Unalloyed titanium n.d. https://www.iso.org/obp/ui/#iso:std:iso:5832:-2:ed-4:v1:en (accessed January 9, 2023).
[261] Jin H, Zhao S, Guillory R, Bowen PK, Yin Z, Griebel A, et al. Novel high-strength, low-alloys Zn-Mg (<0.1wt% Mg) and their arterial biodegradation. Mater Sci Eng C 2018;84:67–79. https://doi.org/10.1016/j.msec.2017.11.021.
[262] Zhao S, McNamara CT, Bowen PK, Verhun N, Braykovich JP, Goldman J, et al. Structural Characteristics and In Vitro Biodegradation of a Novel Zn-Li Alloy Prepared by Induction Melting and Hot Rolling. Metall Mater Trans A 2017;48:1204–15. https://doi.org/10.1007/s11661-016-3901-0.
[263] Wofford JM, Nie S, Thürmer K, McCarty KF, Dubon OD. Influence of lattice orientation on growth and structure of graphene on Cu(001). Carbon 2015;90:284–90. https://doi.org/10.1016/j.carbon.2015.03.056.
[264] Wang S, Zhang Y, Abidi N, Cabrales L. Wettability and Surface Free Energy of Graphene Films. Langmuir 2009;25:11078–81. https://doi.org/10.1021/la901402f.
[265] Nogi K, Ogino K, McLean A, Miller WA. The temperature coefficient of the surface tension of pure liquid metals. Metall Trans B 1986;17:163–70. https://doi.org/10.1007/BF02670829.
[266] Bramfitt BL. The effect of carbide and nitride additions on the heterogeneous nucleation behavior of liquid iron. Metall Mater Trans B 1970;1:1987–95. https://doi.org/10.1007/BF02642799.
[267] Zhou W, Mikulova P, Fan Y, Kikuchi K, Nomura N, Kawasaki A. Interfacial reaction induced efficient load transfer in few-layer graphene reinforced Al matrix composites for high-performance conductor. Compos B Eng 2019;167:93–9. https://doi.org/10.1016/j.compositesb.2018.12.018.
[268] Li Y, Jahr H, Pavanram P, Bobbert FSL, Puggi U, Zhang X-Y, et al. Additively manufactured functionally graded biodegradable porous iron. Acta Biomater 2019;96:646–61. https://doi.org/10.1016/j.actbio.2019.07.013.
[269] Koons GL, Diba M, Mikos AG. Materials design for bone-tissue engineering. Nat Rev Mater 2020;5:584–603. https://doi.org/10.1038/s41578-020-0204-2.
[270] Li Y, Lietaert K, Li W, Zhang X-Y, Leeflang MA, Zhou J, et al. Corrosion fatigue behavior of additively manufactured biodegradable porous iron. Corros Sci 2019;156:106–16. https://doi.org/10.1016/j.corsci.2019.05.003.
[271] Lin D, Richard Liu C, Cheng GJ. Single-layer graphene oxide reinforced metal matrix composites by laser sintering: Microstructure and mechanical property enhancement. Acta Mater 2014;80:183–93. https://doi.org/10.1016/j.actamat.2014.07.038.
[272] Liu X, Zhang L, Xu Y. Microstructure and mechanical properties of graphene reinforced Fe50Mn30Co10Cr10 high-entropy alloy composites synthesized by MA and SPS. Appl Phys A 2017;123:567. https://doi.org/10.1007/s00339-017-1151-7.
[273] Zhang L, Jiang X, Sun H, Zhang Y, Fang Y, Shu R. Microstructure, mechanical properties and damping capacity of Fe-Mn-Co Alloys reinforced with graphene. J Alloy Compd 2023;931:167547. https://doi.org/10.1016/j.jallcom.2022.167547.
[274] Shuang F, Aifantis KE. Modelling dislocation-graphene interactions in a BCC Fe matrix by molecular dynamics simulations and gradient plasticity theory. Appl Surf Sci 2021;535:147602. https://doi.org/10.1016/j.apsusc.2020.147602.
[275] Ishraaq R, Rashid M, Afsar AM. A molecular dynamics investigation of mechanical properties of graphene reinforced iron composite and the effect of vacancy defect distance from the matrix-fiber interface. AIP Conf Proc 2021;2324:030010. https://doi.org/10.1063/5.0037502.
[276] Han E, Yu J, Annevelink E, Son J, Kang DA, Watanabe K, et al. Ultrasoft slip-mediated bending in few-layer graphene. Nat Mater 2020;19:305–9. https://doi.org/10.1038/s41563-019-0529-7.
[277] Ho Y-H, Man K, Joshi SS, Pantawane MV, Wu T-C, Yang Y, et al. *In-vitro* biomineralization and biocompatibility of friction stir additively manufactured AZ31B magnesium alloy-hydroxyapatite composites. Bioact Mater 2020;5:891–901. https://doi.org/10.1016/j.bioactmat.2020.06.009.
[278] Dong J, Lin P, Putra NE, Tümer N, Leeflang MA, Huan Z, et al. Extrusion-based additive manufacturing of Mg-Zn/bioceramic composite scaffolds. Acta Biomater 2022. https://doi.org/10.1016/j.actbio.2022.08.002.
[279] Li J-X, Zhang Y, Li J-Y, Xie J-X. Effect of trace HA on microstructure, mechanical properties and corrosion behavior of Mg-2Zn-0.5Sr alloy. J Mater Sci Technol 2018;34:299–310. https://doi.org/10.1016/j.jmst.2017.06.013.
[280] Wang X, Wang C, Chu C, Xue F, Li J, Bai J. Structure-function integrated biodegradable Mg/polymer composites: Design, manufacturing, properties, and biomedical applications. Bioact Mater 2024;39:74–105. https://doi.org/10.1016/j.bioactmat.2024.05.024.
[281] Ali W, Mehboob A, Han M-G, Chang S-H. Experimental study on degradation of mechanical properties of biodegradable magnesium alloy (AZ31) wires/poly (lactic acid) composite for bone fracture healing applications. Compos Struct 2019;210:914–21. https://doi.org/10.1016/j.compstruct.2018.12.011.
[282] Wang X, Qian Y, Wang S, Wang M, Sun K, Cheng Z, et al. Accumulative Rolling Mg/PLLA Composite Membrane with Lamellar Heterostructure for Enhanced Bacteria Inhibition and Rapid Bone Regeneration. Small 2023;19:2301638. https://doi.org/10.1002/smll.202301638.
[283] Yang H, Qu X, Lin W, Wang C, Zhu D, Dai K, et al. *In vitro* and *in vivo* studies on zinc-hydroxyapatite composites as novel biodegradable metal matrix composite for orthopedic applications. Acta Biomater 2018;71:200–14. https://doi.org/10.1016/j.actbio.2018.03.007.
[284] Chebolu R, Nallu R, Chanamala R. Experimental investigation on mechanical behavior of as cast Zn-Al-Cu/SiC/TiB2 hybrid metal matrix composite by ultrasonic assisted stir casting technique. Eng Res Express 2022;4:025040. https://doi.org/10.1088/2631-8695/ac71f7.
[285] Koç DA. Development and characterization of zinc-incorporated montmorillonite/poly(ε-caprolactone) composite scaffold for osteogenic tissue-engineering applications. Polym Compos 2018;39:E601–8. https://doi.org/10.1002/pc.24780.
[286] Kabir H, Munir K, Wen C, Li Y. Microstructures, mechanical and corrosion properties of graphene nanoplatelet–reinforced zinc matrix composites for implant applications. Acta Biomater 2022. https://doi.org/10.1016/j.actbio.2022.11.060.
[287] Dehestani M, Adolfsson E, Stanciu LA. Mechanical properties and corrosion behavior of powder metallurgy iron-hydroxyapatite composites for biodegradable implant applications. Mater Des 2016;109:556–69. https://doi.org/10.1016/j.matdes.2016.07.092.
[288] Putra NE, Leeflang MA, Klimopoulou M, Dong J, Taheri P, Huan Z, et al. Extrusion-based 3D printing of biodegradable, osteogenic, paramagnetic, and porous FeMn-akermanite bone substitutes. Acta Biomater 2023;162:182–98. https://doi.org/10.1016/j.actbio.2023.03.033.
[289] Tsakiris V, Tardei C, Clicinschi FM. Biodegradable Mg alloys for orthopedic implants – A review. J Magnesium Alloys 2021;9:1884–905. https://doi.org/10.1016/j.jma.2021.06.024.
[290] Heiden M, Walker E, Stanciu L. Magnesium, Iron and Zinc Alloys, the Trifecta of Bioresorbable Orthopaedic and Vascular Implantation - A Review. Journal of Biotechnology & Biomaterials 2015;5:1–9. https://doi.org/10.4172/2155-952X.1000178.
[291] Xiong H, Gu L, Wang J, Zhou L, Ying T, Wang S, et al. The interface structure and property of magnesium matrix composites: A review. J Magnesium Alloys 2024;12:2595–623. https://doi.org/10.1016/j.jma.2024.04.022.
[292] Xiang Y, Wang X, Shi H, Hu X, Xu C, Zhang Q. Decipher the ultra-high strengthening and toughening efficiency of GNS-MgO/Mg layered composite with in-situ enhanced interface. Carbon 2022;196:783–94. https://doi.org/10.1016/j.carbon.2022.04.063.
[293] Liu X, Huang Y, Ding L, Zhao X, Liu P, Li T. Synthesis of covalently bonded reduced graphene oxide-Fe3O4 nanocomposites for efficient electromagnetic wave absorption. J Mater Sci Technol 2021;72:93–103. https://doi.org/10.1016/j.jmst.2020.09.012.
[294] Vitos L, Ruban AV, Skriver HL, Kollár J. The surface energy of metals. Surf Sci 1998;411:186–202. https://doi.org/10.1016/S0039-6028(98)00363-X.
[295] Asif Iqbal A, Parvez Iqbal AKM, Nuruzzaman DM. A review on fatigue fracture characteristics in graphene reinforced nanocomposites. Ain Shams Eng J 2024;15:102730. https://doi.org/10.1016/j.asej.2024.102730.
[296] Hwang B, Kim W, Kim J, Lee S, Lim S, Kim S, et al. Role of Graphene in Reducing Fatigue Damage in Cu/Gr Nanolayered Composite. Nano Lett 2017;17:4740–5. https://doi.org/10.1021/acs.nanolett.7b01431.
[297] Kumar HGP, Xavior MA. Fatigue and Wear Behavior of Al6061–Graphene Composites Synthesized by Powder Metallurgy. Trans Indian Inst Met 2016;69:415–9. https://doi.org/10.1007/s12666-015-0780-9.
[298] Loi F, Córdova LA, Pajarinen J, Lin T, Yao Z, Goodman SB. Inflammation, fracture and bone repair. Bone 2016;86:119–30. https://doi.org/10.1016/j.bone.2016.02.020.

[299] Gibon E, Takakubo Y, Zwingenberger S, Gallo J, Takagi M, Goodman SB. Friend or foe? Inflammation and the foreign body response to orthopedic biomaterials. J Biomed Mater Res A 2024;112:1172–87. https://doi.org/10.1002/jbm.a.37599.
[300] Yoon D, Son Y-W, Cheong H. Negative Thermal Expansion Coefficient of Graphene Measured by Raman Spectroscopy. Nano Lett 2011;11:3227–31. https://doi.org/10.1021/nl201488g.
[301] Wong WLE, Gupta M. Development of Mg/Cu nanocomposites using microwave assisted rapid sintering. Compos Sci Technol 2007;67:1541–52. https://doi.org/10.1016/j.compscitech.2006.07.015.
[302] Lu H, Zhou C, Song Y, Zhang Y, Wu Y, Long F, et al. A strategy to reduce thermal expansion and achieve higher mechanical properties in iron alloys. Nat Commun 2025;16:211. https://doi.org/10.1038/s41467-024-55551-w.
[303] Hornberger H, Virtanen S, Boccaccini AR. Biomedical coatings on magnesium alloys – A review. Acta Biomater 2012;8:2442–55. https://doi.org/10.1016/j.actbio.2012.04.012.
[304] Bowen PK, Drelich J, Goldman J. Zinc Exhibits Ideal Physiological Corrosion Behavior for Bioabsorbable Stents. Adv Mater 2013;25:2577–82. https://doi.org/10.1002/adma.201300226.
[305] Li Y, Shi J, Jahr H, Zhou J, Zadpoor AA, Wang L. Improving the Mechanical Properties of Additively Manufactured Micro-Architected Biodegradable Metals. JOM 2021;73:4188–98. https://doi.org/10.1007/s11837-021-04949-8.
[306] Yin Yee Chin P, Cheok Q, Glowacz A, Caesarendra W. A Review of In-Vivo and In-Vitro Real-Time Corrosion Monitoring Systems of Biodegradable Metal Implants. Appl Sci 2020;10:3141. https://doi.org/10.3390/app10093141.
[307] Chen Y, Zhang W, Maitz MF, Chen M, Zhang H, Mao J, et al. Comparative corrosion behavior of Zn with Fe and Mg in the course of immersion degradation in phosphate buffered saline. Corros Sci 2016;111:541–55. https://doi.org/10.1016/j.corsci.2016.05.039.
[308] Venezuela J, Dargusch MS. Addressing the slow corrosion rate of biodegradable Fe-Mn: Current approaches and future trends. Curr Opin Solid State Mater Sci 2020;24:100822. https://doi.org/10.1016/j.cossms.2020.100822.
[309] Dong H, Lin F, Boccaccini AR, Virtanen S. Corrosion behavior of biodegradable metals in two different simulated physiological solutions: Comparison of Mg. Zn and Fe Corrosion Science 2021;182:109278. https://doi.org/10.1016/j.corsci.2021.109278.
[310] Song G, Johannesson B, Hapugoda S, StJohn D. Galvanic corrosion of magnesium alloy AZ91D in contact with an aluminium alloy, steel and zinc. Corros Sci 2004;46:955–77. https://doi.org/10.1016/S0010-938X(03)00190-2.
[311] Schriver M, Regan W, Gannett WJ, Zaniewski AM, Crommie MF, Zettl A. Graphene as a long-term metal oxidation barrier: worse than nothing. ACS Nano 2013;7:5763–8. https://doi.org/10.1021/nn4014356.
[312] Guo Y, Luo Q, Liu B, Li Q. Elastic properties of long-period stacking ordered phases in Mg–Zn–Y and Mg–Ni–Y alloys: A first-principles study. Scr Mater 2020;178:422–7. https://doi.org/10.1016/j.scriptamat.2019.12.016.
[313] Turan ME, Sun Y, Akgul Y, Turen Y, Ahlatci H. The effect of GNPs on wear and corrosion behaviors of pure magnesium. J Alloy Compd 2017;724:14–23. https://doi.org/10.1016/j.jallcom.2017.07.022.
[314] Cheng L, Liu C, Han D, Ma S, Guo W, Cai H, et al. Effect of graphene on corrosion resistance of waterborne inorganic zinc-rich coatings. J Alloy Compd 2019;774:255–64. https://doi.org/10.1016/j.jallcom.2018.09.315.
[315] Glover CF, Richards C, Baker J, Williams G, McMurray HN. In-coating graphene nano-platelets for environmentally-friendly corrosion protection of iron. Corros Sci 2017;114:169–72. https://doi.org/10.1016/j.corsci.2016.11.009.
[316] Hidalgo-Manrique P, Lei X, Xu R, Zhou M, Kinloch IA, Young RJ. Copper/graphene composites: a review. J Mater Sci 2019;54:12236–89. https://doi.org/10.1007/s10853-019-03703-5.
[317] Lv X, Li X, Li N, Zhang H, Zheng Y, Wu J, et al. ZrO2 nanoparticle encapsulation of graphene microsheets for enhancing anticorrosion performance of epoxy coatings. Surf Coat Technol 2019;358:443–51. https://doi.org/10.1016/j.surfcoat.2018.11.045.
[318] Chapter NKA. Biofouling and Microbially Influenced Corrosion. In: Natarajan KA, editor. Biotechnology of Metals, 12. Amsterdam: Elsevier; 2018. p. 355–93. https://doi.org/10.1016/B978-0-12-804022-5.00012-8.
[319] Cui C, Lim ATO, Huang J. A cautionary note on graphene anti-corrosion coatings. Nature Nanotech 2017;12:834–5. https://doi.org/10.1038/nnano.2017.187.
[320] Pourhashem S, Vaezi MR, Rashidi A, Bagherzadeh MR. Exploring corrosion protection properties of solvent based epoxy-graphene oxide nanocomposite coatings on mild steel. Corros Sci 2017;115:78–92. https://doi.org/10.1016/j.corsci.2016.11.008.
[321] Zhang R, Yu X, Yang Q, Cui G, Li Z. The role of graphene in anti-corrosion coatings: A review. Constr Build Mater 2021;294:123613. https://doi.org/10.1016/j.conbuildmat.2021.123613.
[322] Xu X, Yi D, Wang Z, Yu J, Zhang Z, Qiao R, et al. Greatly Enhanced Anticorrosion of Cu by Commensurate Graphene Coating. Adv Mater 2018;30:1702944. https://doi.org/10.1002/adma.201702944.
[323] Kirkland NT, Schiller T, Medhekar N, Birbilis N. Exploring graphene as a corrosion protection barrier. Corros Sci 2012;56:1–4. https://doi.org/10.1016/j.corsci.2011.12.003.
[324] Ren S, Cui M, Liu C, Wang L. A comprehensive review on ultrathin, multi-functionalized, and smart graphene and graphene-based composite protective coatings. Corros Sci 2023;212:110939. https://doi.org/10.1016/j.corsci.2022.110939.
[325] Keshmiri N, Najmi P, Ramezanzadeh B, Ramezanzadeh M, Bahlakeh G, Nano-scale P. Zn-codoped reduced-graphene oxide incorporated epoxy composite; synthesis, electronic-level DFT-D modeling, and anti-corrosion properties. Prog Org Coat 2021;159:106416. https://doi.org/10.1016/j.porgcoat.2021.106416.
[326] Zhang Y, Sun J, Xiao X, Wang N, Meng G, Gu L. Graphene-like two-dimensional nanosheets-based anticorrosive coatings: A review. J Mater Sci Technol 2022;129:139–62. https://doi.org/10.1016/j.jmst.2022.04.032.
[327] Woods CR, Withers F, Zhu MJ, Cao Y, Yu G, Kozikov A, et al. Macroscopic self-reorientation of interacting two-dimensional crystals. Nat Commun 2016;7:10800. https://doi.org/10.1038/ncomms10800.
[328] Kang D, Kwon JY, Cho H, Sim J-H, Hwang HS, Kim CS, et al. Oxidation resistance of iron and copper foils coated with reduced graphene oxide multilayers. ACS Nano 2012;6:7763–9. https://doi.org/10.1021/nn3017316.
[329] Su Y, Kravets VG, Wong SL, Waters J, Geim AK, Nair RR. Impermeable barrier films and protective coatings based on reduced graphene oxide. Nat Commun 2014;5:4843. https://doi.org/10.1038/ncomms5843.
[330] Aung NN, Zhou W. Effect of grain size and twins on corrosion behaviour of AZ31B magnesium alloy. Corros Sci 2010;52:589–94. https://doi.org/10.1016/j.corsci.2009.10.018.
[331] Gollapudi S. Grain size distribution effects on the corrosion behaviour of materials. Corros Sci 2012;62:90–4. https://doi.org/10.1016/j.corsci.2012.04.040.
[332] Zhao Y-C, Tang Y, Zhao M-C, Liu C, Liu L, Gao C-D, et al. Study on Fe-xGO composites prepared by selective laser melting: microstructure, hardness, biodegradation and cytocompatibility. JOM 2020;72:1163–74. https://doi.org/10.1007/s11837-019-03814-z.
[333] Vijayananth K, Ponnusamy V, Kumar N, Sinnaeruvadi K. Effect of graphene on microstructure, strain hardening and corrosion behaviour of dual phase Mg-Li matrix processed through liquid metallurgy route. Proceedings of the Institution of Mechanical Engineers, Part B: Journal of Engineering Manufacture 2024:09544054241272883. DOI: 10.1177/09544054241272883.
[334] Abazari S, Shamsipur A, Bakhsheshi-Rad HR, Soheilirad MS, Khorashadizade F, Mirhosseini SS. MgO-attached graphene nanosheet (MgO@GNS) reinforced magnesium matrix nanocomposite with superior mechanical, corrosion and biological performance. Int J Miner Metall Mater 2024;31:2062–76. https://doi.org/10.1007/s12613-023-2797-0.
[335] Ambat R, Aung NN, Zhou W. Evaluation of microstructural effects on the corrosion behaviour of AZ91D magnesium alloy. Corros Sci 2000;42:1433–55. https://doi.org/10.1016/S0010-938X(99)00143-2.
[336] Ralston KD, Birbilis N. Effect of Grain Size on Corrosion: A Review. Corrosion 2010;66:075005-075005–13. DOI: 10.5006/1.3462912.
[337] El-Moneim AA, Akiyama E, Ismail KM, Hashimoto K. Corrosion behaviour of sputter-deposited Mg–Zr alloys in a borate buffer solution. Corros Sci 2011;53:2988–93. https://doi.org/10.1016/j.corsci.2011.05.043.
[338] Ralston KD, Birbilis N, Davies CHJ. Revealing the relationship between grain size and corrosion rate of metals. Scr Mater 2010;63:1201–4. https://doi.org/10.1016/j.scriptamat.2010.08.035.

[339] Yang L, Zheng Y, Wan C-L, Gong Q-M, Zhang C, Chen H, et al. Characteristics of oxide pegs in Ti- and Y-doped CoNiCrAl alloys at 1150 °C. Rare Met 2021;40:2059–64. https://doi.org/10.1007/s12598-020-01577-0.
[340] Li L, Huang Z, Chen L, Zhang L, Li M, Hou H, et al. Electrochemical corrosion behavior of AZ91D magnesium alloy-graphene nanoplatelets composites in simulated body fluids. J Mater Res Technol 2023;24:449–62. https://doi.org/10.1016/j.jmrt.2023.01.232.
[341] Kavimani V, Soorya Prakash K, Arun PM. Influence of r-GO addition on enhancement of corrosion and wear behavior of AZ31 MMC. Appl Phys A 2017;123:514. https://doi.org/10.1007/s00339-017-1118-8.
[342] Yang N, Balasubramani N, Venezuela J, Almathami S, Wen C, Dargusch M. The influence of Ca and Cu additions on the microstructure, mechanical and degradation properties of Zn–Ca–Cu alloys for absorbable wound closure device applications. Bioact Mater 2021;6:1436–51. https://doi.org/10.1016/j.bioactmat.2020.10.015.
[343] Shi Z-Z, Gao X-X, Zhang H-J, Liu X-F, Li H-Y, Zhou C, et al. Design biodegradable Zn alloys: Second phases and their significant influences on alloy properties. Bioact Mater 2020;5:210–8. https://doi.org/10.1016/j.bioactmat.2020.02.010.
[344] Scarcello E, Lison D. Are Fe-Based Stenting Materials Biocompatible? A Critical Review of In Vitro and In Vivo Studies. Journal of Functional Biomaterials 2020;11:2. https://doi.org/10.3390/jfb11010002.
[345] Peuster M, Hesse C, Schloo T, Fink C, Beerbaum P, von Schnakenburg C. Long-term biocompatibility of a corrodible peripheral iron stent in the porcine descending aorta. Biomaterials 2006;27:4955–62. https://doi.org/10.1016/j.biomaterials.2006.05.029.
[346] Short-Term Effects of Biocorrodible Iron Stents in Porcine Coronary Arteries - WAKSMAN - 2008 - Journal of Interventional Cardiology - Wiley Online Library n.d. https://onlinelibrary.wiley.com/doi/10.1111/j.1540-8183.2007.00319.x (accessed February 13, 2025).
[347] Peuster M, Wohlsein P, Brügmann M, Ehlerding M, Seidler K, Fink C, et al. A novel approach to temporary stenting: degradable cardiovascular stents produced from corrodible metal—results 6–18 months after implantation into New Zealand white rabbits. Heart 2001;86:563–9. https://doi.org/10.1136/heart.86.5.563.
[348] Rybalchenko O, Anisimova N, Martynenko N, Rybalchenko G, Belyakov A, Shchetinin I, et al. Biocompatibility and Degradation of Fe-Mn-5Si Alloy after Equal-Channel Angular Pressing: In Vitro and In Vivo Study. Applied Sciences 2023;13:9628. DOI: 10.3390/app13179628.
[349] Kraus T, Moszner F, Fischerauer S, Fiedler M, Martinelli E, Eichler J, et al. Biodegradable Fe-based alloys for use in osteosynthesis: Outcome of an in vivo study after 52 weeks. Acta Biomater 2014;10:3346–53. https://doi.org/10.1016/j.actbio.2014.04.007.
[350] Schultze JW, Davepon B, Karman F, Rosenkranz C, Schreiber A, Voigt O. Corrosion and passivation in nanoscopic and microscopic dimensions: the influence of grains and grain boundaries. Corros Eng Sci Technol 2004;39:45–52. https://doi.org/10.1179/147842204225016813.
[351] Dong S, Chen X, La Plante EC, Gussev M, Leonard K, Sant G. Elucidating the grain-orientation dependent corrosion rates of austenitic stainless steels. Mater Des 2020;191:108583. https://doi.org/10.1016/j.matdes.2020.108583.
[352] Wang Y, Li KY, Scenini F, Jiao J, Qu SJ, Luo Q, et al. The effect of residual stress on the electrochemical corrosion behavior of Fe-based amorphous coatings in chloride-containing solutions. Surf Coat Technol 2016;302:27–38. https://doi.org/10.1016/j.surfcoat.2016.05.034.
[353] Wang P, Ma L, Cheng X, Li X. Influence of grain refinement on the corrosion behavior of metallic materials: A review. Int J Miner Metall Mater 2021;28:1112–26. https://doi.org/10.1007/s12613-021-2308-0.
[354] Maurice V, Marcus P. Progress in corrosion science at atomic and nanometric scales. Prog Mater Sci 2018;95:132–71. https://doi.org/10.1016/j.pmatsci.2018.03.001.
[355] Wang Y, Liu B, Zhao X, Zhang X, Miao Y, Yang N, et al. Turning a native or corroded Mg alloy surface into an anti-corrosion coating in excited CO2. Nat Commun 2018;9:4058. https://doi.org/10.1038/s41467-018-06433-5.
[356] Wu Y, Zhu X, Zhao W, Wang Y, Wang C, Xue Q. Corrosion mechanism of graphene coating with different defect levels. J Alloy Compd 2019;777:135–44. https://doi.org/10.1016/j.jallcom.2018.10.260.
[357] Bagherifard S, Molla MF, Kajanek D, Donnini R, Hadzima B, Guagliano M. Accelerated biodegradation and improved mechanical performance of pure iron through surface grain refinement. Acta Biomater 2019;98:88–102. https://doi.org/10.1016/j.actbio.2019.05.033.
[358] Huang S-J, Wang C-F, Subramani M, Selvaraju S, Rajagopal V, Chiang C-C, et al. The impact of graphene on the mechanical properties, corrosion behavior, and biocompatibility of an Mg–Ca alloy. J Am Ceram Soc 2024;107:8312–27. https://doi.org/10.1111/jace.20091.
[359] Liu T, Lyu W, Li Z, Wang S, Wang X, Jiang J, et al. Recent progress on corrosion mechanisms of graphene-reinforced metal matrix composites. Nanotechnol Rev 2023;12. https://doi.org/10.1515/ntrev-2022-0566.
[360] Sun X, Yu X, Li W, Chen M, Liu D. Mechanical properties, degradation behavior and cytocompatibility of biodegradable 3vol%X (X = MgO, ZnO and CuO)/Zn matrix composites with excellent dispersion property fabricated by graphene oxide-assisted hetero-aggregation. Biomaterials Advances 2022;134:112722. https://doi.org/10.1016/j.msec.2022.112722.
[361] Safari N, Golafshan N, Kharaziha M, Reza Toroghinejad M, Utomo L, Malda J, et al. Stable and Antibacterial Magnesium–Graphene Nanocomposite-Based Implants for Bone Repair. ACS Biomater Sci Eng 2020;6:6253–62. https://doi.org/10.1021/acsbiomaterials.0c00613.
[362] Xia D, Qin Y, Guo H, Wen P, Lin H, Voshage M, et al. Additively manufactured pure zinc porous scaffolds for critical-sized bone defects of rabbit femur. Bioact Mater 2023;19:12–23. https://doi.org/10.1016/j.bioactmat.2022.03.010.
[363] Chatterjee N, Eom H-J, Choi J. A systems toxicology approach to the surface functionality control of graphene–cell interactions. Biomaterials 2014;35:1109–27. https://doi.org/10.1016/j.biomaterials.2013.09.108.
[364] Saberi A, Bakhsheshi-Rad HR, Karamian E, Kasiri-Asgarani M, Ghomi H. Magnesium-graphene nano-platelet composites: Corrosion behavior, mechanical and biological properties. J Alloy Compd 2020;821:153379. https://doi.org/10.1016/j.jallcom.2019.153379.
[365] Jabbarzare S, Bakhsheshi-Rad HR, Nourbakhsh AA, Ahmadi T, Berto F. Effect of graphene oxide on the corrosion, mechanical and biological properties of Mg-based nanocomposite. Int J Miner Metall Mater 2022;29:305–19. https://doi.org/10.1007/s12613-020-2201-2.
[366] Saberi A, Bakhsheshi-Rad HR, Karamian E, Kasiri-Asgarani M, Ghomi H, Omidi M, et al. Synthesis and Characterization of Hot Extruded Magnesium-Zinc Nano-Composites Containing Low Content of Graphene Oxide for Implant Applications. Phys Mesomech 2021;24:486–502. https://doi.org/10.1134/S1029959921040135.
[367] Sharifi S, Ebrahimian-Hosseinabadi M, Dini G, Toghyani S. Magnesium-zinc-graphene oxide nanocomposite scaffolds for bone tissue engineering. Arab J Chem 2023;16:104715. https://doi.org/10.1016/j.arabjc.2023.104715.
[368] Tao J-X, Zhao M-C, Zhao Y-C, Yin D-F, Liu L, Gao C, et al. Influence of graphene oxide (GO) on microstructure and biodegradation of ZK30-xGO composites prepared by selective laser melting. J Magnesium Alloys 2020;8:952–62. https://doi.org/10.1016/j.jma.2019.10.004.
[369] Fan M, Zhao F, Peng S, Dai Q, Liu Y, Yin S, et al. Biocompatibility of Zinc Matrix Biodegradable Composites Reinforced by Graphene Nanosheets. Materials 2022;15:6481. https://doi.org/10.3390/ma15186481.
[370] Ebrahimi S, Bordbar-Khiabani A, Yarmand B. Immobilization of rGO/ZnO hybrid composites on the Zn substrate for enhanced photocatalytic activity and corrosion stability. J Alloy Compd 2020;845:156219. https://doi.org/10.1016/j.jallcom.2020.156219.
[371] ISO 2009.
[372] Yamamoto A, Honma R, Sumita M. Cytotoxicity evaluation of 43 metal salts using murine fibroblasts and osteoblastic cells. J Biomed Mater Res 1998;39:331–40. https://doi.org/10.1002/(SICI)1097-4636(199802)39:2<331::AID-JBM22>3.0.CO;2-E.
[373] Mandal A, Tiwari JK, Sathish N, Srivastava AK. Microstructural and mechanical properties evaluation of graphene reinforced stainless steel composite produced via selective laser melting. Mater Sci Eng A 2020;774:138936. https://doi.org/10.1016/j.msea.2020.138936.
[374] Liscio A, Kouroupis-Agalou K, Betriu XD, Kovtun A, Treossi E, Pugno NM, et al. Evolution of the size and shape of 2D nanosheets during ultrasonic fragmentation. 2D Mater 2017;4:025017. https://doi.org/10.1088/2053-1583/aa57ff.
[375] Akhavan O, Ghaderi E, Akhavan A. Size-dependent genotoxicity of graphene nanoplatelets in human stem cells. Biomaterials 2012;33:8017–25. https://doi.org/10.1016/j.biomaterials.2012.07.040.
[376] Gregorio Mendes R, Koch B, Bachmatiuk A, Ma X, Sanchez S, Damm C, et al. A size dependent evaluation of the cytotoxicity and uptake of nanographene oxide. J Mater Chem B 2015;3:2522–9. https://doi.org/10.1039/C5TB00180C.

[377] Ma J, Liu R, Wang X, Liu Q, Chen Y, Valle RP, et al. Crucial Role of Lateral Size for Graphene Oxide in Activating Macrophages and Stimulating Pro-inflammatory Responses in Cells and Animals. ACS Nano 2015;9:10498–515. https://doi.org/10.1021/acsnano.5b04751.
[378] Jennifer M, Maciej W. Nanoparticle Technology as a Double-Edged Sword: Cytotoxic, Genotoxic and Epigenetic Effects on Living Cells. Journal of Biomaterials and Nanobiotechnology 2013;4:53–63. https://doi.org/10.4236/jbnb.2013.41008.
[379] Terrones M, Botello-Méndez AR, Campos-Delgado J, López-Urías F, Vega-Cantú YI, Rodríguez-Macías FJ, et al. Graphene and graphite nanoribbons: Morphology, properties, synthesis, defects and applications. Nano Today 2010;5:351–72. https://doi.org/10.1016/j.nantod.2010.06.010.
[380] Cheng C, Nie S, Li S, Peng H, Yang H, Ma L, et al. Biopolymer functionalized reduced graphene oxide with enhanced biocompatibility via mussel inspired coatings/anchors. J Mater Chem B 2012;1:265–75. https://doi.org/10.1039/C2TB00025C.
[381] Liao K-H, Lin Y-S, Macosko CW, Haynes CL. Cytotoxicity of Graphene Oxide and Graphene in Human Erythrocytes and Skin Fibroblasts. ACS Appl Mater Interfaces 2011;3:2607–15. https://doi.org/10.1021/am200428v.
[382] Ruiz ON, Fernando KAS, Wang B, Brown NA, Luo PG, McNamara ND, et al. Graphene Oxide: A Nonspecific Enhancer of Cellular Growth. ACS Nano 2011;5:8100–7. https://doi.org/10.1021/nn202699t.
[383] Chou SS, De M, Luo J, Rotello VM, Huang J, VinayakP D. Nanoscale Graphene Oxide (nGO) as Artificial Receptors: Implications for Biomolecular Interactions and Sensing. J Am Chem Soc 2012;134:16725–33. https://doi.org/10.1021/ja306767y.
[384] Akhavan O, Ghaderi E. Toxicity of Graphene and Graphene Oxide Nanowalls Against Bacteria. ACS Nano 2010;4:5731–6. https://doi.org/10.1021/nn101390x.
[385] Forman HJ, Zhang H. Targeting oxidative stress in disease: promise and limitations of antioxidant therapy. Nat Rev Drug Discov 2021;20:689–709. https://doi.org/10.1038/s41573-021-00233-1.
[386] Li R, Guiney LM, Chang CH, Mansukhani ND, Ji Z, Wang X, et al. Surface Oxidation of Graphene Oxide Determines Membrane Damage, Lipid Peroxidation, and Cytotoxicity in Macrophages in a Pulmonary Toxicity Model. ACS Nano 2018;12:1390–402. https://doi.org/10.1021/acsnano.7b07737.
[387] Novoselov KS, Geim AK, Morozov SV, Jiang D, Zhang Y, Dubonos SV, et al. Electric Field Effect in Atomically Thin Carbon Films. Science 2004;306:666–9. https://doi.org/10.1126/science.1102896.
[388] Nayak TR, Andersen H, Makam VS, Khaw C, Bae S, Xu X, et al. Graphene for Controlled and Accelerated Osteogenic Differentiation of Human Mesenchymal Stem Cells. ACS Nano 2011;5:4670–8. https://doi.org/10.1021/nn200500h.
[389] Li K, Wang C, Yan J, Zhang Q, Dang B, Wang Z, et al. Evaluation of the osteogenesis and osseointegration of titanium alloys coated with graphene: an in vivo study. Sci Rep 2018;8:1843. https://doi.org/10.1038/s41598-018-19742-y.
[390] Crowder SW, Prasai D, Rath R, Balikov DA, Bae H, Bolotin KI, et al. Three-dimensional graphene foams promote osteogenic differentiation of human mesenchymal stem cells. Nanoscale 2013;5:4171–6. https://doi.org/10.1039/C3NR00803G.
[391] Akhavan O, Ghaderi E, Shahsavar M. Graphene nanogrids for selective and fast osteogenic differentiation of human mesenchymal stem cells. Carbon 2013;59:200–11. https://doi.org/10.1016/j.carbon.2013.03.010.
[392] Xie H, Cao T, Gomes JV, Castro Neto AH, Rosa V. Two and three-dimensional graphene substrates to magnify osteogenic differentiation of periodontal ligament stem cells. Carbon 2015;93:266–75. https://doi.org/10.1016/j.carbon.2015.05.071.
[393] Lee WC, Lim CHYX, Shi H, Tang LAL, Wang Y, Lim CT, et al. Origin of Enhanced Stem Cell Growth and Differentiation on Graphene and Graphene Oxide. ACS Nano 2011;5:7334–41. https://doi.org/10.1021/nn202190c.
[394] Chimene D, Alge DL, Gaharwar AK. Two-Dimensional Nanomaterials for Biomedical Applications: Emerging Trends and Future Prospects. Adv Mater 2015;27:7261–84. https://doi.org/10.1002/adma.201502422.
[395] Kang E-S, Kim D-S, Suhito IR, Choo S-S, Kim S-J, Song I, et al. Guiding osteogenesis of mesenchymal stem cells using carbon-based nanomaterials. Nano Convergence 2017;4:2. https://doi.org/10.1186/s40580-017-0096-z.
[396] Dubey A, Vahabi H, Kumaravel V. Antimicrobial and Biodegradable 3D Printed Scaffolds for Orthopedic Infections. ACS Biomater Sci Eng 2023;9:4020–44. https://doi.org/10.1021/acsbiomaterials.3c00115.
[397] Progress in the application of graphene and its derivatives to osteogenesis: Heliyon n.d. https://www.cell.com/heliyon/fulltext/S2405-8440(23)09080-1?_returnURL=https%3A%2F%2Flinkinghub.elsevier.com%2Fretrieve%2Fpii%2FS2405844023090801%3Fshowall%3Dtrue (accessed December 27, 2023).
[398] Huang S, Zhong Y, Fu Y, Zheng X, Feng Z, Mo A. Graphene and its derivatives: "one stone, three birds" strategy for orthopedic implant-associated infections. Biomater Sci 2023;11:380–99. https://doi.org/10.1039/D2BM01507B.
[399] Ruan J, Wang X, Yu Z, Wang Z, Xie Q, Zhang D, et al. Enhanced Physiochemical and Mechanical Performance of Chitosan-Grafted Graphene Oxide for Superior Osteoinductivity. Adv Funct Mater 2016;26:1085–97. https://doi.org/10.1002/adfm.201504141.
[400] Ku SH, Lee M, Park CB. Carbon-Based Nanomaterials for Tissue Engineering. Adv Healthc Mater 2013;2:244–60. https://doi.org/10.1002/adhm.201200307.
[401] Yan M, Wang F, Han C, Ma X, Xu X, An Q, et al. Nanowire templated semihollow bicontinuous graphene scrolls: designed construction, mechanism, and enhanced energy storage performance. J Am Chem Soc 2013;135:18176–82. https://doi.org/10.1021/ja409027s.
[402] Ou L, Tan X, Qiao S, Wu J, Su Y, Xie W, et al. Graphene-based material-mediated immunomodulation in tissue engineering and regeneration: mechanism and significance. ACS Nano 2023;17:18669–87. https://doi.org/10.1021/acsnano.3c03857.
[403] Zheng Z, Chen Y, Hong H, Shen Y, Wang Y, Sun J, et al. The "Yin and Yang" of Immunomodulatory Magnesium-Enriched Graphene Oxide Nanoscrolls Decorated Biomimetic Scaffolds in Promoting Bone Regeneration. Adv Healthc Mater 2021;10:2000631. https://doi.org/10.1002/adhm.202000631.
[404] Chen J, Zhang X, Cai H, Chen Z, Wang T, Jia L, et al. Osteogenic activity and antibacterial effect of zinc oxide/carboxylated graphene oxide nanocomposites: Preparation and in vitro evaluation. Colloids Surf B Biointerfaces 2016;147:397–407. https://doi.org/10.1016/j.colsurfb.2016.08.023.
[405] Sun X, Yu X, Li W, Chen M, Liu D. Fabrication and characterization of biodegradable zinc matrix composites reinforced by uniformly dispersed beta-tricalcium phosphate via graphene oxide-assisted hetero-agglomeration. Mater Sci Eng C 2021;130:112431. https://doi.org/10.1016/j.msec.2021.112431.
[406] Yuan B, Bao C, Song L, Hong N, Liew KM, Hu Y. Preparation of functionalized graphene oxide/polypropylene nanocomposite with significantly improved thermal stability and studies on the crystallization behavior and mechanical properties. Chem Eng J 2014;237:411–20. https://doi.org/10.1016/j.cej.2013.10.030.
[407] Cai D, E T, Yang S, Ma Z, Li Y, Liu L, et al. Effect of mixed-phase TiO2 doped with Ca2+ on charge transfer at the TiO2/graphene interface. Electrochimica Acta 2022;422:140503. DOI: 10.1016/j.electacta.2022.140503.
[408] Xie H, Cao T, Franco-Obregón A, Rosa V. Graphene-Induced Osteogenic Differentiation Is Mediated by the Integrin/FAK Axis. Int J Mol Sci 2019;20:574. https://doi.org/10.3390/ijms20030574.
[409] Marrella A, Lee TY, Lee DH, Karuthedom S, Syla D, Chawla A, et al. Engineering vascularized and innervated bone biomaterials for improved skeletal tissue regeneration. Mater Today 2018;21:362–76. https://doi.org/10.1016/j.mattod.2017.10.005.
[410] Pan C, Zhao Y, Yang Y, Yang M, Hong Q, Yang Z, et al. Immobilization of bioactive complex on the surface of magnesium alloy stent material to simultaneously improve anticorrosion, hemocompatibility and antibacterial activities. Colloids Surf B Biointerfaces 2021;199:111541. https://doi.org/10.1016/j.colsurfb.2020.111541.
[411] Xue D, Chen E, Zhong H, Zhang W, Wang S, Joomun MU, et al. Immunomodulatory properties of graphene oxide for osteogenesis and angiogenesis. Int J Nanomed 2018;13:5799–810. https://doi.org/10.2147/IJN.S170305.
[412] Li X, Liu H, Niu X, Yu B, Fan Y, Feng Q, et al. The use of carbon nanotubes to induce osteogenic differentiation of human adipose-derived MSCs in vitro and ectopic bone formation in vivo. Biomaterials 2012;33:4818–27. https://doi.org/10.1016/j.biomaterials.2012.03.045.
[413] Kim T-H, Shah S, Yang L, Yin PT, Hossain MK, Conley B, et al. Controlling Differentiation of Adipose-Derived Stem Cells Using Combinatorial Graphene Hybrid-Pattern Arrays. ACS Nano 2015;9:3780–90. https://doi.org/10.1021/nn5066028.
[414] Guilak F, Cohen DM, Estes BT, Gimble JM, Liedtke W, Chen CS. Control of Stem Cell Fate by Physical Interactions with the Extracellular Matrix. Cell Stem Cell 2009;5:17–26. https://doi.org/10.1016/j.stem.2009.06.016.
[415] Dalby MJ, Gadegaard N, Tare R, Andar A, Riehle MO, Herzyk P, et al. The control of human mesenchymal cell differentiation using nanoscale symmetry and disorder. Nature Mater 2007;6:997–1003. https://doi.org/10.1038/nmat2013.

[416] Reilly GC, Engler AJ. Intrinsic extracellular matrix properties regulate stem cell differentiation. J Biomech 2010;43:55–62. https://doi.org/10.1016/j.jbiomech.2009.09.009.
[417] Solanki A, Shah S, Memoli KA, Park SY, Hong S, Lee K-B. Controlling Differentiation of Neural Stem Cells Using Extracellular Matrix Protein Patterns. Small 2010;6:2509–13. https://doi.org/10.1002/smll.201001341.
[418] Dalby MJ, Gadegaard N, Oreffo ROC. Harnessing nanotopography and integrin–matrix interactions to influence stem cell fate. Nature Mater 2014;13:558–69. https://doi.org/10.1038/nmat3980.
[419] Wang X, Song W, Kawazoe N, Chen G. The osteogenic differentiation of mesenchymal stem cells by controlled cell–cell interaction on micropatterned surfaces. J Biomed Mater Res A 2013;101:3388–95. https://doi.org/10.1002/jbm.a.34645.
[420] Parsons JT, Horwitz AR, Schwartz MA. Cell adhesion: integrating cytoskeletal dynamics and cellular tension. Nat Rev Mol Cell Biol 2010;11:633–43. https://doi.org/10.1038/nrm2957.
[421] Dalby MJ, Biggs MJP, Gadegaard N, Kalna G, Wilkinson CDW, Curtis ASG. Nanotopographical stimulation of mechanotransduction and changes in interphase centromere positioning. J Cell Biochem 2007;100:326–38. https://doi.org/10.1002/jcb.21058.
[422] Yang J-W, Hsieh KY, Kumar PV, Cheng S-J, Lin Y-R, Shen Y-C, et al. Enhanced Osteogenic Differentiation of Stem Cells on Phase-Engineered Graphene Oxide. ACS Appl Mater Interfaces 2018;10:12497–503. https://doi.org/10.1021/acsami.8b02225.
[423] Li Z, Xiang S, Lin Z, Li EN, Yagi H, Cao G, et al. Graphene oxide-functionalized nanocomposites promote osteogenesis of human mesenchymal stem cells via enhancement of BMP-SMAD1/5 signaling pathway. Biomaterials 2021;277:121082. https://doi.org/10.1016/j.biomaterials.2021.121082.
[424] Xue H, Zhang Z, Lin Z, Su J, Panayi AC, Xiong Y, et al. Enhanced tissue regeneration through immunomodulation of angiogenesis and osteogenesis with a multifaceted nanohybrid modified bioactive scaffold. Bioact Mater 2022;18:552–68. https://doi.org/10.1016/j.bioactmat.2022.05.023.
[425] Tao B, Chen M, Lin C, Lu L, Yuan Z, Liu J, et al. Zn-incorporation with graphene oxide on Ti substrates surface to improve osteogenic activity and inhibit bacterial adhesion. J Biomed Mater Res A 2019;107:2310–26. https://doi.org/10.1002/jbm.a.36740.
[426] Zhang J, Eyisoylu H, Qin X-H, Rubert M, Müller R. 3D bioprinting of graphene oxide-incorporated cell-laden bone mimicking scaffolds for promoting scaffold fidelity, osteogenic differentiation and mineralization. Acta Biomater 2021;121:637–52. https://doi.org/10.1016/j.actbio.2020.12.026.
[427] La W-G, Park S, Yoon H-H, Jeong G-J, Lee T-J, Bhang SH, et al. Delivery of a therapeutic protein for bone regeneration from a substrate coated with graphene oxide. Small 2013;9:4051–60. https://doi.org/10.1002/smll.201300571.
[428] Daly AC, Pitacco P, Nulty J, Cunniffe GM, Kelly DJ. 3D printed microchannel networks to direct vascularisation during endochondral bone repair. Biomaterials 2018;162:34–46. https://doi.org/10.1016/j.biomaterials.2018.01.057.
[429] Mishima Y, Lotz M. Chemotaxis of human articular chondrocytes and mesenchymal stem cells. J Orthop Res 2008;26:1407–12. https://doi.org/10.1002/jor.20668.
[430] Lee J-H, Choi HK, Yang L, Chueng S-T-D, Choi J-W, Lee K-B. Nondestructive Real-Time Monitoring of Enhanced Stem Cell Differentiation Using a Graphene-Au Hybrid Nanoelectrode Array. Adv Mater 2018;30:1802762. https://doi.org/10.1002/adma.201802762.
[431] Liu F, Xue L, Xu L, Liu J, Xie C, Chen C, et al. Preparation and characterization of bovine serum albumin nanoparticles modified by Poly-l-lysine functionalized graphene oxide for BMP-2 delivery. Mater Des 2022;215:110479. https://doi.org/10.1016/j.matdes.2022.110479.
[432] Chandran R, Knobloch TJ, Anghelina M, Agarwal S. Biomechanical signals upregulate myogenic gene induction in the presence or absence of inflammation. Am J Phys Cell Phys 2007;293:C267–76. https://doi.org/10.1152/ajpcell.00594.2006.
[433] Engler AJ, Sen S, Sweeney HL, Discher DE. Matrix Elasticity Directs Stem Cell Lineage Specification. Cell 2006;126:677–89. https://doi.org/10.1016/j.cell.2006.06.044.
[434] Kern B, Shen J, Starbuck M, Karsenty G. Cbfa1 Contributes to the Osteoblast-specific Expression of type I collagen Genes*. J Biol Chem 2001;276:7101–7. https://doi.org/10.1074/jbc.M006215200.
[435] Wu C, Han P, Xu M, Zhang X, Zhou Y, Xue G, et al. Nagelschmidtite bioceramics with osteostimulation properties: material chemistry activating osteogenic genes and WNT signalling pathway of human bone marrow stromal cells. J Mater Chem B 2013;1:876–85. https://doi.org/10.1039/C2TB00391K.
[436] Wu C, Xia L, Han P, Xu M, Fang B, Wang J, et al. Graphene-oxide-modified β-tricalcium phosphate bioceramics stimulate in vitro and in vivo osteogenesis. Carbon 2015;93:116–29. https://doi.org/10.1016/j.carbon.2015.04.048.
[437] Mirza EH, Khan AA, Al-Khureif AA, Saadaldin SA, Mohamed BA, Fareedi F, et al. Characterization of osteogenic cells grown over modified graphene-oxide-biostable polymers. Biomed Mater 2019;14:065004. https://doi.org/10.1088/1748-605X/ab3ab2.
[438] Chen X, Wang M, Chen F, Wang J, Li X, Liang J, et al. Correlations between macrophage polarization and osteoinduction of porous calcium phosphate ceramics. Acta Biomater 2020;103:318–32. https://doi.org/10.1016/j.actbio.2019.12.019.
[439] Zhang Y, Böse T, Unger RE, Jansen JA, Kirkpatrick CJ, van den Beucken JJJP. Macrophage type modulates osteogenic differentiation of adipose tissue MSCs. Cell Tissue Res 2017;369:273–86. https://doi.org/10.1007/s00441-017-2598-8.
[440] Zou M, Sun J, Xiang Z. Induction of M2-type macrophage differentiation for bone defect repair via an interpenetration network Hydrogel with a GO-Based Controlled Release System. Adv Healthc Mater 2021;10:2001502. https://doi.org/10.1002/adhm.202001502.
[441] Chen G-Y, Chen C-L, Tuan H-Y, Yuan P-X, Li K-C, Yang H-J, et al. Graphene oxide triggers toll-like receptors/autophagy responses in vitro and inhibits tumor growth in vivo. Adv Healthc Mater 2014;3:1486–95. https://doi.org/10.1002/adhm.201300591.
[442] Su J, Du Z, Xiao L, Wei F, Yang Y, Li M, et al. Graphene oxide coated Titanium Surfaces with Osteoimmunomodulatory Role to Enhance Osteogenesis. Mater Sci Eng C 2020;113:110983. https://doi.org/10.1016/j.msec.2020.110983.
[443] Lee J, Byun H, Madhurakkat Perikamana SK, Lee S, Shin H. Current Advances in Immunomodulatory Biomaterials for Bone Regeneration. Adv Healthc Mater 2019;8:1801106. https://doi.org/10.1002/adhm.201801106.
[444] Wu M, Zou L, Jiang L, Zhao Z, Liu J. Osteoinductive and antimicrobial mechanisms of graphene-based materials for enhancing bone tissue engineering. J Tissue Eng Regen Med 2021;15:915–35. https://doi.org/10.1002/term.3239.
[445] Szunerits S, Boukherroub R. Antibacterial activity of graphene-based materials. J Mater Chem B 2016;4:6892–912. https://doi.org/10.1039/C6TB01647B.
[446] Saberi A, Bakhsheshi-Rad HR, Ismail AF, Sharif S, Razzaghi M, Ramakrishna S, et al. The Effect of Co-Encapsulated GO-Cu Nanofillers on Mechanical Properties, Cell Response, and Antibacterial Activities of Mg-Zn Composite. Metals 2022;12:207. https://doi.org/10.3390/met12020207.
[447] Abazari S, Shamsipur A, Bakhsheshi-Rad HR. Reduced graphene oxide (RGO) reinforced Mg biocomposites for use as orthopedic applications: Mechanical properties, cytocompatibility and antibacterial activity. J Magnesium Alloys 2022;10:3612–27. https://doi.org/10.1016/j.jma.2021.09.016.
[448] Zhang X, Hong J, Chen G. Functionalized graphene nano-platelet reinforced magnesium-based biocomposites for potential implant applications. Proceedings of the Institution of Mechanical Engineers, Part B: Journal of Engineering Manufacture 2024:09544054241277590. DOI: 10.1177/09544054241277590.
[449] Wang X, Di T, Li W, Liu D, Sun X. Interfacial strengthening and antibacterial behavior in an ultrafine-grained Zn-Ag-based biocomposites fabricated by the Cu2O-induced in situ wetting approach. J Mater Sci Technol 2023;152:109–34. https://doi.org/10.1016/j.jmst.2022.11.062.
[450] Sun X, Wang X, Xu Y, Li W, Liu D. Microstructure and properties of Cu2O-GO/Zn biocomposites fabricated by a novel in situ wetting strategy. Mater Des 2022;220:110870. https://doi.org/10.1016/j.matdes.2022.110870.
[451] Owhal A, Choudhary M, Pingale AD, Belgamwar SU, Mukherjee S, Rathore JS. Non-cytotoxic zinc/*f*-graphene nanocomposite for tunable degradation and superior tribo-mechanical properties: Synthesized via modified electro co-deposition route. Mater Today Commun 2023;34:105112. https://doi.org/10.1016/j.mtcomm.2022.105112.
[452] Hegab HM, ElMekawy A, Zou L, Mulcahy D, Saint CP, Ginic-Markovic M. The controversial antibacterial activity of graphene-based materials. Carbon 2016;105:362–76. https://doi.org/10.1016/j.carbon.2016.04.046.
[453] Liu C, Shen J, Yeung KWK, Tjong SC. Development and Antibacterial Performance of Novel Polylactic Acid-Graphene Oxide-Silver Nanoparticle Hybrid Nanocomposite Mats Prepared By Electrospinning. ACS Biomater Sci Eng 2017;3:471–86. https://doi.org/10.1021/acsbiomaterials.6b00766.
[454] Zhao R, Kong W, Sun M, Yang Y, Liu W, Lv M, et al. Highly Stable Graphene-Based Nanocomposite (GO–PEI–Ag) with Broad-Spectrum, Long-Term Antimicrobial Activity and Antibiofilm Effects. ACS Appl Mater Interfaces 2018;10:17617–29. https://doi.org/10.1021/acsami.8b03185.

[455] Zou X, Zhang L, Wang Z, Luo Y. Mechanisms of the antimicrobial activities of graphene materials. J Am Chem Soc 2016;138:2064–77. https://doi.org/10.1021/jacs.5b11411.
[456] Ghai I. A Barrier to Entry: Examining the Bacterial Outer Membrane and Antibiotic Resistance. Appl Sci 2023;13:4238. https://doi.org/10.3390/app13074238.
[457] Wang Y, de Carvalho NA, Tan S, Gilbertson LM. Leveraging electrochemistry to uncover the role of nitrogen in the biological reactivity of nitrogen-doped graphene. Environ Sci: Nano 2019;6:3525–38. https://doi.org/10.1039/C9EN00802K.
[458] Jin X, Xie D, Zhang Z, Liu A, Wang M, Dai J, et al. *In vitro* and *in vivo* studies on biodegradable Zn porous scaffolds with a drug-loaded coating for the treatment of infected bone defect. Mater Today Bio 2024;24:100885. https://doi.org/10.1016/j.mtbio.2023.100885.
[459] Zhou J, Fang C, Rong C, Luo T, Liu J, Zhang K. Reactive oxygen species-sensitive materials: A promising strategy for regulating inflammation and favoring tissue regeneration. Smart Mater Med 2023;4:427–46. https://doi.org/10.1016/j.smaim.2023.01.004.
[460] Li Y, Chen M, Yan J, Zhou W, Gao S, Liu S, et al. Tannic acid/Sr2+-coated silk/graphene oxide-based meniscus scaffold with anti-inflammatory and anti-ROS functions for cartilage protection and delaying osteoarthritis. Acta Biomater 2021;126:119–31. https://doi.org/10.1016/j.actbio.2021.02.046.
[461] Hu W, Peng C, Luo W, Lv M, Li X, Li D, et al. Graphene-Based Antibacterial Paper. ACS Nano 2010;4:4317–23. https://doi.org/10.1021/nn101097v.
[462] Gurunathan S, Han JW, Dayem AA, Eppakayala V, Kim J-H. Oxidative stress-mediated antibacterial activity of graphene oxide and reduced graphene oxide in Pseudomonas aeruginosa. IJN 2012;7:5901–14. https://doi.org/10.2147/IJN.S37397.
[463] Shi L, Chen J, Teng L, Wang L, Zhu G, Liu S, et al. The Antibacterial Applications of Graphene and Its Derivatives. Small 2016;12:4165–84. https://doi.org/10.1002/smll.201601841.
[464] Tailoring Materials with Specific Wettability in Biomedical Engineering - Sun - 2021 - Advanced Science - Wiley Online Library n.d. https://advanced.onlinelibrary.wiley.com/doi/10.1002/advs.202100126 (accessed February 19, 2025).
[465] Wei J, Igarashi T, Okumori N, Igarashi T, Maetani T, Liu B, et al. Influence of surface wettability on competitive protein adsorption and initial attachment of osteoblasts. Biomed Mater 2009;4:045002. https://doi.org/10.1088/1748-6041/4/4/045002.
[466] Godoy-Gallardo M, Eckhard U, Delgado LM, de Roo Puente YJD, Hoyos-Nogués M, Gil FJ, et al. Antibacterial approaches in tissue engineering using metal ions and nanoparticles: From mechanisms to applications. Bioact Mater 2021;6:4470–90. https://doi.org/10.1016/j.bioactmat.2021.04.033.
[467] Su Y, Wang K, Gao J, Yang Y, Qin Y-X, Zheng Y, et al. Enhanced cytocompatibility and antibacterial property of zinc phosphate coating on biodegradable zinc materials. Acta Biomater 2019;98:174–85. https://doi.org/10.1016/j.actbio.2019.03.055.
[468] Bryzgalov V, Kistanov AA, Khafizova E, Polenok M, Izosimov A, Korznikova EA. Experimental study of corrosion rate supplied with an ab-initio elucidation of corrosion mechanism of biodegradable implants based on Ag-doped Zn alloys. Appl Surf Sci 2024;652:159300. https://doi.org/10.1016/j.apsusc.2024.159300.
[469] Rai M, Yadav A, Gade A. Silver nanoparticles as a new generation of antimicrobials. Biotechnol Adv 2009;27:76–83. https://doi.org/10.1016/j.biotechadv.2008.09.002.
[470] Slavin YN, Asnis J, Häfeli UO, Bach H. Metal nanoparticles: understanding the mechanisms behind antibacterial activity. J Nanobiotechnol 2017;15:65. https://doi.org/10.1186/s12951-017-0308-z.
[471] Chatterjee AK, Chakraborty R, Basu T. Mechanism of antibacterial activity of copper nanoparticles. Nanotechnology 2014;25:135101. https://doi.org/10.1088/0957-4484/25/13/135101.
[472] Sirelkhatim A, Mahmud S, Seeni A, Kaus NHM, Ann LC, Bakhori SKM, et al. Review on Zinc Oxide Nanoparticles: Antibacterial Activity and Toxicity Mechanism. Nano-Micro Lett 2015;7:219–42. https://doi.org/10.1007/s40820-015-0040-x.
[473] Ning C, Wang X, Li L, Zhu Y, Li M, Yu P, et al. Concentration Ranges of Antibacterial Cations for Showing the Highest Antibacterial Efficacy but the Least Cytotoxicity against Mammalian Cells: Implications for a New Antibacterial Mechanism. Chem Res Toxicol 2015;28:1815–22. https://doi.org/10.1021/acs.chemrestox.5b00258.
[474] Wahab R, Mishra A, Yun S-I, Kim Y-S, Shin H-S. Antibacterial activity of ZnO nanoparticles prepared via non-hydrolytic solution route. Appl Microbiol Biotechnol 2010;87:1917–25. https://doi.org/10.1007/s00253-010-2692-2.
[475] Fowler L, Engqvist H, Öhman-Mägi C. Effect of copper ion concentration on bacteria and cells. Materials 2019;12:3798. https://doi.org/10.3390/ma12223798.
[476] Tian Y, Cao H, Qiao Y, Meng F, Liu X. Antibacterial activity and cytocompatibility of titanium oxide coating modified by iron ion implantation. Acta Biomater 2014;10:4505–17. https://doi.org/10.1016/j.actbio.2014.06.002.
[477] Shahed CA, Ahmad F, Günister E, Foudzi FM, Ali S, Malik K, et al. Antibacterial mechanism with consequent cytotoxicity of different reinforcements in biodegradable magnesium and zinc alloys: A review. J Magnesium Alloys 2023;11:3038–58. https://doi.org/10.1016/j.jma.2023.08.018.
[478] Jennifer M, Maciej W. Nanoparticle Technology as a Double-Edged Sword: Cytotoxic, Genotoxic and Epigenetic Effects on Living. Cells 2013; 2013.. https://doi.org/10.4236/jbnb.2013.41008.
[479] Li P, Dai J, Li Y, Alexander D, Čapek J, Geis-Gerstorfer J, et al. Zinc based biodegradable metals for bone repair and regeneration: Bioactivity and molecular mechanisms. Mater Today Bio 2024;25:100932. https://doi.org/10.1016/j.mtbio.2023.100932.
[480] Cui G, Bi Z, Zhang R, Liu J, Yu X, Li Z. A comprehensive review on graphene-based anti-corrosive coatings. Chem Eng J 2019;373:104–21. https://doi.org/10.1016/j.cej.2019.05.034.
[481] Mohammadrezaei D, Golzar H, Rezai Rad M, Omidi M, Rashedi H, Yazdian F, et al. In vitro effect of graphene structures as an osteoinductive factor in bone tissue engineering: A systematic review. J Biomed Mater Res A 2018;106:2284–343. https://doi.org/10.1002/jbm.a.36422.
[482] Zuo R. Biofilms: strategies for metal corrosion inhibition employing microorganisms. Appl Microbiol Biotechnol 2007;76:1245–53. https://doi.org/10.1007/s00253-007-1130-6.
[483] Lou Y, Chang W, Cui T, Wang J, Qian H, Ma L, et al. Microbiologically influenced corrosion inhibition mechanisms in corrosion protection: A review. Bioelectrochemistry 2021;141:107883. https://doi.org/10.1016/j.bioelechem.2021.107883.
[484] Zhang T, Tremblay P-L. Graphene: An Antibacterial Agent or a Promoter of Bacterial Proliferation? iScience 2020;23:101787. DOI: 10.1016/j.isci.2020.101787.
[485] Cao G, Yan J, Ning X, Zhang Q, Wu Q, Bi L, et al. Antibacterial and antibiofilm properties of graphene and its derivatives. Colloids Surf B Biointerfaces 2021;200:111588. https://doi.org/10.1016/j.colsurfb.2021.111588.
[486] Neoh KG, Hu X, Zheng D, Kang ET. Balancing osteoblast functions and bacterial adhesion on functionalized titanium surfaces. Biomaterials 2012;33:2813–22. https://doi.org/10.1016/j.biomaterials.2012.01.018.
[487] Palmieri V, Lattanzi W, Perini G, Augello A, Papi M, Spirito MD. 3D-printed graphene for bone reconstruction. 2D Mater 2020;7:022004. https://doi.org/10.1088/2053-1583/ab6a5d.
[488] Anselme K, Davidson P, Popa AM, Giazzon M, Liley M, Ploux L. The interaction of cells and bacteria with surfaces structured at the nanometre scale. Acta Biomater 2010;6:3824–46. https://doi.org/10.1016/j.actbio.2010.04.001.
[489] Mukhortova YR, Pryadko AS, Chernozem RV, Pariy IO, Akoulina EA, Demianova IV, et al. Fabrication and characterization of a magnetic biocomposite of magnetite nanoparticles and reduced graphene oxide for biomedical applications. Nano-Struct Nano-Objects 2022;29:100843. https://doi.org/10.1016/j.nanoso.2022.100843.
[490] Tarcan R, Todor-Boer O, Petrovai I, Leordean C, Astilean S, Botiz I. Reduced graphene oxide today. J Mater Chem C 2020;8:1198–224. https://doi.org/10.1039/C9TC04916A.
[491] Tang M, Song Q, Li N, Jiang Z, Huang R, Cheng G. Enhancement of electrical signaling in neural networks on graphene films. Biomaterials 2013;34:6402–11. https://doi.org/10.1016/j.biomaterials.2013.05.024.
[492] Fattahi P, Yang G, Kim G, Abidian MR. A Review of Organic and Inorganic Biomaterials for Neural Interfaces. Adv Mater 2014;26:1846–85. https://doi.org/10.1002/adma.201304496.

[493] Kim S, Zhou S, Hu Y, Acik M, Chabal YJ, Berger C, et al. Room-temperature metastability of multilayer graphene oxide films. Nature Mater 2012;11:544–9. https://doi.org/10.1038/nmat3316.
[494] Huo Y, Guo R, Lin K, Ai Y. Insights into interface mechanism of three typical antibiotics onto the graphene oxide/chitosan composite: Experimental and theoretical investigation. Chin J Chem Phys 2023;36:211. https://doi.org/10.1063/1674-0068/cjcp2106111.
[495] Liu Y, Nie P, Yu F. Enhanced adsorption of sulfonamides by a novel carboxymethyl cellulose and chitosan-based composite with sulfonated graphene oxide. Bioresour Technol 2021;320:124373. https://doi.org/10.1016/j.biortech.2020.124373.
[496] Mohan VB, Brown R, Jayaraman K, Bhattacharyya D. Characterisation of reduced graphene oxide: Effects of reduction variables on electrical conductivity. Mater Sci Eng B 2015;193:49–60. https://doi.org/10.1016/j.mseb.2014.11.002.
[497] Compton OC, Jain B, Dikin DA, Abouimrane A, Amine K, Nguyen ST. Chemically Active Reduced Graphene Oxide with Tunable C/O Ratios. ACS Nano 2011;5:4380–91. https://doi.org/10.1021/nn1030725.
[498] Yang Y, Asiri AM, Tang Z, Du D, Lin Y. Graphene based materials for biomedical applications. Mater Today 2013;16:365–73. https://doi.org/10.1016/j.mattod.2013.09.004.
[499] Xie H, Cao T, Rodríguez-Lozano FJ, Luong-Van EK, Rosa V. Graphene for the development of the next-generation of biocomposites for dental and medical applications. Dent Mater 2017;33:765–74. https://doi.org/10.1016/j.dental.2017.04.008.
[500] Lava Kumar P, Lombardi A, Byczynski G, Narayana Murty SVS, Murty BS, Bichler L. Recent advances in aluminium matrix composites reinforced with graphene-based nanomaterial: A critical review. Prog Mater Sci 2022;128:100948. https://doi.org/10.1016/j.pmatsci.2022.100948.
[501] Güler Ö, Bağcı N. A short review on mechanical properties of graphene reinforced metal matrix composites. J Mater Res Technol 2020;9:6808–33. https://doi.org/10.1016/j.jmrt.2020.01.077.
[502] Qin Y, Wen P, Guo H, Xia D, Zheng Y, Jauer L, et al. Additive manufacturing of biodegradable metals: Current research status and future perspectives. Acta Biomater 2019;98:3–22. https://doi.org/10.1016/j.actbio.2019.04.046.
[503] Demir AG, Monguzzi L, Previtali B. Selective laser melting of pure Zn with high density for biodegradable implant manufacturing. Addit Manuf 2017;15:20–8. https://doi.org/10.1016/j.addma.2017.03.004.
[504] Abou Neel EA, Ahmed I, Pratten J, Nazhat SN, Knowles JC. Characterisation of antibacterial copper releasing degradable phosphate glass fibres. Biomaterials 2005;26:2247–54. https://doi.org/10.1016/j.biomaterials.2004.07.024.
[505] Zhao D, Yu K, Sun T, Jing X, Wan Y, Chen K, et al. Material–Structure–Function Integrated Additive Manufacturing of Degradable Metallic Bone Implants for Load-Bearing Applications. Advanced Functional Materials n.d.;n/a:2213128. DOI: 10.1002/adfm.202213128.
[506] Yamagishi K, Ogawa Y, Ando D, Sutou Y, Koike J. Room temperature superelasticity in a lightweight shape memory Mg alloy. Scr Mater 2019;168:114–8. https://doi.org/10.1016/j.scriptamat.2019.04.023.
[507] Zhao W, Zhang K, Guo E, Zhao L, Tian X, Tan C. Martensitic transformation mechanism of Mg-Sc lightweight shape memory alloys. Scr Mater 2022;207:114316. https://doi.org/10.1016/j.scriptamat.2021.114316.
[508] Felice IO, Shen J, Barragan AFC, Moura IAB, Li B, Wang B, et al. Wire and arc additive manufacturing of Fe-based shape memory alloys: Microstructure, mechanical and functional behavior. Mater Des 2023;231:112004. https://doi.org/10.1016/j.matdes.2023.112004.
[509] Amini A, Hameed N, Church JS, Cheng C, Asgari A, Will F. Effect of graphene layers on the thermomechanical behaviour of a NiTi shape memory alloy during the nanoscale phase transition. Scr Mater 2013;68:420–3. https://doi.org/10.1016/j.scriptamat.2012.11.012.
[510] Kausar A, Ahmad I, Aldaghri O, Ibnaouf KH, Eisa MH. Shape Memory Graphene Nanocomposites—Fundamentals, Properties, and Significance. Processes 2023;11:1171. https://doi.org/10.3390/pr11041171.
[511] Lu HZ, Ma HW, Luo X, Wang Y, Wang J, Lupoi R, et al. Microstructure, shape memory properties, and in vitro biocompatibility of porous NiTi scaffolds fabricated via selective laser melting. J Mater Res Technol 2021;15:6797–812. https://doi.org/10.1016/j.jmrt.2021.11.112.
[512] Tiwari JK, Mandal A, Sathish N, Agrawal AK, Srivastava AK. Investigation of porosity, microstructure and mechanical properties of additively manufactured graphene reinforced AlSi10Mg composite. Addit Manuf 2020;33:101095. https://doi.org/10.1016/j.addma.2020.101095.
[513] Carluccio D, Demir AG, Caprio L, Previtali B, Bermingham MJ, Dargusch MS. The influence of laser processing parameters on the densification and surface morphology of pure Fe and Fe-35Mn scaffolds produced by selective laser melting. J Manuf Process 2019;40:113–21. https://doi.org/10.1016/j.jmapro.2019.03.018.
[514] Dong R, Zhang T, Feng X. Interface-Assisted Synthesis of 2D Materials: Trend and Challenges. Chem Rev 2018;118:6189–235. https://doi.org/10.1021/acs.chemrev.8b00056.
[515] Fereiduni E, Ghasemi A, Elbestawi M. Characterization of composite powder feedstock from powder bed fusion additive manufacturing perspective. Materials 2019;12:3673. https://doi.org/10.3390/ma12223673.
[516] Chen M, Qin X, Zeng G. Biodegradation of Carbon Nanotubes, Graphene, and Their Derivatives. Trends Biotechnol 2017;35:836–46. https://doi.org/10.1016/j.tibtech.2016.12.001.
[517] Wang J, Cui C, Nan H, Yu Y, Xiao Y, Poon E, et al. Graphene sheet-induced global maturation of cardiomyocytes derived from human induced pluripotent stem cells. ACS Appl Mater Interfaces 2017;9:25929–40. https://doi.org/10.1021/acsami.7b08777.
[518] Niknam Z, Hosseinzadeh F, Shams F, Fath-Bayati L, Nuoroozi G, Mohammadi Amirabad L, et al. Recent advances and challenges in graphene-based nanocomposite scaffolds for tissue engineering application. J Biomed Mater Res A 2022;110:1695–721. https://doi.org/10.1002/jbm.a.37417.
[519] Shen X, Kim J-K. 3D graphene and boron nitride structures for nanocomposites with tailored thermal conductivities: recent advances and perspectives. Funct Compos Struct 2020;2:022001. https://doi.org/10.1088/2631-6331/ab953a.
[520] Gu D, Shi X, Poprawe R, Bourell DL, Setchi R, Zhu J. Material-structure-performance integrated laser-metal additive manufacturing. Science 2021;372:eabg1487. https://doi.org/10.1126/science.abg1487.
[521] Fang TH, Li WL, Tao NR, Lu K. Revealing extraordinary intrinsic tensile plasticity in gradient nano-grained copper. Science 2011;331:1587–90. https://doi.org/10.1126/science.1200177.
[522] Chen K, Wang C, Hong Q, Wen S, Zhou Y, Yan C, et al. Selective laser melting 316L/CuSn10 multi-materials: Processing optimization, interfacial characterization and mechanical property. J Mater Process Technol 2020;283:116701. https://doi.org/10.1016/j.jmatprotec.2020.116701.
[523] Kolken HMA, Janbaz S, Leeflang SMA, Lietaert K, Weinans HH, Zadpoor AA. Rationally designed meta-implants: a combination of auxetic and conventional meta-biomaterials. Mater Horiz 2018;5:28–35. https://doi.org/10.1039/C7MH00699C.
[524] Peng C, Fox K, Qian M, Nguyen-Xuan H, Tran P. 3D printed sandwich beams with bioinspired cores: Mechanical performance and modelling. Thin-Walled Struct 2021;161:107471. https://doi.org/10.1016/j.tws.2021.107471.
[525] Zhang X, Jiang L, Yan X, Wang Z, Li X, Fang G. Revealing the apparent and local mechanical properties of heterogeneous lattice: a multi-scale study of functionally graded scaffold. Virtual and Physical Prototyping 2023;18:e2120406. https://doi.org/10.1080/17452759.2022.2120406.
[526] Chu W-S, Kim C-S, Lee H-T, Choi J-O, Park J-I, Song J-H, et al. Hybrid manufacturing in micro/nano scale: A Review. Int J of Precis Eng and Manuf-Green Tech 2014;1:75–92. https://doi.org/10.1007/s40684-014-0012-5.
[527] Sefene EM, Hailu YM, Tsegaw AA. Metal hybrid additive manufacturing: state-of-the-art. Prog Addit Manuf 2022;7:737–49. https://doi.org/10.1007/s40964-022-00262-1.
[528] Kim D, Ferretto I, Leinenbach C, Lee W. 3D and 4D Printing of Complex Structures of Fe-Mn-Si-based shape memory alloy using laser powder bed fusion. Adv Mater Interfaces 2022;9:2200171. https://doi.org/10.1002/admi.202200171.
[529] Ferretto I, Kim D, Della Ventura NM, Shahverdi M, Lee W, Leinenbach C. Laser powder bed fusion of a Fe–Mn–Si shape memory alloy. Addit Manuf 2021;46:102071. https://doi.org/10.1016/j.addma.2021.102071.
[530] Sun J, Gu D, Lin K, et al. Laser powder bed fusion of diatom frustule inspired bionic NiTi lattice structures: compressive behavior and shape memory effect[J]. Smart Materials and Structures, 2022, 31(7): 074003. doi. 10.1088/1361-665X/ac767f.
[531] Kilian D, Cometta S, Bernhardt A, Taymour R, Golde J, Ahlfeld T, et al. Core–shell bioprinting as a strategy to apply differentiation factors in a spatially defined manner inside osteochondral tissue substitutes. Biofabrication 2022;14:014108. https://doi.org/10.1088/1758-5090/ac457b.

[532] Chen C, Chen J, Wu W, Shi Y, Jin L, Petrini L, et al. In vivo and in vitro evaluation of a biodegradable magnesium vascular stent designed by shape optimization strategy. Biomaterials 2019;221:119414. https://doi.org/10.1016/j.biomaterials.2019.119414.
[533] Zhu J, Zhou H, Wang C, Zhou L, Yuan S, Zhang W. A review of topology optimization for additive manufacturing: Status and challenges. Chin J Aeronaut 2021; 34:91–110. https://doi.org/10.1016/j.cja.2020.09.020.
[534] Balla VK, Bodhak S, Bose S, Bandyopadhyay A. Porous tantalum structures for bone implants: Fabrication, mechanical and in vitro biological properties. Acta Biomater 2010;6:3349–59. https://doi.org/10.1016/j.actbio.2010.01.046.
[535] Garner E, Kolken HMA, Wang CCL, Zadpoor AA, Wu J. Compatibility in microstructural optimization for additive manufacturing. Addit Manuf 2019;26:65–75. https://doi.org/10.1016/j.addma.2018.12.007.
[536] Garner E, Wu J, Zadpoor AA. Multi-objective design optimization of 3D micro-architected implants. Comput Methods Appl Mech Eng 2022;396:115102. https://doi.org/10.1016/j.cma.2022.115102.
[537] Gao Z, Ren P, Wang H, Tang Z, Wu Y, Wang H. Additive manufacture of ultrasoft bioinspired metamaterials. Int J Mach Tool Manu 2024;195:104101. https://doi.org/10.1016/j.ijmachtools.2023.104101.
[538] Du JR, Yang H, Zheng J, Ma K, Du C, Du F. Electric-field-assisted formation of cellulose triacetate/edge-oxidized graphene oxide mixed-matrix membranes for pervaporation desalination. Carbon 2023;215:118478. https://doi.org/10.1016/j.carbon.2023.118478.
[539] Wan S, Zheng Y, Shen J, Yang W, Yin M. "On–off–on" Switchable Sensor: A Fluorescent Spiropyran Responds to Extreme pH Conditions and Its Bioimaging Applications. ACS Appl Mater Interfaces 2014;6:19515–9. https://doi.org/10.1021/am506641t.
[540] Kalelkar PP, Riddick M, García AJ. Biomaterial-based antimicrobial therapies for the treatment of bacterial infections. Nat Rev Mater 2022;7:39–54. https://doi.org/10.1038/s41578-021-00362-4.
[541] Callens SJP, Arns CH, Kuliesh A, Zadpoor AA. Decoupling Minimal Surface Metamaterial Properties Through Multi-Material Hyperbolic Tilings. Adv Funct Mater 2021;31:2101373. https://doi.org/10.1002/adfm.202101373.
[542] Smith WPJ, Wucher BR, Nadell CD, Foster KR. Bacterial defences: mechanisms, evolution and antimicrobial resistance. Nat Rev Microbiol 2023;21:519–34. https://doi.org/10.1038/s41579-023-00877-3.